Alma Mater Studiorum – Università di Bologna

DOTTORATO DI RICERCA IN
GEOFISICA

Ciclo XXVII

Settore Concorsuale di afferenza: 04/A4- GEOFISICA

Settore Scientifico disciplinare: GEO/10 – GEOFISICA DELLA TERRA SOLIDA

UNDERSTANDING BLOCK ROTATION OF STRIKE-SLIP FAULT ZONES: PALEOMAGNETIC AND STRUCTURAL APPROACH

Presentata da: CATALINA HERNANDEZ MORENO

Coordinatore Dottorato

_____

Prof. Michele Dragoni

Relatore

_____

Dr. Fabio Speranza

Esame finale anno 2015

ALMA MATER STUDIORUM
UNIVERSITÀ DEGLI STUDIO DI BOLOGNA
Facoltà di Scienze Matematiche Fisiche e Naturali

Dottorato di ricerca in Geofisica
XXVII Ciclo
Settore scientifico disciplinare: GEO/10

UNDERSTANDING BLOCK ROTATION OF STRIKE-SLIP FAULT ZONES: PALEOMAGNETIC AND STRUCTURAL APPROACH

PhD. Thesis by:
Catalina Hernandez Moreno

Tutor:
Dr. Fabio Speranza

Coordinator:
Prof. Michele Dragoni

2015

Agradecimientos

Quiero agradecer a todas aquellas personas que han contribuido a despertar en mí la pasión por la investigación. A Yolanda Aguirre profesora de la Universidad de Caldas y a Jairo Alonso Osorio de la Agencia Nacional de Hidrocarburos (Colombia), quienes desde el inicio de mi carrera como geóloga me impulsaron a continuar; y en especial a Hans Diederix del Servicio Geológico Colombiano, con quien compartí equipo de trabajo y con quien aún hoy conservo una valiosa amistad, porque con su energía inagotable y amor por la tectónica activa me ha demostrado cuán importante es dar valor a lo que haces y sobretodo hacerlo con pasión.

A Giovanny Jimenez Diaz por haberme apoyado al inicio de este recorrido.

A Fabio Speranza, tutor de este trabajo, por haberme dado la oportunidad de continuar con mi preparación académica y por haberme introducido en el interesante mundo del paleomagnetismo llevándome a descubrir zonas geológicamente privilegiadas como lo son el centro-sur de Chile y la Tierra de Fuego. En quien además de encontrar un profesor siempre disponible, he encontrado un amigo. Le agradezco su paciencia y todos sus consejos.

A Marco Maffione del Departamento de Ciencias de la Tierra de la Universidad de Utrecht (Holanda) con quien participé del trabajo en Tierra de Fuego y quien ha colaborado en la elaboración de la publicación relacionada con dicho trabajo.

A la profesora Natalia Gómez-Pérez de la Universidad de los Andes con quien colaboré durante mi estancia en Bogotá, y en general a todo el equipo de Geociencias que hicieron mi estadía más amable.

A las bellas personas que he encontrado en mi camino que hacen que todo sea especial y que todos los lugares a los que llego parezcan llenos de encanto y cosas buenas. A todos los amigos del "pollaio" de los que he recibido una amistad incondicional y sin los que mis años en Roma no hubieran sido iguales, con quienes he aprendido tantas cosas, desde el idioma hasta cuales son los rincones más bonitos de la ciudad eterna, lugar que seguramente añoraré siempre: Enkelejda Qamili mi asesora legal y experta en burocracia italiana, a Giovanna Forlenza amiga sincera, Matteo Taroni, Irene Munafò, Maria Grazia De Caro; y muy especialmente a Anita Di Chiara y Javier Pavón-Carrasco quienes además me han compartido desinteresadamente sus conocimientos en paleomagnetismo y experiencias en el mundo de la investigación, son un ejemplo para mí. A Anita Di Chiara debo además agradecer los buenos recuerdos que me quedan de nuestras campañas de campo en Chile y por toda su ayuda con el muestreo paleomagnético, sobre el que se basa gran parte de esta investigación.

No quiero olvidar a mis amigos de siempre, del alma, de la UDC, Laura Montoya y Juan Diego Jiménez, quienes aunque lejos, están disponibles y me acompañan siempre.

Quiero agradecer también a Alberto Tomé, la alegría de mi vida, que con su apoyo y compañía ha hecho más fácil sacar adelante este mi proyecto de vida, a pesar de todos estos años en los que he estado lejos de mi familia y de mi tierra. Por algún tiempo fue el mejor asiste de campo en Chile!

A mi familia que cada vez que regreso hace parecer como si el tiempo que hemos estado lejos fuera poco y se esfuerzan siempre porque estemos unidos. Pero sobretodo quiero agradecer a mi Mamá, a quien le debo todo lo que soy. Por su constancia sin límites y su compañía, porque sé que aunque para ella han pesado mucho las ausencias y la distancia, ha sabido transmitirme su fuerza y me ha impulsado siempre a alcanzar mis metas. Para ella siempre serán todos mis logros.

TABLE OF CONTENTS

Abstract

This thesis is focused on the analysis of the paleomagnetic rotation pattern inside the deforming zone of strike-slip faults, and the kinematics and geodynamics that can describe it. These topics have been addressed in different tectonically active zones along the Chilean margin (38º-42ºS) and the Austral Andes (around 54ºS) of South America through detailed paleomagnetic investigations.

At 38°-42°S the margin-parallel component of the strain partitioning lead by the oblique subduction of the Nazca oceanic plate below South America since at least 50 Ma, has been accommodated along the Liquiñe-Ofqui fault zone (LOFZ), a major active dextral strike-slip system that straddles the volcanic arc of south-central Chile. This fault system is composed by two NNE-trending right stepping straight lineaments that decoupled a fore-arc sliver (Chiloé Block) from the rest of the overriding plate, and by NW-trending curved sinistral faults that seem to splay off west of the straight lineaments. NW faults control along-strike fore-arc segmentation, separating blocks with different Pre-Andean orogeny stories.

The paleomagnetic investigation carried out along the LOFZ and inside the fore-arc sliver (98 paleomagnetic sites gathered from Oligocene to Pleistocene volcanics and Miocene granites) revealed an asymmetric rotation pattern, consistently with previous studies. East of the LOFZ and adjacent to it, rotations are up to 150°-170° clockwise (CW), and fade out ~10 km east of fault. In turn, west of the LOFZ, an unexpected counterclockwise (CCW) rotation pattern has been documented. While sites at 42ºS (Chiloé Island) and ~130 km away from the LOFZ yield systematic CCW rotations (between 27° and 164º), paleomagnetic sites at 40°-41°S (Ranco-Osorno domain) and adjacent to the LOFZ (fore-arc eastern margin) revealed CW rotations up to 136° before evolving to CCW rotations at ~30 km from the fault. Around 39°S (Villarrica domain) ubiquitous CCW rotations have been observed.

These data may suggest that the rotation sense distribution is function of plate coupling along subduction interface. Zones of high coupling will induce high LOFZ strength, yielding to a ~30 km wide deforming zone west of the LOFZ characterized by CW rotations. Conversely, low coupling imply a weak LOFZ, a lack of CW rotations, and a fore-arc entirely dominated by CCW rotations related to NW-SE sinistral fault kinematics. These inferences on plate locking are in good agreement with those derived by GPS analysis, and indicate that seismotectonic segments coupling has remained virtually unchanged during the last 5 Ma.

Considering geodynamic models the rotation pattern is consistent with a quasi-continuous crust kinematics, characterized by small rigid blocks (1 to10 km size range) drag by the underlying

ductile crust flow, where CW (CCW) rotations are related to dextral (sinistral) faults. However, it seems unlikely that the lower crust flux can control the block rotation in the upper crust, considering that the cold and thick fore-arc crust inhibits the gradient velocity transmission of the underlying material flux until the upper crust. Therefore, I suggest that the rotations are the consequence of forces applied directly on the block edges themselves and along the main fault, within the upper crust.

Farther south, the southernmost segment of the Andean chain (Austral Andes, 54°S) is the result of alternating compressive, extensional and strike-slip tectonics occurring during Cretaceous-Miocene times. Here I aimed at evaluating the influence of the Magallanes-Fagnano sinistral strike-slip fault on the configuration of the arcuate Patagonian Orocline, but the paleomagnetism of the collected samples failed. Consequently, I measured the anisotropy of magnetic susceptibility (AMS) of 22 Upper Cretaceous to Upper Eocene sites gathered from the Magallanes fold-thrust belt internal domains. The data document that the Southern Andes underwent continuous compression from the Early Cretaceous until the Late Oligocene. Magnetic anisotropy data also show that the tectonic inversion of pre-existing Jurassic extensional faults during the Late Cretaceous compressive phase may have controlled the Cenozoic kinematic evolution of the Magallanes fold-thrust belt, yielding slip partitioning that can effectively explain both the current geometry and the kinematic evolution of the Southern Andes.

Guide of this thesis

This research is divided in six parts.

The Part I includes three chapters. The first one contains a state-of-the-art of the kinematic models of block rotation, fundamental setting to this research. The subsequent chapters describe the aim of this research and a brief overview of the paleomagnetic application in the solution of tectonic problems, in special making reference to obtain vertical-axis rotation and strain proxy.

The subsequent parts of the text are dedicated to present the results of the research of vertical-axis rotation pattern related to strike-slip faults. Thus, in the Part II are reported the outcomes from the research along the Liquiñe-Ofqui fault zone (LOFZ) in the southern-central Chile, published on *Tectonics* as *Hernandez-Moreno et al*. [2014]. Part III includes the results of the paleomagnetic analysis of the rotation pattern along the Chiloé fore-arc sliver, also in the central-southern Chile, and is presented for first time the application of the paleomagnetism as a tool to inferred coupling degree variations along the subduction interface.

Part IV contains the results of the paleomagnetic research carried out at the internal structural domain of the Magallanes fold and thrust belt, in the austral part of the Andean Cordillera (Tierra de Fuego-Argentina). There using anisotropy of magnetic susceptibility (AMS) measurements was possible inferred how has been the evolution of the Southern Andes from the Early Cretaceous until the Late Oligocene. However a rotational pattern could not obtained due to the erratic magnetic behavior of the sampled rocks.

Part V includes a short part of the research developed during my stage at the Universidad de los Andes at Bogotá, during the second PhD year. In this stage I developed a 2D basic numerical model with the aim to reproduce the starting configuration of the Liquiñe-Ofqui deforming zone, using the paleomagnetic results and all the available geologic information.

Finally, in part VI there are the concluding remarks of this research.

PART I. Kinematic models of block rotation related to strike-slip faulting

PART I. KINEMATIC MODELS OF BLOCK ROTATION RELATED TO STRIKE-SLIP FAULTING

1. Introduction

A fundamental component of the intraplate deformation of Earth occurs in strike-slip tectonic domains, yielding both strike-slip fault displacement and vertical-axis rotation of crustal blocks [*Freund*, 1974*; Garfunkel*, 1974; *MacDonald*, 1980; *Lamb and Bibby*, 1989; *Jackson and Molnar*, 1990].

During the last decades, several different geometric models have been suggested to explain the pattern of deformation and paleomagnetic rotation into strike-slip fault zones. These models consider geologic parameters as crust rheology, length, sense and total slip of the main shear zone, structural arrangement, deforming zone width, and deformation scale. When some of these parameters are known with good approximation, the rotation amount can be quantified using simple mathematic relations. Paleomagnetic measurements along first-order strike-slip faults have been used to validate the models: Dead Sea transform fault [Israel, *Ron et al.*, 1984], North Anatolian fault zone [Turkey, *Piper et al.*, 1997], Las Vegas Valley shear zone [Western US, *Sonder et al.*, 1994], Alpine Fault [New Zealand, *Randall et al.*, 2011], Eneko and Tanna fault zones [Japan, *Kimura et al.*, 2004, 2011], fault systems of the Aegean Sea [central Greece, *McKenzie and Jackson*, 1986], Alpine Himalayan Belt [Iran, *Jackson and McKenzie*, 1984], and San Andreas Fault System [Central California, *McKenzie and Jackson*, 1983; *Terres and Luyendyk*, 1985; *Titus et al.*, 2011].

Depending on block size and shape, and rotation pattern, models can be subdivided in three main groups, called discontinuous, continuous, or quasi-continuous models.

The *discontinuous* or *discrete models* consider the bookshelf tectonics [*Ransome et al.*, 1910; *Morton and Black*, 1975; *Cowan et al.*, 1986; *Mandl*, 1987]. Here sets of strike-slip faults (secondary faults) inside a shear zone bound rigid or undeformed blocks with similar dimensions to the width of the shear zone [*Ron et al.*, 1984; *Garfunkel and Ron*, 1985; *McKenzie and Jackson*, 1986; *Nur et al.*, 1986] (Figure 1). These blocks rotate around vertical axis as a consequence of space accommodation problem within the deforming zone bounded by the two main strike-slip faults. Therefore, secondary faults rotate along with adjacent blocks [*McKenzie and Jackson*, 1986; *Nur et al*., 1986].

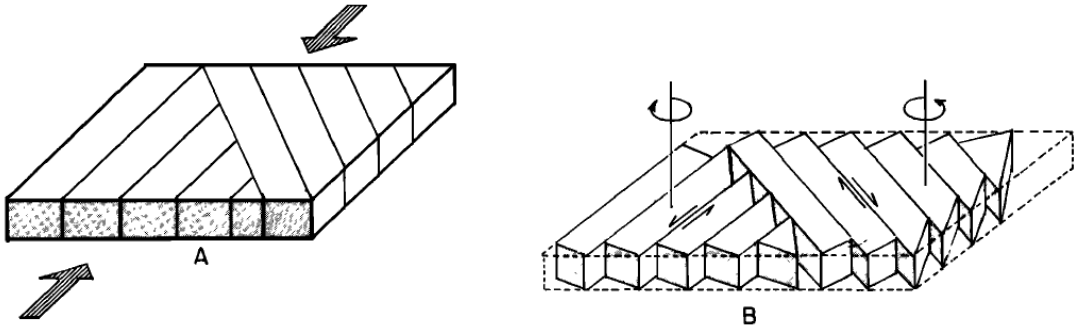

Figure 1. 3D model showing simultaneous strike-slip displacement and rotation of fault-bounded blocks. A) Initial configuration, B) After deformation. Modified from *Ron et al*. [1984].

Within the same domain, rotation is spatially constant in amount and sense, cannot exceed 90º, and decreases to zero when the secondary faults become parallel to the domain boundary. In the case of sets of conjugate faults, expected rotations should be of both senses: CW (CCW) at blocks bounded by sets of left-lateral (right-lateral) strike-slip faults (Figure 1) [*Freund*, 1974; *Garfunkel*, 1974; *Ron et al.*, 1984; *Garfunkel and Ron*, 1985; *McKenzie and Jackson*, 1986; *Beck et al.*, 1993]. The block length changes to accommodate rotations, and the geometry at the strike-slip bounding faults tips may be complex. It can be represented by splaying faults [*Freund*, 1974] or bending [*Hoeppener et al.*, 1969], and the strike-slip motion is transformed to dip slip or to diffuse deformation [*Ron et al.*, 1984].

Among the discrete models there is the *slate model* [*Ron et al.*, 1984; *Garfunkel and Ron*, 1985; *Mckenzie and Jackson*, 1986; *Nur et al.*, 1986] (Figure 2). This model predicts the amount of vertical axis rotation and the overall strain of the faulted domain parallel to the boundary, as:

$$\frac{d}{w} = \frac{sin\,\delta}{sin\,\propto \sin\,(\propto -\delta)} = cot\,(\propto -\delta) - cot \propto \quad (\mathbf{1})\,; \quad \lambda = \frac{l}{l_0} = \frac{\sin(\propto -\delta)}{\sin \propto} \qquad (\mathbf{2})$$

Where d: displacement along the fault (positive when right-lateral)

w: faulted block width

α: initial angle between faults and domain boundary

δ: rotation angle (positive when CCW)

λ: faulted domain length parallel to the its boundary

l_0: faulted block initial width

l: faulted block width after rotation

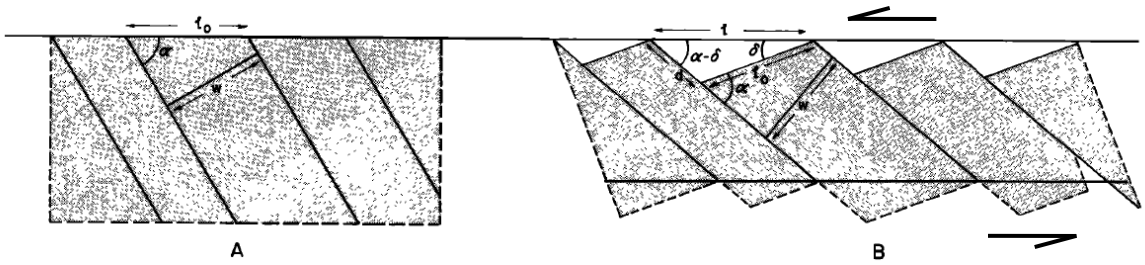

Figure 2. Slate or floating block model. Quantitative relation between the strike-slip displacement and the rotation of the fault-bounded blocks. Modified from *Ron et al*. [1984].

McKenzie and Jackson [1986] proposed the *floating block model*, compatible with the previous *slate model* [*Ron et al.*, 1984], and the *pinned block model* where the length of each rotating block will remain constant because they are pinned to moving apart plates on either side of the deforming zone (Figure 3).

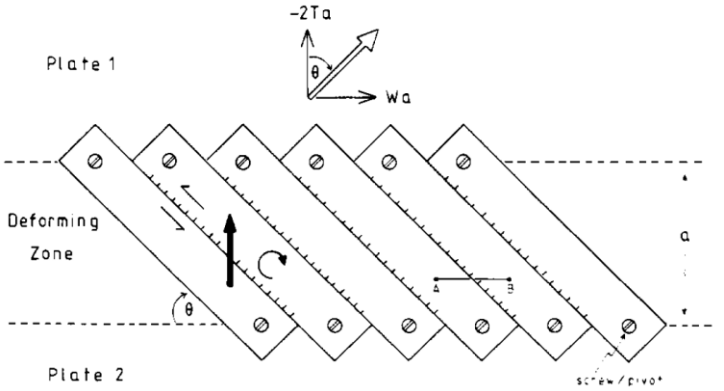

Figure 3. Pinned block model constructed from wooden slats screwed to two parallel, larger slats. The large white arrow indicates Plate 1 motion relative to Plate 2, with components *-2Ta* normal to the zone and *Wa* parallel to the zone. The large black arrow indicates the slip vector between adjacent blocks, which involves both normal and left-lateral strike-slip motion. The blocks rotate in a clockwise direction. *a* deforming zone width, *2T* rate of crustal thickening (negative if crustal extension occurs). Modified from *McKenzie and Jackson* [1986].

In the pinned block model the plates motion will be distributed inside the deforming zone by block rotations and extension between them, by the instantaneous components of velocity -2*Ta* normal to the zone and *Wa* along the strike of the zone. Given the relative movement across the

whole zone (W and T), there is only one possible orientation of the faults (θ) to satisfy the deformation distribution:

$$tan\,\theta = -{}^{W}/_{2T} \qquad (\mathbf{3})$$

If $W = 0$ then $\theta = 0$, so there is no strike-slip motion neither rotation. The θ value will change over time. The *simple broken slat model* of *Taymaz et al.* [1991] (Figure 4) shares the statements of the pinned model of *McKenzie and Jackson* [1986].

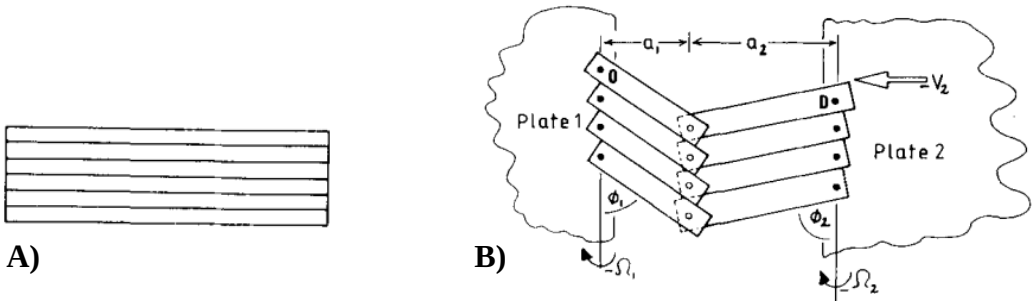

Figure 4. Simple broken slat model. The slats are attached to the plates 1 and 2 though screws (black circles). White circles are screws that join only the two arms of each broken slat. A) Starting configuration, B) After deformation. Modified from *Taymaz et al*. [1991].

A different geometric configuration of the secondary faults which bound rigid blocks inside the shear zone is the *buttress effect model* [*Beck*, 1991; *Beck et al.*, 1993] (Figure 5). It explains the rotation pattern along margin-parallel strike-slip faults as a consequence of unfavorable displacement conditions of the fore-arc or crust sliver at the overriding plate in a convergence margin, due to buttress or physical impediment which can prevent its displacement or reduce its velocity.

The buttress can be geometric when the continental margin trend changes abruptly, or due to changes in the physical properties of the overriding plate, subducting plate age, or angle of both plate convergence and subduction. In this way the sliver velocity (*Vs*) would be a small fraction of its predicted magnitude:

$$\mathrm{Vs} = V * \sin\theta \qquad (\mathbf{4})$$

Where Vs: sliver displacement velocity

V: plates convergence velocity

θ : plates convergence angle

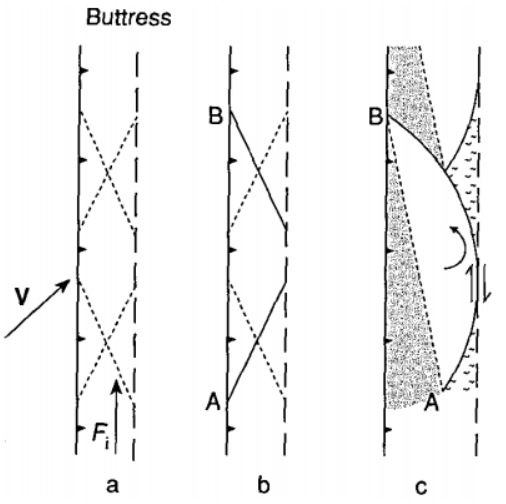

Figure 5. Buttress effect model. a) Northward sliver motion by oblique subduction is prevented by buttress. Resulting compression produces conjugate fractures (short-dash lines). Incipient master strike-slip fault shown by long-dash line; b) Roughly half-lens shaped blocks form; c) Half-lens shaped blocks move northward by rotating counterclockwise and overlapping one another. Sliver widens thereby. Dot pattern indicates areas of potential sedimentary basins; wriggle pattern shows areas of compression and potential uplift. Modified from *Beck et al*. [1993].

The buttress causes a space problem solved by crust thickening and/or widening. Widening results in curved strike-slip fault segments that break the sliver into arcuate crustal blocks, which driven by the shear coming from the oblique subduction, rotate CCW (CW) in dextral shear zone (sinistral) and move forward overlapping one another causing areas of extension and compression (Figure 5).

The second group models correspond to the *continuous models*. *McKenzie and Jackson* [1986] postulated that if the scale of deformation has a large wavelength compared to the brittle layer crust thickness, the surface deformation can be expected to look continuous. Conversely to the discontinuous models, the shear is here distributed inside the deforming zone with no through-going faults over a wide uniform domain (Figure 6). Rotations are expected to be CW (CCW) in right-lateral (left-lateral) fault systems, to progressively increase towards the fault, and to be up to 90º in magnitude [*Kimura et al.*, 2004, 2011].

Based on the assumption that the entire lithosphere behaves as a thin viscous sheet [*Bird and Piper*, 1980; *England and McKenzie*, 1982; *Sonder and England*, 1986], these models suggest that the rotation occurs in the brittle upper crust that forms a thin rigid plastic veneer upon the rest of the lithosphere. Deforming upper crust presumably follows passively the motion of the deeper parts of

the lithosphere, expected to behave like a viscous medium [*England et al*., 1985; *Sonder et al*., 1986; *England and Wells*, 1991].

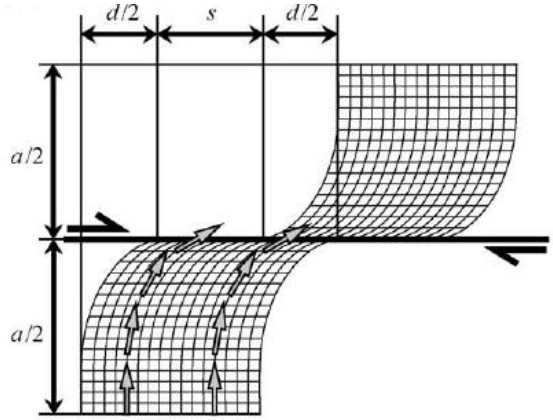

Figure 6. Continuous deformation model. The amount of rotation at a point close to the fault trace is larger than at a point far from the fault. *a* width of the shear zone; *d* displacement parallel to the fault caused by strike-slip deformations, *s* strike-slip offset on the fault trace. Modified from *Nelson and Jones* [1987].

The continuous models consider necessary add the drag deformation within the shear zone (*d*, continuous rotational drag) to the offset on the fault trace (*s*, rigid deformation) to quantify the total displacement of strike-slip faults (Figure 6). Ignore the drag deformation yields to underestimation of both individual faulting events magnitude and fault slip rates [*Salyards et al.*, 1992; *Nagy and Sieh*, 1993; *Kimura et al.*, 2004, 2011].

The continuous drag deformation *d* along a strike-slip fault and the amount of rotation at any point following the *Kimura et al.* [2004; 2011] equations are defined respectively by:

$$d = 2 \text{ x} \int_0^{(1/2)a} \tan(D - Do)\, dx \qquad (5) \; ; \qquad D = ix + j \qquad (6)$$

Where: a: shear zone width

D: paleomagnetic declination (º)

D_0: regional rotation or reference declination at the site *a/2* from the fault

$(D\text{-}D_0)$: relative rotation

i: declination increase rate with distance

j: declination when $x = 0$

x: distance from the fault (m)

The continuous drag deformation *d* can also be calculated based on the power law rheology model [*England et al.,* 1985]. Thus, *Kimura et al.* [2011] propose an equation that expresses the relation between distance from a fault trace *y* (km) and the relative rotation θ around vertical-axis (rad):

$$\theta = arctan\left(\frac{4Ds\pi\sqrt{n}}{L} exp\left(-\frac{4\pi\sqrt{n}}{L}y\right)\right) \qquad (7)$$

Where: *Ds*: displacement in one side of the fault (km)

L/2: fault length (km)

n: power-law exponent or stress exponent. It provides an indication of the relative contributions of brittle and ductile behavior to the average lithospheric strength [*McKenzie and Jackson*, 1983; *Sonder and England*, 1986; *Nelson and Jones*, 1987]. A *n* value between 3 to 5 indicates ductile behavior of the lower crust [*Sonder et al*., 1986], while greater values correspond to brittle faulting near the surface [*Sonder and England*, 1986].

The third group, the *quasi-continuous* models, are also based on a viscous model for lithospheric deformation [*England and McKenzie*, 1982; *England et al.*, 1985; *Sonder et al.*, 1986; *Sonder and England*, 1986; *England and Wells*, 1991]. Here the thin viscous sheet represents the ductile middle and lower crusts under the uppermost brittle seismogenic crust, which unlike to the continuous models, are broken into small rigid blocks with sizes smaller than the shear zone width (Figure 7). Block rotations occur in response to the angular velocity of the ductile deformation taking place at great depth in the lower crust [*Beck*, 1976; *McKenzie and Jackson*, 1983; *Lamb*, 1987; *Nelson and Jones*, 1987; *Salyards et al*., 1992; *Sonder et al*., 1994; *Piper et al*., 1997; *Randall et al*., 2011].

The rotation magnitude will depend on fault length, displacement amount, lithosphere rheology, block aspect ratio (short/long axis) and their orientation with respect to the system-bounding fault [*Lamb*, 1987; *Piper et al.*, 1997; *Randall et al.*, 2011]. The rotation is CW (CCW) in regions of dextral (sinistral) shear, and increases gradually getting closer to the fault, reaching values greater than 90º [*Nelson and Jones*, 1987; *Sonder et al.*, 1994; *Piper et al.*, 1997].

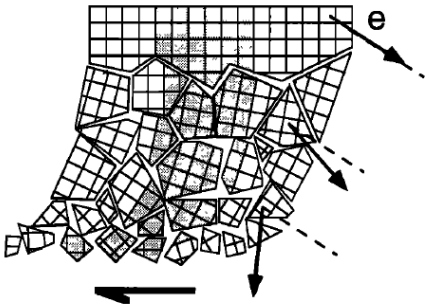

Figure 7. Small-block (quasi-continuous model). Modified from *Lamb* [1987].

One of the most simple quasi-continuous models is the *ball bearing fashion* [*Beck*, 1976; *Piper et al.*, 1997], where crustal blocks can rotate freely like balls in a bearing into narrow zones bounded by strike-slip faults parallel to the main shear zone (Figure 8). As the rotation is a continue process, brittle destruction at the corners of the blocks tends to produce subrounded equidimensional blocks.

The relationship between fault displacement D and rotation φ (expressed as a proportion of 360º) of a fault block of width a approximated by a freely moving circular block is:

$$D = \varphi \pi a \qquad (\mathbf{8})$$

But rotating blocks are not usually equidimensional, as might be required to accommodate very large rotations prevented by the friction between them [*Nur et al.*, 1986].

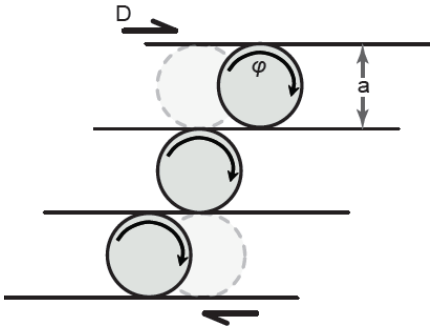

Figure 8. Ball bearing fashion model. Modified from *Beck* [1976] and *Piper et al*. [1997].

As from structural observations may not be possible to know the block size or size distribution since its edges may or may not correlate with mapped faults, *Sonder et al.* [1994] present two block geometry models to estimate the maximum characteristic block size associated with a strike-slip fault (Figure 9).

The first model to equal blocks rotating independently, considers a rigid circular block of radius *R* sampled at a distance *r* from its center (Figure 9a). The probability $\bar{p}$ that a locality a distance *L* away from *r* has indistinguishable from that at *r* is given by:

$$p(R,L,Q,r) = \begin{cases} 1 & L \leq R - r \\ Q + \frac{(1-Q)}{\pi} cos^{-1}\left[\frac{R^2+r^2-L^2}{2rL}\right] & R - r < L < R + r \\ Q & R + r \leq L \end{cases} \quad (9)$$

The probability *Q* depends on the measurement uncertainties of the two localities and is defined by *Q* = 2(average declination difference (Δ*D*) between the analyzed sites)/360, in any case would be <<1.

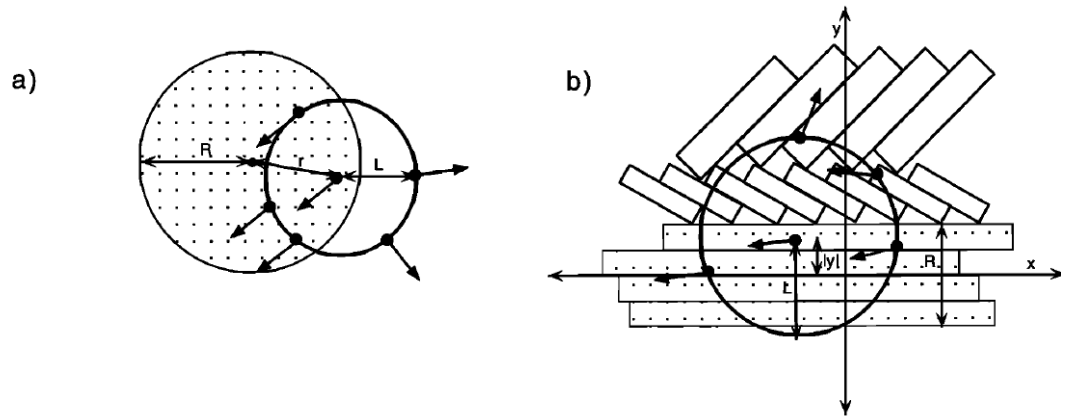

Figure 9. Models proposed by *Sonder et al*. [1994] to estimate block size. Arrows indicate paleomagnetic declinations at hypothetical localities. a) Circular block model, *R* is the radius of shaded rigid circular block, *r* the position of a locality relative to the center of the block, and *L* the interlocality distance, $\bar{p}$ (the average probability that a site a distance *L* from the locality at *r* is indistinguishable from that at *r*) is related to the fraction of the circle of radius *L* inside the rigid block (shaded circle). b) Domain block model. In this case *R* is the width of the domain, |*y*| the distance from the domain axis of a locality, and *L* the distance of other localities from the first. Modified from *Sonder et al*. [1994].

The equation (9) assumes that all paleomagnetic localities in different blocks from a reference site have a probability *Q* ($0 \leq Q \leq 1$) of being indistinguishable, but localities within the same block are identical (*Q* = 1). As usually *r* value is unknown, the average probability $\bar{p}$ may be calculated in function of the block area, where:

$$\bar{p}(R,L,Q) = \int_0^R p(R,L,Q,r)\frac{2\pi r}{\pi R^2}dr \qquad (\mathbf{10})$$

If declination differences between pairs of paleomagnetic localities are plot as function of the distances between localities and then it is compares with theoretical values (Figure 8 therein *Sonder et al.* [1994]), a measure of block size *R* may be estimated.

The second case concerns to highly elongated blocks rotating together as domains [*McKenzie and Jackson*, 1983, 1986; *Ron et al.*, 1984; *Taymaz et al.*, 1991] (Figure 9b). If *R* is the width domain perpendicular to the direction of elongation, domain length is >>*R*, and rotations of different domains are random. For a locality positioned at a perpendicular distance |y| from the axis of symmetry of a domain, the probability $\bar{p}$ that a second locality a distance *L* away is indistinguishable, is given by:

$$p(R,L,Q,|y|) = \begin{cases} 1 & |y|+L \le R/2 \\ \frac{(1+Q)}{2} + \frac{1}{\pi}(1-Q)\sin^{-1}\left[\frac{\frac{R}{2}-|y|}{L}\right] & R/2 < |y|+L < R \\ Q + \frac{1}{\pi}(1-Q)\left[\sin^{-1}\left[\frac{\frac{R}{2}-|y|}{L}\right] + \sin^{-1}\left[\frac{\frac{R}{2}+|y|}{L}\right]\right] & R \le |y|+L \end{cases} \qquad (\mathbf{11})$$

For *L/R* < 1 (locality spacing less than block size), $\bar{p}$ is the same as that given by a circular model. Only when *L/R* >1 in a domain model, regardless of the value *L*, there are always localities along domain strike with indistinguishable rotations. In return in a circular block model when *L* is large, the localities pairs always lie in two different blocks and thus have a finite chance of being indistinguishable. As in this domain model the interlocality distance *L* is measured perpendicular to the domain strike, rather than along the line connecting localities, the average probability $\bar{p}$ can be determined analytically as:

$$\bar{p} = \begin{cases} Q\,\frac{L}{R} + \left(1 - \frac{L}{R}\right) & L \le R \\ Q & L > R \end{cases} \qquad (\mathbf{12})$$

Sonder et al. [1994], using a thin viscous sheet model [e.g. *England and McKenzie*, 1982; 1983], also give an equation to calculate the rotation rate assuming infinitesimal circular blocks lying on

top of the thin sheet, when the along-strike component of fluid velocity (u) is much greater than the across-strike component (v) (Figure 10):

$$\dot{\theta} = -\frac{1}{2}\frac{\partial u}{\partial y} = -\frac{2u_0 n^{\frac{1}{2}}\pi}{\lambda}\sin(2\pi x/\lambda)\exp(-4n^{\frac{1}{2}}\pi y/\lambda) \qquad (\mathbf{13})$$

Positive (negative) values represent CCW (CW) rotations. If velocities are constant in time, then the rotation of any material point is approximately:

$$\theta = -\frac{2d(x)n^{1/2}\pi}{\lambda}\exp(-4n^{\frac{1}{2}}\pi y/\lambda) \qquad (\mathbf{14})$$

Where $d(x)$ is the displacement of the boundary point ($x,0$) with respect to the point at (x,a) and λ shear zone length. The n value can range from 3, corresponding to creep of lower crustal or mantle materials (olivine), to infinity to plastic deformation of the upper crust [*Sonder and England*, 1986].

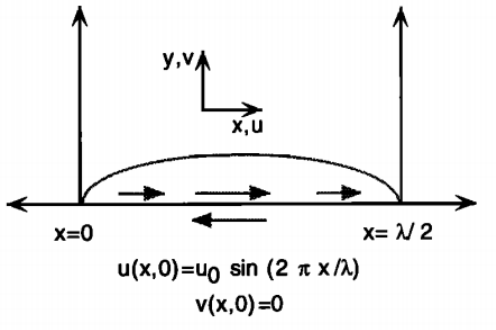

Figure 10. Sketch of boundary conditions used to calculate distribution of rotations using the thin viscous sheet model. Modified from *Sonder et al*. [2004].

Conversely, *Lamb* [1987] and *Randall et al.* [2011] in their *shear rotation model* showed ellipsoidal blocks whose rotation rate and amount are in function of both their aspect ratio (k = short axis b/long axis a) and orientation with respect to the system bounding fault through time (Figure 11). Thus, this model predicts a marked decrease in rotation rate for elongate blocks (k <1, constant) when they rotate into a direction more nearly parallel with the shear zone margins [*Randall et al*., 2011]. Conversely, if the aspect ratio k increases by breakup during rotation (k ~ 1), the resulting equidimensional block will continue to rotate at a constant rate [*Lamb*, 1987].

For a width shear zone *W*, and fault displacement *D*, the total amount of rotation at any particular time, given the initial orientation ϕ_i of the long block axis *a*, is determined by the ratio *D*/*W* and the aspect ratio *k* [*Lamb*, 1987].

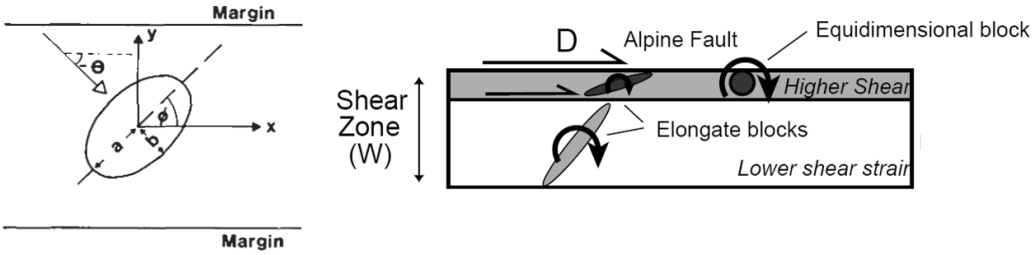

Figure 11. Shear rotation model. The fixed axis (*x*,*y*) have origin in the center of the ellipsoidal block, and the deforming zone margins are parallel to the *x* axis. φ is the angle of the relative velocity vector between *a* (long axis of the ellipse) and the *x* axis, θ is the angle of the relative velocity vector between the two margins with the *x* axis. Negative θ values implies dextral shear and compression. Modified from *Lamb* [1987] and *Randall et al*. [2011].

For a width shear zone *W*, and fault displacement *D*, the total amount of rotation at any particular time, given the initial orientation ϕ_i of the long block axis *a*, is determined by the ratio *D*/*W* and the aspect ratio *k* [*Lamb*, 1987].

The block rotation for $k > 5$ can be approximated within 10% accuracy to that of a passive marker line, equation 15, while for $k \sim 1$ is defined by the equation 16 [*Lamb*, 1987]:

$$\theta = 90° - \phi_i + \text{atan}(D/W\ - \tan(90° - \phi_i)) \quad (\mathbf{15}) \quad ; \quad \theta = 0.5D/W \qquad (\mathbf{16})$$

If *k* does not equal to 1, also there is a simplified expression for *R*, the instantaneous rotation rate ($d\phi/dt$), by *Lamb* [1987]:

$$R = \frac{W}{2}\left[\left(\frac{1-k^2}{1+k^2}\right)(\cos 2\phi + tan\theta \sin 2\phi) - 1\right] \qquad (\mathbf{17})$$

Positive values of *R* indicate CCW rotations.

When $k = 1$, *R* is constant and equals $-W/2$ (CW to dextral shear). For $k < 1$, the rotation rate varies with orientation. For sufficiently small values of *k*, *R* changes sign for certain orientations and hence the block will rotate in the opposite direction. The overall effect of all this deformation is

a “straightening-out” of the major faults, where shear could be taken up by slip on the faults without any rotation of the intervening faults blocks or slow rotation.

The end-member of the quasi-continuous models would be in the case of elongated blocks trending approximately parallel to the relative plate motion across the strike-slip zone. Pure strike-slip is applied to blocks displacing parallel to the deformation zone, implying a lack of rotations [*Geissman et al.*, 1984; *Platzman and Platt*, 1994; *Bourne et al.*, 1998] (Figure 12). If the frictional forces on faults walls are negligible in comparison with basal traction, the block will be in equilibrium when the net drag force on their base is zero [*Bourne et al.*, 1998]. This coincides with one of the stationary states of *Lamb* [1987].

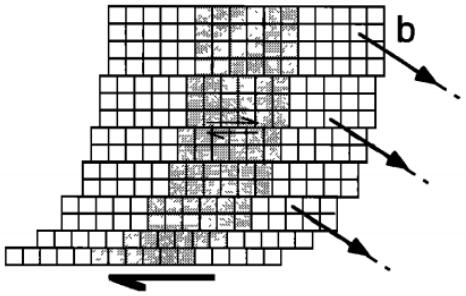

Figure 12. Transcurrent deformation by displacement on parallel faults, with no rotation. Modified from *Sonder et al*. [1994].

A different quasi-continuous model is the *S-C kinematics model* [*Rosenau et al.*, 2006], considering a conjugate set of faults into a shear zone, in turn enclosing sigmoidal shaped domains (Figure 13). In a hypothetical 2-D strain ellipse of maximum tangential shear strain ψ, right-lateral (synthetic *C*) and left-lateral (antithetic *S*) strike-slip faults represent the a/a’ and b/b’ lines, respectively (a and b undeformed state, a’ and b’ deformed state). These lines include the angle φ with the long (extensional) axis of the strain ellipse (e_1), which is 45° in the undeformed state and decrease during progressive deformation [*Wettstein*, 1886]. Thereby, into a dextral shear zone the expected rotation would be CCW for a’ (dextral synthetic faults C) and CW for b’ (sinistral antithetic faults S). According to *Rosenau et al*. [2006], both the set of conjugate faults and the blocks limited by them rotate.

The distribution of vertical axis rotations induced by shear along the conjugate faults can be inferred considering the two components of rotation in a Cartesian reference frame: line rotation $\Delta\Theta$, and rotation induced by tangential shear strain ψ along the fault. Even in absence of

quantitative fault offset constraints, this model predicts according to *Wettstein* [1886] the decrease of the angle φ between the lines a/a' and b/b' during the progressive deformation:

$$\varphi = arctan\ (1/R) \qquad (\mathbf{18})$$

Where R is the ellipticity of the finite strain ellipse. The angle φ bisector indicates the long (extensional) axis of the strain ellipse (e_1) (45º to undeformed state).

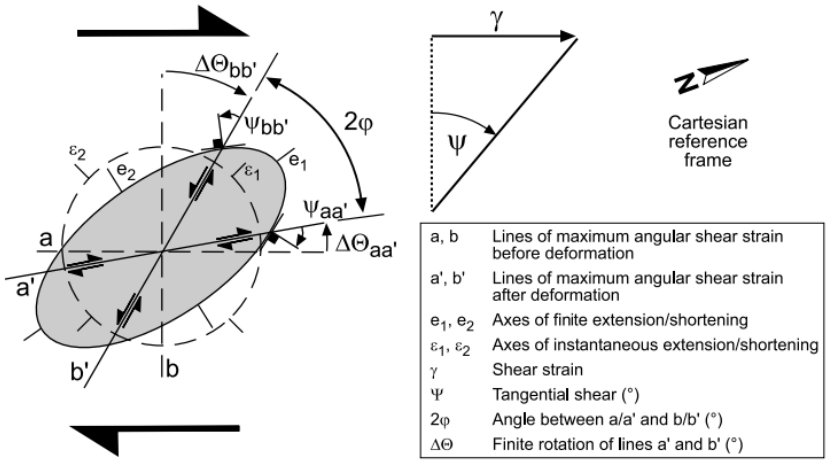

Figure 13. S-C kinematics model. Modified form *Rosenau et al.* [2006].

The shear strain γ and the tangential shear strain ψ necessary to produce the finite strain ellipse by simple shear are given by *Ramsey and Huber* [1983]:

$$\gamma = \tan\psi = (R^2 - 1)tan\varphi\ /\ (1 + R^2 tan^2\varphi) \qquad (\mathbf{19})$$

While the orientation of the shear plane with respect to the strain ellipse is given by:

$$\tan 2\theta = 2/\gamma \qquad (\mathbf{20})$$

Where θ is the angle between the long (extensional) axis of the finite strain ellipse (e_1) and the shear plane [*Ramsay and Graham*, 1970].

2. Aim of this research

Rotation pattern inside the deforming zone of strike-slip faults up today remains highly controversial. It seems that rotation pattern variability is high, depending upon fault slip rate and total amount, as well as upon crust characteristics and rheology (in turn linked to geothermal regime), and locking (i.e., shear strength) of the main fault walls [*McKenzie and Jackson*, 1986; *Sonder et al*., 1994; *Piper et al*., 1997; *Kimura et al*., 2011].

Through the paleomagnetism we are able to accurately document the distribution, sense, and amount of rotation of each single block in the fault damage zone, but the density of the reported paleomagnetic data on a specific fault are typically low that it would required. Usually, only a small percentage of the deformed rocks inside a fault zone are suitable to paleomagnetic studies, but not always these rocks give us complete information because some can lost their original paleomagnetic signal due to later overprint, a frequent drawback of paleomagnetic studies. Rotations predicted from structural data analysis, usually can lose it values because they are carry on rocks which may be rotated, without a previous quantification.

Therefore, with this research I wish to give a contribution to (**1**) understanding of the vertical-axis rotation pattern associated to strike-slip fault systems, (**2**) which is the mechanism driving it, and (**3**) how the crust behaves during the rotation process.

To reach these objectives I investigated the distribution of vertical-axis rotations inside the deforming zone of the dextral Liquiñe-Ofqui fault zone (LOFZ) and the adjacent fore-arc sliver (central-southern Chile), that are interpreted as being due the oblique convergence between the Nazca and the South American plates.

I also carried out a part of this research at the northern Magallanes fold and thrust belt border, in the austral part of the Andean Cordillera (Argentina). There, the cordillera abruptly changes its N-S trend to E-W. This trend change has been related with an oroclinal bending process arising from a CCW rotation related to the Drake Passage opening and to the development of the sinistral Magallanes-Fagnano at the South America-Scotia plate boundary.

3. Methodology

3.1. Paleomagnetism and tectonics

This subject has been vastly addressed in the last forty years by both research papers and books [*Irving* 1964; *McElhinny*, 1973; Beck 1976, 1980, 1984; *McElhinny* 1976; *Jelinek* 1977, 1978;

Hillhouse 1977; *Simpson and Cox* 1977; *Beck and Burr*, 1979; *Kamerling and Luyendyk* 1979; *Coney et al*., 1980; *Magill and Cox*, 1980; *Bates et al*., 1981; *Magill et al*., 1981; *Globerman et al*., 1982; *Magill et al*., 1982; *Demarest* 1983; *Merril and McElhinny* 1983; *Tarling* 1983; *Hillhouse and Grommé* 1984; *Coe et al*., 1985; *Luyendyk et al*., 1985; *Wells and Coe* 1985; *Beck et al*., 1986; *Grommé et al*., 1986; *May and Butler* 1986; *Hagstrum et al*., 1987; *Wells and Heller* 1988; *Butler et al*., 1989; *Butler*, 1992; *Dunlop and Özdemir* 1997; *Tauxe* 1998, 2009; *McElhinny and McFadden* 2000]. As the method is classical and well-known I will not report on it. Below I just briefly introduce some basic concepts that are essentials to understand what the rotation (*R*) and flattening (*F*) parameters investigated in this thesis at various tectonic deformation zones mean.

The geomagnetic field, if assumed as a dipolar geocentric field, can be represented as a vector framed into a three-dimensional, orthogonal coordinate system usually with origin in a specific point on the earth surface. This vector has an *H* magnitude and can be broken into two components, *Hv* vertical and *Hh* horizontal (Figure 14). Inclination *I* (angle between the horizontal plane and the geomagnetic field vector, ranging from -90° to 90° and positive when downward) and declination *D* (angle from geographic north to horizontal component, ranging from 0º to 360º, positive clockwise) completely describe the direction of the geomagnetic field.

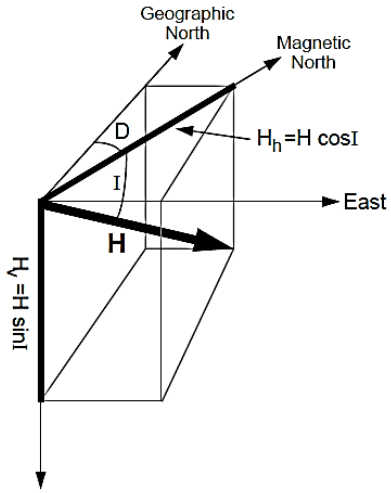

Geomagnetic field components

$$H_v = H \sin I \; ; H_h = H \cos I$$

Geographic north and east components

$$H_N = H \cos I \cos D; \; H_E = H \cos I \sin D$$

Total intensity of the geomagnetic field

$$H = \sqrt{{H_N}^2 + {H_E}^2 + {H_V}^2}$$

Figure 14. Geomagnetic field *H* components: *Hv* vertical component, *Hh* horizontal component, *I* inclination, *D* declination. Modified from *McElhinny* [1973].

The "ferromagnetic" (sensu lato) minerals contained in the rocks, record the geomagnetic field that has acted on the material and can "frozen" parallel to it under specific conditions. This is known as natural remanent magnetization (NRM). When the magnetization has been acquired at the

rock formation times it is called primary magnetization, while posterior magnetizations are known as secondary [*Butler*, 1992; *Sagnoti and Meloni*, 1993]. The paleomagnetism is the unique tool that permits us measure the intensity *H*, inclination *I* and declination *D*, and therefore deduce all the components of a remanent magnetization.

The paleomagnetism has played a central role in the solution of tectonic problems from plate scale to local events, because tectonic motions can be detected with respect to a paleomagnetic pole. Figure 15 illustrates how paleomagnetism can be used to detect vertical-axis rotation and latitudinal motion of crustal blocks. The apparent polar wander (APW) path of the continent indicates how that continent has moved with respect to the rotation axis. The set of paleomagnetic poles that make up the APW path also serve as reference poles for determining motions of crustal blocks. Each reference pole was determined by paleomagnetic analysis of rocks of a particular age from the continental interior. The reference pole can be used to calculate the expected paleomagnetic direction for rocks of that age at any point on the continent. If the measured paleomagnetic declination and inclination are different with respect to those expected, in function of the geographic position and the age of the analyzed rocks, tectonic rotations can be inferred.

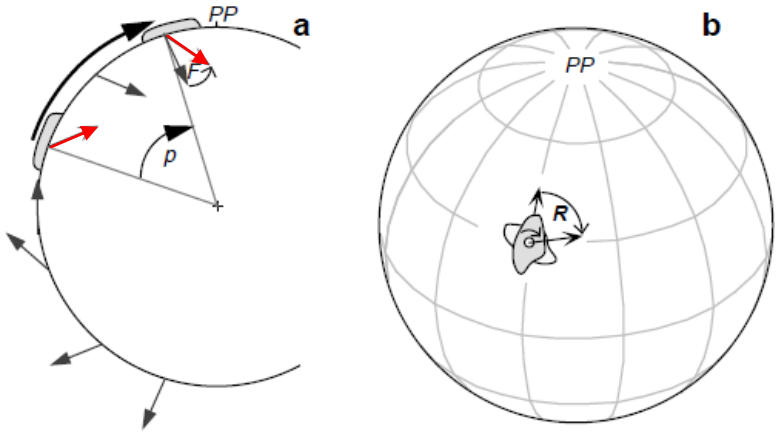

Figure 15. Discordant paleomagnetic directions resulting from tectonic movements. *PP* paleomagnetic pole. **a**) Meridional cross section of the Earth showing the directions of a dipolar magnetic field with magnetic pole at *PP*; arrows at the Earth's surface show *expected inclinations*. A block magnetized at low paleolatitude acquires a magnetization in the direction of the red arrow; transport of the block toward the paleomagnetic pole by the angle *p* results in its magnetization being shallower than the expected direction by the angle *F* (*flattening*). **b**) Rotation of the paleomagnetic declination by tectonic rotation about a vertical axis internal to the crustal block. The original orientation of the block is shown by the partially hidden outline; the present orientation is

shown by the outline filled with the heavier stippling. The paleomagnetism of rocks of this crustal block would originally have pointed along the *expected declination* toward the paleomagnetic pole *PP*. But the vertical-axis rotation produces a clockwise rotation *R*, of the *observed declination* from the *expected declination*. Modified from *Butler* [1992].

There are two basic methods of analyzing vertical-axis rotations and latitudinal motions from paleomagnetic directions, the direction-space and pole-space approaches. These methods have been developed by *Beck* [1976, 1980], *Demarest* [1983], and *Beck et al*. [1986]. In this research I use the *direction-space* approach, where the observed paleomagnetic direction for a particular site (I_o, D_o) is simply compared with the expected direction (I_x, D_x) obtained on rocks of the same age from the stable part of the continent (Figure 16). The inclination flattening or latitudinal motion *F* and the rotation *R* of declination is given by, respectively:

$$F = I_x - I_o \qquad ; \qquad R = D_o - D_x$$

R is defined as positive when D_o is clockwise with respect to D_x. The expected and observed directions both have associated confidence cones (α_{95}), so *F* and *R* have 95% confidence limits ΔF and ΔR, respectively. Results of direction-space analyses are usually reported by listings of $R \pm \Delta R$ and $F \pm \Delta F$. To a complete explanation of the confidence limit mathematical development refer to *Demarest* [1983] and *Butler* [1992].

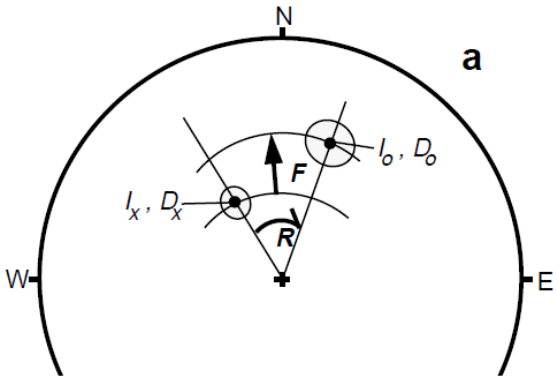

Figure 16. Equal-areal projection of an observed discordant paleomagnetic direction, inclination I_o and declination D_o, compared to an expected direction, inclination I_x and declination D_x. The observed direction is shallower than the expected direction by the flattening angle *F*. Observed declination is clockwise from the expected declination by the rotation angle *R*. Modified from *Butler* [1992].

This analytical approximation can be use when the 95% confidence cone of the paleomagnetic direction is less than 10º and the mean inclination is not too close to vertical [*Clark and Morrison*, 1981; *Demarest*, 1983]. To I >80º the paleomagnetic declination is poorly defined.

Important structural information may also come from the magnetic anisotropy studies, a field also widely investigated in the last forty years [*Janák* 1967; *Hrouda and Janák* 1976; *Jelinek* 1977, 1978; *Lowrie and Kligfield* 1981; *Borradaile* 1981, 1987, 1988; *Hrouda*, 1982; *Borradaile and Tarling* 1984; *MacDonald and Ellwood*, 1987, *Hrouda and Jelinek*, 1990; *Parés et al*., 1999]. Rocks in which intensity of magnetization, induced or remanent, depends on direction of the applied magnetic field have magnetic anisotropy. One type of magnetic susceptibility is the AMS or anisotropy of magnetic susceptibility, in which susceptibility is a function of direction of the applied field. The AMS can be use as a powerful tool for fabric analysis in different rock types [e.g. *Goldstein* 1980; *Pearce and Fueten* 1989; *Jackson and Tauxe*, 1991; *Rochette et al*., 1992; *Sagnoti and Speranza* 1993; *Tarling and Hrouda*, 1993; *Borradaile and Henry*, 1997; *Bouchez* 1997; *Mattei et al*., 1997; *Cifelli et al*., 2005].

The AMS is commonly geometrically expressed in terms of a three-axis ellipsoid: $K_1 \geq K_2 \geq K_3$, maximum, intermediate, and minimum susceptibility. The AMS ellipsoid, principal axes usually correspond to the strain ellipsoid axes, indicating that the magnetic fabric is a strain proxy, and suggesting that magnetic fabric measurements are significant with respect to the strain history of rocks [e.g. *Goldstein & Brown*, 1988]. Main AMS parameters as anisotropy degree and its shape, *Pj* and *T* respectively [*Jelinek*, 1981; *Hrouda*, 1982], are commonly used.

In weakly deformed (non-metamorphic) sedimentary rocks, AMS reflects the pristine fabric produced during incipient deformation at the time of, or shortly after, deposition and diagenesis of the sediment [*Sintubin*, 1994; *Mattei et al*., 1995; *Sagnotti et al*., 1998, 1999; *Parés et al*., 1999; *Coutand et al*., 2001; *Cifelli et al*., 2004, 2005; *Soto et al*, 2009]. AMS analysis of weakly deformed sediments have frequently been used in orogenic settings to document the syn-sedimentary tectonic regime [*Mattei et al*., 1999; *Sagnotti and Speranza*, 1993; *Sagnotti et al*., 1998; *Parés et al*., 1999; *Maffione et al*., 2008, 2012; *Macrì et al*., 2014]. During deposition, sedimentary rocks acquire a so-called 'sedimentary fabric' characterized by the k_{max} and k_{int} axes dispersed within a plane (magnetic foliation (F)) that is sub-parallel to the stratification plane. This sedimentary fabric can be partially overprinted by a 'tectonic fabric' during incipient deformation (e.g., *Parés et al*. [1999]).

The result of this process is the development of a magnetic lineation (L) whereby k_{max} aligns parallel to the maximum axis of stretching (ε_1), hence perpendicular to the maximum axis of compression (σ_1). This mechanism allows a direct correlation between the AMS and strain

ellipsoids (e.g., *Parés et al*. [1999]). In extensional settings, the magnetic lineation coincides with the local dip of the bedding, and is therefore perpendicular to the local normal fault planes [*Sagnotti et al*., 1994; *Mattei et al*., 1997, 1999; *Cifelli et al*., 2004, 2005; *Maffione et al*., 2012]. In compressional settings, the magnetic lineation is usually subhorizontal and parallel to both the local strike of the strata and the folds axes [*Sagnotti and Speranza* 1993; *Mattei et al*., 1997; *Sagnotti et al*., 1998; *Maffione et al*., 2008]. The relationship between the direction of the magnetic lineation and that of the local structure of the rock is therefore diagnostic to distinguish between a compressional and extensional tectonic magnetic lineation (e.g., *Mattei et al*., [1997]).

Increasing deformation progressively modifies the shape of the AMS ellipsoid from a pure sedimentary fabric (oblate ellipsoid: $k_{max} \approx k_{int} >> k_{min}$), to a sedimentary fabric with a marked tectonic imprint (triaxial ellipsoid: $k_{max} > k_{int} > k_{min}$), to a tectonic fabric (prolate ellipsoid: $k_{max} >> k_{int} \approx k_{min}$), and eventually returning during the highest strain to an oblate ellipsoid with the magnetic foliation parallel to the cleavage/schistosity (e.g., Parés, 2004) (Figure 17).

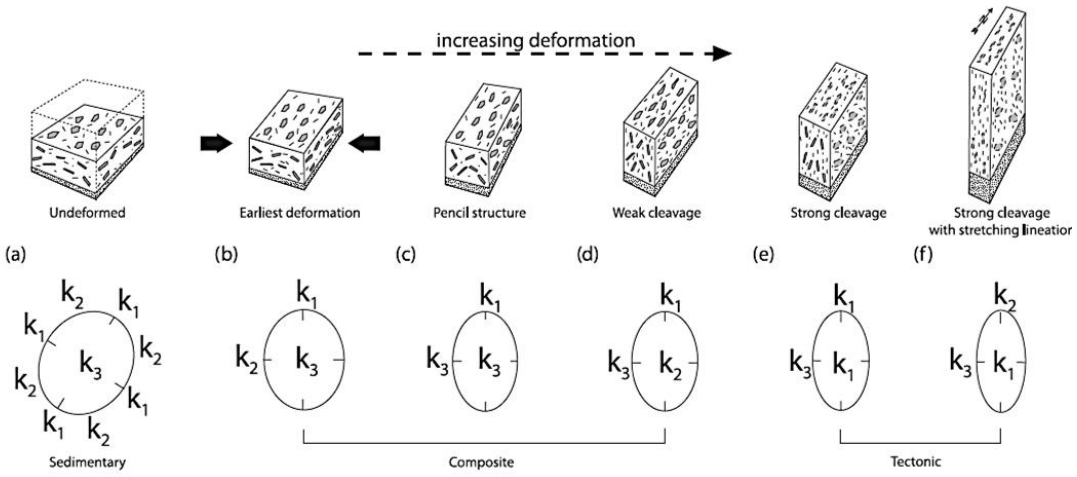

Figure 17. Magnetic fabric evolution during progressive deformation. The ellipsoid is oblate (flattened) when $K_1 \gg K_2$ but $K_2 > K_3$, and prolate (cigar-shaped) when $K_1 > K_2$, $K_2 \gg K_3$. Modified from *Graham* [1966].

In the last stage of deformation, which corresponds to incipient metamorphism, the pristine tectonic fabric developed during the initial (syn-sedimentary) phases of deformation is completely obliterated. Conversely, the pristine tectonic fabric is not easily overprinted by small strains at low temperature (e.g., *Borradaile*, 1988; *Sagnotti et al*., 1994, 1998; *Cifelli et al*., 2004, 2005; *Parés*,

2004; *Soto et al*., 2009]. This implies that, compared to classical structural geological analysis where the definition of the age of deformation requires additional constraints (i.e., crosscutting relationships or unconformities), the finite strain determined from AMS analyses of weakly deformed rocks is a direct and powerful tool that can be used to study the deformation active at the time of sedimentation.

3.2. Sampling and laboratory methods

To carry out this research, about 1400 oriented core samples were collected using a portable drill and following a classic paleomagnetic sampling scheme: several sites in the same rock unit and several samples in the same site (~10 on average). The samples include volcanic and sedimentary rocks.

All samples were demagnetized at the shielded room of the paleomagnetic laboratory of the Istituto Nazionale di Geofisica e Vulcanologia (INGV, Roma) by alternating field (AF), using a 2G Enterprises DC-superconducting quantum interference device cryogenic magnetometer and online AF device reaching a peak field of 150 mT; twin specimens from some cores were also thermally cleaned up to 680°C using a Pyrox shielded oven. Demagnetization data were plotted on orthogonal vector component diagrams [*Zijderveld*, 1976].

Analysis of low-field anisotropy of magnetic susceptibility (AMS) was done using a MFK1 Kappabridge (AGICO). The AMS parameters were evaluated using Jelinek statistics [*Jelinek*, 1977, 1978].

Magnetization components were identified by principal component analysis [*Kirschvink*, 1980]. Site-mean paleomagnetic directions were computed using *Fisher* [1953] statistics and were plotted on equal-angle projections. Rotation and flattening values with respect to South America were evaluated according to *Demarest* [1983], using the reference paleopoles from *Torsvik et al*. [2008]. To define the sense and amount of rotation, we always considered the smaller angle between the observed and expected declinations, thereby calculating rotation values always $\leq|180°|$. This is a conservative approach, although we are aware that in the past, some authors considered rotation values exceeding 180° [e.g., *Nelson and Jones*, 1987; *Piper et al*., 1997].

PART II. Understanding kinematics of intra-arc transcurrent deformation: Paleomagnetic evidence from the Liquiñe-Ofqui fault zone (Chile, 38-41º)

AGU PUBLICATIONS

Tectonics

RESEARCH ARTICLE
10.1002/2014TC003622

Key Points:
- Paleomagnetism of the Liquiñe-Ofqui dextral strike-slip fault (southern Chile)
- East of the fault blocks rotate CW up to 170 and imply a 120 km fault offset
- West of the fault, in the Chiloé fore-arc sliver, blocks rotate CCW

Correspondence to:
C. Hernandez-Moreno,
catalina.hernandezmoreno@ingv.it

Citation:
Hernandez-Moreno, C., F. Speranza, and A. Di Chiara (2014), Understanding kinematics of intra-arc transcurrent deformation: Paleomagnetic evidence from the Liquiñe-Ofqui fault zone (Chile, 38–41°S), *Tectonics*, *33*, 1964–1988, doi:10.1002/2014TC003622.

Received 25 APR 2014
Accepted 22 AUG 2014
Accepted article online 28 AUG 2014
Published online 21 OCT 2014

Understanding kinematics of intra-arc transcurrent deformation: Paleomagnetic evidence from the Liquiñe-Ofqui fault zone (Chile, 38–41°S)

Catalina Hernandez-Moreno[1,2], Fabio Speranza[1], and Anita Di Chiara[1,3]

[1]Istituto Nazionale di Geofisica e Vulcanologia, Rome, Italy, [2]Dipartimento di Fisica, Università di Bologna, Bologna, Italy, [3]Now at Department of Geophysics, University of São Paulo, São Paulo, Brazil

Abstract The Liquiñe-Ofqui fault zone (LOFZ) is a major ~1000 km long dextral shear zone of southern Chile, likely related to strain partitioning of Nazca Plate oblique convergence with South America. To understand block rotation pattern along the LOFZ, we paleomagnetically sampled 55 sites (553 samples) between 38°S and 41°S. We gathered Oligocene to Pleistocene volcanics and Miocene granites at a maximum distance of 20 km from the LOFZ, and at both sides of it. Rotations with respect to South America, evaluated for 36 successful sites, show that crust around the LOFZ is fragmented in small blocks, ~1 to 10 km in size. While some blocks (at both fault edges) undergo very large 150°–170° rotations, others do not rotate, even adjacent to fault walls. We infer that rotations affected equidimensional blocks, while elongated crust slivers were translated subparallel to the LOFZ, without rotating. Rotation pattern across the LOFZ is markedly asymmetric. East of the fault and adjacent to it, rotations are up to 150°–170° clockwise, and fade out ~10 km east of fault. These data support a quasi-continuous crust kinematics, characterized by small rigid blocks drag by the underlying ductile crust flow, and imply 120 km of total fault offset. Conversely, crust west of the LOFZ is cut by seismically active NW-SE sinistral antithetic faults, and yields counterclockwise rotations up to 170° at 8–10 km from LOFZ, besides the unrotated blocks. Further data from the Chile fore arc are needed to understand block rotation kinematics and plate dynamics west of the LOFZ.

1. Introduction

A fundamental component of the intraplate deformation of Earth occurs in strike-slip tectonic domains, yielding both strike-slip fault displacement and vertical-axis rotation of crustal blocks [*Freund*, 1974; *Garfunkel*, 1974; *MacDonald*, 1980; *Lamb and Bibby*, 1989; *Jackson and Molnar*, 1990].

Relying on both structural data and paleomagnetic measurements collected on relevant strike-slip fault zones, several different kinematic models have attempted to predict the distribution, sense, and amount of rotation inside the deforming zone [*McKenzie and Jackson*, 1986; *Sonder et al*., 1994; *Piper et al*., 1997; *Kimura et al*., 2004, 2011; *Taymaz et al*., 2007; *Randall et al*., 2011]. These attempts have been hindered by two major drawbacks: first, structural analysis data lose their value if significant rotations of the measured rocks have occurred but paleomagnetic data are lacking. Second, although paleomagnetism is in principle able to accurately document the rotation magnitude of each single block in the fault damage zone, the areal density of reported paleomagnetic data is typically low.

The main problem is that—as a rule—a small percentage of the deformed rocks inside a fault zone are suitable to paleomagnetic investigations, and, among them, some lost their original paleomagnetic signal due to later overprint, a frequent drawback of paleomagnetic studies. Therefore, the rotation pattern in a strike-slip fault zone is rarely elucidated with the high resolution that would be required. Furthermore, it seems that rotation pattern variability is high, depending upon slip rate and total amount, as well as upon crust characteristics and rheology (in turn linked to geothermal regime), and locking (i.e., shear strength) of the main fault walls [*McKenzie and Jackson*, 1986; *Sonder et al*., 1994; *Piper et al*., 1997; *Kimura et al*., 2011].

In summary, the kinematics and rotation pattern of strike-slip fault zones remain nowadays highly controversial. Several different kinematic models to accommodate transcurrent deformation have been put forward, including continuous and discontinuous deformation of the crust, and, among discontinuous end-members, different models for crustal block and/or slate rotation and displacement [e.g., *Sonder et al*., 1994].

In this paper we report on an extensive paleomagnetic investigation (55 sites and 553 paleomagnetic samples) of the Liquiñe-Ofqui fault zone (LOFZ, southern Chile, 38°S–48°S, Figure 1). Considering its dimensions (more than 1000 km in length) and the present-day activity (testified by both seismic and GPS data, yielding a displacement rate of 6.5 mm/yr [*Wang et al*., 2007]), the LOFZ is perhaps the more relevant active strike-slip fault of South America.

LOFZ is a classic intra-arc strike-slip fault system [*Hervé*, 1976, 1994; *Hervé and Thiele*, 1987; *Cembrano and Herve*, 1993; *Thomson*, 2002], interpreted as accommodating the trench parallel component of the strain partitioning between the obliquely converging Nazca and South American plates since at least 50 Ma [*Hervé*, 1976, 1994; *Beck*, 1988; *Garcia et al*., 1988; *Lavenu and Cembrano*, 1999], as well as the post 10 Ma indentation of the Chile Rise beneath the continent [*Forsythe and Nelson*, 1985] (Figure 1). The LOFZ also controls a spectacular sequence of andesitic volcanoes, arising from the subduction of the Nazca Plate beneath South America. Previous paleomagnetic studies at 29 localities [*Garcia et al*., 1988; *Cembrano et al*., 1992; *Rojas et al*., 1994; *Beck et al*., 1998, 2000] had shown moderate rotations, clockwise (CW, 8° to 49°) and counterclockwise (CCW, 8° to 30°) at the eastern and western fault walls, respectively.

Our work confirms the rotational pattern previously reported along the LOFZ and reveals further details about it. We document a quasi-continuous crust deformation pattern into a 20 km fault zone width, characterized by small blocks with 1–10 km of size range that rotate in opposite sense, and frequently exceeding 90°, at the two sides of the fault. Block rotation magnitudes seem to depend upon the distance from the fault and the block aspect ratio.

2. Kinematic Models of Block Rotation and Transcurrent Deformation

During the last decades, different geometric models have been suggested to explain the pattern of deformation and vertical-axis rotation in a strike-slip fault zone (Figure 2). These models consider geologic parameters as crust rheology, length, sense of strike-slip motion and total slip of the main shear zone, structural arrangement, deforming zone width, and deformation scale. When some of these parameters are known with good approximation, the rotation amount can be quantified using simple mathematic relations. Paleomagnetic measurements along first-order strike-slip faults have been used to validate the models: Dead Sea transform fault (Israel [*Ron et al*., 1984]), North Anatolian fault zone (Turkey [*Piper et al*., 1997; *Platzman and Platt*, 1994]), Las Vegas Valley shear zone (Western U.S. [*Sonder et al*., 1994]), Alpine Fault (New Zealand [*Randall et al*., 2011]), Eneko and Tanna fault zones (Japan [*Kimura et al*., 2004, 2011]), fault systems of the Aegean Sea (central Greece [*McKenzie and Jackson*, 1986]), Alpine Himalayan Belt (Iran [*Jackson and McKenzie*, 1984]), and San Andreas Fault System (Central California [*McKenzie and Jackson*, 1983; *Terres and Luyendyk*, 1985; *Titus et al*., 2011]).

Depending on block size and shape, and rotation pattern, models can be subdivided in three main groups, called discontinuous, continuous, or quasi-continuous models (Figure 2). The *discontinuous* or *discrete models* consider the bookshelf tectonics [*Ransome et al*., 1910; *Morton and Black*, 1975; *Cowan et al*., 1986; *Mandl*, 1987]. Here sets of strike-slip faults (secondary faults) inside a fault zone bound rigid or undeformed blocks with similar dimensions to the width of the shear zone [*Ron et al*., 1984; *Garfunkel and Ron*, 1985; *McKenzie and Jackson*, 1986; *Nur et al*., 1986]. These blocks rotate around vertical axis as a consequence of space accommodation within the deforming zone bounded by the two main strike-slip faults. Therefore, secondary faults rotate along with adjacent blocks [*McKenzie and Jackson*, 1986; *Nur et al*., 1986] (Figures 2a–2c).

Within the same domain, rotation is spatially constant in amount and sense, cannot exceed 90°, and decreases to zero when the secondary faults become parallel to the domain boundary. In the case of sets of conjugate faults, expected rotations should be of both senses: CW (CCW) at blocks bounded by sets of left-lateral (right-lateral) strike-slip faults (Figure 2b) [*Freund*, 1974; *Garfunkel*, 1974; *Ron et al*., 1984; *Garfunkel and Ron*, 1985; *McKenzie and Jackson*, 1986; *Beck et al*., 1993]. The block length changes to accommodate rotations, and the geometry at the strike-slip bounding faults tips may be complex. It can be represented by splaying faults [*Freund*, 1974] or bending [*Hoeppener et al*., 1969], and the strike-slip motion is transformed to dip slip or to diffuse deformation [*Ron et al*., 1984].

A different geometric configuration of the secondary faults inside the shear zone is proposed in the *buttress effect model* (Figure 2c) [*Beck*, 1991; *Beck et al*., 1993]. Here motion of crust slivers along a margin-parallel fault (typically a fore-arc block of the overriding plate edge) is hampered by geometric, physical, and kinematic

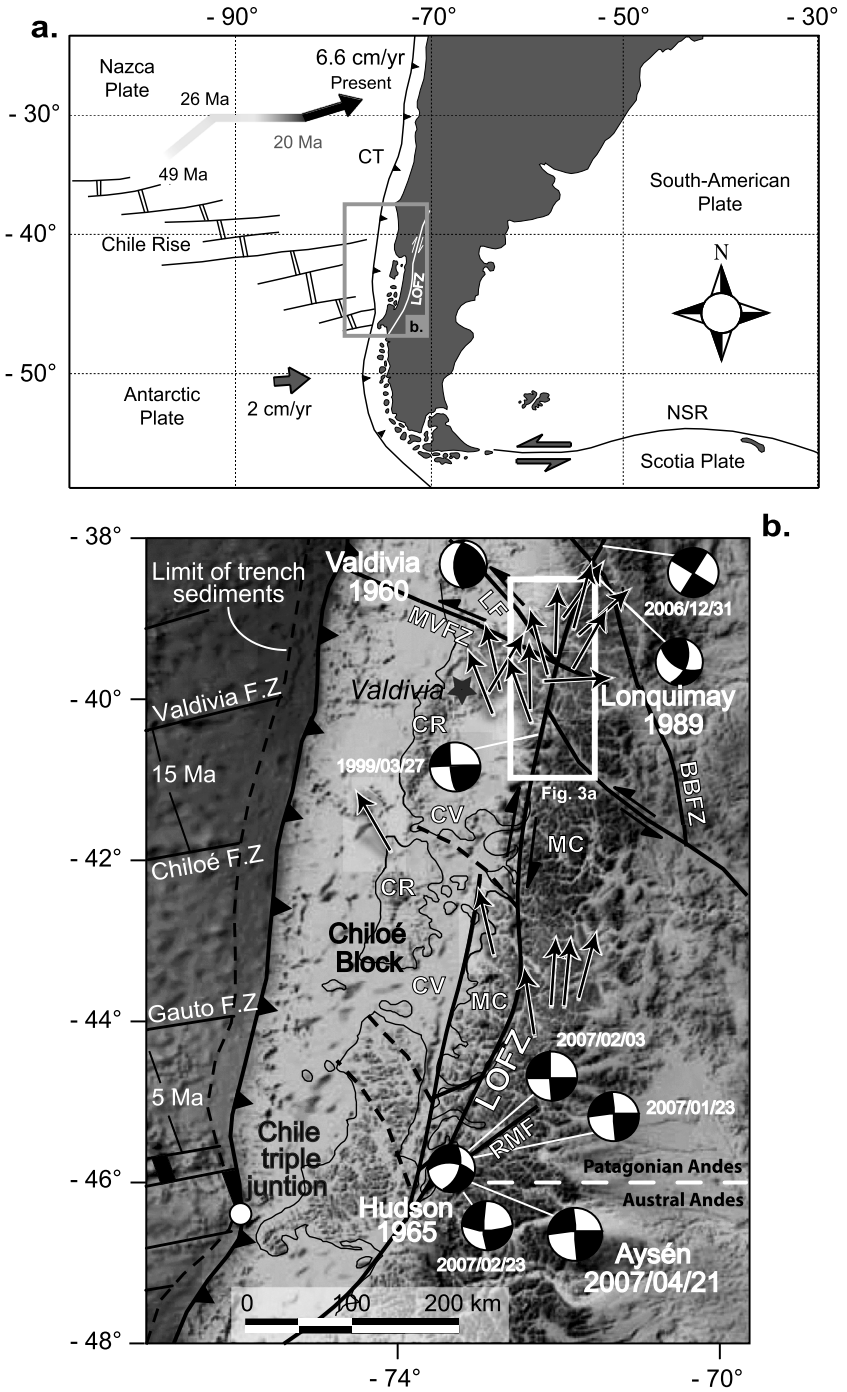

Figure 1. (a) Tectonic setting of southern South America (modified from *Diraison et al.* [1998]). Arrows indicate motions of oceanic plates relative to South America [*Pardo-casas and Molnar*, 1987; *Angermann et al.*, 1999; *Kendrick et al.*, 2003; *Quinteros and Sobolev*, 2013]. LOFZ Liquiñe-Ofqui fault zone, CT Chile Trench, NSR North Scotia Ridge. (b) Tectonic setting of Patagonian Andes showing the LOFZ traces (modified from *Lange et al.* [2008] and *Melnick et al.* [2009]). The white box marks the study area. Arrows correspond to paleomagnetic rotations recalculated from *Garcia et al.* [1988], *Cembrano et al.* [1992], and *Rojas et al.* [1994], using updated South American poles by *Torsvik et al.* [2008]. Shallow crustal focal mechanisms are also shown [*Chinn and Isacks*, 1983; *Dziewonski et al.*, 1991; *Barrientos and Acevedo-Aránguiz*, 1992]. MVFZ Mocha-Villarrica Fault Zone, BBFZ Bio-Bio fault zone, LF Lanalhue Fault, RMF Rio Mañihuales Fault, CR Coastal Range, CV Central Valley, MC Main Cordillera.

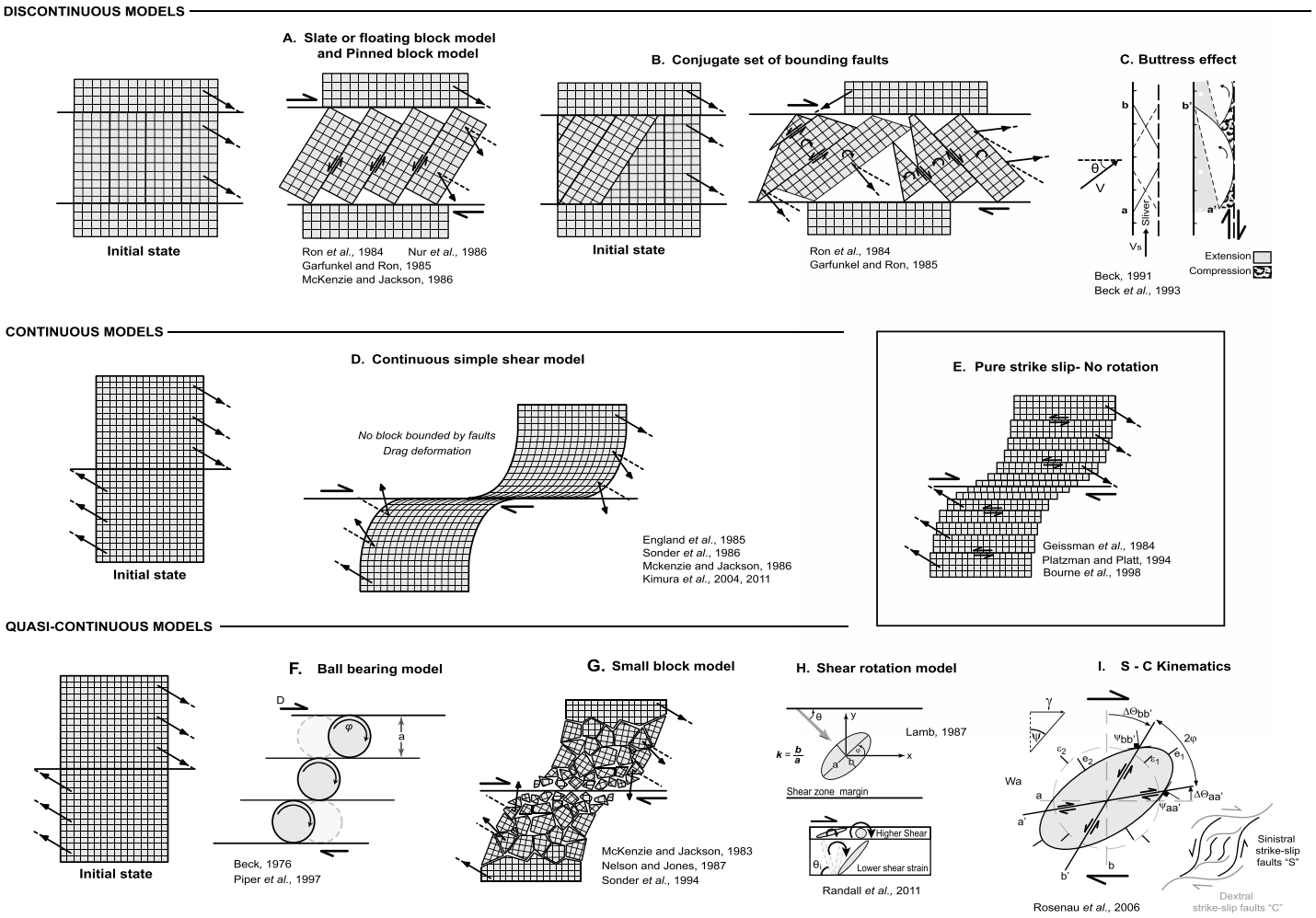

Figure 2. Kinematic models attempting to explain the distribution and amount of rotations in strike-slip fault systems. Arrows represent an original magnetization direction, subsequently rotated by tectonics (the unrotated magnetization direction is shown by dashed lines). Discontinuous or discrete models: (a) Slate or floating and pinned block models, (b) conjugate set of bounding faults into a strike-slip domain, and (c) buttress effect model overcome by sliver widening. *Continuous models*: (d) Continuous simple shear models, (e) pure strike slip—no rotation, shearing along faults parallel to the main shear zone, and *quasi-continuous models*: (f) Ball bearing model, (g) small block model, (h) shear rotation model, (i) *S-C* kinematics model.

features that induce blocks to escape laterally and rotate. This model considers curved strike-slip faults and adjacent blocks that rotate CCW (CW) in dextral (sinistral) shear zones and move forward overlapping between them and yielding domains of extension and compression.

The second group models correspond to the continuous models (Figure 2d). *McKenzie and Jackson* [1986] postulated that if the scale of deformation has a large wavelength compared to the brittle layer crust thickness, the surface deformation can be expected to look continuous. Conversely to the discontinuous models, the shear is here distributed inside the deforming zone with no through-going faults over a wide uniform domain. Rotations are expected to be CW (CCW) in right-lateral (left-lateral) fault systems, to progressively increase toward the fault, and to be up to 90° in magnitude [*Kimura et al*., 2004, 2011]. Based on the assumption that the entire lithosphere behaves as a thin viscous sheet [*Bird and Piper*, 1980; *England and McKenzie*, 1982; *Sonder and England*, 1986], this model suggests that the rotation occurs in the brittle upper crust that forms a thin rigid plastic veneer upon the rest of the lithosphere. Deforming upper crust presumably follows passively the motion of the deeper parts of the lithosphere, expected to behave like a viscous medium [*England et al*., 1985; *Sonder et al*., 1986; *England and Wells*, 1991].

The third group, the quasi-continuous models, is also based on a viscous model for lithospheric deformation [*England and McKenzie*, 1982; *England et al*., 1985; *Sonder et al*., 1986; *Sonder and England*, 1986; *England and*

Wells, 1991] (Figures 2f–2i). Here the thin viscous sheet represents the ductile middle and lower crusts under the uppermost brittle seismogenic crust, which unlike to the continuous models, are broken into small rigid blocks with sizes smaller than the shear zone width. Block rotations occur in response to the angular velocity of the ductile deformation taking place at great depth in the lower crust [*Beck*, 1976; *McKenzie and Jackson*, 1983; *Lamb*, 1987; *Nelson and Jones*, 1987; *Salyards et al*., 1992; *Sonder et al*., 1994; *Piper et al*., 1997; *Randall et al*., 2011]. The rotation magnitude will depend on fault length, displacement amount, lithosphere rheology, block aspect ratio (short/long axis), and their orientation with respect to the system-bounding fault [*Lamb*, 1987; *Piper et al*., 1997; *Randall et al*., 2011]. The rotation is CW (CCW) in regions of dextral (sinistral) shear and increases gradually getting closer to the fault, reaching values greater than 90° [*Nelson and Jones*, 1987; *Sonder et al*., 1994; *Piper et al*., 1997].

One of the most simple quasi-continuous models is the *ball bearing fashion* [*Beck*, 1976; *Piper et al*., 1997] (Figure 2f), where crustal blocks can rotate freely like balls in a bearing into narrow zones bounded by strike-slip faults parallel to the main shear zone. Brittle destruction at the block corners tends to produce equidimensional subrounded blocks. But rotating blocks are not usually equidimensional, as might be required to accommodate large rotations that are usually inhibited by friction between them [*Nur et al*., 1986]. Block rotation estimated by *Sonder et al*. [1994] do not depend significantly upon block geometry (Figure 2g). Conversely, *Lamb* [1987] and *Randall et al*. [2011] in their *shear rotation model* showed that rotation rate and amount of blocks are mainly in function of both their aspect ratio (k = short axis b/long axis a) and orientation with respect to the system bounding fault through time (Figure 2h). Thus, this model predicts a marked decrease in rotation rate for elongate blocks ($k < 1$, constant) when they rotate into a direction more nearly parallel with the shear zone margins [*Randall et al*., 2011]. Conversely, if the aspect ratio k increases by breakup during rotation ($k \sim 1$), the resulting equidimensional block will continue to rotate at a constant rate [*Lamb*, 1987].

The end-member of the quasi-continuous models would be in the case of elongated blocks trending approximately parallel to the relative plate motion across the strike-slip zone. Pure strike-slip is applied to blocks displacing parallel to the deformation zone, implying a lack of rotations [*Geissman et al*., 1984; *Platzman and Platt*, 1994; *Bourne et al*., 1998] (Figure 2e). Blocks are in equilibrium when the net drag force on their base is annulled, as the frictional forces on faults walls are negligible in comparison with basal traction [*Bourne et al*., 1998]. This coincides with one of the stationary states of *Lamb* [1987].

A different quasi-continuous model is the *S-C kinematics model* [*Rosenau et al*., 2006], considering a conjugate set of faults into a shear zone, in turn enclosing sigmoidal shaped domains (Figure 2i). In a hypothetical 2-D strain ellipse of maximum tangential shear strain ψ, right-lateral (synthetic *C*) and left-lateral (antithetic *S*) strike-slip faults represent the a/a' and b/b' lines, respectively (a and b undeformed state, a' and b' deformed state). These lines include the angle φ with the long (extensional) axis of the strain ellipse (e_1), which is 45° in the undeformed state and decrease during progressive deformation [*Wettstein*, 1886]. Thereby, into a dextral shear zone the expected rotation would be CCW for a' (dextral synthetic faults *C*) and CW for b' (sinistral antithetic faults *S*). According to *Rosenau et al*. [2006], both the set of conjugate faults and the blocks limited by them rotate.

3. Plate Tectonic Setting

The central-southern margin of Chile is one of the most active plate boundaries of Earth, where the oceanic Nazca Plate is subducting obliquely beneath the continental South American Plate (Figure 1). This area comprises the rupture zone of the 1960 Valdivia earthquake, the largest earthquake ever recorded, with M_w 9.6 and a rupture of more than 1000 km in the fore arc between ~37 and 46°S [*Plafker and Savage*, 1970].

The relative convergence between the two plates has changed both in direction and rate along the geological past [*Pardo-Casas and Molnar*, 1987; *Somoza*, 1998; *Quinteros and Sobolev*, 2013] (Figure 1a), either as a consequence of major deformational events in the South American Plate [*Somoza*, 1998] or as a result of the Nazca Plate penetration into the transition zone and lower mantle [*Quinteros and Sobolev*, 2013].

The Farallon Plate started subducting beneath South America ~50 Ma ago with a highly oblique NE direction. Afterward, between 26 and ~20 Ma ago, as a response of breakup of the Farallon Plate in the Nazca and Cocos plates, the convergence direction changed to nearly trench-orthogonal and to a higher rate (10 to ~15 cm/yr) [*Pardo-Casas and Molnar*, 1987; *Somoza*, 1998]. This period coincided with the beginning of the growth of the Andes Mountains [*Sempere et al*., 1990; *Somoza*, 1998]. Since 20 Ma ago the convergence follows a N77°E

trend [*Pardo-Casas and Molnar*, 1987; *Kendrick et al*., 2003] with a present-day rate between 6.3 and 7.9 cm/yr [*Angermann et al*., 1999; *Kendrick et al*., 2003] (Figure 1).

During the late Miocene (10 Ma), the Chile Ridge started colliding with the South American Plate, giving rise to the Chile triple junction [*Forsythe and Nelson*, 1985].

The relatively steady dextral oblique convergence between Farallon (Nazca) and South American plates since at least the Eocene (50 Ma), induces strain partitioning, with almost pure E-W shortening in the fore-arc and dextral shear in the arc, defining a typical transpressive environment, as confirmed by regional seismicity studies [*Cifuentes*, 1989; *Dewey and Lamb*, 1992; *Murdie et al*., 1993].

The dextral shear component of the oblique subduction is recorded along the intra-arc LOFZ [*Hervé*, 1976; *Beck*, 1988; *Dewey and Lamb*, 1992; *Hervé*, 1994; *Rojas et al*., 1994; *Cembrano et al*., 1996a, 2000; *Diraison et al*., 1998; *Lavenu and Cembrano*, 1999]. Different obliquity values of the Farallon (Nazca)-South America convergence vector likely yielded episodic dextral strike-slip and dip-slip deformation events along the arc [*Cembrano et al*., 1996b]. As about 26 Ma the orthogonal subduction phase caused strike-slip motion cessation and underthrusting [*Cembrano et al*., 1996b].

Besides the subduction, some authors consider the Chile Ridge collision and subduction since the middle Miocene (10–15 Ma), as the major driving force for the transpression and hence the strain partitioning [*Forsythe and Nelson*, 1985; *Murdie et al*., 1993; *Nelson et al*., 1994; *Thomson*, 2002]. The Chile Ridge acted as an indenter and together with the LOFZ caused the detachment and northward translation of the fore-arc sliver known as the Chiloé Block (37°S to ~47°S, Figure 1) parallel to the continental margin with respect to South America [*Beck*, 1988; *Beck et al*., 2000; *Forsythe and Nelson*, 1985; *Hervé*, 1976, 1994; *Nelson et al*., 1994; *Cembrano et al*., 1996a, 2000, 2002; *Lavenu and Cembrano*, 1999; *Rosenau*, 2004; *Hoffmann-Rothe et al*., 2006; *Rosenau et al*., 2006]. The northward movement of the fore-arc sliver seems to be hampered north of ~33°S by the thickened central Andean crust, the flat slab geometry, and the absence of volcanic activity that precludes strain partitioning at lithospheric scale [*Siame et al*., 2005; *Rosenau et al*., 2006].

4. Liquiñe-Ofqui Fault Zone

The LOFZ is a prominent intra-arc dextral strike-slip fault system running throughout the margin of the Main Andean Cordillera along the Miocene to the present-day volcanic arc for more than 1000 km [*Cembrano et al*., 1996a, 2007] (Figures 1 and 3). Since it is discovery by *Steffen* [1944], different authors have provided various fault length estimates [*Moreno and Parada*, 1976; *Solano*, 1978]. Currently, it is acknowledged that the LOFZ begins immediately south of the Chile triple junction in the Golfo de Penas (47°S), considered as an extensional Cenozoic basin at the trailing edge of the Chiloé Block [*Forsythe and Nelson*, 1985; *Cande and Leslie*, 1986; *Rojas et al*., 1994]. Northward, the LOFZ extends until the Copahue volcano (38°S) [*Lavenu and Cembrano*, 1999; *Rosenau et al*., 2006], where it gets into Argentina and continues through the Arauco transfer zone, in a dextral step with the active contractional Antiñir-Copahue fault zone [*Folguera et al*., 2004; *Melnick et al*., 2006a, 2006b]. In our work, we investigated the LOFZ central segment located into the Patagonian Andes, between the Llaima Volcano (38°41′S) and Rupanco Lake (41°S) (Figures 1b and 3).

The LOFZ is considered as a strike-slip duplex defined by two major NNE-trending right-stepping straight segments faults linked between 44°S and 47°S by at least four minor en echelon NE-trending structures. Curved NW-trending fault segments splay off west of the straight major fault system toward the trench (Figure 1) [*Hervé*, 1976; *Hervé and Thiele*, 1987; *Cembrano and Herve*, 1993]. Some of the curved splays are the Bio-Bio fault zone [*Bohm et al*., 2002], the Mocha-Villarrica Fault [*Melnick et al*., 2003], and the Lanalhue Fault [*Glodny et al*., 2008] (dashed lines in Figure 1b). They are mostly interpreted as long-lived basement structures reactivated as sinistral reverse strike-slip faults (displacing segments of the LOFZ) during the arc development, and not actually connected nor genetically related to the LOFZ [*Glodny et al*., 2008; *Lange et al*., 2008; *Melnick et al*., 2009]. Conversely, *Rosenau et al*. [2006] relying on cross-cutting relations, consider these arc-oblique sinistral strike-slip faults as contemporaneous with the LOFZ. Some of them cross the upper plate from the Pacific coast into the Main Cordillera, accommodate sliver motion, and separate blocks with different histories related with the pre-Andean orogeny [*Bohm et al*., 2002; *Hackney et al*., 2006; *Rehak et al*., 2008; *Melnick et al*., 2009]. Temporary seismic networks clearly document their current left-lateral strike-slip activity [*Lange et al*., 2008].

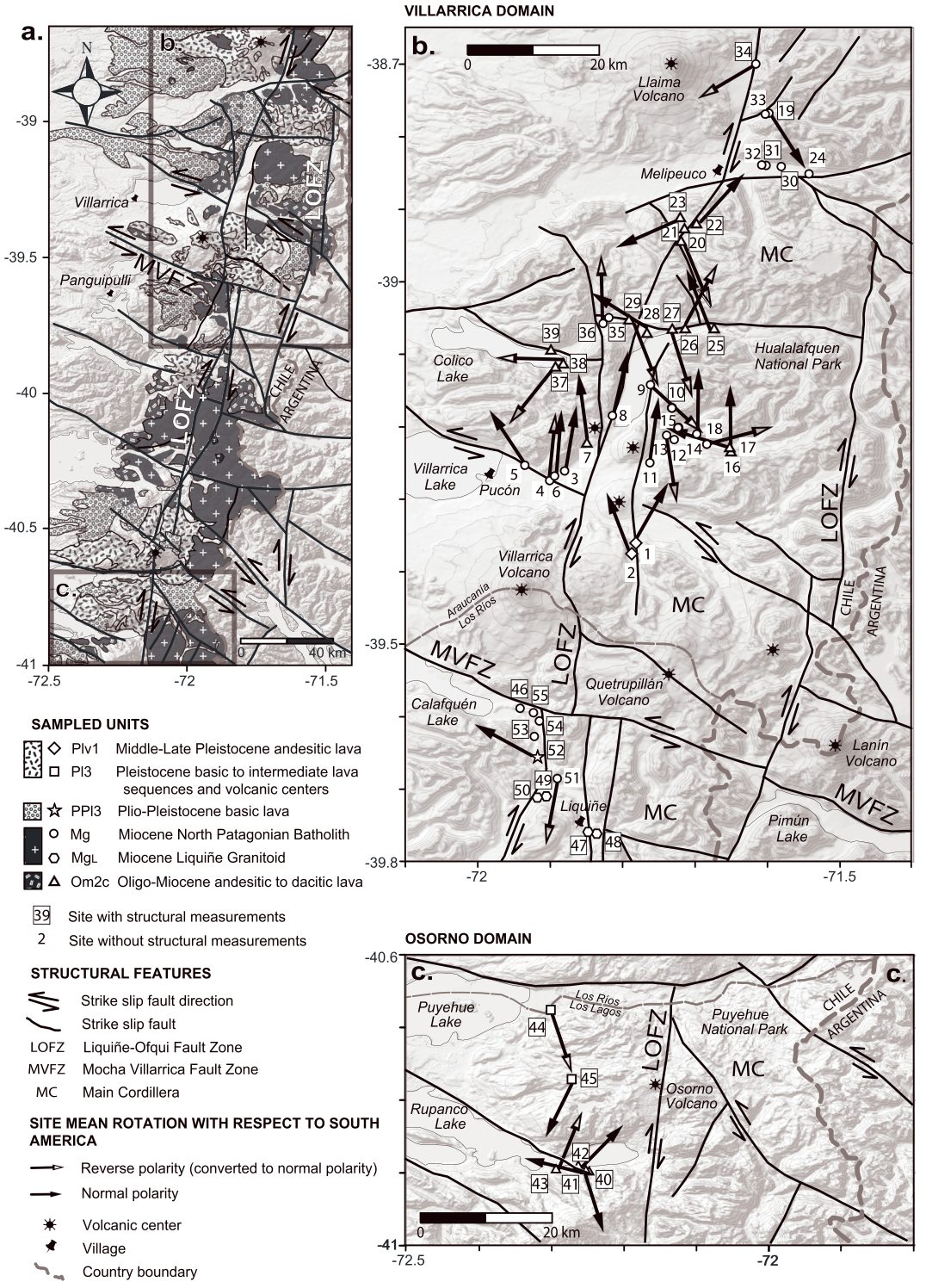

Figure 3. Digital elevation model (DEM) of the study area and paleomagnetic rotation distribution along the LOFZ. (a) Stretch of the LOFZ located into the Patagonian Andes between the Llaima Volcano (38°41′S) and Rupanco Lake (40°53′S). (b) Villarrica domain. (c) Osorno domain. Geological units are from *Sernageomin* [2003] and *Moreno and Clavero* [2006]. Some faults are referred to *Thomson* [2002] and *Rosenau et al.* [2006]; others were interpreted by us from the DEM.

East of the LOFZ, in the sub-Andean region between 41° and 42°30′S, the N-S to NNW-SSE North Patagonian Andes belt arises from post late Oligocene eastward propagation of the orogenic front [*Giacosa and Heredia*, 2004; *Giacosa et al*., 2005; *Ramos et al*., 2011].

The nature and timing of the LOFZ activity suggest that it may be a long-lived shear zone accommodating continental-scale deformation arising from the Farallon (Nazca)-South America plate convergence [*Cembrano et al*., 1996a, 1996b]. *Pankhurst et al*. [1992] proposed that the LOFZ initiated in the pre-Late Cretaceous along the magmatic arc, based on a 2 km wide mylonitic belt at the northernmost LOFZ (north of ~41°S) predating a ~100 Ma cross-cutting dike [*Cembrano et al*., 1996a, 2000]. Late Eocene to early Miocene basins formation close to the LOFZ north of ~46°S [*Hervé*, 1993; *Rojas et al*., 1994] documents a transtensional regime coinciding with the right-oblique subduction between 48 and 26 Ma [*Pardo-Casas and Molnar*, 1987], when the LOFZ started behaving as a dextral strike-slip fault [*Hervé*, 1993; *Cembrano et al*., 1996b]. At 26 Ma with the almost orthogonal convergence [*Pardo-Casas and Molnar*, 1987], the basins were underthrust and a widespread calc-alkaline granitoid intrusive activity occurred [*Hervé*, 1993; *Cembrano et al*., 1996a, 1996b]. At 20 Ma, when the plate convergence became right-oblique again with a high convergence rate [*Pardo-Casas and Molnar*, 1987], a young buoyant subducting ocean plate north of the Chile ridge may have led to strong coupling with upper plate, favoring dextral transpression along the magmatic arc [*Beck*, 1991; *Cembrano et al*., 1996a, 1996b]. Intrusive and metamorphic rocks within the LOFZ central segment (39°S–42°S) also testify a subsequent Miocene-Pliocene dextral strike-slip deformation accompanied by syntectonic pluton emplacement [*Nakamura*, 1977; *Cembrano et al*., 1996a, 2007]. Late Miocene (~6 Ma) collision of three segments of the Chile Rise between 46.5°S and 47.5°S caused a transpressional regime and rapid exhumation [*Cembrano et al*., 2002; *Thomson*, 2002; *Melnick et al*., 2009]. According to *Lavenu and Cembrano* [1999] and *Cembrano et al*. [2000], this process may explain the most recent dextral motion along the LOFZ southern segment (42°–47°30′S). Finally, the whole Patagonian Andes between 38°S and 47°S experienced Plio-Quaternary dextral strike-slip faulting along LOFZ-related faults [*Lavenu and Cembrano*, 1999; *Rosenau et al*., 2006].

Despite the low seismic activity reported along the LOFZ, focal plane solutions of shallow earthquakes in the intra-arc region ($<$25 km) demonstrate its current dextral strike slip and its relationship with volcanism, although accuracy of earthquake depth determinations is limited [*Chinn and Isacks*, 1983; *Dziewonski et al*., 1991; *Barrientos and Acevedo-Aránguiz*, 1992; *Nelson et al*., 1994; *López-Escobar et al*., 1995; *Lavenu and Cembrano*, 1999; *Lara et al*., 2004; *Melnick et al*., 2006b; *Lange et al*., 2007, 2008; *Cembrano and Lara*, 2009] (Figure 1b). Seismic activity seems to be concentrated at the northern and southern LOFZ ends [*Hackney et al*., 2006; *Lange et al*., 2008] (Figure 1b). This has been interpreted as a response of along-strike coupling variations at the subduction interface, being low at the northern LOFZ tip and high at its central segment [*Hackney et al*., 2006].

Relying on structural data, *Rosenau et al*. [2006] predict a long-term (~5 Ma) LOFZ slip rate of 32 ± 6 mm/yr for its southern segment (46°S–42°S), decreasing northward (42°S–38°S) to 13 ± 3 mm/yr. However, GPS data document a northward translation of the Chiloé Block sliver along the LOFZ occurring at a maximum rate of 6.5 mm/yr, and tapering to zero at the northern termination of the LOFZ [*Wang et al*., 2007]. Comparison between GPS data and the present-day Nazca-South America convergence direction and rate [*Angermann et al*., 1999; *Pardo-Casas and Molnar*, 1987] implies that ~44% of the margin-parallel convergence component is accommodated by northward translation of the Chiloé Block. The remaining 56% could be represented by permanent and elastic deformation released during coseismic periods [*Klotz et al*., 2001; *Wang et al*., 2007]. Furthermore, *Wang et al*. [2007] suggests that south of 42°S the margin-normal plate velocity decreases, due to a possible narrower interface subduction because of the occurrence in the south of younger (thus warmer) oceanic lithosphere.

Along most of its length, the LOFZ goes through Miocene plutons from the North Patagonian Batholith [*Cembrano and Herve*, 1993; *Hervé*, 1994] (Figures 3 and 4), where available K/Ar and Rb-Sr whole rock determinations indicate an age between 8.5 and 12.8 Ma [*Munizaga et al*., 1988]. In general, the North Patagonian Batholith is composed by calcalkaline granitoids varying from gabbro to monzogranite, with tonalite and granodiorite as the predominant rock types [*Pankhurst et al*., 1992; *Hervé*, 1994]. They form a hundreds of kilometers long belt (39°S to 53°S), built episodically from Early Cretaceous to Miocene by subduction-related processes [*Moreno and Parada*, 1976; *Munizaga et al*., 1988; *Pankhurst et al*., 1999]. Locally this Batholith has taken different names, as close to the Liquiñe town, where it is called Liquiñe Granitoid (*MgL*) [*Hervé*, 1977; *Moreno and Parada*, 1976].

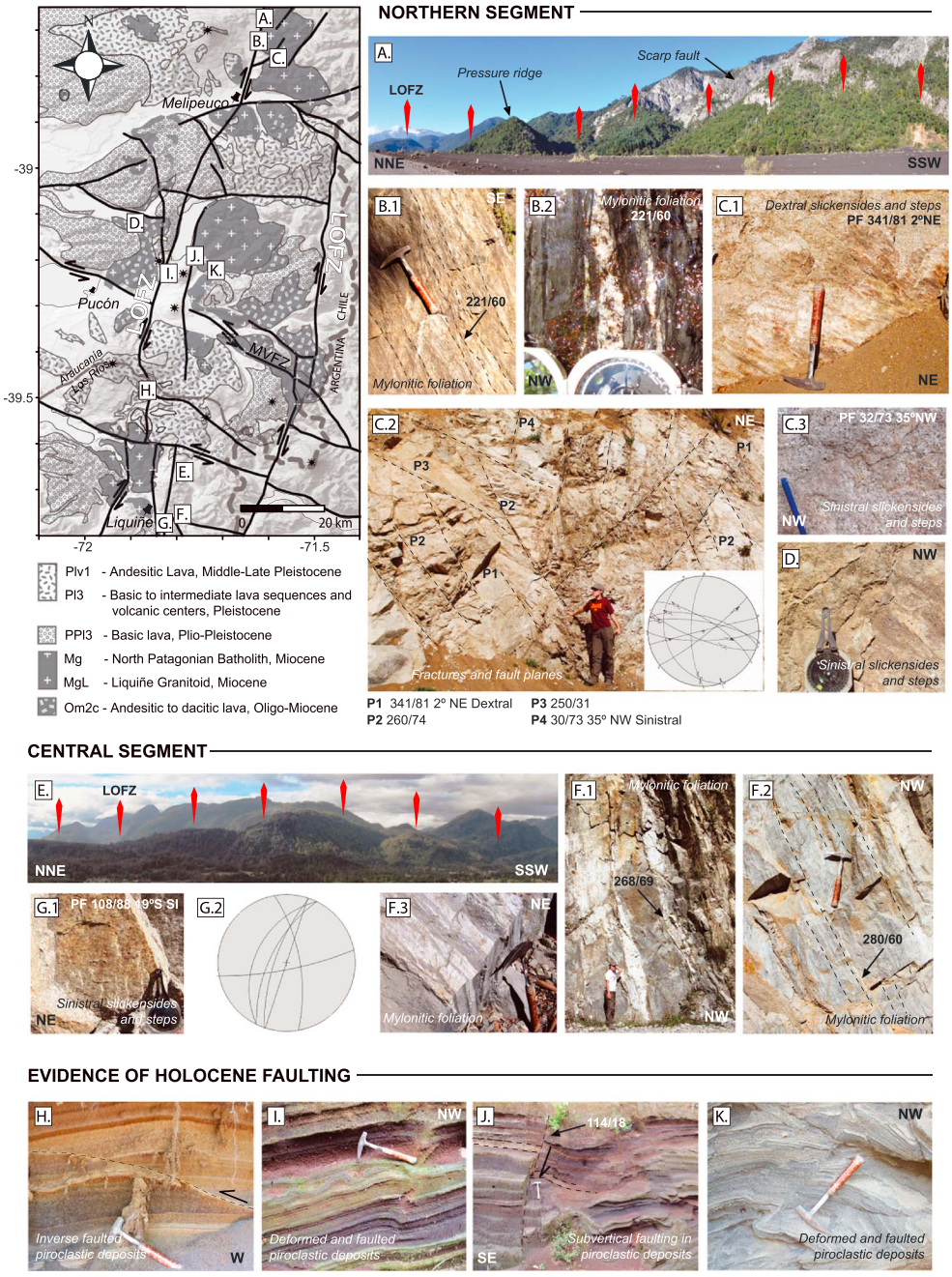

Figure 4. Field features of the LOFZ. Evident geomorphological expression, as long fault scarps and pressure ridges at (a) Conguillio National Park and (e) around Liquiñe town. (b and f) Ductile strain evidence close to the fault trace, (c, d, and g) brittle deformation kinematic indicators, and (h–k) faulting of Holocene postglacial volcanoclastic deposits.

Close to the fault and associated with the magmatic arc, Oligo-Miocene lavas, and ignimbrites rest unconformably upon the North Patagonian Batholith (Figure 3a). In turn, Oligo-Miocene volcanics are locally covered by Plio-Pleistocene basaltic and andesitic lavas, as well as by Holocene basic to intermediate lavas from adjacent Quaternary volcanoes aligned along the LOFZ [*Moreno and Clavero*, 2006] (Figure 3).

Where the North Patagonian Batholith is cut by the LOFZ, there is clear geomorphological evidence of strike-slip faulting, such as long fault scarps and pressure ridges (Figures 4a and 4e). In the Conguillio National Park (38°70′S) and near Liquiñe town (39°75′S) we observed ductile strain zones, characterized by few kilometers

long elongated bodies of mylonite with a predominant NW to N-S foliation (Figures 4b and 4f). Kinematic indicators (slickensides on fault planes) of brittle strain over the plutonic rocks are abundant (Figures 4c, 4d, and 4g). These observations are consistent with *Hervé* [1976], *Hervé and Thiele* [1987], *Hervé* [1993], and *Thomson* [2002]. We also found widespread evidence of Holocene faulting at 39°00′S to 39°50′ latitudes, where the postglacial pyroclastic deposits from active volcanoes are cut by normal and reverse faults (Figures 4h to 4k).

5. Previous Paleomagnetic Studies on the LOFZ

The paleomagnetic survey in the west margin of South America begun in the 1980s, in an attempt to search analogous settings to the northward displaced crustal block slivers documented in the U.S. Western Cordillera [*Beck*, 1976, 1989, 1991; *Irving et al*., 1985]. Relying on paleomagnetic evidences, *Beck* [1986, 1988, 1994] suggested that there is no comparable evidence of margin-parallel displacement in the Andes.

First paleomagnetic evidence from the LOFZ was reported by *Garcia et al*. [1988], who investigated upper Paleozoic to upper Tertiary intrusives and basaltic rocks in the Lake District (Southern Chile), documenting up to ~49° CW rotations east of the LOFZ, and 4° to 39° CCW rotations west of it (Figure 1 and Table 1, all rotation were recalculated by us using updated South American reference poles from *Torsvik et al*. [2008]). They suggested the occurrence of small independent crustal blocks into a distributed shear zone. The paleomagnetic investigation of the Eocene-Miocene marine volcanoclastic Ayacara Formation west of the LOFZ (42°S) revealed an insignificant CCW rotation of 12.4° ± 14.9° [*Rojas et al*., 1994], while east of the LOFZ (~43°S to 44°S) volcanic rocks remagnetized by the Patagonian Batholith intrusion at ~90 Ma, yielded a small CW rotations between ~11° and 17° CW [*Cembrano et al*., 1992; *Beck et al*., 1998]. *Beck et al*. [2000] studied over 100 sites in the northernmost North Patagonian Batholith and dikes (~40–46°S), reporting ~10° CW and CCW rotations east and west of the LOFZ, respectively. They estimated a post mid-Cenozoic rotation age, because the rotation magnitude is nearly the same for both the North Patagonian Batholith and the younger rocks (Eocene-Miocene Ayacara volcanics and Cocotue basalts). Paleomagnetic data from late Paleozoic granitoids west of the LOFZ (~40°S) reveal a mean CW mean rotation of 7.5° [*Beck*, 1991].

Two hypotheses have been put forward to explain this distribution of paleomagnetic rotations along the LOFZ. The first is the buttress effect [*Beck et al*., 1993], suggesting that the northward fore-arc sliver motion is hampered by a thick crust buttress at its north leading edge, in turn related to both changes in subducting plate age (~35 Ma at 38°S to ~0 Ma at 46°S [*Herron*, 1981]) and the concave westward shape of the central Andes. As a consequence, sliver widens through conjugate faults breaking it into CCW rotating lens-shaped crustal blocks bounded to the east by the LOFZ [*Beck et al*., 1993]. This model justifies the domains of both extension and compression documented in the LOFZ, the CCW rotation of the sliver adjacent to a dextral shear zone, and a CW rotation within and east of the LOFZ arising from the dextral oblique subduction (see Figure 2c).

In the second model, *Rosenau et al*. [2006] explain the rotational pattern of the LOFZ through SC kinematics, considering a conjugate set of NE-SW dextral arc-parallel (synthetic, *C* structures) and NW-SE sinistral arc-oblique (antithetic *S* structures) faults, enclosing less deformed sigmoidal domains (Figure 2i). They suggest that domain motion and slip are driven by diffusive deformation within the ductile lower crust [*Bourne et al*., 1998; *Roy and Royden*, 2000; *Cowgill et al*., 2004]. Based on the assumption that the 2φ angle between the *S-C* faults decreases during progressive deformation, they predict the total displacement accommodated by the brittle LOFZ system, the associated long-term deformation rates, and the spatial distribution and amount of associated local vertical axis rotations. *Rosenau et al*. [2006] predict 31° CW and 9° CCW rotations for the *C* and *S* faults (respectively).

6. Paleomagnetic Sampling and Methods

We collected 553 paleomagnetic samples in 55 sites, located within a maximum distance of 20 km from the main trace of the LOFZ, and at both sides of it. Sites were gathered from two main areas (called hereinafter Villarrica and Osorno domains), from Llaima Vulcano in the north until Rupanco Lake in the south (Figure 3). The 40 km sampling transect across the fault was established considering that several studies demonstrated that shear-related rotations virtually end within 10–20 km from the fault trace [*Ron et al*., 1984; *Sonder et al*., 1994; *Piper et al*., 1997; *Randall et al*., 2011].

Table 1. Recalculated Paleomagnetic Site Mean Directions Along the Liquiñe-Ofqui Fault Zone (LOFZ) From Previous Investigations[a]

				Geographic Coordinates			
		Site	Unit	Latitude S	Longitude W	Age	Age (Ma)
Garcia et al. [1988]	W LOFZ	85CJ38	Paleozoic intrusives	40.32	72.37	Paleozoic	309 ± 8
		85CJ39	Paleozoic intrusives	40.33	72.37	Paleozoic	309 ± 8
		85CJ44	Paleozoic intrusives	40.12	72.33	Paleozoic	295 ± 7
		85CJ15	Panguipulli formation	39.82	72.1	Jurassic	160?
		85CJ24	Panguipulli Batholith	39.58	72.03	Mesozoic	200–190
		85CJ05	Miocene intrusives	39.26	71.76	Miocene	8.5 ± 0.1
		85CJ06	Miocene intrusives	39.26	71.76	Miocene	8.5 ± 0.1
		85CJ07	Miocene intrusives	39.15	71.75	Miocene	8.5 ± 0.1
		85CJ08	Miocene intrusives	39.24	71.83	Miocene	8.5 ± 0.1
		85CJ14	Miocene intrusives	40.00	72.00	Miocene	8.2 ± 2.1
		85CJ41	Miocene intrusives	40.23	72.27	Miocene	13.1 ± 0.6
		85CJ35	Cocotue beach basalts	41.92	74.02	Lower Miocene	40.4 ± 1.8
		85CJ36	Cocotue beach basalts	41.92	74.02	Lower Miocene	21.7 ± 1.7
		85CJ37	Cocotue beach basalts	41.92	74.02	Lower Miocene	21.7 ± 1.7
	E LOFZ	85CJ25	Miocene intrusives	39.78	71.73	Miocene	28.9 ± 1.2
		85CJ10	Curarrehue formation	39.38	71.56	Pliocene	3.0 ± 0.5
		85CJ11	Curarrehue formation	39.33	71.62	Pliocene	4.2 ± 0.5
		85CJ12	Curarrehue formation	39.35	71.62	Pliocene	4.1 ± 0.4
Cembrano et al. [1992]	W LOFZ	pa18*	Alto Palena formation	43.62	71.80	Lower Cretaceous	145–125
		pa19*	Alto Palena formation	43.62	71.80	Lower Cretaceous	145–125
		pa20	Alto Palena formation	43.62	71.80	Lower Cretaceous	145–125
		pa21*	Alto Palena formation	43.62	71.80	Lower Cretaceous	145–125
		pa23	Alto Palena formation	43.60	71.73	Lower Cretaceous	145–125
		pa25	Alto Palena formation	43.60	71.80	Lower Cretaceous	145–125
		pa26	Alto Palena formation	43.62	71.87	Lower Cretaceous	145–125
		fu46	Alto Palena formation	43.60	71.85	Lower Cretaceous	145–125
		fu47	Alto Palena formation	43.60	71.85	Lower Cretaceous	145–125
		fu48	Alto Palena formation	43.60	71.83	Lower Cretaceous	145–125
		fu50	Alto Palena formation	43.63	71.82	Lower Cretaceous	145–125
		pa07	North Patagonian Batholith	44.05	72.27	Lower Cretaceous	120–110
		fu51	North Patagonian Batholith	43.63	71.93	Lower Cretaceous	120–110
		fu52	North Patagonian Batholith	43.63	71.93	Lower Cretaceous	120–110
		fu53	North Patagonian Batholith	43.60	72.05	Lower Cretaceous	120–110
Rojas et al. [1994]	W LOFZ	89EM01	Isla Manzano - Ayacara Formation	40.02	72.67	Eocene-Miocene	16.5 ± 0.5
		89FA01	Isla Manzano - Ayacara Formation	40.02	72.67	Eocene-Miocene	16.5 ± 0.5
		89FA05	Isla Manzano - Ayacara Formation	40.02	72.67	Eocene-Miocene	16.5 ± 0.5
		89FA06	Isla Manzano - Ayacara Formation	40.02	72.67	Eocene-Miocene	16.5 ± 0.5
		89A04	Caleta Ayacara - Ayacara Formation	40.3	72.8	Eocene-Miocene	16.5 ± 0.5
		89A06	Caleta Ayacara - Ayacara Formation	40.3	72.8	Eocene-Miocene	16.5 ± 0.5
		89A09	Caleta Ayacara - Ayacara Formation	40.3	72.8	Eocene-Miocene	16.5 ± 0.5
		89FU58	Isla Puduhuapi - Ayacara Formation	42.93	72.79	Eocene-Miocene	16.5 ± 0.5
		89FU59	Isla Puduhuapi - Ayacara Formation	42.93	72.79	Eocene-Miocene	16.5 ± 0.5
		89FU60	Isla Puduhuapi - Ayacara Formation	42.93	72.79	Eocene-Miocene	16.5 ± 0.5
		90PA28	Isla Puduhuapi - Ayacara Formation	42.93	72.79	Eocene-Miocene	16.5 ± 0.5
Beck et al. [1998]	E LOFZ	93bs09	Ibáñez Group or Divisadero Group	44.2	71.91	Jurassic or early to middle Cretaceous	Remagnetized at 90
		93bs10	Ibáñez Group or Divisadero Group	44.2	71.91	Jurassic or early to middle Cretaceous	Remagnetized at 90
		93bs11	Ibáñez Group or Divisadero Group	44.35	71.83	Jurassic or early to middle Cretaceous	Remagnetized at 90
		93bs12	Ibáñez Group or Divisadero Group	44.26	71.85	Jurassic or early to middle Cretaceous	Remagnetized at 90
		93bs13	Ibáñez Group or Divisadero Group	44.26	71.88	Jurassic or early to middle Cretaceous	Remagnetized at 90
		93bs14	Ibáñez Group or Divisadero Group	44.26	71.88	Jurassic or early to middle Cretaceous	Remagnetized at 90
		93bs16	Ibáñez Group or Divisadero Group	44.26	71.86	Jurassic or early to middle Cretaceous	Remagnetized at 90
		93bs17	Ibáñez Group or Divisadero Group	44.26	71.9	Jurassic or early to middle Cretaceous	Remagnetized at 90
		93bs18	Ibáñez Group or Divisadero Group	44.26	71.9	Jurassic or early to middle Cretaceous	Remagnetized at 90
		93bs20	Ibáñez Group or Divisadero Group	44.28	71.91	Jurassic or early to middle Cretaceous	Remagnetized at 90
		93bs21	Ibáñez Group or Divisadero Group	44.28	71.95	Jurassic or early to middle Cretaceous	Remagnetized at 90
		93bs22	Ibáñez Group or Divisadero Group	44.2	71.9	Jurassic or early to middle Cretaceous	Remagnetized at 90
Beck [1991]	W LOFZ	86cj38	Paleozoic Granitoids	40.31	72.37	Paleozoic	309 ± 8
		85cj39	Paleozoic Granitoids	40.31	72.36	Paleozoic	309 ± 8
		85cj44	Paleozoic Granitoids	40.11	72.35	Paleozoic	295 ± 7
		88bc06	Paleozoic Granitoids	40.13	72.24	Paleozoic	295 ± 7
		88bc07	Paleozoic Granitoids	40.11	72.35	Paleozoic	295 ± 7
		88bc08	Paleozoic Granitoids	40.17	72.24	Paleozoic	295 ± 7
		88bc14	Paleozoic Granitoids	40.32	72.33	Paleozoic	309 ± 8

Table 1. (continued)

ChRM/Low-Coercivity Component										
Tilt Corrected		In Situ					Recalculated by Us			
D (deg)	*I* (deg)	*D* (deg)	*I* (deg)	*k*	α_{95} (deg)	*n*	*R* (deg)	Δ*R* (deg)	*F* (deg)	Δ*F* (deg)
-	-	**110.4**	**70.7**	250.0	3.8	7	−25.0	10.9	2.9	4.0
-	-	**343.4**	**−72.9**	90.9	5.8	8	28.0	16.8	5.1	5.3
-	-	**136.5**	**69.8**	583.4	2.3	8	−3.1	6.1	−0.7	2.2
-	-	**344.2**	**−63.6**	95.9	5.7	8	−19.1	12.2	−1.4	5.7
-	-	**17.2**	**−57.1**	98.6	5.6	8	−4.4	9.0	−7.1	4.9
-	-	**13.4**	**−47.5**	34.9	15.7	4	13.7	18.6	−13.4	12.4
-	-	**25.3**	**−63.0**	28.6	12.6	6	25.6	22.6	2.1	10.0
-	-	**229.9**	**61.8**	9.8	22.6		50.1	42.5	1.0	17.7
-	-	**235.2**	**71.3**	36.4	10.1	7	55.5	26.0	10.4	8.1
-	-	**265.5**	**61.2**	74.1	8.9	5	85.8	14.8	−0.3	7.1
-	-	**343.6**	**−60.0**	190.5	5.6	5	−16.1	9.2	−1.7	4.7
168	**70.7**	-	-	333.3	3.7	6	−8.8	9.4	4.6	3.3
144	**64.6**	-	-	1000.0	2.1	6	−33.0	5.0	−1.5	2.3
138	**52.0**	-	-	52.1	9.4	6	−39.0	12.4	−14.1	7.5
-	-	**30.7**	**−52.7**	34.8	13.2	5	33.2	17.6	−11.8	10.4
50.9	**−56**	-	-	111.1	11.6	3	50.9	20.7	−2.0	11.6
227	**55.1**	-	-	230.8	4.0	7	−132.7	7.0	−113.1	4.0
43.2	**−68**	-	-	189.2	4.0	8	43.2	10.8	10.0	4.0
6.00	**−45**	18.1	−61.9	375.0	2.0	4	13.1	3.7	−14.5	2.5
6.00	**−45**	15.9	−63.4	136.0	2.0	4	13.1	3.7	−14.5	2.5
360	**−40**	4.5	−59.9	83.0	6.6	7	6.6	−19.5	−19.5	5.5
6.00	**−45**	14.8	−64.0	857.0	2.0	7	13.1	3.7	−14.5	2.5
11.9	**−59**	334.6	−71.1	190.0	5.5	5	19.0	8.9	−0.5	4.7
22.3	**−63**	67.0	−75.6	131.0	5.9	6	29.4	10.6	3.5	5.0
9.4	**−55**	1.9	−49.7	102.0	6.7	6	16.5	9.6	−4.5	5.6
14.2	**−67**	10.2	−57.3	109.0	6.5	6	21.3	13.5	7.5	5.5
20.9	**−59**	16.5	−49.3	113.0	6.3	6	28.0	10.0	−0.5	5.3
352	**−67**	354.5	−57.1	143.0	5.6	6	−0.6	11.7	7.5	4.8
352	**−63**	11.5	−62.6	167.0	5.2	6	−1.0	9.5	3.49	4.5
-	-	**351.0**	**−63.1**	286.0	3.6	7	−6.9	7.3	2.5	3.7
-	-	**358.1**	**−58.9**	29.0	14.5	5	0.3	22.9	−1.4	11.6
-	-	**15.6**	**−60.8**	57.0	10.2	5	17.8	17.0	0.5	8.3
-	-	**3.9**	**−53.0**	148.0	6.3	5	6.0	9.0	−7.2	5.5
28.7	**−79**	325.4	−32.7	-	7.3	7	29.3	32.7	15.5	6.0
320	**−72**	318.7	−24.4	-	9.1	9	−39.3	24.2	8.5	7.3
357	**−79**	328.1	−32.7	-	4.7	7	−2.2	20.1	15.5	4.1
350	**−74**	329.0	−27.4	-	9.4	6	−9.8	27.5	10.5	7.6
138	**56.8**	98.2	16.4	-	4.4	6	−41.0	7.1	−6.9	3.9
4.0	**−50**	292.0	−26.1	-	5.0	6	4.6	6.9	−13.7	4.3
169	**59.1**	89.3	17.2	-	3.6	7	−10.1	8.3	−4.6	4.3
168	**43.4**	187.1	51.7	-	7.3	5	−11.2	8.6	−22.4	6.0
3.0	**−54**	10.4	−63.2	-	7.9	6	3.7	11.1	−11.8	6.4
154	**57.7**	150.9	67.6	-	5.9	6	−25.8	9.3	−8.1	4.9
145	**51.9**	166.6	66.2	-	5.9	7	−34.5	8.3	−13.9	4.9
30.2	−66	**20.6**	**−75.3**	34.5	13.2	5	25.9	50.1	8.8	10.4
16.4	−57	**6.5**	**−65.0**	13.3	15.8	8	11.8	31.4	−1.5	12.4
25	−65	**13.6**	**−73.6**	20.5	13.7	7	18.9	44.6	7.0	10.8
3.1	−56	**9.7**	**−63.8**	260.0	3.8	7	15.0	7.4	−2.7	3.3
355.5	−50	**359.0**	**−58.8**	203.2	4.7	6	4.3	7.7	−7.7	4.0
356.3	−39	**358.7**	**−47.3**	49.9	9.6	6	4.0	11.5	−19.2	7.6
2.9	−43	**6.8**	**−51.4**	94.2	6.9	6	12.1	9.2	−15.1	5.6
5.4	−52	**11.7**	**−60.4**	151.3	5.5	6	17.0	9.3	−6.1	4.5
11.3	−46	**17.2**	**−53.8**	30.9	12.2	6	22.5	16.6	−12.7	9.6
351.2	−47	**353.5**	**−56.1**	281.7	4.0	6	−1.2	6.4	−10.5	3.5
39.2	−59	**47.4**	**−64.1**	300.2	5.3	4	52.7	10.0	−2.5	4.4
359.8	−68	**11.2**	**−75.9**	171.0	5.9	5	16.5	19.7	9.4	4.8
		110.4	**71**		3.8		−29.1	9.7	0.4	3.2
		343.4	**−73**		5.8		23.9	16.1	2.4	4.7
		136.5	**70**		2.3		−3.1	6.1	−0.5	2.2
		27.7	**85**		10.7		-	-	-	-
		189.3	**79**		9.5		49.7	46.8	8.5	7.5
		172.4	**64**		10.8		32.8	20.0	−6.6	8.5
		110	**50**		13.2		−29.4	16.5	−20.6	10.4

[a]Age in Ma is from the geologic timescale of *Gradstein et al.* [2004]. *D* and *I* are site mean declination and inclination calculated before and after tectonic correction. After *Fisher* [1953], *k* and α_{95} are statistical parameters. *D* and *I* values in bold were used to recalculate *R*, Δ*R*, *F* and Δ*F* for each site. Recalculated rotation (*R*) and flattening (*F*) values, and relative errors Δ*R* and Δ*F* (according to *Demarest* [1983]) are relative to coeval *D* and *I* South American values expected at the sampling area considering updated South American paleopoles from *Torsvik et al.* [2008].

We gathered 31 paleomagnetic sites in the Miocene North Patagonian Batholith granitoids (*Mg*, MgL), 19 sites in the Oligo-Miocene ignimbrites and lavas (*Om2c*), and 5 sites in the Plio-Pleistocene andesitic and dacitic lavas (one site in the PPl_3, two sites in the Plv_1, and two sites in the Pl_3 formation, Figure 3 and Table 2). Bedding (occurrence of intraflow sedimentary or volcanoclastic layers, evidence of geometric relations with substratum) was retrievable in only 10 volcanic sites.

The samples were drilled using a petrol-powered portable drill cooled by water and oriented in situ using the Sun (when possible) and a magnetic compass, corrected for the local magnetic declination for year 2012 (between 6°E and 8°E according to NOAA's National Geophysical Data Center, http://www.ngdc.noaa.gov/geomag/declination.shtml). Afterward, the cores were cut into standard paleomagnetic specimens of 22 mm height.

Measurements were carried out in the shielded room of the paleomagnetic laboratory of the Istituto Nazionale di Geofisica e Vulcanologia (INGV, Roma), using a 2G Enterprises DC-superconducting quantum interference device cryogenic magnetometer. Samples were demagnetized in 12 steps by alternating field (AF) yielded by three coils online with the magnetometer until a maximum AF peak of 150 mT. Twin specimens from some samples were also thermally demagnetized using a Pyrox shielded oven in 12 steps up to 680°C. The specimens from three sites (LOF04 from Mg, and LOF29 and LOF37 from Om2c), that were still strongly magnetic at 150 mT due to a high coercivity magnetization, were thermally cleaned in additional 11 steps up to 680°C. Demagnetization data were plotted on orthogonal vector component diagrams [*Zijderveld*, 1976] (Figure 5).

The magnetization components were identified by principal component analysis [*Kirschvink*, 1980], and the site mean paleomagnetic directions were computed using *Fisher* [1953] statistics, and these were plotted on equal-angle projections (Figure 6). Finally, the rotation and flattening values with respect to South America were evaluated according to *Demarest* [1983], using the reference paleopoles from *Torsvik et al*. [2008]. To define the sense and amount of rotation, we always considered the smaller angle between the observed and expected declinations, thereby calculating rotation values always $\leq|180°|$. This is a conservative approach, although we are aware that in the past, some authors considered rotation values exceeding 180° [e.g., *Nelson and Jones*, 1987; *Piper et al*., 1997].

7. Paleomagnetic Results

Samples from 13 out of 55 sites yielded erratic magnetization directions and were discarded from further considerations. Demagnetization diagrams from the remaining 42 sites (Figure 5) show that as a rule, a viscous component is removed between 10 and 30 mT, and a characteristic magnetization (ChRM) is isolated between 30 and 150 mT. Samples from three sites, LOF04 (Mg-granite), LOF29, and LOF37 (Om2c-volcanics), yielded both a low coercivity (LC) component of magnetization isolated by AF demagnetization, and a high coercivity (HC) component subsequently demagnetized by thermal cleaning (Figures 5e and 5i and Table 2). The hard fraction shows a significant remanence drop between 300 and 350°C, and in one sample a complete demagnetization at 680°C. This seems to show that in these three sites, the LC component (probably magnetite) is associated with maghemite and hematite. As both minerals may arise from chemical overprint, the HC component isolated in these three sites was discarded by further consideration (Table 2).

The α_{95} values relative to the site mean paleomagnetic directions from the reliable 42 sites vary from 7.4° to 84.3° (average 15.5° excluding the latter value). From these, further six sites were discarded as their α_{95} value exceeded 30°, or their mean in situ inclination (bedding was not apparent in these sites) was $<|10.0°|$. In fact, sites yielding subhorizontal directions have undefined magnetic polarity (the local normal polarity geocentric axial dipole (GAD) field inclination is $-58°/-60°$) and cannot be used to evaluate tectonic rotations.

To sum up, 36 site mean directions passed the above quality criteria and were classified as reliable to infer on the rotation pattern of the study area.

8. Rotation Pattern Along the Liquiñe-Ofqui Fault Zone

In Figure 6, site mean directions are grouped depending on formation age. Tilt-corrected directions could be calculated only for six Oligo-Miocene and two Plio-Pleistocene volcanic sites, as in the remaining 28 sites bedding was not apparent (Table 2). For all three age groups, both normal and reverse polarities are

Table 2. Paleomagnetic Site Mean Directions From Liquiñe-Ofqui Fault Zone (LOFZ)[a]

							ChRM/Low-Coercivity Component	
		Geographic Coordinates					Tilt Corrected	
Site	Unit	Latitude S	Longitude W	Age	Age (Ma)	Bedding (deg)	*D* (deg)	*I* (deg)
LOF1	Plv_1	39°21′28.0404″	71°46′45.2388″	Middle to late Pleistocene	<1.81	-	-	-
LOF2	Plv_1	39°22′21.0612″	71°47′5.7660″	Middle to late Pleistocene	<1.81	-	-	-
LOF3	Mg	39°15′29.8368″	71°52′39.3852″	Miocene	8–12	-	-	-
LOF4	Mg	39°16′17.9904″	71°53′53.6928″	Miocene	8–12	-	-	-
LOF5	Mg	39°15′2.0448″	71°55′57.1008″	Miocene	8–12	-	-	-
LOF6	Mg	39°15′55.1196″	71°53′29.3748″	Miocene	8–12	-	-	-
LOF7	Om2c	39°13′15.8736″	71°50′48.6636″	Late Oligocene Early Miocene	29–18.8	-	-	-
LOF8	Mg	39°10′55.3080″	71°48′41.8428″	Miocene	8–12	-	-	-
LOF9	Mg	39°08′22.1784″	71°45′32.8536″	Miocene	8–12	-	-	-
LOF10	Mg	39°10′17.7852″	71°43′46.6536″	Miocene	8–12	-	-	-
LOF11	Mg	39°14′49.4016″	71°45′35.6508″	Miocene	8–12	-	-	-
LOF12	Mg	39°12′54.4464″	71°43′34.8096″	Miocene	8–12	-	-	-
LOF13	Mg	39°12′33.0660″	71°44′12.6168″	Miocene	8–12	-	-	-
LOF14	Mg	39°12′26.7372″	71°41′42.9216″	Miocene	8–12	-	-	-
LOF15	Mg	39°11′55.6548″	71°43′15.8340″	Miocene	8–12	-	-	-
LOF16	Om2c	39°13′59.2464″	71°38′52.9656″	Late Oligocene Early Miocene	29–18.8	-	-	-
LOF17	Om2c	39°13′38.4924″	71°38′59.0352″	Late Oligocene Early Miocene	29–18.8	-	-	-
LOF18	Mg	39°13′17.3856″	71°40′52.6872″	Miocene	8–12	-	-	-
LOF19	Mg	38°45′53.3916″	71°35′44.4516″	Miocene	8–12	-	-	-
LOF20	Om2c	38°56′33.8964″	71°43′0.8256″	Late Oligocene Early Miocene	29–18.8	152/13	337.3	25.3
LOF21[b]	Om2c	38°55′31.6344″	71°42′43.7292″	Late Oligocene Early Miocene	29–18.8	75/39	10.7	−15
LOF22	Om2c	38°55′6.9960″	71°41′44.4300″	Late Oligocene Early Miocene	29–18.8	259/28	41.8	−25
LOF23	Om2c	38°54′36.1224″	71°43′4.9692″	Late Oligocene Early Miocene	29–18.8	103/42	245.7	−58
LOF24	Mg	38°50′54.8952″	71°32′25.2276″	Miocene	8–12	-	-	-
LOF25	Om2c	39°03′48.1860″	71°40′16.4028″	Late Oligocene Early Miocene	29–18.8	30/30	338.1	−53
LOF26	Om2c	39°03′48.2508″	71°42′40.2228″	Late Oligocene Early Miocene	29–18.8	-	-	-
LOF27	Om2c	39°03′50.1228″	71°43′44.4504″	Late Oligocene Early Miocene	29–18.8	-	-	-
LOF28	Om2c	39°04′10.6104″	71°45′50.0904″	Late Oligocene Early Miocene	29–18.8	-	-	-
LOF29	Om2c	39°03′4.3632″	71°47′19.4784″	Late Oligocene Early Miocene	29–18.8	-	-	-
LOF30	Mg	38°50′18.3300″	71°34′43.1760″	Miocene	8–12	-	-	-
LOF31[b]	Mg	38°50′12.9012″	71°35′58.4232″	Miocene	8–12	-	-	-
LOF32	Mg	38°50′10.5684″	71°36′19.9764″	Miocene	8–12	-	-	-
LOF33[b]	Mg	38°45′58.2588″	71°36′2.4120″	Miocene	8–12	-	-	-
LOF34	Mg	38°41′49.0416″	71°36′49.4640″	Miocene	8–12	-	-	-
LOF35[b]	Mg	39°02′48.9228″	71°48′59.7240″	Miocene	8–12	-	-	-
LOF36	Mg	39°03′17.9280″	71°49′28.4808″	Miocene	8–12	-	-	-
LOF37	Om2c	39°06′58.4172″	71°53′24.6624″	Late Oligocene Early Miocene	29–18.8	-	-	-
LOF38	Om2c	39°06′42.7608″	71°52′45.8112″	Late Oligocene Early Miocene	29–18.8	257/79	91	28.2
LOF39[b]	Om2c	39°05′34.1196″	71°53′47.3532″	Late Oligocene Early Miocene	29–18.8	130/34	135.6	−45
LOF40	Om2c	40°53′54.4488″	72°15′2.8260″	Late Oligocene Early Miocene	29–18.8	-	-	-
LOF41	Om2c	40°53′46.6512″	72°15′14.2596″	Late Oligocene Early Miocene	29–18.8	-	-	-
LOF42	Om2c	40°53′31.0920″	72°15′27.6984″	Late Oligocene Early Miocene	29–18.8	228/52	43.9	−45
LOF43	Om2c	40°53′33.4212″	72°17′15.9540″	Late Oligocene Early Miocene	29–18.8	-	-	-
LOF44	Pl_3	40°40′34.1040″	72°17′49.7436″	Pleistocene	<1.81	38/1	342.5	23.2
LOF45	Pl_3	40°46′17.6196″	72°16′5.2392″	Pleistocene	<1.81	-	-	-
LOF46	Mg	39°35′8.8008″	71°56′20.5656″	Miocene	8–12	-	-	-
LOF47	MgL	39°45′22.7160″	71°50′44.3004″	Miocene	15 ± 1	-	-	-
LOF48	MgL	39°45′32.2092″	71°50′3.6132″	Miocene	15 ± 1	-	-	-
LOF49	MgL	39°42′25.0272″	71°54′11.9484″	Miocene	15 ± 1	-	-	-
LOF50[b]	MgL	39°42′30.8196″	71°54′53.6796″	Miocene	15 ± 1	-	-	-
LOF51	Mg	39°40′57.2556″	71°53′15.6660″	Miocene	8–12	-	-	-
LOF52	PPl_3	39°39′11.6928″	71°54′53.3016″	Pliocene Pleistocene	<5.33	186/45	298.3	−43
LOF53	Mg	39°37′28.5564″	71°55′9.9516″	Miocene	8–12	-	-	-
LOF54	Mg	39°36′11.6856″	71°54′44.7264″	Miocene	8–12	-	-	-
LOF55	Mg	39°35′30.6384″	71°55′14.1492″	Miocene	8–12	-	-	-

observed. Directions show a significant spread and are generally far from both the normal ($D = 0°$, $I = -58$ to -60) and reverse polarity ($D = 180°$, $I = 58°$ to $60°$) GAD field direction, thus excluding a possible recent magnetic overprint. Declination spread is mostly due to vertical axis rotations, as it is also observed for the tilt-corrected sites (Figure 6). However, the lack of bedding for most of the sites surely translates into errors for the rotation and flattening values calculated in Table 2. This is a classical problem of paleomagnetism addressed to igneous rocks and could not be overcome [*Cembrano et al.*, 1992; *Beck et al.*, 2000].

Table 2. (continued)

In Situ								
D (deg)	*I* (deg)	*k*	α_{95} (deg)	*n*/*N*	*R* (deg)	Δ*R* (deg)	*F* (deg)	Δ*F* (deg)
30.2	−46.2	8.3	18.9	9/10	30.2	27.3	−11.8	18.9
338.9	−44.4	17.4	11.9	10/10	−21.1	16.7	−13.6	11.9
9.3	−24.9	4.6	26.8	9/10	9.6	23.4	−36.0	21.0
185.4	80.9	37.8	9.1	8/10	5.7	0.2	20.0	9.1
342	**−66.9**	**23.4**	**11.7**	**8/10***	**HC**			
326.2	−40.8	36.9	8.6	9/10	−33.5	9.3	−20.1	6.9
4.3	−39.9	18.1	18.5	5/10	4.6	19.2	−21.0	14.5
352.0	−51.4	12.2	15.3	9/10	−7.5	19.8	−11.5	12.1
12.8	−21.0	28.3	11.5	7/10	13.1	10.0	−39.8	9.1
312.9	52.3	11.4	17.2	8/10	133.1	22.7	−8.5	13.5
-	-	-	-	-	-	-	-	-
7.4	−50.4	17.4	22.7	4/10	7.7	29.2	−10.5	17.8
-	-	-	-	-	-	-	-	-
351.2	77.9	12.1	18.1	7/10	171.4	0.2	17.0	18.1
0.6	−52.8	9.9	22.4	6/10	0.84	30.6	−8.1	17.6
-	-	-	-	-	-	-	-	-
359.0	−46.3	11.6	14.8	10/10	−0.5	17.2	−16.6	11.7
286.7	−69.5	12.4	22.6	5/10	−72.8	63.4	6.62	22.8
255.3	32.9	11.3	16.0	9/10	75.5	15.2	−28.0	12.6
147.2	−24.4	23.7	12.7	7/10	147.4	11.2	−36.1	10.0
337.0	12.3	41.9	9.4	7/10	157.8	8.7	−37.4	7.6
14.1	3.8	40.2	8.8	8/10	11.2	7.8	−47.9	7.1
28.0	−45.0	46.2	8.2	8/10	42.3	7.8	−38.0	6.7
155.2	−65.9	17.5	11.9	10/10	−113.8	18.1	−4.8	9.5
-	-	-	-	-	-	-	-	-
356.9	−30.7	21.8	13.2	7/10	−21.4	17.8	−9.4	10.5
206.9	68.1	15.8	14.4	8/10	27.4	32.8	5.4	11.4
342.3	26.7	50.2	7.4	9/10	162.8	7.2	−36.0	6.1
301.5	−62.7	8.4	17.8	10/10	−58.0	32.8	−5.4	14.0
338.0	50.0	8.5	18.8	9/10	158.5	23.7	−12.7	14.8
11.6	**30.8**	**17.6**	**22.5**	**4/10***	**HC**			
-	-	-	-	-	-	-	-	-
22.3	−3.8	27.7	10.0	9/10	22.5	8.2	−56.8	8.0
-	-	-	-	-	-	-	-	-
150.3	−3.9	16.9	12.9	9/10	150.5	10.4	−56.6	10.2
59.2	39.4	28.4	10.6	8/10	−120.6	11.1	−21.0	8.4
56.6	5.3	1.3	84.3	10/10	−123.1	68.6	−55.4	65.8
178.5	32.9	17.5	14.9	7/10	−1.2	14.2	−27.8	11.7
38.1	40.6	13.4	17.1	7/10	−141.4	18.1	−22.2	13.5
65.1	**4.1**	**27.5**	**24**	**3/10***	**HC**			
95.9	−48.5	17.6	13.6	8/10	−88.5	12.5	−34.6	10.8
134.0	−10.8	5.4	31.7	6/10	136.1	37.6	−17.8	24.8
162.9	−47.1	19.6	11.9	9/10	163.5	14.2	−17.1	9.5
283.7	−26.8	15.5	15.8	7/10	−75.7	14.3	−37.4	12.5
249.7	−82.1	16.9	13.9	8/10	44.5	15.9	−19.0	11.0
203.8	46.2	4.0	29.3	9/10	24.4	35.3	−18.0	22.9
342.1	23.8	29.1	9.1	10/10	162.5	9.9	−34.8	9.1
206.0	−25.4	21.9	13.2	7/10	−154.0	14.6	−32.6	13.2
-	-	-	-	-	-	-	-	-
-	-	-	-	-	-	-	-	-
-	-	-	-	-	-	-	-	-
-	-	-	-	-	-	-	-	-
323.9	23.1	3.3	31.8	10/10	144.2	27.4	−38.2	24.9
10.4	45.7	23.9	10.7	9/10	−169.3	12.3	−15.6	8.5
252.6	−42.9	23.5	10.8	9/10	−61.7	20.4	−15.0	10.8
-	-	-	-	-	-	-	-	-
-	-	-	-	-	-	-	-	-
-	-	-	-	-	-	-	-	-

[a]The geological units are referring to the Geological Map of Chile at scale 1:1.000.000 (2003), Geology of the Villarrica Volcano at scale 1:50.000 (2006), and *Munizaga et al.* [1988]. Plv_1 = Andesitic Lava, Middle to Late Pleistocene; Pl_3 = Basic to intermediate lava sequences and volcanic centers, Pleistocene; PPl_3 = Mainly basic lava, Plio-pleistocene; Mg = North Patagonian Batholith, Miocene; MgL = Liquiñe Granitoid, Miocene; Om2c = Andesitic to dacitic lava, Oligo-Miocene. The geographic coordinates are referred to WGS84 datum. Age in Ma is from the geologic timescale of *Gradstein et al.* [2004]. Bedding is expressed in dip azimuth/dip values. *D* and *I* are site mean declination and inclination calculated before and after tectonic correction for low and high coercivity (in bold and identified with ***HC**) component; *k* and α_{95} are statistical parameters after *Fisher* [1953]; *n*/*N* is number of samples giving reliable results/number of studied samples at a site. Site mean rotation *R* and flattening *F* values, and relative errors Δ*R* and Δ*F* (according to *Demarest* [1983]) are relative to coeval *D* and *I* South American values expected at the sampling area considering South American paleopoles from *Torsvik et al.* [2008].

[b]Rejected sites with values of $\alpha_{95} > 30°$ and $I < |10°|$ (see text).

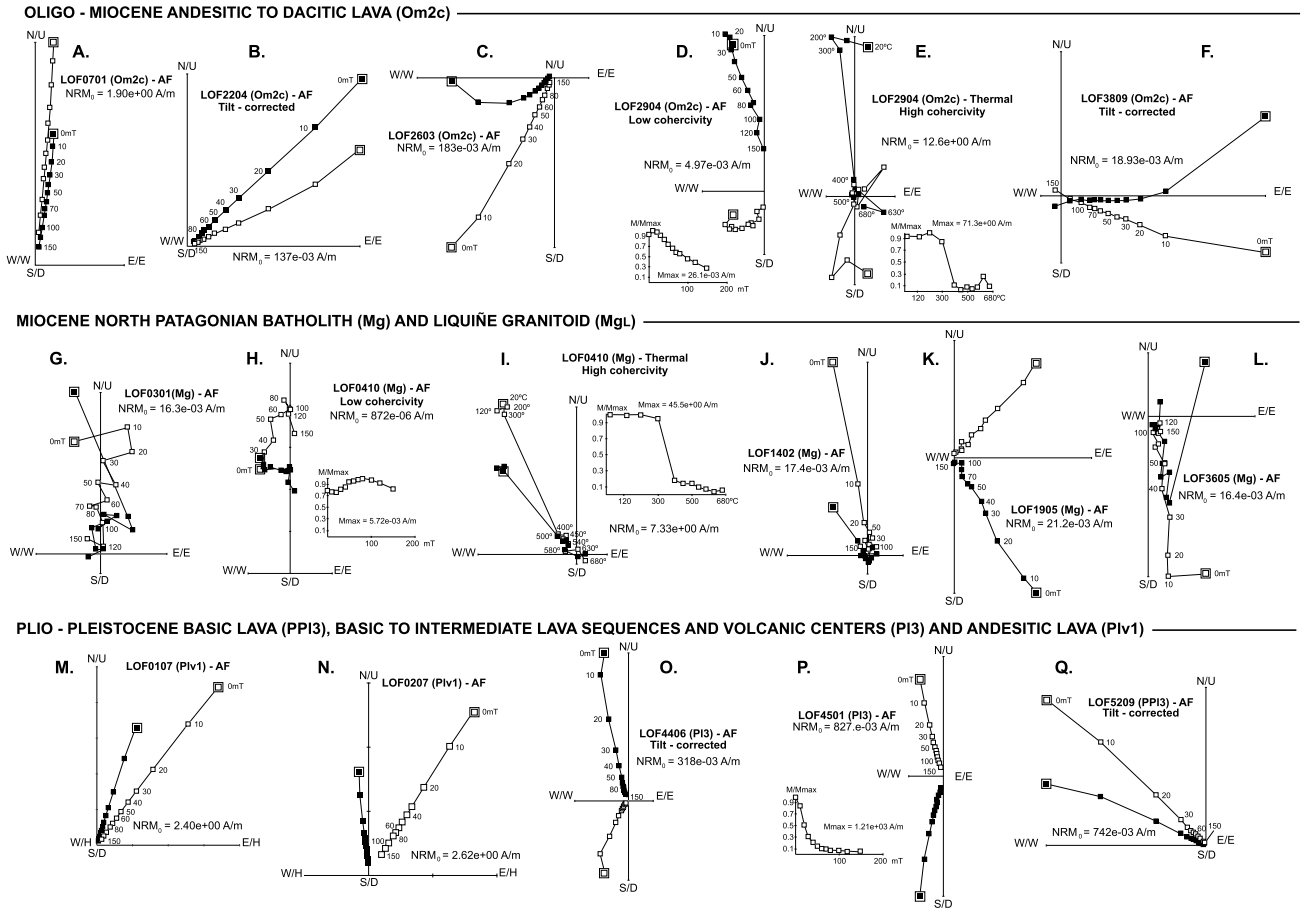

Figure 5. (a–q) Orthogonal vector diagrams of typical demagnetization data, in situ coordinates (tilt corrected when specified), showing representative samples carrying single magnetization components. Solid (open) squares represent projection onto the horizontal (vertical) plane. Demagnetization step values are in mT and °C for the alternating field and thermally demagnetized samples, respectively.

Site rotations with respect to South America are shown in Figure 7. Although most of the rotations are calculated using the in situ paleomagnetic directions, rotation sense and values are often consistent with those from close sites where bedding is apparent. This suggests the first-order validity of the rotation pattern documented in Figure 7, although we are aware that the lack of bedding for most of the sites represents the main weakness point of our work. Flattening values are mostly negative but show a great variability, even in rocks of the same age at the same side of the LOFZ (Table 2), implying that they cannot be used to assess microplate latitudinal drift.

In the whole studied area, rotations change significantly in close sites, so that the size of the rotating blocks seems to be very small, in the order of 1 km for the smallest domains. The largest coherent block is depicted by six nonrotated sites (LOF03 to LOF08, Figure 3b) east of Pucón and shows a long axis, subparallel to the LOFZ, of approximately 15 km.

A possible age dependence of the rotation amount cannot be properly evaluated, as rotations vary greatly up to |170°| depending strongly on the distance to the main fault of independent small blocks inside the LOFZ deforming zone. Although most of the sites yielding rotations >|100°| are Oligo-Miocene in age (e.g., sites 20 and 27), some of the Plio-Pleistocene sites (e.g., sites 44 and 45) show rotations of similar magnitude. We conclude that rotations are surely post 5 Ma in age, but the occurrence of older rotations cannot be assessed in our data set (180° is the maximum rotation value that we admit). In any case, this is in agreement with the post mid-Cenozoic rotational timing suggested by *Beck et al.* [2000].

The Villarrica domain yields the more complete rotation pattern (Figures 3 and 7a). Two completely different behaviors are observed east and west of the LOFZ. East of the LOFZ, some sites yield a 150°–170° CW rotation adjacent to the fault. CW rotations progressively decrease moving eastward, until no significant rotation is

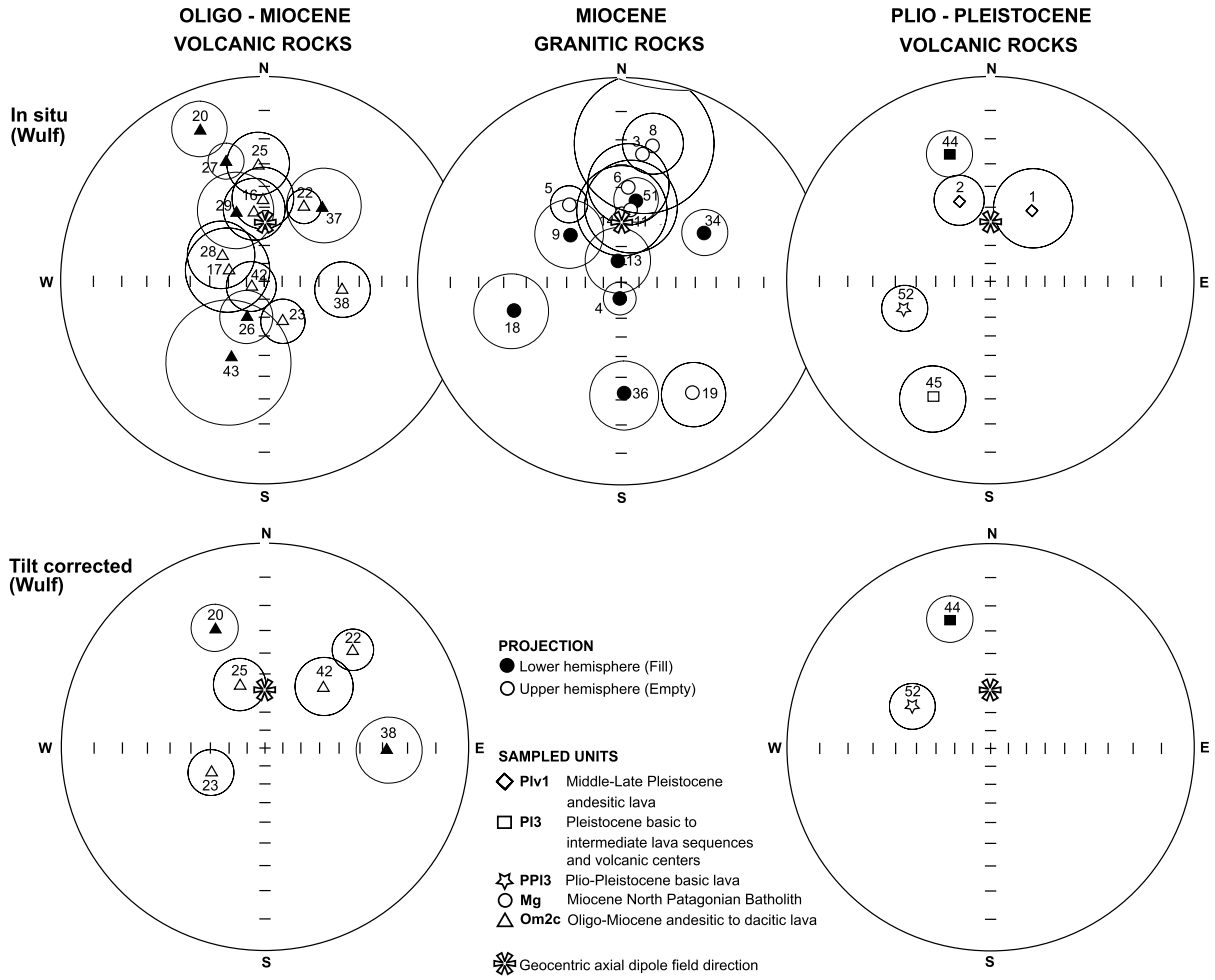

Figure 6. Equal-angle projection of the site mean paleomagnetic directions gathered along the LOFZ. Solid (open) symbols represent projection onto the lower (upper) hemisphere. Open circles are the projections of the α_{95} cones about the mean directions. Numbers correspond to sites shown in Figure 3 and detailed in Table 2. The asterisk represents the normal polarity geocentric axial dipole (GAD) field direction ($D = 0°$; $I = -58°/-60°$) expected at the study area.

observed at approximately 10 km from fault trace. On the other hand, other sites located east of the fault are nonrotated, independently of their distance from the LOFZ. Within 2 km from the fault trace, two CCW rotated sites also occur.

West of the LOFZ, a complete different rotational pattern occurs (Figure 7a). Some sites are similarly not rotated, independent of their distance to the fault, but most of the sites yield CCW rotations, up to a maximum 150°–170° value. Four CW rotated sites also occur in the Osorno domain.

In Figure 7b, we consider the case of rotation values $>|180°|$ based on the assumption that CW rotation amount increases toward a dextral fault [e.g., *Nelson and Jones*, 1987; *Piper et al*., 1997]. Figure 7b shows that, besides the unrotated blocks, CW rotations would reach values of ~300° within 4 km east and west from the LOFZ.

Rotation senses documented by us along the LOFZ are consistent with previous results by *Garcia et al*. [1988], *Cembrano et al*. [1992], *Rojas et al*. [1994], and *Beck et al*. [1998, 2000], who documented CCW and CW rotations west and east of the LOFZ, respectively. However, reported rotation magnitudes were smaller than in our study, as they did not exceed −30° and 49°, respectively.

9. Kinematic Model of Block Rotation in the Liquiñe-Ofqui Fault Zone

The paleomagnetic data documented by us show that the rotation pattern is not symmetrical along the LOFZ and that it cannot be accounted by any of the kinematic models of block rotation proposed so far. First, we

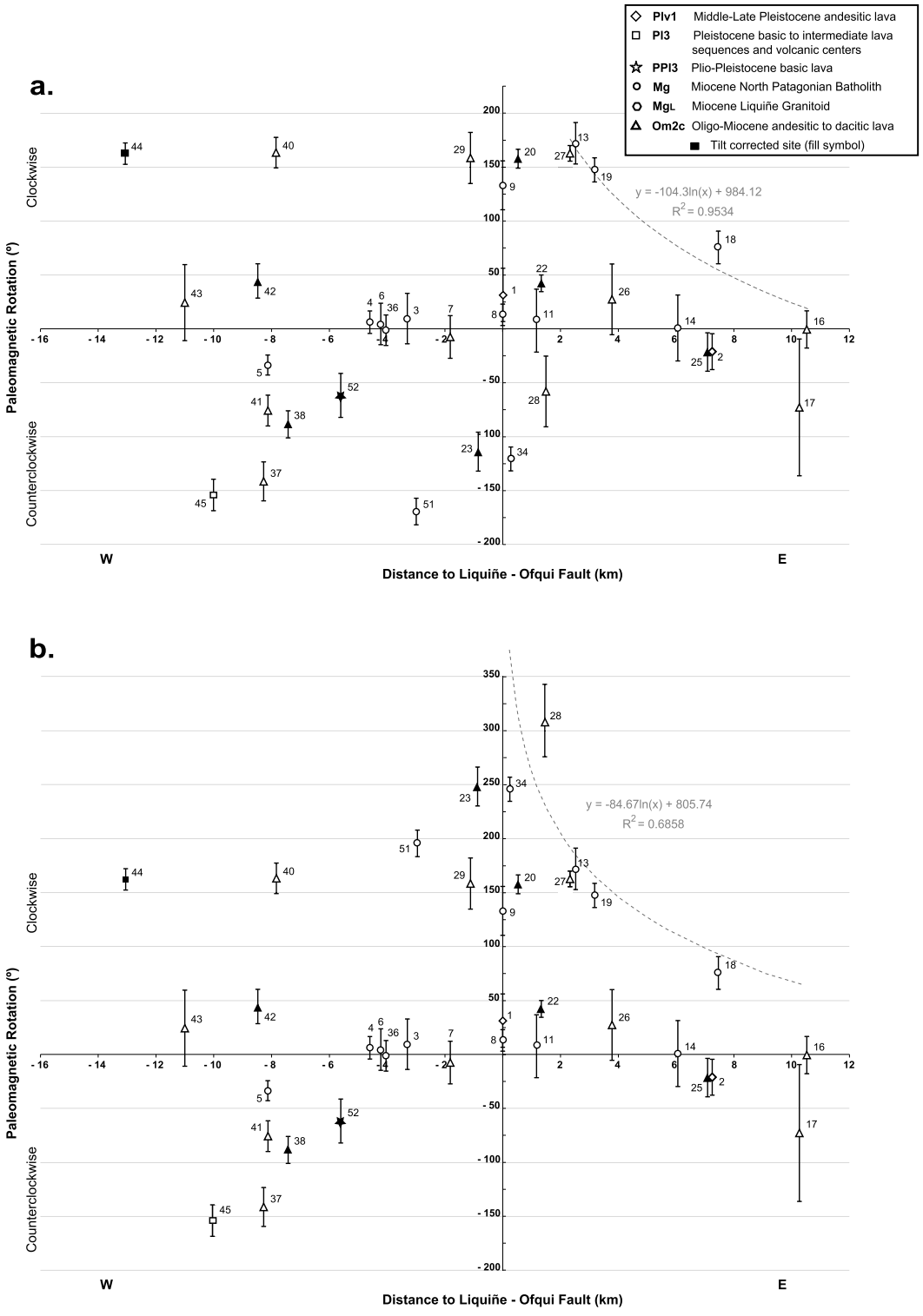

Figure 7. Plot of paleomagnetically determined rotations with respect to South America versus site distance to the LOFZ main trace (see Figure 3 for location). Dashed lines are a logarithmic best fit curve for the CW rotated sites located east of the LOFZ. (a) Sense and amount of rotation defined by the smaller angle between the observed and expected declinations for South America (rotation values by definition $\leq|180°|$); (b) Same as Figure 7a, but assuming that CW rotation magnitude increases toward the fault. Sites rotated CCW and located within 4 km from the fault were considered as rotating CW more than 180°.

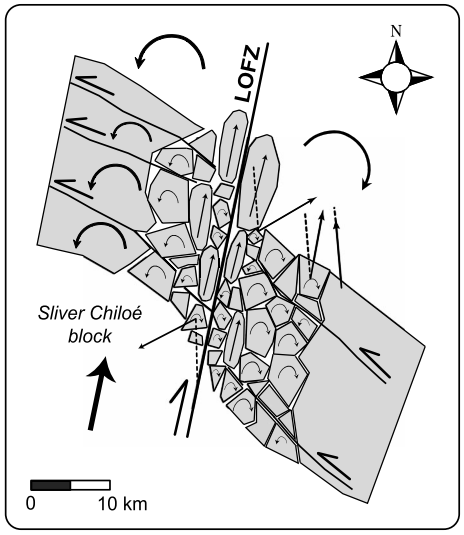

Figure 8. Quasi-continuous block rotation model of the Patagonian Andes around the LOFZ based on paleomagnetically observed rotations. The dimension and shape of the individual crustal blocks are hypothetic, but consistent with the areal variability of the paleomagnetic rotations and the location of both the LOFZ main strand and the secondary fault system (Figure 3).

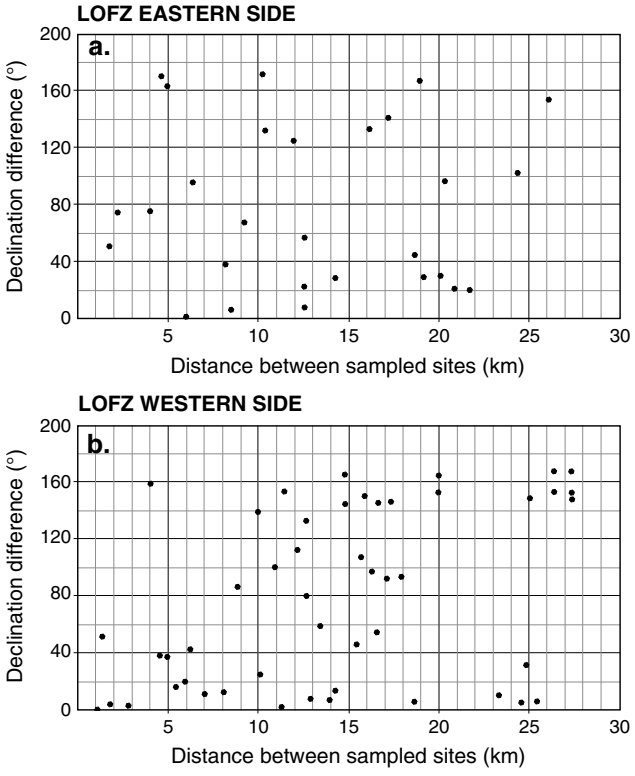

Figure 9. Rotation difference between pairs of sites along the LOFZ with respect to the distance between them. We considered the zone between 39.0 and 39.4°S where there is the greatest paleomagnetic data concentration. (a) LOFZ eastern side, (b) LOFZ western side.

note that the continuous models do not apply, as rotations largely exceed 90°, which is the maximum possible value if the crust is entirely assimilated to a thin viscous sheet [*Nelson and Jones*, 1987; *Kimura et al*., 2004, 2011]. Crust is clearly subdivided in small (~1–10 km) blocks, which underwent rotations largely exceeding 90°. The occurrences of blocks smaller than LOFZ deforming zone width, as well as block rotation distribution, are also inconsistent with discontinuous kinematic models of block rotation [*Ron et al*., 1984; *Garfunkel and Ron*, 1985; *McKenzie and Jackson*, 1986].

Both block size and rotation magnitude are very similar to those documented for the Alpine Fault of New Zealand by *Randall et al*. [2011]. We note that the maximum rotation documented by us (170°) is probably a lower bound, as a rotation greater than 180° would be interpreted as lower than 180° and with opposite rotation sense (Figure 7b).

The existence of different small blocks along the LOFZ was also postulated by *Thomson* [2002], who relying on fission tracks thermochronology reported south of ~43°S an important vertical component of displacement along the LOFZ, distributed in different blocks, each one with different rates and amounts of denudation and cooling. Reverse and oblique-slip rather than purely strike slip was documented, demonstrating the transpressive nature of the LOFZ.

East of the LOFZ, some sites yield 150°–170° CW rotations adjacent to fault, decreasing to null rotations approximately 10 km east of the fault. We fit this CW rotation trend using a logarithmic regression curve (Figure 7a), defined by an *R*-squared value of 0.9534. Rotation sense (CW in a dextral shear zone), magnitude (>90°), and pattern seem to support the quasi-continuous model of *McKenzie and Jackson* [1983], *Nelson and Jones* [1987], and *Sonder et al*. [1994] (Figure 8).

A significant difference with respect to the quasi-continuous models is represented by the unrotated sites, observed along and very close to the fault. We think that the nonrotated sites occur on elongated slivers with the long axis subparallel to the fault (Figures 3 and 8). These blocks are simply translated parallel to the fault and are unable to rotate due

to their low aspect ratio. A similar crust deformation pattern was documented by *Randall et al*. [2011] on the Alpine Fault of New Zealand. Unrotated blocks occur also west of the LOFZ. Here the distribution of unrotated sites LOF03–LOF08 adjacent to the fault supports the occurrence of an elongated block subparallel to the LOFZ (Figure 3). Our data could also explain why several paleomagnetic studies of major strike-slip fault zones (North Anatolian and San Andreas faults) have puzzlingly documented the lack of rotations [*Haeussler et al*., 1991; *Platzman and Platt*, 1994].

An estimate of the maximum block size into the LOFZ deforming zone can be provided by the rotation difference between site pairs. If two or more sites belong to the same block, a low or null rotation difference between them is expected. We considered the zone between 39.0 and 39.4°S where there is the greatest paleomagnetic data concentration and evaluated the distribution of rotation difference between site pairs with respect to the distance between them (Figure 9). Figure 9a shows that east of the LOFZ, the sites more than 2 km distant each other have rotation differences $>40°$. Conversely, west of the LOFZ, rotations differences increase significantly ($>80°$) only for sites more than 9 km far, while closer sites have rotation differences mostly $<40°$ (Figure 9b). Inferred block sizes again support a quasi-continuous deformation model east of the LOFZ, as shear zone width is ~10 km (according to rotation distribution, Figure 7) and block sizes are smaller than 2 km.

This small block size implies a shallow décollement depth, of the same order of magnitude. Rotating blocks are expected to detach along the brittle-ductile transition, which is inferred to occur at 350 ± 50°C within the crust [*Chen et al*., 2013]. Thus, our data indicate a high geothermal gradient at the LOFZ, consistent with the widespread occurrence of volcanoes along the fault trace. Differences of estimated block sizes east and west of the LOFZ may be related to inherited crust rheology differences and/or different geothermal gradients at the two sides of the fault. This is consistent with expected geothermal gradient decrease moving from a volcanic arc toward a subduction fore arc.

Considering that the vertical-axis rotations are distributed among a great number of different irregular blocks and therefore that the LOFZ deforming zone does not behave as a single continuously deforming block, we cannot discard the possibility of interaction between adjacent blocks, which could induce changes in block rotation magnitude and sense. However, in the aim of simplifying the problem, block interaction was never mentioned by the kinematic models proposed so far [e.g., *Nur et al*., 1986].

The total displacement along the LOFZ can be predicted using the equation for a constant slip velocity of rotating circular blocks obeying to the thin viscous sheet model [*Nelson and Jones*, 1987; *Sonder et al*., 1994]:

$$\theta = -\frac{2d(x)n^{1/2}\pi}{\lambda}\exp\left(-4n^{1/2}\pi y/\lambda\right) \quad (1)$$

where

θ rotation, positive (negative) values represent CCW (CW) rotations;
$2d(x)$ displacement;
λ twice the shear zone length;
n power law exponent.

Considering a 3–5 n value, typical for ductile behavior of the lower crust that drives block rotation [*Sonder et al*., 1986], a λ value of 2000 km (twice LOFZ fault length), and our maximum CW rotation value of 171° (site LOF13), we get a 1112 km offset, which is clearly too big for a 1000 km long fault. Conversely, the equation of *Lamb* [1987] relates fault width (W) and displacement (D) with the rotation value of equidimensional blocks (θ)

$$\theta = 0.5\ D/W \quad (2)$$

By considering a 20 km W value (double of the CW rotated domain east of the LOFZ) and again a 171° θ value, we get a total offset of 120 km. This value is consistent to a 1000 km total fault length [*Sylvester*, 1988] and about double of the 65 km Plio-Pleistocene offset for the central LOFZ segment proposed by *Rosenau et al*. [2006] (13 mm/yr for the last 5 Ma).

The quasi-continuous kinematic model predicts a symmetrical rotation pattern at both fault edges (Figure 2). Conversely, CCW rotations dominate west of the LOFZ and do not seem to fade out moving away from the LOFZ (most of the strongly CCW rotated sites occur at 8–10 km from fault, Figures 3 and 7). This area is characterized by a set of NW-SE left-lateral faults, antithetic to the LOFZ, and spaced by 20–40 km, whose

present-day activity has been recently demonstrated by seismicity distribution and focal mechanisms [*Lange et al*., 2008].

The unique models postulating CCW rotations into a dextral shear zone are the "slate" models by *Ron et al*. [1984] and *McKenzie and Jackson* [1986] (Figure 2a). However, the slate models cannot explain our data, as they would require a set of NE-SW synthetic dextral faults bounding CCW rotating slates inside the deforming zone (Figure 2b), which are not apparent. Similarly, the continuous and the quasi-continuous models cannot explain the "wrong-way rotation" [*Beck et al*., 1993; *Rojas et al*., 1994], because CW rotations increasing in magnitude toward the fault are expected in dextral strike-slip fault zones. This evidence suggests that the LOFZ itself actually does not drive directly the rotations along its west side and that these CCW rotations are mainly consequence of the kinematics of or within the Chiloé Block. We put forward two possible explanations for the occurrence of a CCW rotation domain west of the LOFZ:

1. Left-lateral antithetic faults locally yield a quasi-continuous rotation pattern similar to that observed east of the LOFZ, but characterized by CCW rotations because fault kinematics is left-lateral here. This seems to be confirmed by the occurrence of some CCW rotated sites (LOF05, LOF37, and LOF38, Figure 3) adjacent to the antithetic faults, although other CCW rotated sites (LOF34 and LOF52) are definitely located far from them.
2. *Beck et al*. [1993] and *Rojas et al*. [1994] explained CCW rotations west of the LOFZ with the occurrence of buttresses hampering the northward drift of a fore-arc crustal sliver pushed by the oblique Nazca subduction (buttress effect model of *Beck* [1991] and *Beck et al*. [1993], Figure 2c). The sliver would be segmented into lens-shaped blocks, which rotate CCW and overlap one another as they move forward. If we consider the first 14 km west from the LOFZ (Figure 7), our rotation pattern is barely consistent with this model, requiring the occurrence of great lens-shaped block rotating rigidly. Conversely we have evidence on small (1-10 km) blocks undergoing variable amounts of CCW rotations, as well as other (possibly elongated) blocks not rotating at all.

In any case, the asymmetrical rotational pattern at the two LOFZ sides suggests that the NW-SE left-lateral faults mostly apparent in the western fore-arc sliver are connected and genetically related to the LOFZ, as suggested by *Rosenau et al*. [2006] relying on cross-cutting relations. In fact, the occurrence of NW-SE sinistral faults inverting older basement structures and displacing the LOFZ (thus not connected nor genetically related to it [e.g., *Glodny et al*., 2008; *Lange et al*., 2008; *Melnick et al*., 2009]) would likely yield the same rotation scenario at both LOFZ edges.

It is clear that further paleomagnetic data from the Andean fore arc are needed to properly understand the kinematic meaning of the CCW rotations west of the LOFZ. Finally, we are aware that a few data do not fit with the rotation patterns described above: five sites rotate CCW and CW east and west of the LOFZ, respectively (Figures 3 and 7a). It is difficult to assess the validity of these data as two potential sources of error exist: first, all these directions but two are calculated in situ (no bedding is apparent) implying a possible rotation error; second, it is possible that these sites (and mostly those located adjacent to the fault) rotated in fact more than 180° in the opposite sense (Figure 7b).

10. Conclusions

Paleomagnetic data from the Chile fore arc at 38°S–41°S reveal unprecedented kinematics of crust deformation along the Liquiñe-Ofqui fault zone, a major 1000 km long dextral shear zone that takes up the margin-parallel component of the Nazca Plate oblique subduction beneath South America. The data do not completely match any of the kinematic models proposed so far and have evidence on a different behavior at the two fault edges. Crust within 20 km from the fault is fragmented into ~1–10 km wide blocks, and their small size suggests similarly shallow detachment depth and brittle-ductile transition as well as high heat flow, consistently with the occurrence of andesitic volcanoes along fault trace. While some block show large (up to 150°–170°) rotations, others are not rotated, even adjacent to the fault walls. We infer that this is related to block aspect ratio and that equidimensional blocks are prone to rotate, while elongated crust slivers parallel to the fault are displaced and undergo no rotation.

Rotating blocks east of the LOFZ yield 150°–170° CW rotations, ending at approximately 10 km from fault trace (Figure 7a). These data, considering the dextral shear sense of the LOFZ, are consistent with the

quasi-continuous deformation model proposed by *Sonder et al*. [1994] and *Randall et al*. [2011]. Thus, we infer that upper crust is subdivided in small blocks that are dragged by the flow of the underlying ductile crust rotating even more than 90°. Plio-Pleistocene sites rotate more than 150°, implying that block rotation is very recent and occurred during the last 5 Ma. Conversely, the possible occurrence of older rotations cannot be evaluated by our data set (as a conservative approach, we consider 180° as the maximum possible rotation value). By using the equation of *Lamb* [1987], relating rotations to fault displacement, we find a total LOFZ offset of 120 km, which is consistent to a 1000 km total fault length and about the double of the 65 km offset proposed by *Rosenau et al*. [2006] for the last 5 Ma.

West of the LOFZ, a different structural and rotation pattern is apparent. Crust is cut by seismically active NW-SE antithetic faults spaced by 20–40 km, and CCW rotations, reaching 170°, dominate. CCW rotations do not diminish moving away from the LOFZ, as the majority of the rotated sites occur at 8–10 km from fault trace (Figure 7a). This suggests that the LOFZ activity does not drive directly the rotations along its west side and that CCW rotations are mainly consequence of the kinematics and/or faulting of the Chiloé Block. Although more data are needed to understand crust kinematics yielding the observed paleomagnetic data west of the LOFZ, it is clear that some models, as the slate discrete model by *Ron et al*. [1984] and *McKenzie and Jackson* [1986], would predict CW rotations of the blocks bounded by the NW-SE left-lateral antithetic faults and are thus not consistent with our data set.

Our study reveals that the pattern of rotations along continental transcurrent zones is more complex than previously believed and that the existing models for kinematics of crust deformation are unable to explain the observed kinematic complexity. It is clear that the rotation pattern we documented is related to the peculiar setting of a strike-slip fault occurring on the fore arc of a subduction zone and controlling volcanism, thus characterized by high heat flow. More work is needed to relate each peculiar paleomagnetic rotation pattern to local tectonics of transcurrent shear zones.

Acknowledgments

We are grateful to the Chilean people and authorities who made possible our long field trips and allowed us to enjoy their superb landscape and geology. We thank S. Zapata and A. Tomé for their valuable help in the field work and paleomagnetic sampling. This work was financed by INGV funds. The paleomagnetic data reported here is available upon e-mail request to C.H.M. Two anonymous referees provided careful and constructive reviews of our manuscript. Thanks also to the Associate Editor and Editor Claudio Faccenna for carefully evaluating our work.

References

Angermann, D., J. Klotz, and C. Reigber (1999), Space-geodetic estimation of the Nazca-South America euler vector, *Earth Planet. Sci. Lett.*, *171*(3), 329–334.

Barrientos, S., and P. Acevedo-Aránguiz (1992), Seismological aspects of the 1988–1989 Lonquimay (Chile) volcanic eruption, *J. Volcanol. Geotherm. Res.*, *53*, 73–87.

Beck, M. E. (1976), Discordant paleomagnetic pole positions as evidence of regional shear in the western Cordillera of North America, *Am. J. Sci.*, *276*, 694–712.

Beck, M. E. (1986), Model for late Mesozoic-early Tertiary tectonics of coastal California and western Mexico, and speculations on the origin of the San Andreas Fault, *Tectonics*, *5*, 49–64, doi:10.1029/TC005i001p00049.

Beck, M. E. (1988), Analysis of late Jurassic—Recent paleomagnetic data from active plate margins of South America, *J. South Am. Earth Sci.*, *1*(1), 39–52, doi:10.1016/0895-9811(88)90014-4.

Beck, M. E. (1989), Paleomagnetism of continental North America: Implications for displacement of crustal blocks within the Western Cordillera, Baja California to British Columbia, in *Geophysical Framework of the Continental United States*, edited by L. C. Pakiser and W. D. Mooney, *Mem. Geol. Soc. Am.*, *172*, 471–492.

Beck, M. E. (1991), Coastwise transport reconsidered: Lateral displacements in oblique subduction zones, and tectonic consequences, *Phys. Earth Planet. Inter.*, *68*(1-2), 1–8, doi:10.1016/0031-9201(91)90002-Y.

Beck, M. E., R. F. Burmester, and B. C. Steele (1998), Paleomagnetism of probably remagnetized late Mesozoic volcanic rocks near Lago Verde, Aisén, Southern Chile, *Andean Geol.*, *25*(2), 153–163.

Beck, M., C. Rojas, and J. Cembrano (1993), On the nature of buttressing in margin-parallel strike-slip fault systems, *Geology*, *21*, 755–758, doi:10.1130/0091-7613(1993)021<0755.

Beck, M., R. Burmester, R. Drake, and P. Riley (1994), A tale of two continents: Some tectonic contrasts between the central Andes and the North American Cordillera, as illustrated by their paleomagnetic signatures, *Tectonics*, *13*(1), 215–224, doi:10.1029/93TC02398.

Beck, M., R. Burmester, J. Cembrano, and R. Drake (2000), Paleomagnetism of the North Patagonian Batholith, southern Chile. An exercise in shape analysis, *Tectonophysics*, *326*, 185–202.

Bird, P., and K. Piper (1980), Plane-stress finite element models of tectonic flow in southern California, *Phys. Earth Planet. Inter.*, *21*, 158–175.

Bohm, M., S. Lüth, H. Echtler, G. Asch, and K. Bataille (2002), The Southern Andes between 36 and 40°S latitude: Seismicity and average seismic velocities, *Tectonophysics*, *356*, 275–289.

Bourne, S., P. England, and B. Parsons (1998), The motion of crustal blocks driven by flow of the lower lithosphere and implications for slip rates of continental strike-slip faults, *Nature*, *391*, 655–659.

Cande, S., and R. Leslie (1986), Late Cenozoic tectonics of the southern Chile trench, *J. Geophys. Res.*, *91*(B1), 471–496, doi:10.1029/JB091iB01p00471.

Cembrano, J., and F. Herve (1993), The Liquiñe-Ofqui fault zone: A major Cenozoic strike slip duplex in the Southern Andes, in *Second ISAG, Oxford (U. K.)*, pp. 175–178, ORSTOM Editions, Paris.

Cembrano, J., and L. Lara (2009), The link between volcanism and tectonics in the southern volcanic zone of the Chilean Andes: A review, *Tectonophysics*, *471*(1–2), 96–113, doi:10.1016/j.tecto.2009.02.038.

Cembrano, J., M. E. Beck, R. F. Burmester, C. Rojas, A. Garcia, and F. Herve (1992), Paleomagnetism of lower Cretaceous rocks from east of the Liquiñe-Ofqui fault zone, southern Chile: Evidence of small in-situ clockwise rotations, *Earth Planet. Sci. Lett.*, *113*(4), 539–551, doi:10.1016/0012-821X(92)90130-N.

Cembrano, J., F. Hervé, and A. Lavenu (1996a), The Liquiñe-Ofqui fault zone: A long-lived intra-arc fault system in southern Chile, *Tectonophysics*, *1*, 55–66.
Cembrano, J., E. Schermer, A. Lavenu, F. Hervé, S. Barrientos, B. McClelland, and G. Arancibia (1996b), Nature and timing of Cenozoic intra-arc deformation, southern Chile, paper presented at Third ISAG, St. Malo, France.
Cembrano, J., E. Schermer, A. Lavenu, and A. Sanhueza (2000), Contrasting nature of deformation along an intra-arc shear zone, the Liquiñe-Ofqui fault zone, southern Chilean Andes, *Tectonophysics*, *319*, 129–149.
Cembrano, J., A. Lavenu, and P. Reynolds (2002), Late Cenozoic transpressional ductile deformation north of the Nazca-South America-Antarctica triple junction, *Tectonophysics*, *354*, 289–314.
Cembrano, J., A. Lavenu, G. Yañez, R. Riquelme, M. García, G. González, and G. Hérail (2007), Neotectonics, in *The Geology of Chile*, edited by T. Moreno and W. Gibbons, pp. 231–262, Geol. Soc. London, U. K.
Chen, W.-P., C.-Q. Yu, T.-L. Tseng, Z. Yang, C. Wang, J. Ning, and T. Leonard (2013), Moho, seismogenesis, and rheology of the lithosphere, *Tectonophysics*, *609*, 491–503, doi:10.1016/j.tecto.2012.12.019.
Chinn, D., and B. Isacks (1983), Accurate source depths and focal mechanisms of shallow earthquakes in western South America and in the New Hebrides island arc, *Tectonics*, *2*(6), 529–563, doi:10.1029/TC002i006p00529.
Cifuentes, I. N. I. S. L. (1989), The 1960 Chilean earthquakes, *J. Geophys. Res.*, *94*(B1), 665–680, doi:10.1029/JB094iB01p00665.
Cowan, D., M. Botros, and H. Johnson (1986), Bookshelf tectonics: Rotated crustal blocks within the Sovanco Fracture Zone, *Geophys. Res. Lett.*, *13*(10), 995–998, doi:10.1029/GL013i010p00995.
Cowgill, E., J. R. Arrowsmith, A. Yin, W. Xiaofeng, and C. Zhengle (2004), The Akato Tagh bend along the Altyn Tagh fault, northwest Tibet 2: Active deformation and the importance of transpression and strain hardening within the Altyn Tagh system, *Geol. Soc. Am. Bull.*, *116*, 1443, doi:10.1130/B25360.1.
Demarest, H. (1983), Error analysis for the determination of tectonic rotation from paleomagnetic data, *J. Geophys. Res.*, *88*(B5), 4321–4328, doi:10.1029/JB088iB05p04321.
Dewey, J. F., and S. H. Lamb (1992), Active tectonics of the Andes, *Tectonophysics*, *205*(1–3), 79–95, doi:10.1016/0040-1951(92)90419-7.
Diraison, M., P. R. Cobbold, E. A. Rossello, and A. J. Amos (1998), Neogene dextral transpression due to oblique convergence across the Andes of northwestern Patagonia, Argentina, *J. South Am. Earth Sci.*, *11*(6), 519–532.
Dziewonski, A. M., G. Ekström, J. H. Woodhouse, and G. Zwart (1991), Centroid-moment tensor solutions for April–June 1990, *Phys. Earth Planet. Inter.*, *66*(3–4), 133–143, doi:10.1016/0031-9201(91)90072-P.
England, P., and D. McKenzie (1982), A thin viscous sheet model for continental deformation, *Geophys. J. Roy. Astron. Soc.*, *70*, 295–321, doi:10.1111/j.1365-246X.1982.tb04969.x.
England, P., and R. E. Wells (1991), Neogene rotations and quasicontinuous deformation of the Pacific Northwest continental margin, *Geology*, *19*, 978–981.
England, P., G. Houseman, and L. Sonder (1985), Length scales for continental deformation in convergent, divergent, and strike-slip environments: Analytical and approximate solutions for a thin viscous sheet model, *J. Geophys. Res.*, *90*(B5), 3551–3557, doi:10.1029/JB090iB05p03551.
Fisher, R. A. (1953), Dispersion on a sphere, *Proc. R. Soc. London, Ser. A*, *217*, 295–305.
Folguera, A., V. A. Ramos, R. L. Hermanns, and J. Naranjo (2004), Neotectonics in the foothills of the southernmost central Andes (37°–38°S): Evidence of strike-slip displacement along the Antiñir-Copahue fault zone, *Tectonics*, *23*, TC5008, doi:10.1029/2003TC001533.
Forsythe, R., and E. Nelson (1985), Geological manifestations of ridge collision: Evidence from the Golfo de Penas-Taitao basin, southern Chile, *Tectonics*, *4*(5), 477–495, doi:10.1029/TC004i005p00477.
Freund, R. (1974), Kinematics of transform and transcurrent faults, *Tectonophysics*, *21*, 93–134.
Garcia, A., M. Beck, R. Burmester, F. Munizaga, and F. Herve (1988), Pelomagnetic reconnaissance of the region de los Lagos, southern Chile, and its tectonic implications, *Rev. geológica Chile*, *15*(1), 13–30.
Garfunkel, Z. (1974), Model for the late Cenozoic tectonic history of the Mojave Desert, California, and for its relation to adjacent regions, *Geol. Soc. Am. Bull.*, *85*(12), 1931–1944, doi:10.1130/0016-7606(1974)85<1931.
Garfunkel, Z., and H. Ron (1985), Block rotation and deformation by strike-slip faults: 2. The properties of a type of macroscopic discontinuous deformation, *J. Geophys. Res.*, *90*(B10), 8589, doi:10.1029/JB090iB10p08589.
Geissman, J., J. Callian, J. Oldow, and S. Humphries (1984), Paleomagnetic assessment of oroflexural deformation in west-central Nevada and significance for emplacement of allochthonous assemblages, *Tectonics*, *3*(2), 179–200, doi:10.1029/TC003i002p00179.
Giacosa, R. E., and N. Heredia (2004), Estructura de los Andes Nordpatagónicos en los cordones Piltriquitrón y Serrucho y en el valle de El Bolsón (41°30′–42°002 S), Río Negro, *Revista de la Asociación Geológica Argentina*, *59*(1), 91–102.
Giacosa, R. E., J. C. Afonso, N. Heredia, and J. Paredes (2005), Tertiary tectonics of the sub-Andean region of the North Patagonian Andes, southern central Andes of Argentina (41–42°30′S), *J. South Am. Earth Sci.*, *20*(3), 157–170.
Glodny, J., H. Echtler, S. Collao, M. Ardiles, P. Burón, and O. Figueroa (2008), Differential late Paleozoic active margin evolution in South-Central Chile (37°S–40°S)—The Lanalhue fault zone, *J. South Am. Earth Sci.*, *26*(4), 397–411, doi:10.1016/j.jsames.2008.06.001.
Gradstein, F. M., J. G. Ogg, and A. G. Smith (2004), *A Geologic Time Scale*, vol. 86, Cambridge Univ. Press, Cambridge, U. K.
Hackney, R., et al. (2006), The segmented overriding plate and coupling at the south-central Chilean margin (36–42°S), in *The Andes: Active Subduction Orogeny: Frontiers in Earth Sciences*, edited by O. Oncken et al., pp. 355–374, Springer-Verlag, Berlin, Heidelberg, New York.
Haeussler, P. J., R. E. Wells, J. W. Hillhouse, A. Sarna-Wojcicki, and W. Thatcher (1991), Are there vertical axis rotations in the San Francisco Bay Region? Implications from paleomagnetic studies of the 6 m.y. Roblar Tuff, paper presented at Fall Meeting supll., *Eos Trans. AGU*, *72*, pp. 44.
Herron, E. M. (1981), Chile Margin near lat 38°S: Evidence for a genetic relationship between continental and marine geologic features or a case of curious coincidences?, *Geol. Soc. Am. Mem.*, *154*, 755–760.
Hervé, F. (1993), Paleozoic metamorphic complexes in the Andes of Aysén (west of Occidentalia), in *Proceedings of First Circum-Pacific and Circum-Atlantic Terrane Conference*, edited by F. Gutiérrez et al., pp. 64–65, Guanajuato, Mexico.
Hervé, F. (1994), The southern Andes between 39° and 44°S latitude: The geological signature of a transpressive tectonic regime related to a magmatic arc, in *Tectonics of the Southern Central Andes: Structure and Evolution of an Active Continental Margin*, edited by K. J. Reutter, E. Scheuber, and P. J. Wigger, pp. 243–248, Springer, Berlin.
Hervé, F., and R. Thiele (1987), Estado de conocimiento de las magafallas en Chile y su significado tectónico, *Comun. Univ. Chile*, *38*, 67–91.
Hervé, M. (1976), Estudio Geológico de la falla Liquiñe-Reloncaví en el área de Liquiñe; antecedentes de un movimiento transcurrente (Provincia de Valdivia), paper presented at I Congreso Geológico Chileno, Serv. Nac de Geol y Min., Santiago de Chile, Chile.
Hervé, M. (1977), Geología del área al este de Liquiñe, Provincia de Valdivia, X Región, Thesis, Depto. de Geología, Univ. de Chile, Chile.
Hoeppener, R., E. Kalthoff, and P. Schrader (1969), Zur physikalischen Tektonik: Bruchbildung bei verschiedenen Deformationen im Experiment, *Geol. Rundsch.*, *59*, 179–193.

Hoffmann-Rothe, A., N. Kukowski, N. Dresen, G. Echtler, O. Oncken, J. Klotz, E. Scheuber, and A. Kellner (2006), Oblique convergence along the Chilean margin: Partitioning, margin-parallel faulting and force interaction at the plate interface, in *The Andes: Active Subduction Orogeny*, edited by O. Oncken, pp. 125–146, Springer, Berlin, Heidelberg.

Irving, E., G. J. Woodsworth, P. J. Wynne, and A. Morrison (1985), Paleomagnetic evidence for displacement from the south of the Coast Plutonic Complex, British Columbia, *Can. J. Earth Sci.*, *22*(4), 584–598.

Jackson, J., and D. McKenzie (1984), Active tectonics of the Alpine-Himalayan Belt between western Turkey and Pakistan, *Geophys. J. Int.*, *77*, 185–264.

Jackson, J., and P. Molnar (1990), Active faulting and block rotations in the western Transverse Ranges, California, *J. Geophys. Res.*, *95*(B13), 22,073–22,087, doi:10.1029/JB095iB13p22073.

Kendrick, E., M. Bevis, R. Smalley, B. Brooks, R. B. Vargas, E. Lauría, and L. P. S. Fortes (2003), The Nazca–South America Euler vector and its rate of change, *J. South Am. Earth Sci.*, *16*(2), 125–131, doi:10.1016/S0895-9811(03)00028-2.

Kimura, H., Y. Itoh, and H. Tsutsumi (2004), Quaternary strike-slip crustal deformation around an active fault based on paleomagnetic analysis: A case study of the Enako fault in central Japan, *Earth Planet. Sci. Lett.*, *226*(3–4), 321–334, doi:10.1016/j.epsl.2004.08.003.

Kimura, H., N. Ishikawa, and H. Sato (2011), Estimation of total lateral displacement including strike-slip offset and broader drag deformation on an active fault: Tectonic geomorphic and paleomagnetic evidence on the Tanna fault zone in central Japan, *Tectonophysics*, *501*(1–4), 87–97, doi:10.1016/j.tecto.2011.01.016.

Kirschvink, J. L. (1980), The least-squares line and plane and the analysis of paleomagnetic data, *Geophys. J. Roy. Astron. Soc.*, *62*(3), 699–718.

Klotz, J., G. Khazaradze, D. Angermann, C. Reigber, R. Perdomo, and O. Cifuentes (2001), Earthquake cycle dominates contemporary crustal deformation in central and southern Andes, *Earth Planet. Sci. Lett.*, *193*, 437–446, doi:10.1016/S0012-821X(01)00532-5.

Lamb, S. H. (1987), A model for tectonic rotations about a vertical axis, *Earth Planet. Sci. Lett.*, *84*(1), 75–86, doi:10.1016/0012-821X(87)90178-6.

Lamb, S., and H. Bibby (1989), The last 25 Ma of rotational deformation in part of the New Zealand plate-boundary zone, *J. Struct. Geol.*, *11*(4), 473–492.

Lange, D., A. Rietbrock, C. Haberland, K. Bataille, T. Dahm, F. Tilmann, and E. R. Flüh (2007), Seismicity and geometry of the south Chilean subduction zone (41.5°S–43.5°S): Implications for controlling parameters, *Geophys. Res. Lett.*, *34*, L06311, doi:10.1029/2006GL029190.

Lange, D., J. Cembrano, A. Rietbrock, C. Haberland, T. Dahm, and K. Bataille (2008), First seismic record for intra-arc strike-slip tectonics along the Liquiñe-Ofqui fault zone at the obliquely convergent plate margin of the southern Andes, *Tectonophysics*, *455*(1–4), 14–24, doi:10.1016/j.tecto.2008.04.014.

Lara, L. E., J. Cembrano, A. Lavenu, and J. Darrozes (2004), Monogenetic volcanoes in Southern Andes and their relationship with vertical displacements along major strike-slip intra-arc faults, in *IAVCEI General Assembly*, 104.

Lavenu, A., and J. Cembrano (1999), Compressional- and transpressional-stress pattern for Pliocene and Quaternary brittle deformation in fore arc and intra-arc zones (Andes of Central and Southern Chile), *J. Struct. Geol.*, *21*(12), 1669–1691, doi:10.1016/S0191-8141(99)00111-X.

López-Escobar, L., J. Cembrano, and H. Moreno (1995), Geochemistry and tectonics of the Chilean Southern Andes basaltic Quaternary volcanism (37–46°S), *Andean Geol.*, *22*(2), 219–234.

MacDonald, W. D. (1980), Net tectonic rotation, apparent tectonic rotation, and the structural tilt correction in paleomagnetic studies, *J. Geophys. Res.*, *85*(B7), 3659, doi:10.1029/JB085iB07p03659.

Mandl, G. (1987), Tectonic deformation by rotating parallel faults: The "bookshelf" mechanism, *Tectonophysics*, *141*(4), 277–316, doi:10.1016/0040-1951(87)90205-8.

McKenzie, D., and J. Jackson (1983), The relationship between strain rates, crustal thickening, palaeomagnetism, finite strain and fault movements within a deforming zone, *Earth Planet. Sci. Lett.*, *65*(1), 182–202, doi:10.1016/0012-821X(83)90198-X.

McKenzie, D., and J. Jackson (1986), A block model of distributed deformation by faulting, *J. Geol. Soc. London*, *143*(2), 349–353, doi:10.1144/gsjgs.143.2.0349.

Melnick, D., M. Sanchez, H. P. Echtler, and V. Pineda (2003), Geología estructural de la Isla Mocha, centro-sur de Chile (38°30'S, 74°W): Implicancias en la tectónica regional, paper presented at X Congreso Geológico Chileno, Serv. Nac de Geol y Min., Santiago de Chile, Chile.

Melnick, D., F. Charlet, H. P. Echtler, and M. De Batist (2006a), Incipient axial collapse of the Main Cordillera and strain partitioning gradient between the central and Patagonian Andes, Lago Laja, Chile, *Tectonics*, *25*, TC5004, doi:10.1029/2005TC001918.

Melnick, D., A. Folguera, and V. A. Ramos (2006b), Structural control on arc volcanism: The Caviahue–Copahue complex, Central to Patagonian Andes transition (38°S), *J. South Am. Earth Sci.*, *22*(1–2), 66–88, doi:10.1016/j.jsames.2006.08.008.

Melnick, D., B. Bookhagen, M. R. Strecker, and H. P. Echtler (2009), Segmentation of megathrust rupture zones from fore-arc deformation patterns over hundreds to millions of years, Arauco peninsula, Chile, *J. Geophys. Res.*, *114*, B01407, doi:10.1029/2008JB005788.

Moreno, H., and J. Clavero (2006), Geología del área del Volcán Villarrica, 1:50,000, Carta Geológica de Chile, Serie Geología Básica 98, *Ser. Nac. de Geol. y Min.*, Santiago de Chile, Chile.

Moreno, H., and M. A. Parada (1976), Esquema geológico de la cordillera de los Andes, entre los paralelos 39°00' y 41°30'S, in *I Congreso Geológico Chileno*, pp. 213–226, Santiago de Chile, Chile.

Morton, W. H., and R. Black (1975), Crustal attenuation in Afar, in *Afar Depression of Ethiopia*, edited by A. Pilger and A. Rösler, pp. 55–65, Schweizerbart, Stuttgart, Germany.

Munizaga, F., F. Herve, R. Drake, R. J. Pankhurst, M. Brook, and N. Snelling (1988), Geochronology of the Lake Region of south-central Chile (39°–42°S): Preliminary results, *J. South Am. Earth Sci.*, *1*(3), 309–316.

Murdie, R., D. Prior, P. Styles, S. Flint, R. Pearce, and S. Agar (1993), Seismic responses to ridge-transform subduction: Chile triple junction, *Geology*, *21*(12), 1095–1098, doi:10.1130/0091-7613(1993)021<1095.

Nakamura, K. (1977), Volcanoes as possible indicators of tectonic stress orientation—Principle and proposal, *J. Volcanol. Geotherm. Res.*, *2*(1), 1–16.

Nelson, E., R. Forsythe, and I. Arit (1994), Ridge collision tectonics in terrane development, *J. South Am. Earth Sci.*, *7*(3–4), 271–278, doi:10.1016/0895-9811(94)90013-2.

Nelson, M., and C. Jones (1987), Paleomagnetism and crustal rotations along a shear zone, Las Vegas Range, southern Nevada, *Tectonics*, *6*(1), 13–33, doi:10.1029/TC006i001p00013.

Nur, A., H. Ron, and O. Scotti (1986), Fault mechanics and the kinematics of block rotations, *Geology*, *14*, 746–749, doi:10.1130/0091-7613(1986)14<746.

Pankhurst, R. J., F. Hervé, L. Rojas, and J. Cembrano (1992), Magmatism and tectonics in continental Chiloé, Chile (42°–42°30'S), *Tectonophysics*, *205*, 283–294.

Pankhurst, R. J., S. D. Weaver, F. Hervé, and P. Larrondo (1999), Mesozoic-Cenozoic evolution of the North Patagonian batholith in Aysen, southern Chile, *J. Geol. Soc.*, *156*(4), 673–694.

Pardo-Casas, F., and P. Molnar (1987), relative motion of the Nazca (Farallon) and South American plates since late Cretaceous time, *Tectonics*, *6*(3), 233–248, doi:10.1029/TC006i003p00233.
Piper, J., O. Tatar, and H. Gürsoy (1997), Deformational behaviour of continental lithosphere deduced from block rotations across the North Anatolian Fault Zone in Turkey, *Earth Planet. Sci. Lett.*, *150*, 191–203.
Plafker, G., and J. Savage (1970), Mechanism of the Chilean earthquakes of May 21 and 22, 1960, *Geol. Soc. Am. Bull.*, *81*(4), 1001–1030, doi:10.1130/0016-7606(1970)81.
Platzman, E., and J. Platt (1994), Why are there no clockwise rotations along the North Anatolian fault zone?, *J. Geophys. Res.*, *99*(B11), 21,705–21,715, doi:10.1029/94JB01665.
Quinteros, J., and S. V. Sobolev (2013), Why has the Nazca plate slowed since the Neogene?, *Geology*, *41*(1), 31–34, doi:10.1130/G33497.1.
Ramos, M. E., D. Orts, F. Calatayud, P. J. Pazos, A. Folguera, and V. A. Ramos (2011), Estructura, Estratigrafía y evolución tectónica de la cuenca de Ñirihuau en las nacientes del río Cushamen, Chubut, *Revista de la Asociación Geológica Argentina*, *68*(2), 210–224.
Randall, K., S. Lamb, and C. Mac Niocaill (2011), Large tectonic rotations in a wide zone of Neogene distributed dextral shear, northeastern South Island, New Zealand, *Tectonophysics*, *509*(3–4), 165–180, doi:10.1016/j.tecto.2011.05.006.
Ransome, F. L., W. H. Emmons, and G. H. Garrey (1910), Geology of ore deposits of the Bullfrog district, Govt. Print. Off., *U. S. Geol. Surv. Bull.*, *407*, pp. 1–130, Nev.
Rehak, K., M. R. Strecker, and H. P. Echtler (2008), Morphotectonic segmentation of an active forearc, 37°–41°S, Chile, *Geomorphology*, *94*(1–2), 98–116, doi:10.1016/j.geomorph.2007.05.002.
Rojas, C., M. Beck, and R. Burmester (1994), Paleomagnetism of the mid-Tertiary Ayacara Formation, southern Chile: Counterclockwise rotation in a dextral shear zone, *J. South Am. Earth Sci.*, *7*(1), 45–56.
Romero, G. A. (1983), Geología del sector Alto Palena-Puerto Ramirez. Chiloé continental, Thesis, Univ. de Chile, Santiago de Chile, Chile.
Ron, H., R. Freund, Z. Garfunkel, and A. Nur (1984), Block rotation by strike-slip faulting: Structural and paleomagnetic evidence, *J. Geophys. Res.*, *89*(B7), 6256–6270, doi:10.1029/JB089iB07p06256.
Rosenau, M. (2004), Tectonics of the southern Andean intra-arc zone (38°–42°S), PhD thesis, 159 pp., *Freie Univ.*, Berlin.
Rosenau, M., D. Melnick, and H. Echtler (2006), Kinematic constraints on intra-arc shear and strain partitioning in the southern Andes between 38°S and 42°S latitude, *Tectonics*, *25*, TC4013, doi:10.1029/2005TC001943.
Roy, M., and L. Royden (2000), Crustal rheology and faulting at strike-slip plate boundaries: 2. Effects of lower crustal flow, *J. Geophys. Res.*, *105*(B3), 5599–5613, doi:10.1029/1999JB900340.
Salyards, S. L., K. E. Sieh, and J. L. Kirschvink (1992), Paleomagnetic measurement of nonbrittle coseismic deformation across the San Andreas fault at Pallett Creek, *J. Geophys. Res.*, *97*(B2), 12,457–12,470, doi:10.1029/92JB00194.
Sempere, T., G. Hérail, J. Oller, and M. Bonhomme (1990), Late Oligocene-early Miocene major tectonic crisis and related basins in Bolivia, *Geology*, *18*(10), 946–949, doi:10.1130/0091-7613(1990)018<0946.
Sernageomin (2003), Mapa Geológico de Chile: Versión digital, N°4, CD-ROM versión 1.0, *Ser. Nac. de Geol. y Min.*, Publicación Geológica Digital, Santiago de Chile, Chile.
Siame, L. L., O. Bellier, M. Sébrier, and M. Araujo (2005), Deformation partitioning in flat subduction setting: Case of the Andean foreland of western Argentina (28°S–33°S), *Tectonics*, *24*, TC5003, doi:10.1029/2005TC001787.
Solano, A. (1978), Geología del sector costero de Chiloé continental entre los 41°50′ y 42°10′ de latitud sur, Thesis, pp. 122, Univ. de Chile, Santiago de Chile, Chile.
Somoza, R. (1998), Updated Nazca (Farallon)-South America relative motions during the last 40 My: Implications for mountain building in the central Andean region, *J. South Am. Earth Sci.*, *11*(3), 211–215.
Sonder, L., and P. England (1986), Vertical averages of rheology of the continental lithosphere: Relation to thin sheet parameters, *Earth Planet. Sci. Lett.*, *77*, 81–90.
Sonder, L. J., P. C. England, and G. A. Houseman (1986), Continuum calculation of continental deformation in transcurrent environments, *J. Geophys. Res.*, *91*, 4797–4810, doi:10.1029/JB091iB05p04797.
Sonder, L. J., C. H. Jones, S. L. Salyards, and K. M. Murphy (1994), Vertical axis rotations in the Las Vegas Valley Shear Zone, southern Nevada: Paleomagnetic constraints on kinematics and dynamics of block rotations, *Tectonics*, *13*(4), 769–788, doi:10.1029/94TC00352.
Steffen, H. (1944), Patagonia occidental, las cordilleras patagónicas y sus regiones circundantes: Descripción del terreno basada en exploraciones propias, con un bosquejo de la historia de las expediciones practicadas en la región, in *Ediciones de la Universidad de Chile*, vol. 2, Universidad de Chile, Santiago de Chile, Chile. [Available at http://www.facso.uchile.cl/proyectos/proyectosteffen/documentos.html.]
Sylvester, A. G. (1988), Strike-slip faults, *Geol. Soc. Am. Bull.*, *100*(11), 1666–1703.
Taymaz, T., Y. Yilmaz, and Y. Dilek (2007), The geodynamics of the Aegean and Anatolia: Introduction, *Geol. Soc. London, Spec. Publ.*, *291*(1), 1–16, doi:10.1144/SP291.1.
Terres, R., and B. Luyendyk (1985), Neogene tectonic rotation of the San Gabriel region, California, suggested by paleomagnetic vectors, *J. Geophys. Res.*, *90*(B14), 12,467–12,484, doi:10.1029/JB090iB14p12467.
Thomson, S. N. (2002), Late Cenozoic geomorphic and tectonic evolution of the Patagonian Andes between latitudes 42°S and 46°S: An appraisal based on fission-track results from the transpressional intra-arc Liquiñe-Ofqui fault zone, *Geol. Soc. Am. Bull.*, *114*(9), 1159–1173, doi:10.1130/0016-7606(2002)114<1159.
Titus, S. J., S. Crump, Z. McGuire, E. Horsman, and B. Housen (2011), Using vertical axis rotations to characterize off-fault deformation across the San Andreas fault system, central California, *Geology*, *39*(8), 711–714, doi:10.1130/G31802.1.
Torsvik, T., R. Müller, R. Van der Voo, B. Steinberger, and C. Gaina (2008), Global plate motion frames: Toward a unified model, *Rev. Geophys.*, *46*, RG3004, doi:10.1029/2007RG000227.
Wang, K., Y. Hu, M. Bevis, E. Kendrick, R. Smalley, R. B. Vargas, and E. Lauría (2007), Crustal motion in the zone of the 1960 Chile earthquake: Detangling earthquake-cycle deformation and forearc-sliver translation, *Geochem. Geophys. Geosyst.*, *8*, Q10010, doi:10.1029/2007GC001721.
Wettstein, A. (1886), Über die Fischfauna des Tertiären Glarner Schiefers, *Schweiz. Palaeontol. Ges. Abh.*, *13*, 1–101.
Zijderveld, J. D. (1976), A. C. demagnetization of rocks: Analysis of results, in *Methods in Paleomagnetism, Dev. in Solid Earth Geophys.* vol. 3, edited by D. W. Collinson, K. M. Creer, and S. K. Runcorn, pp. 254–286, Elsevier, New York.

PART III. Paleomagnetic rotation pattern of the southern Chile fore-arc sliver (38-42ºS): A new tool to evaluate along-arc locking of the subducting plate

Paleomagnetic rotation pattern of the southern Chile fore-arc sliver (38-42ºS): A new tool to evaluate along-arc locking variations of the subducting plate

Catalina Hernandez-Moreno[1,2], Fabio Speranza[1], Anita di Chiara[1,3]

[1]Istituto Nazionale di Geofisica e Vulcanologia, Rome, Italy

[2]Dipartimento di Fisica, Università di Bologna, Bologna, Italy

[3]Now at Department of Geophysics, University of São Paulo, São Paulo, Brazil

Abstract

The southern Chile fore-arc between 37° and 47°S represents the inland co-seismic deformation zone of the great 1960 M_w 9.5 Valdivia earthquake. Gravity anomalies and GPS displacements have been used to infer on along-arc variations of coupling between the subducting Nazca plate and the fore-arc, but their conclusions disagree. Here we report on a paleomagnetic investigation of 43 Oligocene-Pleistocene volcanic sites from the fore-arc sliver between 38° and 42°S. Seven sites from the Chiloé Island (42°S) at ca. 130 km from the Liquiñe-Ofqui fault zone (LOFZ, a 1000 km long dextral fault bounding the sliver to the east) yield systematic counterclockwise (CCW) rotations, ranging between -27° and -164º. CCW rotation variability (even at close sites) and rapidity (>20°/Myr considering Pleistocene sites at 39°N) suggest that block rotation pattern is related to NW-SE seismically active sinistral faults crosscutting the whole fore-arc. Paleomagnetic sites were also gathered at the eastern margin of the fore-arc (adjacent to the LOFZ), at 40°-41°S (Ranco Osorno Domain) and around 39°S (Villarrica Domain). While in the Ranco-Osorno domain clockwise (CW) rotations up to 136° occur before evolving to CCW rotations at ca. 30 km from the LOFZ, in the Villarrica domain the fore-arc is characterized by ubiquitous CCW rotations. According to previously published data, CW rotations up to at least 170° also occur east of the LOFZ, and have been related to 50-100 km dextral fault shear in the last 5 Ma. We suggest that the width of the eastern fore-arc (just west of the LOFZ) undergoing CW rotations is a function of plate coupling along subduction interface. Zones of high coupling enhance stress normal to the LOFZ, induce high LOFZ strength, and yield a wide deforming zone characterized by CW rotations. Conversely, low coupling imply a weak LOFZ, a lack of CW rotations, and a fore-arc entirely dominated by CCW rotations related to NW-SE sinistral fault kinematics. Our locking inferences

are in good agreement with those recently derived by GPS analysis, and indicate that seismotectonic segment coupling has remained virtually unchanged during the last 5 Ma.

1. Introduction

Understanding crust kinematics of fore-arc slivers lying on top of obliquely subducting oceanic slabs yielding M_w ~9 mega-thrust earthquakes is becoming one of the most addressed issues of plate tectonics. Slivers of fore-arc crust are formed along active continental margins, when an extensive portion of crust is displaced along margin-parallel strike-slip faults generated or reactivated in response to either oblique subduction or ridge collision [*Nelson et al*., 1993]. Oblique convergence is usually partitioned in pure dip-slip subduction mega-earthquakes and trench-parallel strike-slip faulting, occurring as a rule along the volcanic arc [*Beck*, 1980; *Dewey and Lamb*, 1992; *Wallace et al*., 2004]. Fore-arc crustal motion has been usually addressed by the analysis of earthquake slip vectors and, since the last twenty years, by velocity fields derived from Global Positioning System (GPS) data. Yet this observation time window (few decades) can be significantly shorter than a complete seismic cycle, or constrained to interseismic periods where the post-seismic deformation release, the vicinity of other important faults, and the slip partitioning in oblique subduction may hinder the finite deformation pattern [*Minster et al*., 1974; *Minster and Jordan*, 1978; *Dewey*, 1980; *DeMets et al*., 1990; *Argus and Gordon*, 1990; *Hofmann-Wellenhof et al*., 1993; *Larson et al*., 1997; *Chamot-Rooke et al*., 1999; *Wallace et al*., 2004; *McCaffrey et al*., 2000, 2002].

On the other hand, paleomagnetic data yield finite rotations occurring since rock formation age, thus provide a much longer observation time span in the order of millions or tens of millions of years. The cumulative permanent or nonreversing deformation in function of the considered geological formation age can represent the average over many seismic cycles, thus significantly complement "instantaneous" information derived from seismic and GPS data. Rates of rotation about vertical axes from residual geodetic velocity field may also differ from those inferred from paleomagnetic rotations because the deformation is non-uniform, either in space or in time [*Feigl et al*., 1993].

One of the best modern examples of a fore-arc sliver is located in the leading margin of the South American plate above the obliquely subducting Nazca plate, where the strongest earthquake ever recorded (Valdivia 1960, M_w 9.5) occurred (Figure 1).

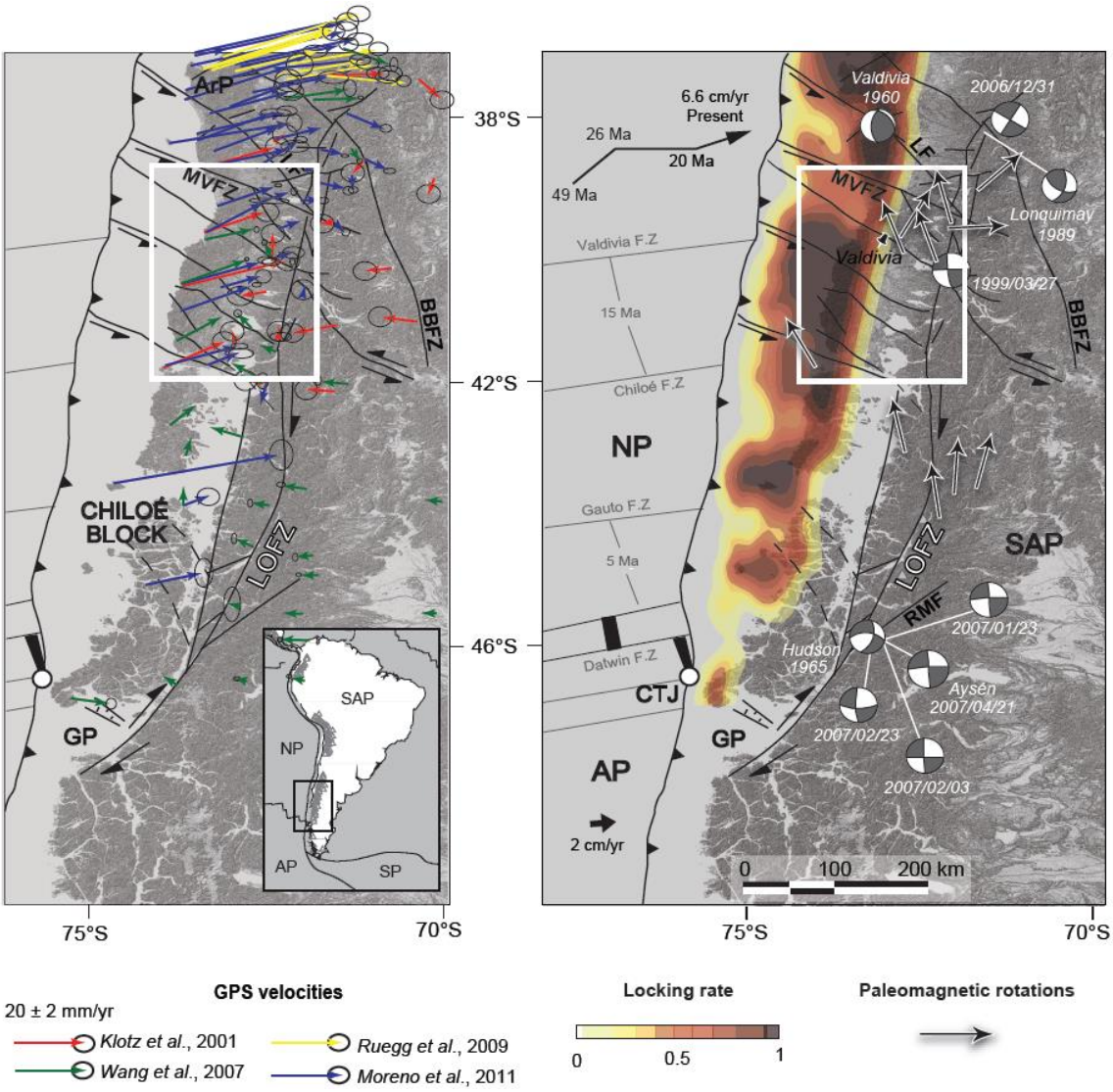

Figure 1. Plate tectonic configuration of the southern Chile and main structural features within the Chiloé Block. Main faults after *Hackney et al*. [2006], black arrows indicate motion of oceanic plates relative to South America [*Pardo-casas and Molnar*, 1987; *DeMets et al*., 1994; *Angermann et al*., 1999; *Kendrick et al*., 2003; *Quinteros and Sobolev*, 2013]. Arrows with white stroke correspond to paleomagnetic rotations from *Garcia et al*. [1988], *Cembrano et al*. [1992] and *Rojas et al*. [1994], recalculated by *Hernandez-Moreno et al*. [2014] using updated South American poles by *Torsvik et al*. [2008]. Shallow crustal focal mechanisms are also shown [*Chinn and Isacks*, 1983; *Dziewonski et al*., 1991; *Barrientos and Acevedo-Aránguiz*, 1992]. The white box marks the study area of this research. SAP South American Plate, NP Nazca Plate, AP Antarctic Plate, SP Scotia Plate, ArP Arauco Peninsula, CTJ Chile Triple Junction, GP Golfo de Penas, LOFZ Liquiñe-Ofqui fault zone, MVFZ Mocha-Villarrica Fault Zone, LF Lanalhue fault, BBFZ Bio-Bio fault zone. Tinny arrow represent the GPS velocity vector by: red *Klotz et al*. [2001]; green *Wang et al*. [2007], yellow *Ruegg et al*. [2009] and blue *Moreno et al*. [2008]. Locking rate by *Moreno et al*. [2011].

The sliver (also called Chiloé Block) is bounded to the east by the Liquiñe-Ofqui fault zone (LOFZ), a dextral strike-slip fault system more than 1000 km long coinciding with the volcanic arc of Southern Chile. The LOFZ is considered to be related to the strain partitioning of oblique convergence between Nazca and South American plates since at least 50 Ma [*Hervé*, 1976; *Cembrano and Herve*, 1993], and/or the post-10 Ma indentation of the Chile Rise beneath the continent [*Forsythe and Nelson*, 1985]. The Chiloé Block sliver occurs between Concepcion (37ºS) and the Golfo de Penas (~47ºS), an extensional Cenozoic basin located at its trailing edge [*Forsythe and Nelson*, 1985; *Hervé*, 1976; *Nelson et al*., 1994; *Lavenu and Cembrano*, 1999]. The northward movement of the fore-arc sliver seems to be hampered north of ~38ºS by the thickened central Andean crust, the flat slab older than 30 Ma, and the absence of volcanic activity that precludes strain partitioning at lithospheric-scale [*Siame et al*., 2005; *Rosenau et al*., 2006].

Minor intraplate seismicity and shallow earthquakes reveal margin-normal shortening close to the coast and recent, brittle deformation of the forearc along the LOFZ and the NW crustal-scale transverse faults splaying off west of it [*Chinn and Isacks*, 1983; *Barrientos and Acevedo*, 1992; *Haberland et al*., 2006]. In fact, GPS velocity vectors also pointing to strain partitioning within the fore-arc. GPS data yield a LOFZ dextral slip of 6.5 mm/yr decreasing northward [*Wang et al*., 2007], and margin-normal shortening toward both inland and seaward, which suggest current locking of the seismic zone and protracted effects of the post Valdivia earthquake mantle rebound, respectively [*Khazaradze et al*., 2002; *Hu et al*., 2004, *Wang et al*., 2007].

Recently a debate has developed on the zones (or segments) above the 1000 km long rupture of the Valdivia earthquake where changes occur in the coupling between the subducting Nazca plate and the overriding fore-arc sliver. Locked fore-arc segments are expected to yield maximum slip patches during megathrust earthquakes. *Hackney et al*. [2006], by analyzing gravity anomaly and the geoid suggested that segments characterized by high gravity anomalies are related to a shallower subducting plate. The thinner fore-arc wedge would be responsible of low coupling, mainly as a result of reduced normal stress acting on the subduction interface. In this way, they identify a northern segment (Arauco-Lonquimay) characterized by low coupling, followed to the south by two locked segments down to 42°S. In turn, *Tassara* [2010] also based in gravity anomalies and other geophysics information interpreted that low-gravity fore-arc regions likely indicates a conditionally-stable regime dominated by low normal stress loading the plate interface because a forearc wedge formed by low density rocks (low coupling), whereas high-gravity regions predict stick-slip behavior dominated by larges normal stresses imposed by a dense fore-arc (high coupling). He conclude that in general the southern Andes fore-arc is low coupling with an exception of high coupling along the Arauco Peninsula (36º-38ºS).

Thus while low gravity values are considered for the *Hackney et al.* [2006] as consequence of fore-arc thickness and its subsequent larger normal shear on the subducting plate that yield to high coupling, to *Tassara* [2010] low gravity values are considered as consequence of lighter fore-arc and its subsequent small vertical shear on the subducting plate that yield to low coupling.

More recently, *Moreno et al*. [2011] evaluated coupling by analyzing new GPS data, as well as those previously gathered by *Wang et al*. [2007]. *Moreno et al*. [2011] argue for a strong coupling at 36°-38°S and 40°-42°S, separated by a low coupling zone around 39°S. Thus, apart for the 40º-42°S segment where locking is indicated by *Hackney et al*. [2006] and *Moreno et al*. [2011], the conclusions of these authors on subduction segment coupling are in disagreement, while in general the conclusions by *Tassara* [2010] are relatively close to them by *Moreno et al*. [2011].

Paleomagnetic studies carried out along the LOFZ and at both sides of it show an asymmetric rotation pattern [*Garcia*, 1988; *Rojas et al*., 1994; *Cembrano et al*., 1998; *Hernandez-Moreno et al*., 2014] (Figure 1). East of the fault and adjacent to it, rotations are up to 150°-170° clockwise (CW), and fade out ~10 km east of fault. These data support a quasi-continuous crust kinematics, characterized by small rigid blocks in the 1-10 km size range likely drag by the underlying ductile crust flow [*England et al*., 1985; *Sonder et al*., 1994]. On the other hand west of the LOFZ, within the Chiloé fore-arc sliver, an unexpected counterclockwise (CCW) rotation pattern, even at ca. 200 km away from the fault, has been documented. Most of the paleomagnetic sites are located within 20 km from the LOFZ, so that it is not clear whether CCW rotations arise from LOFZ or fore-arc sliver kinematics. The few models considering CCW rotations in a dextral strike-slip fault system require a set of synthetic dextral faults inside the deforming zone [*Ron et al*., 1984; *Garfunkel and Ron*, 1985; *McKenzie and Jackson*, 1986; *Hernandez-Moreno et al*., 2014] that are definitely lacking in the fore-arc, broken up by a set of NW-trending seismogenetic sinistral faults that cut through almost the whole forearc crust [*Melnick and Echtler*, 2006; *Haberland et al*., 2006] (Figures 1 and 2).

In this paper we report on a detailed paleomagnetic investigation of the fore-arc sliver between 38° and 42°S. Our data, along with previous paleomagnetic evidence (e.g. *Hernandez-Moreno et al*. [2014]) helps understanding crust fragmentation pattern, block rotation and overall kinematics of fore-arc slivers. We also propose for the first time that paleomagnetic data from fore-arc blocks can be used to infer on along-arc locking variations of subducting plate segments.

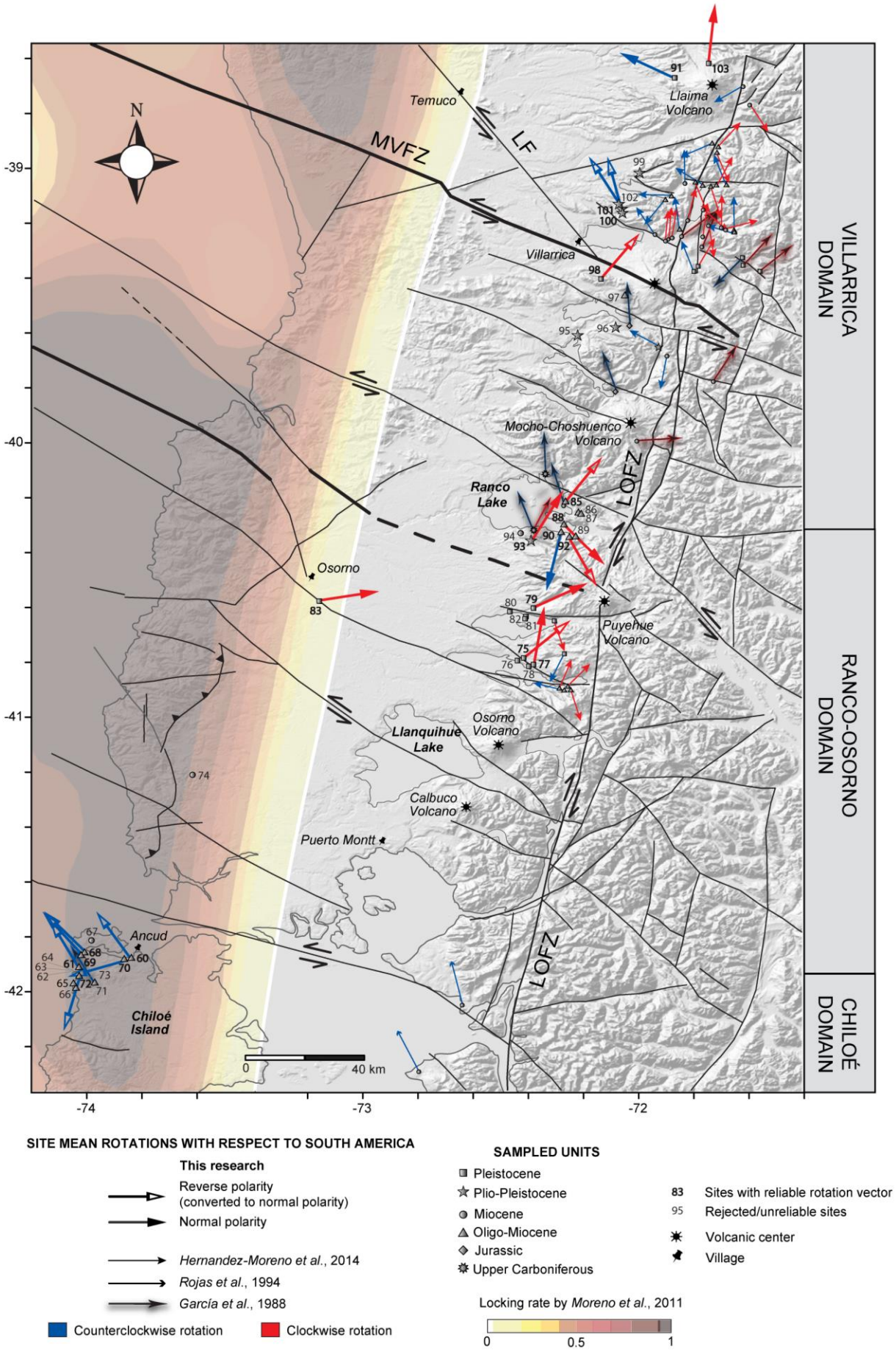
N
MVFZ
LF
Temuco
Villarrica
Llaima Volcano
Mocho-Choshuenco Volcano
Ranco Lake
LOFZ
Osorno
Puyehue Volcano
Osorno Volcano
Llanquihue Lake
Calbuco Volcano
Puerto Montt
Ancud
Chiloé Island
VILLARRICA DOMAIN
RANCO-OSORNO DOMAIN
CHILOÉ DOMAIN
-39
-40
-41
-42
-74
-73
-72
0
40 km
SITE MEAN ROTATIONS WITH RESPECT TO SOUTH AMERICA
This research
Reverse polarity (converted to normal polarity)
Normal polarity
Hernandez-Moreno et al., 2014
Rojas et al., 1994
García et al., 1988
Counterclockwise rotation
Clockwise rotation
SAMPLED UNITS
Pleistocene
Plio-Pleistocene
Miocene
Oligo-Miocene
Jurassic
Upper Carboniferous
83 Sites with reliable rotation vector
95 Rejected/unreliable sites
Volcanic center
Village
Locking rate by Moreno et al., 2011
0
0.5
1

Figure 2. Paleomagnetically detected vertical-axis rotations along the Chiloé Block fore-arc sliver between the Llaima Volcano (38º36'S) and the Chiloé Island (42ºS), southern Chile. Arrows represent vertical- axis rotations by us and recalculated from *Garcia et al*. [1988]; *Rojas et al*. [1994] and *Hernandez-Moreno et al*., 2014, as specified. Some faults are referred to *Hackney et al*. [2006] and *Rosenau et al*. [2006], others were interpreted by us from the DEM. LOFZ Liquiñe-Ofqui Fault Zone, MVFZ Mocha-Villarrica Fault Zone, LF Lanalhue fault, CR Coastal Range, CV Central Valley, MC Main Cordillera. Thick NW-trending faults indicate the fore-arc segments defined by *Hackney et al*. [2006]: MVZ- boundary between the Arauco-Lonquimay segment (36ºS to 38ºS) northward and the Valdivia-Liquiñe segment (38ºS to 39ºS) southward, unnamed NW-fault close to the Puyehue Volcano- boundary between the Valdivia-Liquiñe segment northward and the Bahia Manso-Osorno segment (39ºS to 42ºS) southward. Locking plate rate range from 0 (plate convergence accommodates by full slip) to 1 (non-slipping areas or fully locked) [modified from *Moreno et al*. 2011].

---

2. Tectonics and geodynamics of fore-arc slivers

A fore-arc sliver can be generated as a detached part of a continent by rifting [*Karig*, 1971], or most commonly by margin-parallel strike-slip generated or reactivated in response to either oblique subduction or ridge collision [*Fitch*, 1972; *Dewey*, 1980; *Jarrard*, 1986; *McCaffrey*, 1992; *Nelson et al*., 1994].

Oblique subduction has been suggested as a principal cause of fore-arc sliver formation [e.g. *Beck et al*., 1981; *Beck*, 1986]. Here plate convergence vector is decomposed in trench orthogonal compression usually confined to the subduction interface and the fore-arc, and trench parallel strike-slip motion accommodated by distributed wrench and shortening and/or discrete margin-parallel transcurrent faults. Strike-slip faults usually develop near magmatic arc axis, as this is the weakest part of the overriding plate because of heating-related lithospheric thinning [*Fitch*, 1972; *Beck*, 1983, 1986; *McCaffrey*, 1992; *Tikoff et al*., 1995; *Saint Blanquat et al*., 1998].

The orthogonal subduction compression/strike-slip fault pair represents a low-energy alternative to oblique subduction, because a vertical surface can concentrate shear more effectively than an inclined subduction interface, minimizing the shearing area [*Beck* 1983; *Jarrard*, 1986]. Margin-parallel strike-slip faults occur in about 50% of all modern subduction zones, even in cases where obliquity is less than 45° [*Jarrard*, 1986, *Woodcock*, 1986].

Strike-slip faults detach fore-arc slivers from the leading edge of the overriding plate, bounded to the other side by the subduction thrust fault. *Fitch* [1972] first described a modern example of sliver

lateral transport driven by oblique subduction ("Sunda type"). In an ideal situation, the fore-arc will move consistently with the direction of the oblique convergence, yielding to extension and compression at its trailing and leading edge, respectively [*Fitch*, 1972; *Beck*, 1983; *Jarrard*, 1986]. The most outstanding examples of strike-slip faults related to strain partitioning are the Atacama (Chile), Longitudinal (Taiwan), Philippine [*Allen*, 1965], and Semangko faults (Sumatra) [e.g., *Katili*, 1970; *Fitch*, 1972], median tectonic line (SW Japan) [*Karneko*, 1966; *Okada*, 1971], Nicaragua trough (Central America) [*Maldonado-Koerdell*, 1966], and western North American Cordillera [*Beck*, 1976, 1980; *Irving*, 1979; *Coney et al*., 1980].

In addition to oblique subduction, margin-parallel faults detaching fore-arc slivers can be generated or reactivated by collision of a seamount on the subducting plate, which acts as an indenter [*Ben-Avraham et al*., 1981; *Tapponnier et al*., 1982; *Tapponnier and Molnar*, 1976]. The collision of a buoyant and thermally-active oceanic ridge can also yield significant thermal and tectonic effects along the trench [*Nelson and Forsythe*, 1989; *Nelson et al*., 1994]. Tectonic consequences include a dip decrease of the subducting slab and convergence rates changes [*Dewey*, 1980], while thermal effects imply heat flow rise [*DeLong et al*., 1979; *Cande et al*., 1987] due to asthenosphere window opening after ridge collision [*Dickinson and Snyder*, 1979].

Fore-arc sliver drift parallel to plate margin is favored by the occurrence of continental overriding plates, high-obliquity convergence, low subduction angle, strong interplate coupling, and thermal "softening" of the magmatic arc **[***Fitch*, 1972; *Beck*, 1983; *Vink et al*., 1984; *Jarrard*, 1986**]**. Statistical analysis of slivers' motion shows that fore-arc drift velocities are significantly lower than predicted considering oblique subduction partitioning [*Jarrard*, 1986; *Beck*, 1986; *Beck*, 1991]. This has been related to the "buttress effect" or motion impediment at the fore-arc leading edge, as well as to changes in plate margin geometry, overriding plate physical properties, and subduction parameters [*Beck*, 1986; *Beck et al*., 1993; *Wang*, 1996]. A sliver will move only insofar as the buttress can be overcome by crustal thickening (Peru-northern Chile trench) or/and sliver widening (southern-central Chile).

Owing to the shear arising from strain partitioning, the fore-arc sliver translation can be accompanied by block rotation [*Beck*, 1980, 1987; 1989]. *Beck* [1980] first noticed that the fore-arc may be mechanically unstable and responds to surface stresses by breaking into roughly equant blocks that would rotate (CCW in a sliver bounded by a dextral fault) in response to shear caused by ductile flow in the lower crust.

3. Plate tectonic framework of the southern-central Chile margin (37°-47°S)

One of the best modern examples of detached fore-arc slivers driven by oblique subduction occurs in southern Chile (Figure 1). The fore-arc block lies above the rupture zone of the 1960 Valdivia earthquake, the largest earthquake ever recorded characterized by a M_w 9.5 and a rupture more than 1000 km long [*Plafker and Savage*, 1970].

Along the Chile Trench since at least 50 Ma ago the convergence vector between the Farrallon and South American plates has been dextral oblique, with an exceptional nearly trench-orthogonal, convergence period following the breakup of the Farallon into the Nazca and Cocos plates between 26 and ~20 Ma [*Pardo-Casas and Molnar*, 1987; *Somoza*, 1998; *Quinteros and Sobolev*, 2013]. Afterwards the convergence vector between Nazca and South America plates has maintained a largely constant N77°E trend, with a present-day rate between 6.3 and 7.9 cm/yr [*Pardo-Casas and Molnar*, 1987; *Angermann et al*., 1999; *Kendrick et al*., 2003]. This relatively steady northeast convergence has favored the strain partitioning with almost pure E-W shortening in the fore-arc and right-lateral component of horizontal displacement. The latter been accommodated by the 1000 km long dextral Liquiñe-Ofqui fault system (LOFZ). It is composed by two NNE-trending right stepping straight lineaments running near the thermally-weakened axis of the southern Chile magmatic arc, and by NW-trending curved sinistral faults that splay off west of the straight lineaments [*Hervé*, 1976, 1994; *Hervé and Thiele*, 1987; *Cembrano and Hervé*, 1993; *Lavenu and Cembrano*, 1999; Cembrano *et al*., 1996, 2000]. The fore-arc is bounded to the west by the Chile trench and to the east by the LOFZ from Concepción (37°S) to the Golfo de Penas-Taitao pull-apart basin (~47ºS) [*Hervé*, 1976; *Forsythe and Nelson*, 1985; *Nelson et al*., 1994; *Cembrano et al*., 1996, 2000; *Lavenu and Cembrano*, 1999; *Beck et al*., 2000; *Hoffmann-Rothe et al*., 2006; *Rosenau et al*., 2006] (Figure 1).

Further south, four Chile Rise segments (dated at 10-15, 5-6, 3.0, and 0.5 Ma) have collided and subducted from middle Miocene onward under South America. Consequently, the Chile triple junction between Antarctic, Nazca and South American plates has been migrating northward alternating trench-transform-trench and trench-ridge-trench configuration (currently at ~46ºS) [*Herron et al*., 1981; *Cande and Leslie*, 1986; *Nelson and Forsythe*, 1989; *Murdie et al*., 1993].

Rise collision has acted as an indenter, being another possible driving force for the strain partitioning and fore-arc northward drift [*Forsythe and Nelson*, 1985; *Muerdie et al.*, 1993; *Nelson et al*., 1994; *Lavenu and Cembrano*, 1999; *Cembrano et al*., 2000; *Cembrano et al*., 2002].

4. Tectonics of the southern Chile fore-arc sliver

The fore-arc sliver correspond to the southern Chilean margin segment, which has three main morphologic units: the uplift Coastal range which includes a Permo-Triassic accretionary complex and a Permo-Carboniferous magmatic arc, the Central Valley to the east, and father east approaching to the LOFZ, the Main Cordillera which includes the southern active volcanic arc and the middle Jurassic to Neogene North Patagonian Batholith [*Hervé*, 1994; *Nelson et al*., 1994]. In contrast to the central Chilean margin, the fore-arc is characterized by the low-relief and narrow southern Patagonian Andes (1 km mean elevation, 300 km wide), a reduced crustal thickness (< 40 km), the small distance between the trench and the volcanic front, and a subducting slab dipping ~20º whose age and depth decrease southward (~25 Ma at 38°S to ~0 Ma at 46°S at the Chile triple junction) [*Herron et al*., 1981, *Jarrard*, 1986; *Tassara et al*., 2006, *Tassara and Echaurren*, 2012].

The uplift and exhumation along the fore-arc increase towards the south, probably as a consequence of the decreasing age of subducting oceanic lithosphere and lower slab dip as the triple junction is approached [*DeLong and Fox*, 1977; *Forsythe and Nelson*, 1985; *Cande and Leslie*, 1986; *Barrientos and Ward*, 1990; *Thomson*, 2002; *Rosenau*, 2004].

Left-lateral NW-trending faults, extending even until the offshore, accommodate sliver motion and control along-strike fore-arc segmentation separating blocks with different Pre-Andean orogeny stories [*Echtler et al*., 2003; *Kus et al*., 2006; *Hackney et al*., 2006; *Moreno et al*., 2008; *Melnick et al*., 2009] (Figures 1 and 2). Strike-slip earthquakes delineated along these faults reach 30 km depth, indicating that those are deep structures cutting almost the whole fore-arc crust [*Bohm et al*., 2002; *Haberland et al*., 2006]. They have been interpreted either as long-lived basement faults not genetically related to the LOFZ, reactivated as sinistral-reverse strike-slip faults during the arc development [*Glodny et al*., 2008; *Lange et al*., 2008; *Melnick et al*., 2009], or as Riedel (*R*) shears consistent with the LOFZ right-lateral slip component [*Nelson et al*., 1994; *Lopez-Escobar et al*., 1995; *Cembrano et al*., 1996; *Rosenau et al*., 2006]. The Bio-Bio Fault is the most prominent NW structure, because it separates Plio-Quaternary back-arc shortening in the central Chile from the dominant LOFZ strike-slip motion at the southern Chile [*Bohm et al*., 2002; *Folguera et al*., 2002; *Folguera et al*., 2003; *Melnick et al*., 2006a]. The Mocha-Villarrica [*Melnick et al*., 2003] and Lanalhue faults [*Glodny et al*., 2008] are also significant NW-trending structures.

Focal plane solutions of shallow earthquakes along the fore-arc suggest that it is currently undergoing strain partitioning though a trench-orthogonal shortening and a small trench-parallel dextral component absorbed along the volcanic arc [*Chinn and Isacks*, 1983; *Cifuentes*, 1989; *Barrientos and Acevedo*, 1992; *Dewey and Lamb*, 1992; *Murdie*, 1994; *Bohm et al*., 2002; *Lange et*

al., 2008]. Recent GPS analyses into the 1960 Valdivia earthquake (M_w 9.5) rupture zone also document this fore-arc deformation (Figure 1A).

Margin-parallel GPS velocities, especially between 42ºS and 44ºS, show a current northward fore-arc sliver motion of 6.5 mm/yr [*Wang et al*., 2007] which represents only the ~44% of the margin-parallel plate convergence component [*Hernandez-Moreno et al*., 2014]. At ~38ºS the margin-parallel velocities tapers to ca. 25% of the total margin-parallel component, as reveals the 6.9 mm/yr dextral strike-slip of a N30ºE fault, parallel to the continental margin [*Moreno et al*., 2008].

GPS velocities also indicate opposite motion between inland and coastal sites. While inland sites move seaward (7 to <3 mm/yr [*Wang et al*., 2007]) supporting the model of prolonged post Valdivia earthquake deformation from viscous stress relaxation in the mantle [*Khazaradze et al*., 2002; *Hu et al*., 2004; *Wang et al*., 2007]; coastal sites move landward following the plate convergence direction as result of current locking between the Nazca and South American plates [*Klotz at al*., 2001; *Ruegg et al*., 2009; *Moreno et al*., 2011]. Thus, whereas at the fore-arc end (36º to 37.5ºS) coastal GPS velocities decrease toward the arc from 40 mm/yr to 15 mm/yr at 300 km inland, within the fore-arc these velocities have lower magnitudes and decrease rapidly from 32 mm/yr to 18 mm/yr at only 10 km from the coast [*Moreno et al*., 2008], while also decrease southward. This distribution of the interseismic surface velocity has been interpreted in terms of southward narrowing (from 120 to 80 km in plan view [*Wang et al*. 2007]) and shallowing (from 49 km downdip depth at 36ºS to 40 km at 42ºS [*Moreno et al*. 2008, 2009]) of the interplate locked zone, possibly due to the younger subducting plate and warmer thermal regime southward [*Moreno et al*., 2011].

Residual velocities obtained by *Moreno et al*. [2008] subtracting interseismic velocities from GPS observations; put in evidence the upper plate faults effects on the fore-arc surface velocity. Between 37.5º and 39ºS, high magnitude residual velocities reveal CCW vertical-axis rotation in a limited region between the coast and the sinistral NW-trending Lanalhue fault. This rotation is possibly caused by the collision of the Chiloé fore-arc against the Arauco-Nahuelbuta block, partly accommodated along the Lanalhue fault. This also suggests that the fault has been active during the interseismic period coinciding with seismic information [*Lange et al*., 2008].

Different temporal scale estimations of the locking degree along the fore-arc are contradictory. Long-term interplate locking variations proposed by *Hackney et al*., [2006] and *Tassara* [2010], both based on gravity anomaly values, seismic distribution and 3D density models, are not agree. While to the formers high/low gravity anomalies are related with a thinner/thicker fore-arc,

shallow/depth slab geometry and therefore to low/high coupling, for the second high/lows gravity anomalies can be related to a dense/light fore-arc crust and therefore high/low coupling.

Thereby, *Hackney et al*. [2006] using the three-dimensional density model by *Tašárová* [2004] have interpreted gradually southward: slab depth increases (5 km between 36ºS and 40ºS), subsequent fore-arc crust thickness, and interplate locking degree (following *Song and Simons* [2003] statements to infer shear stress on the plate interface). The authors identified three different fore-arc segments of locking plate (Figure 2): The northern *Arauco-Lonquimay segment* (36ºS to 38ºS), at the fore-arc north end, characterized by positive gravity anomaly and widespread seismicity interpreted in terms of shallow slab and thinner fore-arc which yield to low subduction coupling; and the *Valdivia-Liquiñe* (38ºS to 39ºS) and *Bahia Mansa-Osorno* (39ºS to 42ºS) segments, where negative gravity anomalies and limited fore-arc seismicity were related to a thicker fore-arc and a 5 km deeper slab yielding high interface coupling. *Hoffman-Rothe et al*. [2006] also agree with these arguments, but put in evidence the lack of precise information about the slab geometry at that time.

In turn, *Tassara* [2010] based on an update three-dimensional density model [*Tassara et al*., 2006] and the spatial distribution of VSA (vertical stress anomaly: lithostatic overpressure loading the seismogenic intraplate fault) suggest that the long-term coupling degree is rules by fore-arc density. Positive/negative VSA values were correlated to high/lows of the gravity field caused by dense/light fore-arc crust. Thus, between 34º and 45ºS the author defines a general low coupling supported by the scarce seismicity recorded along the fore-arc, the presumably wet subduction channel (low friction μ and high pore pressure p) full with water-rich sediments, and the neutral to negative VSA values that suggest a light fore-arc column exerting a small vertical load on the subduction interplate. Relatively high VSA were only found at the Arauco Peninsula (36º-38ºS) leading to the author to propound high coupling sufficient to allow elastic stress accumulation and the consequent episodic release associated to the initiation of large earthquakes, as the 1960 Valdivia earthquake.

Recently *Moreno et al*. [2011], based on new and previous GPS vectors, indicate current high locking plate at 36°-38° (interseismic strain accumulation as indicated by high GPS costal velocities) and 40°-42°S separated by a zone of low coupling at ca. 39°S (Figure 1B and 2).

The region between 36º-38ºS corresponds with the southern termination of the 2010 Maule earthquake, unveiling that even before the earthquake was highly coupled. The coastal zone ca. 39ºS is characterized by high slip during the 1960 Valdivia earthquake but current low margin-normal GPS velocities (a not persistent asperite), features that lead the authors to proposed current creeping without not much slip accumulation since 1960, and therefore a wide, less locked area

[*Moreno et al*., 2008; 2011]. South of it, between 39°S and 42°S, where the highest coseismic slip occurred (>40 m) and where the maximum postseismic viscoelastic motion is found, they defined a fully coupled interplate accumulating at present significant amounts of interseismic strain. It means that this segment behaves as a persistent asperity over the least two seismic cycles. South of 43°S, the interface appears to be less locked, with two locking patches representing emerged sectors of the continental shelf. Thus, after correcting the signals for mantle relaxation (post-seismic motion), the residual GPS velocity pattern suggests that the plate interface accumulates slip deficit in a spatially and presumably temporally variable way towards the next great event. Their interpretation is in agreement with the intersection of the slab with the continental Moho, determined independently by tomography [*Bohm et al*., 2002; *Haberland et al*., 2006], seismic reflection and refraction profiles [*Lüth et al*., 2003; *Krawczyk et al*., 2006*; Groß et al*., 2007], and modeling of gravity data [*Tassara et al*., 2006; *Tassara*, 2010; *Tassara and Echaurren*, 2012].

5. Previous paleomagnetic evidence from the LOFZ and the south Chile fore-arc sliver

Although strike-slip partitioning since Eocene has favored the northward displacement of the Chiloé Block, there is no clear paleomagnetic evidence for late Mesozoic-Cenozoic latitudinal drift [*Beck*, 1988, 1991; *Cembrano et al*., 1992; *Beck et al*., 1994; *Beck et al*., 2000]. However, it must be considered that the minimum measurable paleomagnetic inclination shallowing (considering error bars) is on the order of 10°-20°, implying that any drift lower than some 2000 km is not paleomagnetically detectable at these latitudes.

Consequently, paleomagnetic analyses have been focused on the rotation pattern around the LOFZ [*Garcia et al*., 1988; *Cembrano et al*., 1992; *Beck et al*., 1993; *Rojas et al*., 1994; *Beck et al*., 1998, 2000; *Hernandez-Moreno et al*., 2014], while rotations within the fore-arc sliver have not been studied in great detail.

Paleomagnetism shows very recent rotations (mostly occurring within the last 5 Ma) and an asymmetric rotational pattern at LOFZ edges (Figures 1 and 2). CW rotations occur in a 10 km wide deforming zone east of the LOFZ, with CW rotation values progressively increasing towards the fault up to 150-170°, consistently with dextral fault kinematics [*Hernandez-Moreno et al*., 2014]. The deforming zone is broken into small blocks of 1-10 km of size range, which seem to follow a quasi-continuous crust behavior [*McKenzie and Jackson*, 1983; *Nelson and Jones*, 1987; *Sonder et al*., 1994]. Moreover, unrotated elongate blocks parallel to the LOFZ and at both sides of it, seem to be simply translated without rotating, following fault kinematics. The rotation pattern west of the LOFZ, within the Chiloé Block, is less clear and according to *Hernandez-Moreno et al*. [2014] does not support an univocal interpretation. Here CW rotations also occur, but CCW rotations dominate

and exceed values of 150° at ca. 10 km west of the LOFZ (Figures 1 and 2). All data from the fore-arc were gathered at a maximum distance of 50 km from the LOFZ, with the exception of a three sites collected in the Oligo-Miocene Cocotue Beach basalts close to Ancud (northern Chiloé Island) at ~120 km from the LOFZ that yields -27º CCW rotation [*García et al*., 1988].

Few authors have tried to explain the significance of both the northward translation and the "wrong-way" CCW rotations of the fore-arc sliver. According to *Beck* [1991], *Beck et al*. [1993], and *Rojas et al*. [1994], the Chiloé Block cannot translate freely northward because of a buttress occurring at its leading edge. Therefore ongoing dextral slip along the LOFZ would generate a space problem inducing the formation of lens-shaped blocks bounded by both NE and NW trending dextral faults. The lens-shaped blocks would escape laterally towards the trench rotating CCW, yielding domains of extension and compression. Thereby this model requires very little northward transport. The problem with this model is that dextral faults are not apparent in the fore-arc sliver, which is cut in fact by a set of NW trending seismically active sinistral faults (Figures 1 and 2).

6. Paleomagnetic Sampling and Methods

We collected 479 paleomagnetic samples (43 sites) in the fore-arc sliver, between ~38°S (Llaima Vulcano) and 42°S (Ancud, northern Chiloé Island) (Figure 2). Samples were gathered from Oligocene to Pleistocene lavas and ignimbrites (except one site from Lower-Mid Miocene sedimentary rocks) in three different zones, henceforth named as Chiloé (15 sites), Ranco-Osorno (18 sites), and Villarrica (10 sites) domains (Figure 2 and Table 1).

In the Chiloé domain we sampled one site (LOFZ74) in the Lower-Mid Miocene Lacui Formation (**M1m**), described as a sedimentary marine sequence of coarse light grey sandstone [*Antinao et al*., 2000]. The remained 14 sites belong to the Ancud Volcanic Complex (**Om3b**), the main unit exposed at the Chiloé Island, formed by Upper Oligocene to Lower Miocene basaltic-andesitic lava flows interlayered with Lower Miocene marine fossils-bearing sediments [*Duhart et al*., 2000]. The Ancud Complex age was constrained between 20.4 and 27.7 Ma relying on K-Ar dating [*Vergara and Munizaga*, 1974; *Stern and Vergara*, 1992].

In the Ranco-Osorno domain we sampled six different volcanic sequences: (**i**) the Lower-Mid Miocene Estratos del Lago Ranco (**Omlr**, seven sites), which correspond to a sequence of subhorizontal marine sediments, conglomerates, breccia and andesitic lava, dated between 20.7±2.4 [*Campos et al*., 1998] and 13.1±2.0 Ma [*Garcia et al*., 1988] both by K-Ar method (whole rock and plagioclase crystals, respectively); (**ii**) the Upper Miocene-Pliocene Estratos de Pitreño (**MPlipb**, one site), a subhorizontal volcanic and sedimentary sequence unconformably on the top of the Estratos del Lago Ranco sequence. It is constituted by basaltic to andesitic lava, pyroclastic flows

and lahar deposits on the upper layers and by conglomerates and lutites in the lower levels [*Campos et al*., 1998]. K-Ar whole rock age determinations give 5.2±0.5 Ma to 2.4±0.6 Ma from basaltic and andesitic rocks [*Campos et al*., 1998]; (**iii**) the Lower Pleistocene Cordillera Nevada-Cordon Caulle volcanic sequence (**Pliv**, one site), related to an old stratovolcano and primitive fissural volcanism before the formation of the caldera of the Cordillera Nevada Volcano. The sequence includes columnar basalt to dacitic lava, pyroclastic flows, volcanic breccias, tuffs, and subvolcanic structures (dikes, veins and necks). K-Ar whole rocks determinations from lava indicate ages between 1.4± 0.6 and <1 Ma [*Campos et al*., 1998]; (**iv**) the Cordon Caulle 2 (**Plcc2**, four sites). It belongs to the Cordón Caulle Volcano deposits and consists of a subhorizontal sequence of andesitic to dacitic lava, breccias and tuffy sands intruded by hypabyssal bodies. $^{40}Ar/^{39}Ar$ analysis in whole rock and matrix yield ages between 0.31 to 0.08 Ma, respectively [*Lara and Moreno*, 2006; *Lara et al*., 2006; *Singer et al*., 2008]; (**v**) The Sarnoso Volcanic Complex (**Pl3**, four sites), emplaced SE of the Casablanca Volcano, is a basaltic to andesitic eroded dome on which have been emplaced pyroclastic cones aligned N-S [*Lara et al*., 2001]. Radiometric K-Ar ages in whole rock indicate 0.9±0.1 Ma [*Lara et al*., 2001]; (**vi**) The Secuencia piroclástica-epiclástica San Pablo (**Plsp**, one site). It includes a series of acid to intermediate pyroclastic flows with ash and lapilli, lacustrine deposits and epiclastic flows, originated during the quaternary interaction of glacial and volcanic events. Its age has been constrained stratigraphically as Upper Pleistocene (0.132-0.073 Ma) [*Perez et al*., 2003], because it is under the Llanquihue glaciations deposit (ca. 73.000 to 14.000 BP) and above of the Santa Maria Glaciation (262.000 to 132.000 BP) [*Porter*, 1981].

In the Villarica domain we sampled five units: (**i**) Estratos de Pino Huacho Formation (**Omeph**, one site), a folded sequence of stratified andesitic lavas and epiclastic sediments [*Moreno and Clavero*, 2006]. There are not radiometric ages reported for this formation, therefore we estimated an age interval close to the Oligocene-Miocene limit (29 to 18.8 Ma); (**ii**) Plio-Pleistocene Malleco Formation (**PPlm**, four sites), which is an extended sub-horizontal volcanic sequence of proximal and distal volcanic facies of interbedded laharic and epiclastic deposits of basaltic and andesitic composition, dated by K-Ar as 4.4±0.5 to 0.8±0.3 Ma [*Suárez and Emparan* 1997; *Lara et al*., 2001]; (**iii**) Sierra de Quinchilca Volcano (**Plsq**, two sites), which corresponds to an annular volcanic structure with an eroded core flanked by basaltic to andesitic volcaniclastic rocks and lava levels. K-Ar whole rock ages on olivinic basalts from the upper part of the structure indicated 1.4±0.6 and 0.8±0.6 Ma, while lava flows in the distal zone always indicate ages of less than 1 Ma [*Lara et al*., 2001]; (**iv**) Curacautin Ignimbrite (**Llic**, two sites). It is part of the Llaima 2 pyroclastic sequences of the Llaima Volcano, active since the Upper Pleistocene to the Holocene (maximum age ~250 ka) [*Suarez and Emparan*, 1997].

Table 1. Paleomagnetic site-mean directions from Liquiñe – Ofqui Fault[a]

							ChRM / Low-Coercivity Component										
		Geographic Coordinates					Tilt Corrected		In situ								
Site	Unit	Latitude S	Longitude W	Age	Age (Ma)	Bedding (deg)	*D* (deg)	*I* (deg)	*D* (deg)	*I* (deg)	*k*	α_{95} (deg)	n/N	*R* (deg)	*ΔR* (deg)	*F* (deg)	*ΔF* (deg)
Chiloé domain																	
LOF60	OM3b	41° 52' 57.6"	73° 50' 37.9"	Upper Oligocene Lower Miocene	25.6±0.7	355/16	141.8	56.8	150.9	42.7	79.5	5.8	9/9	-35.3	9.0	-9.2	4.8
LOF61	OM3b	41° 52' 57.6"	74° 01' 38.9"		20.4-27.7	-	-	-	149.4	28.9	31.4	10.0	8/9	-27.6	9.5	-37.2	8.0
LOF62[d]	OM3b	41° 55' 39.6"	74° 01' 41.6"		20.4-27.7	-	-	-	186.5	72.7	57.9	6.8	9/9	9.5	18.6	6.6	5.5
LOF63[d]	OM3b	41° 55' 44.9"	74° 01' 58.7"		20.4-27.7	-	-	-	64.9	-81.8	9.3	19.1	8/9	68.0	133.9	-15.7	15.3
LOF64[d]	OM3b	41° 55' 40.1"	74° 02' 13.8"		20.4-27.7	-	-	-	33.2	80.0	25.6	11.2	8/8	-144	64.5	13.9	9.1
LOF65[d]	OM3b	41° 58' 21.3"	74° 02' 52.9"		20.4-27.7	Subhzt	-	-	257.5	56.8	5.9	41.4	4/4	80.5	75.6	-9.3	33.1
LOF66	OM3b	41° 59' 15.4"	74° 02' 30.1"		20.4-27.7	-	-	-	-	-	-	-	-	-	-	-	-
LOF67	OM3b	41° 49' 12.3"	73° 58' 58.9"		24.2-16.1	285/1	-	-	-	-	-	-	-	-	-	-	-
LOF68	OM3b	41° 52' 0.2"	74° 00' 56.1"		20.4-27.7	-	-	-	130.4	41.1	12.1	20.1	6/8	-46.7	21.4	-25.0	15.8
LOF69	OM3b	41° 52' 2.4"	74° 01' 12.2"		20.4-27.7	-	-	-	131.4	42.5	11.1	15.2	10/10	-45.7	16.6	-23.5	12.0
LOF70	OM3b	41° 53' 17.3"	73° 52' 7.9"		20.4-27.7	-	-	-	72.2	23.7	14.1	21.1	5/5	-105	18.3	-42.3	16.5
LOF71[d]	OM3b	41° 58' 24.8"	73° 58' 56.9"		20.4-27.7	-	-	-	213.0	6.1	7.2	22.2	8/10	36	17.7	-60.0	17.4
LOF72	OM3b	41° 56' 39.3"	74° 01' 49"		20.4-27.7	Subhzt			12.5	67.2	9.0	21.2	7/8	-164.6	53.9	1.1	16.6
LOF73[d]	OM3b	41° 56' 58.6"	74° 01' 40.1"		20.4-27.7	-	-	-	239.5	72.9	22.8	10.3	10/10	62.5	29.4	6.8	8.2
LOF74	M1m	41° 12' 36.6"	73° 37' 6.5"	Lower-Mid Miocene	24.2-16.1	-	-	-	-	-	-	-	-	-	-	-	-
LOF75	Pl3	40° 46' 58.1"	72° 24' 48.6"	Pleistocene	0.9±0.1	-	-	-	231.4	50.2	34.9	8.8	9/10	51.4	13.7	-9.8	8.8
LOF76[d]	Pl3	40° 47' 25"	72° 25' 56.6"		0.9±0.1	-	-	-	63.3	-9.9	14.9	11.6	12/18	63.3	12.0	-50.1	11.6
LOF77	Pl3	40° 48' 38.7"	72° 23' 8.7"		0.9±0.1	-	-	-	12.6	-55.3	16.3	12.3	9/10	12.6	21.6	-4.7	12.3
LOF78[d]	Pl3	40° 48' 41.7"	72° 23' 21.4"		0.9±0.1	-	-	-	49.4	-89.8	9.4	15.0	12/12	49.4	4297.2	29.8	15.0
LOF79	Plcc2	40° 36' 27 "	72° 23' 8"		0.31-0.08	Subhzt	-	-	63.6	-35.0	12.9	12.6	12/12	63.6	15.4	-25	12.6
LOF80[d]	Plcc2	40° 36' 12.4"	72° 27' 56.6"		0.31-0.08	Subhzt	-	-	359.5	-78.5	11.7	14.8	10/11	-0.5	74.2	18.5	14.8

Ranco – Osorno domain	LOF81	Plcc2	40° 37' 18.6"	72° 24' 46.6"		0.31-0.08	Subhzt	-	-	-	-	-	-	-	-	-	-	-
	LOF82[d]	Plcc2	40° 37' 13.5"	72° 24' 47.1"		0.31-0.08	Subhzt	-	-	356.3	5.8	48.2	8.1	8/10	176.3	8.1	-54.2	8.1
	LOF83	Plsp	40° 34' 41.9"	73° 09' 33.3"	Upper Pleistocene	0.132-0.073	355/15	81.8	-43.8	68.2	-41.1	7.3	14.6	16/16	81.8	20.2	-16.2	14.6
	LOF85	Omlr	40° 12' 49.7"	72° 15' 54.9"		>20.7-13.1	Subhzt	-	-	216.8	31.0	20.1	11.8	9/10	37.4	11.3	-32.7	9.4
	LOF86	Omlr	40° 15' 10.6"	72° 13' 0.4"	Lower-Mid Miocene	>20.7-13.1	Subhzt	-	-	-	-	-	-	-	-	-	-	-
	LOF87[d]	Omlr	40° 15' 15.5"	72° 12' 40.6"		>20.7-13.1	Subhzt	-	-	236.6	-39.0	4.2	30.6	8/9	-123	32.5	-24.0	24.0
	LOF88	Omlr	40° 17' 55.9"	72° 16' 33.9"		>20.7-13.1	Subhzt	-	-	135.2	-38.2	13.6	17.0	7/7	136	17.4	-25.5	13.4
	LOF89	Omlr	40° 20' 12.8"	72° 14' 46.7"		>20.7-13.1	Subhzt	-	-	-	-	-	-	-	-	-	-	-
	LOF90	Omlr	40° 19' 58.8"	72° 16' 57.3"		>20.7-13.1	Subhzt	-	-	194.1	-58.3	8.5	22.0	7/7	-165.3	35.6	-5.5	17.2
	LOF92	Omlr	40° 20' 9.6"	72° 15' 21.5"	Upper Oligocene - Lower Miocene	>20.7-13.1	Subhzt			332.6	68.6	8.8	27.4	5/6	153.1	75.1	8.6	27.4
	LOF93	Pliv	40° 21' 6.8"	72° 23' 5.2"	Lower Pleistocene	1.4 - <1	Subhzt	-	-	31.3	-53.4	20.3	10.4	11/11	31.3	17.4	-6.6	10.4
	LOF94	MPlipb	40° 19' 51.9"	72° 26' 2.6"	Upper Miocene - Pliocene	5.2-2.4	Sbhztal	-	-	-	-	-	-	-	-	-	-	-
Villarrica domain	LOF91	Llic	38° 40' 24.7"	71° 51' 50.6"	Pleistocene	0.013-0.012	-	-	-	294.9	-31.0	33.7	7.6	12/12	-65.1	8.9	-29.0	7.6
	LOF95	Plsq	39° 35' 51.4"	72° 12' 57.1"	Pleistocene	1.4-0.8	-	-	-	-	-	-	-	-	-	-	-	-
	LOF96[d]	Plsq	39° 34' 4.7"	72° 04' 41.2"		1.4-0.8	-	-	-	184.3	8.6	46.7	7.6	9/10	4.3	7.7	-51.4	7.6
	LOF97[d]	Omeph	39° 27' 7.5"	72° 02' 50.7"	Oligocene Miocene	29-18.8	-	-	-	115.5	-76.1	29.8	8.5	11/11	118	29.8	11.9	6.8
	LOF98	Ppleh	39° 23' 45.2"	72° 07' 54.8"	Pliocene Pleistocene	4.4-0.8	241/9	223.0	39.8	220.1	48.2	16.0	9.9	15/15	43.0	12.9	-19.2	9.9
	LOF99	PPlm	39° 01' 20.6"	72° 00' 4.3"		4.4-0.8	40/40	-	-	-	-	-	-	-	-	-	-	-
	LOF100	PPlm	39° 09' 29.6"	72° 03' 29.3"	Pliocene Pleistocene	4.4-0.8	suhztal	-	-	165.0	10.4	17.7	11.8	10/11	-15	12.0	-47.6	11.8
	LOF101	PPlm	39° 08' 27.8"	72° 03' 42.5"		4.4-0.8	158/47	124.9	45.4	50.5	66.3	50.4	6.2	12/12	-55.1	9.0	-12.6	6.2
	LOF102[d]	PPlm	39° 07' 34.6"	72° 04' 20.1"		4.4-0.8	66/23	141.0	-10.9	138.0	-4.3	49.2	8.7	7/10	141.0	8.9	-47.1	8.7
	LOF103	Llic	38° 36' 51.8"	71° 44' 48"	Pleistocene	0.013 -0.012	-	-	-	9.2	-58.4	14.8	12.3	11/11	9.2	23.5	0.4	12.3

[a] Geological units: OM3b-Volcanic Complex of Ancud, Omlr-Estratos del Lago Ranco, Omeph-Estratos de Pino Huacho, M1m-Lacui Formation, MPlipb-Estratos de Pitreño, Pl3-Sarnoso Complex, Plcc2-Cordón Caulle 2, Plsp-Secuencia piroclastica-epiclastica de San Pablo, Llic-Curacautín Ignimbrite, Pliv-Cordillera Nevada - Cordón Caulle, Plsq-Volcan Sierra de Quinchilca, Ppleh-Estratos de Huincacara, PPlm-Formacion Malleuco. Geographic coordinates are referred to WGS84 datum. Age in Ma is from the geologic timescale of *Gradstein et al*. [2004]. Bedding is expressed in dip azimuth/dip values. *D* and *I* are site-mean declination and inclination calculated before and after tectonic correction; *k* and *α95* are statistical parameters after *Fisher* [1953]; *n/N* is number of samples giving reliable results/number of studied samples at a site. Site-mean rotation *R* and flattening *F* values, and relative errors *ΔR* and *ΔF* (according to *Demarest* [1983]) are relative to coeval *D* and *I* South American values expected at the sampling area considering South American paleo-poles from *Torsvik et al*. [2008]. [d] Rejected sites with values of α95 >30° and 70°>I<10º were rejected.

It consists of an extended deposit of scoria and ash pyroclastic flow of basaltic to andesitic composition, mainly distributed along the valley bottom that radially start from the volcano [*Naranjo and Moreno*, 1991]. The Curacautín Ignimbrite was erupted at the beginning of the last post-glacial period from 13,460±400 BP to 12,760±130 BP, as suggested by four ^{14}C ages obtained from charcoal within the ignimbrite deposit [*Naranjo and Moreno*, 2004]; (**v**) Estratos de Huincacara Formation (**Ppleh**, one site), a subhorizontal eplicastic and volcaniclastic sequence of conglomerates, sands and breccias of basaltic to andesitic composition. It is equivalent to the Upper Pliocene to Lower Pleistocene Malleco Formation [*Moreno and Clavero*, 2006]. There are not radiometric ages reported to this formation, therefore for further considerations we assume the same Malleuco Formation age.

Bedding (occurrence of volcaniclastic layers or sedimentary layers interbedded within the volcanics) was retrievable in only 23 (out of 43) sites. At each site we collected 18 to 4 samples (11 on average) using a petrol-powered portable drill cooled by water, and oriented them in-situ using a magnetic compass corrected for the local magnetic declination for year 2013 (between 7º and 10ºE according to NOAA's National Geophysical Data Center, http://www.ngdc.noaa.gov/geomag/declination.shtml), and when possible also using a sun compass.

The oriented cores were cut into standard paleomagnetic specimens at the paleomagnetic laboratory of the Istituto Nazionale di Geofisica e Vulcanologia (INGV, Roma). The natural remanent magnetization (NRM) of each specimen was measured in a magnetically shielded room

using a 2G Enterprises DC-superconducting quantum interference device cryogenic magnetometer. The lava specimens were demagnetized in 10 steps by alternating magnetic field (AF) yielded by three coils online with the magnetometer until a maximum AF peak of 100 mT. Ignimbrites (13 sites) and the sedimentary site (LOF74) were thermally demagnetized using a Pyrox shielded oven in 11 steps up to a maximum temperature of 600ºC. Highly magnetic specimens (NRM>20 A/m) from site LOF60 were thermally cleaned and their NRM was measured using an AGICO JR6 spinner magnetometer.

Demagnetization data were plotted on orthogonal diagrams [*Zijderveld,* 1976], and the magnetization components of each specimen were isolated by principal component analysis [*Kirschvink,* 1980]. Site-mean paleomagnetic directions were computed using *Fisher* [1953] statistics and plotted on equal-angle projections. Site-mean rotation and flattening values with respect to South America were calculated according to *Demarest* [1983] using reference paleopoles from *Torsvik et al*. [2008].

As a conservative approach, we always considered the smaller angle between the calculated and expected South American declinations to define the sense and amount of rotation. As a consequence, rotation values are always ≤|180°|, although it cannot be excluded that some sites rotated by more than 180º in the opposite sense [e.g., *Nelson and Jones*, 1987; *Piper et al*., 1997, *Hernandez-Moreno et al*., 2014].

7. Paleomagnetic Results

Samples from 9 out of 43 sites yielded erratic magnetization directions and were discarded from further considerations. Demagnetization diagrams from the 34 remaining sites show a rather homogeneous magnetic behavior (Figure 3). A viscous component was removed during the first demagnetization steps, 10-20 mT or 120-200ºC during AF or thermal demagnetization, respectively. Afterwards a well-defined characteristic magnetization (ChRM) was isolated in the 20-100 mT or 200-600ºC interval, depending on the demagnetization method.

By considering the low magnetic coercivities, the remanence drops between 200º and 300ºC observed at several sites, and the complete demagnetization systematically occurring around 600ºC, we infer that the ferromagnetic content is represented by titanomagnetite and magnetite.

The α_{95} values relative to the site-mean paleomagnetic directions vary from 5.8º to 41.4º (13º on average, Figure 4 and Table 1). Further 14 sites were rejected from the 34 sites yielding valuable ChRMs, because their α_{95}values were greater than 30°, and/or their in-situ (or tilt-corrected for site LOFZ102) mean inclinations were < |10º| or > |70°|. In fact, sites yielding subhorizontal directions have undefined magnetic polarity (the local normal polarity geocentric axial dipole (GAD) field

inclination is -58°/-61°) and cannot be used to evaluate tectonic rotations. On the other hand, the declination error is defined by $\Delta D=\alpha_{95}/CosI$, thus declinations (and rotations) tend to become indefinite for subvertical paleomagnetic directions with I>|70°|. After applying our reliability criteria, 20 site-mean paleomagnetic directions were retained to infer on the tectonic rotation pattern.

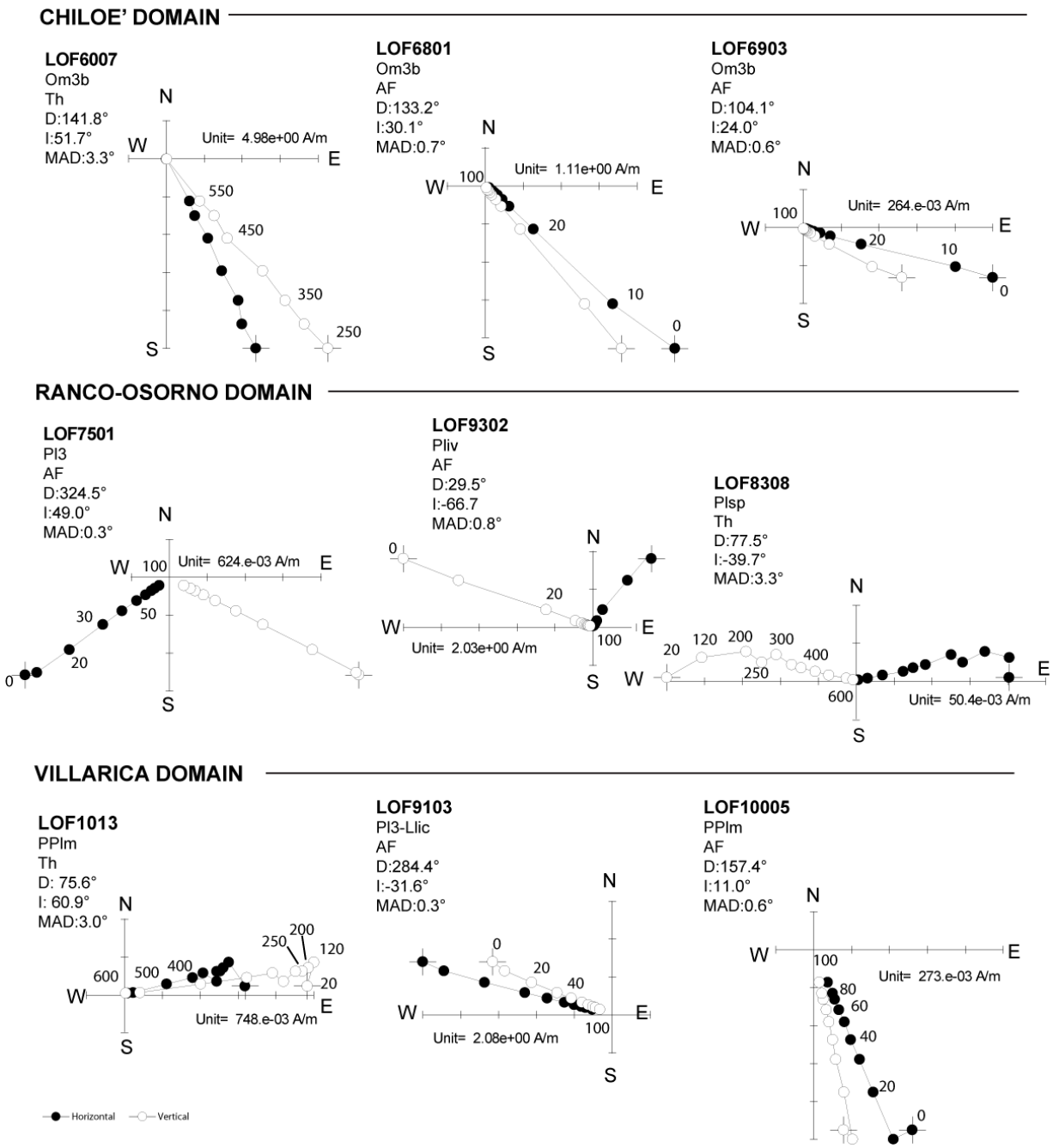

Figure 3. Orthogonal vector diagrams (in-situ coordinates) of representative samples carrying typical demagnetization data for each domain. Solid (open) squares represent projection onto the horizontal (vertical) plane. Demagnetization step values are in mT and °C for the alternating field and thermally demagnetized samples, respectively.

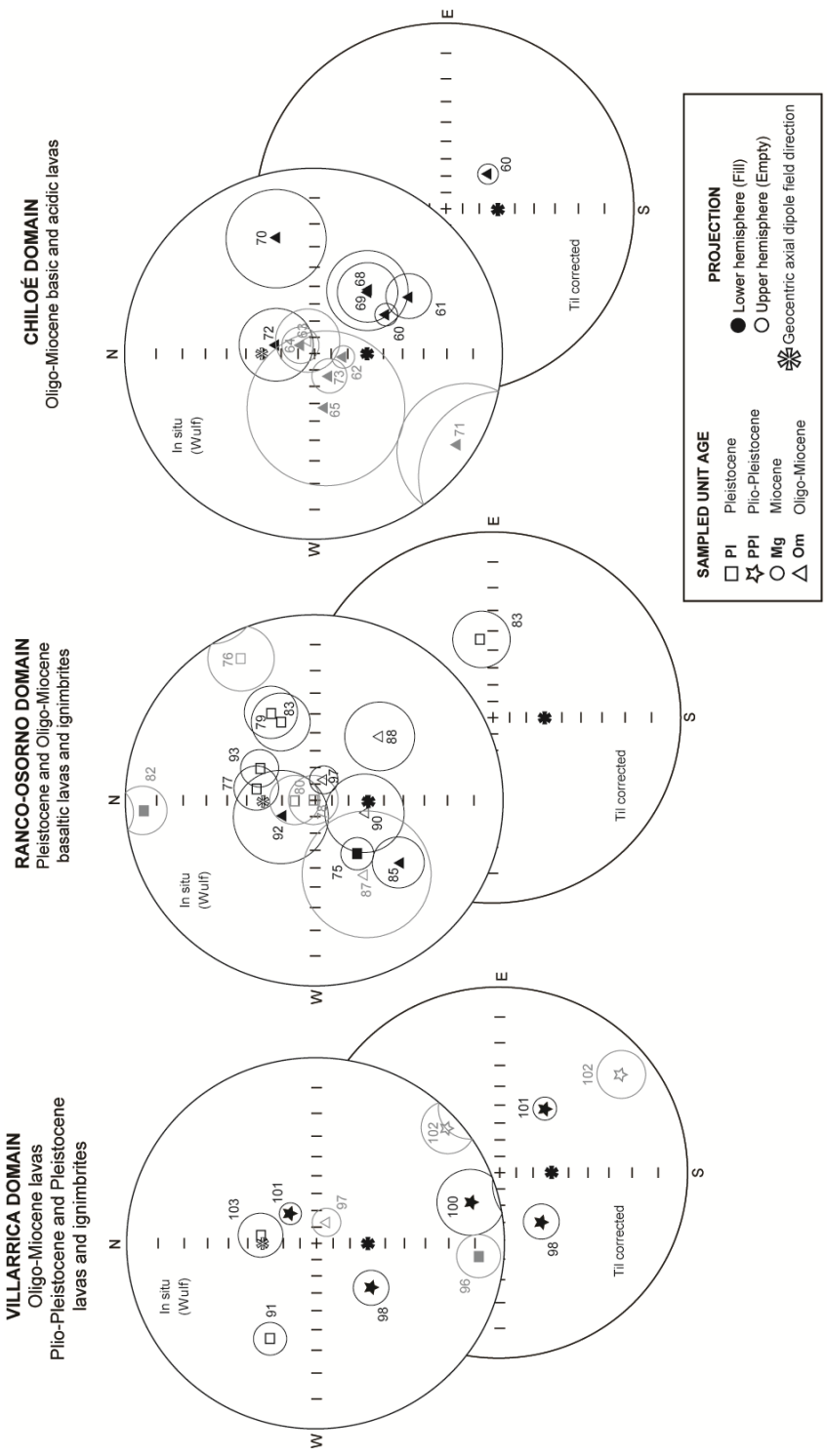

Figure 4. Equal-angle projection of the site-mean paleomagnetic directions gathered along the Chiloé Block, west of the Liquiñe-Ofqui Fault Zone (Southern Chile). Solid (open) symbols represent projection onto the lower (upper) hemisphere. Open circles are the projections of the α_{95} cones about the mean directions. Numbers correspond to sites shown in Figure 2 and detailed in Table 1. In gray are indicated the discarded sites. The asterisk empty (solid) represents the normal (inverse) polarity geocentric axial dipole (GAD) field direction (D = 0°; I = -58°/-61º) expected at the study area.

Site mean directions are shown in Figure 4, grouped according to the respective domain (see Figure 2 for location). Only 4 out of the 20 reliable directions could be tilt corrected, implying that an error on the rotation values cannot be excluded for the remaining 16 in-situ directions. However, in the Chiloé Island the volcanics from the Ancud Complex (Om3b) are interbedded and overlaid by the subhorizontal pelagic sediments of the Lacui Formation, thus excluding the occurrence of tilting errors. Beside those sites other 7 belong to subhorizontal volcanic sequences, excluding also tilting errors (Plcc2, Omlr, Pliv, PPlm; Table 1). We interpret the difference between observed and expected South American declinations as entirely due to tectonic rotations, although the paleosecular variation of the geomagnetic field certainly played a role in the paleomagnetic directions recorded by the studied volcanics. However this effect is expected to be small (mostly within ±20° at similar latitudes [*Speranza et al*., 2008; *Di Chiara et al*., 2012], with respect to the tectonic rotations that here and in the adjacent LOFZ reach (and probably exceed) 180° (e.g. *Hernandez-Moreno et al*. [2014]). Both a fold and a reversal test could not be performed due to the few tilt-corrected directions and the great directional scatter related to individual block rotation. In any case, paleomagnetic directions are always far from both the normal (D= 0º, I= -58 to -61º) and reverse polarity (D= 180º, I= 58 to 61º) GAD field directions (Figure 4), thus excluding a possible recent magnetic overprint.

In the Chiloé domain it is noteworthy the systematic reverse polarity of the Oligo-Miocene Ancud Volcanic Complex, while in the other two domains both normal and reverse polarities occur. Data from the Chiloé domain might suggest that all sampled volcanics are almost synchronous and belong to the same reverse polarity chron, although new ad-hoc radiometric data would be needed to verify this hypothesis. The great majority of the sites from the Ranco-Osorno domain show a normal polarity that, considering their Mid-Upper Pleistocene age, constrain them to the Brunhes polarity chron (0-0.78 Ma [*Cande and Kent* 1995]).

Flattening values with respect to South America are mostly negative but show a great variability, even in closer sites of the same age, implying that they cannot be used to assess microplate latitudinal drift (Table 1).

8. Rotation pattern in the south Chile fore-arc

Each studied domain is characterized by a different rotation pattern (Figures 2 and 4, Table 1). All six reliable Oligo-Miocene volcanics from the Chiloé Island, located far from LOFZ (120-140 km, Figure 5) yield significant CCW rotations, ranging from -28° to -165° (mean -71°± 21). CCW rotations are consistent with *Garcia et al*. [1988] who reported to the same distance from the LOFZ rotations around -27°± 9, and *Rojas et al*. [1994] who even close to the LOFZ (~20 km) found CCW

ca. -10±18.1). Data scatter suggest independent block rotations of small blocks with sizes in the order of few km.

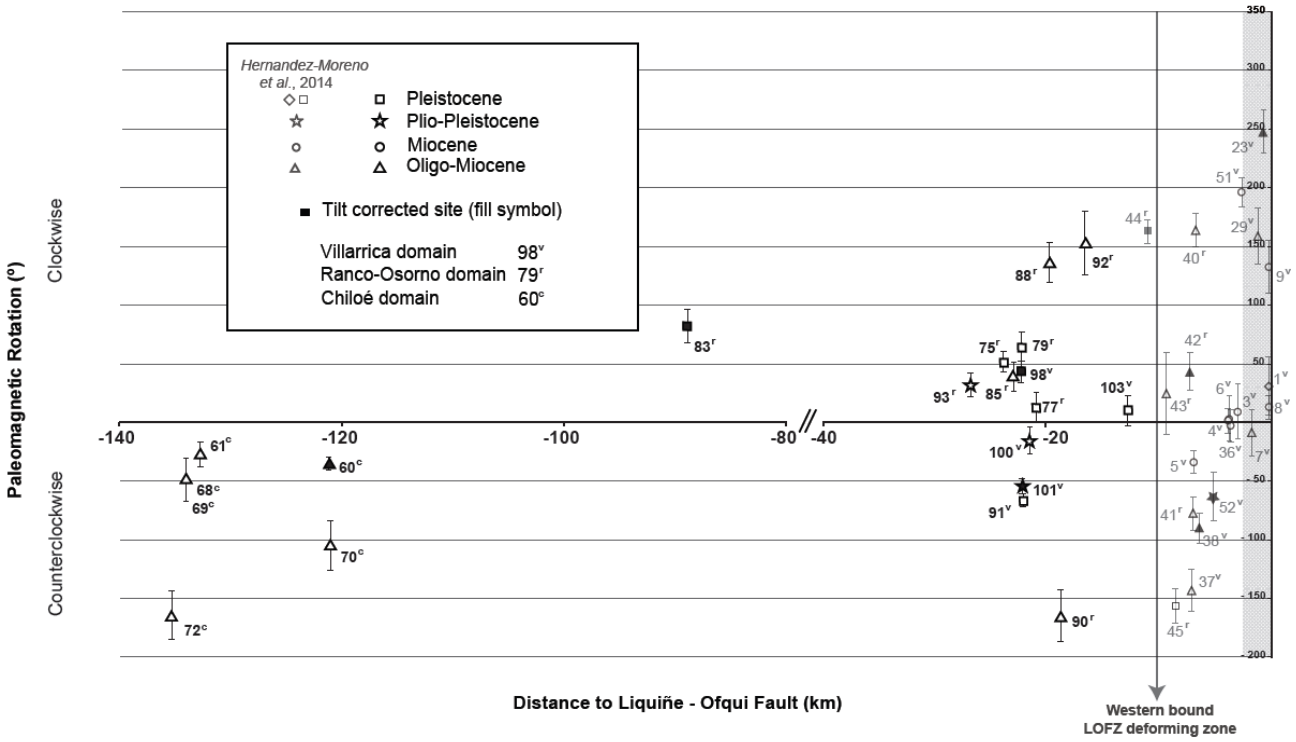

Figure 5. Plot of paleomagnetically detected rotations with respect to South America vs. distance from the LOFZ main trace (see Figure 2 for location). In gray are indicated the paleomagnetic data reported by *Hernandez-Moreno et al*., [2014] (Table 2 and Figure 3 therein).

Conversely, at the Ranco-Osorno domain, rotations from both normal and reverse polarity sites gathered within 30 km from LOFZ are predominantly CW, and range from 13° to 165° (mean 45°± 25). At Ranco Lake, the -14°±8.5 and -16.1°±9.2 CCW rotations documented from two Upper Carboniferous and one Miocene sites respectively, by *García et al*., [1988], might represent the western boundary of the CW rotation domain shown by us adjacent to the LOFZ. Further west, an upper Pleistocene site LOF83 located close to Osorno at 90 km from LOFZ, gives a 82° CW rotation (but the low 7.3 value for the k precision parameter makes this result suspicious). It is noteworthy that three of the CW rotating sites (excluding site LOF83) are mid-upper Pleistocene in age, translating into rotation rates of 64°/Myr. This confirms that protracted activity of the LOFZ during the last 20 Ma may have induced CW block rotations largely exceeding 180°, as already hypothesized by *Hernandez-Moreno et al*. [2014]. Two Oligo-Miocene sites (LOF88 and LOF92) yield greater 136° and 153° CW rotations, but a rotational evolution vs. age considering Pleistocene data cannot be assessed as these two sites are closer to the dextral LOFZ, thus stronger CW

rotations are expected. Finally, it is likely that the adjacent site LOF90 has been in fact rotated CW by 195° (a CCW rotation of 165° is evaluated considering the smaller angle between observed and expected declination).

In the Villarrica domain only five reliable Plio-Pleistocene data are available, and rotations are both CW and CCW. However, this domain had been already investigated by *Hernandez-Moreno et al*. [2014]. Considering the whole available paleomagnetic data set, west of the LOFZ CCW rotations dominate and occur even adjacent to the LOFZ (Figures 2 and 5). Five sites by *Hernandez-Moreno et al*. [2014] located just west of the LOFZ at 39.2°S do not rotate and, according to them, define one of the elongated crust slivers translating without rotations parallel to the LOFZ. CCW rotations must have also occurred recently and rapidly (>10°/Myr), as the Plio-Pleistocene site LOF101 rotated by -55°. Three Oligo-Miocene sites by *Hernandez-Moreno et al*. [2014] reveal a rotation rate for the last 24 Ma of ~5º/Myr We regard as suspicious the 65° CW rotation of the upper Pleistocene site LOF91, which would yield the puzzling rotation rate of ca. 5000°/Myr.

9. Discussion

9.1. Crustal block kinematics in the fore-arc sliver

Our data confirm at first approximation previous results by *Beck et al*. [1993] on the occurrence of "wrong way" CCW rotations in fore-arc sliver, although we also document CW rotations in the easternmost 40 km of the fore-arc adjacent to LOFZ at 40°-41°S. *Beck et al*. [1993] suggested that the foreland is undergoing N-S shortening, as its northward drift is hampered by a buttress located at its northern edge (flat slab and thick crust occurrence). Therefore the fore-arc would be segmented by lens-shaped blocks exceeding 100 km in width that tend to escape laterally towards the trench by rotating CCW (see also Figure 2C by *Hernandez-Moreno et al*. [2014]). We note that this model is inconsistent with both structural and paleomagnetic data. First CCW rotating lens shaped blocks need to be decoupled by the rest of the fore-arc by right-lateral strike-slip faults (both NE-SW and NW-SE), but in fact there is no evidence for such faults. On the other hand, the whole fore-arc (from LOFZ to trench) is crosscut by an array of NW-trending seismically active left-lateral faults, possibly reactivating (at least close to LOFZ) inherited basement faults [*Glodny et al*., 2008; *Lange et al*., 2008; *Melnick et al*., 2009]. Second, the rotation difference between sites (Figure 6) evaluated in the Chiloé Island and in the Villarrica domain (where CCW rotation dominate) document that crust of the fore-arc is fragmented in small blocks undergoing CCW rotations of different magnitudes. According to data of Figure 6, crustal block size seems to be in

the order of 1-2 km in the Chiloé Island, and 10 km in the Villarrica and Ranco domains, in agreement with previous estimates by *Hernandez-Moreno et al*. [2014].

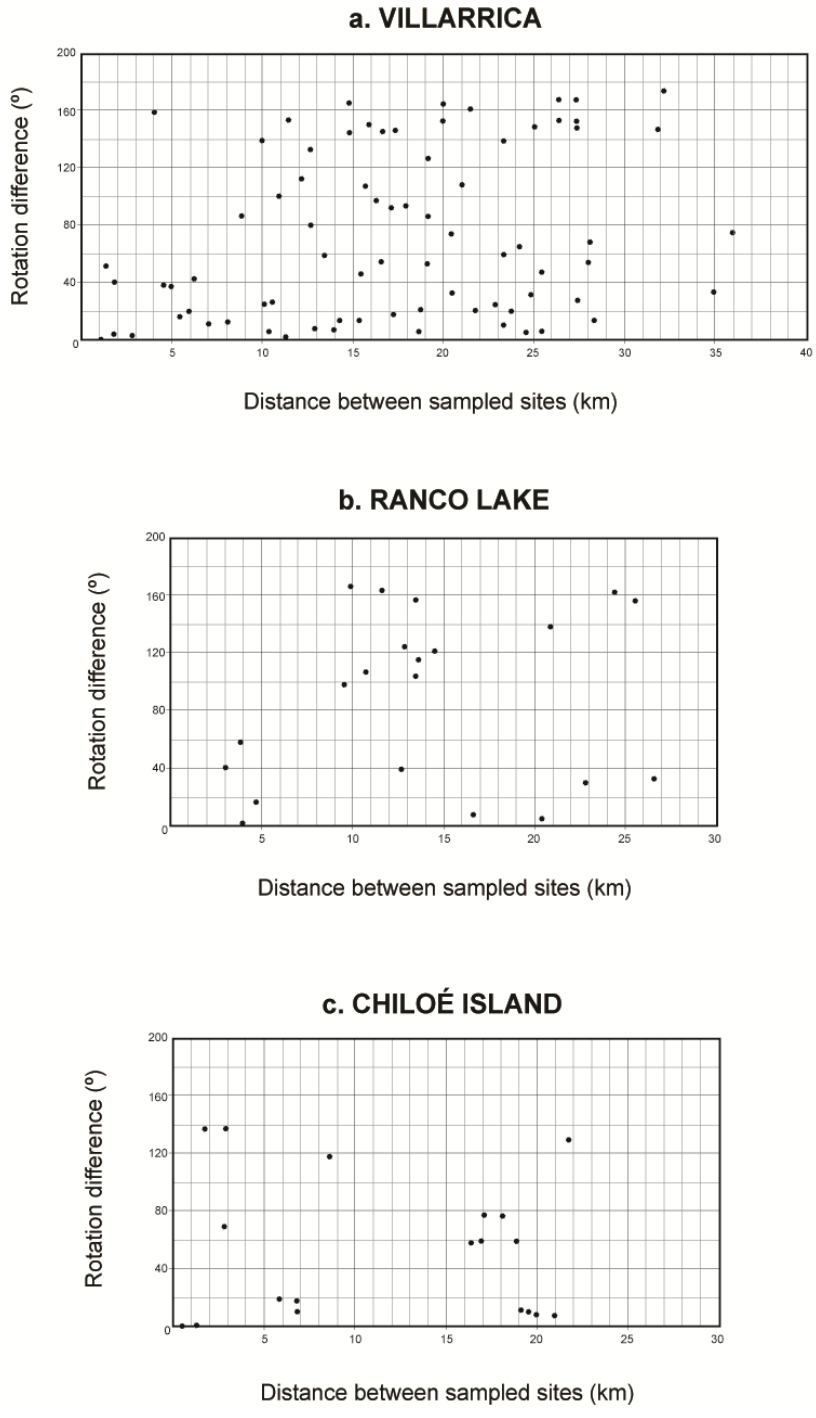

Figure 6. Rotation difference between pairs of sites along the Chiloé fore-arc sliver with respect to the distance between them. These plots were built only for zones where there is a high paleomagnetic data concentration: **(a)** Villarrica, **(b)** Ranco Lake, **(c)** Chiloé Island.

Wider block size in the eastern fore-arc likely reflects pre-existing crust fabric of pre-Andean orogenic episodes. Conversely moving towards the trench the fore-arc becomes thinner and, at least at depth, should be made by a chaotic mélange of upper crust slices detached from subducting plate and accreted to wedge. Thus a thinner and more densely faulted fore-arc moving towards the trench justifies the 1-2 km size blocks documented at Chiloé Island.

The occurrence of NW trending sinistral faults and of 1-10 wide crustal blocks rotating independently CCW up to at least 180° is consistent with the quasi-continuous crust deformation model proposed by *Sonder et al*. [1994] and *Randall et al*. [2011] (Figure 7). CCW rotations would occur in the deforming zones of the left lateral faults that according to *Sonder et al*. [1994] may be up to 15 km wide. CCW rotations occurred very recently (Plio-Pleistocene site LOF101 from the Villarrica domain rotated 55°), and this is consistent with the present-day seismic activity of the NW sinistral faults, according to *Bohm et al*., 2002; *Haberland et al*., 2006; and *Lange et al*., [2008]. The rotation pattern of the fore-arc is conversely inconsistent with both continuous crust deformation (admitting rotations $\leq|90°|$ [*England et al*., 1985; *Sonder et al*., 1986; *McKenzie and Jackson*, 1986, *Kimura et al*., 2004, 2010]), and with the slate block model by *Ron et al*. [1984], *Nur et al*. [1986]; and *Mckenzie and Jackson* [1986], where CCW rotating blocks are bounded by dextral faults that are not apparent in the south Chile fore-arc (Figure 7).

However, the quasi-continuous model by *Sonder et al*. [1994] and *Randall et al*. [2011] consider that block rotation is due to the drag exerted by the underlying ductile crust flowing subparallel to faults. That was indeed a viable mechanism to justify large CW rotations observed east of the LOFZ, where at least 50 km of dextral displacement occurred in the last 5 Ma [*Rosenau et al*., 2006] and the occurrence of volcanoes and high heat flow implies a shallow brittle-ductile transition in the crust. But a similar dynamics is difficult to reconcile with the fore-arc, that is thought to be composed by a stack of "cold" crustal slices with virtually no ductile flowing lower crust [*Bohm et al*., 2002; *Tassara et al*., 2006; *Tassara*, 2010]. Therefore we must admit that CCW rotations in the fore-arc are due to the drag exerted on adjacent crust by fault walls. Crust fragmentation pattern and rotations sense (CW/CCW for dextral/sinistral faults) and amount (>90°) would be similar to that considered by the quasi-continuous model of *Sonder et al*. [1994], but dynamics is definitely different.

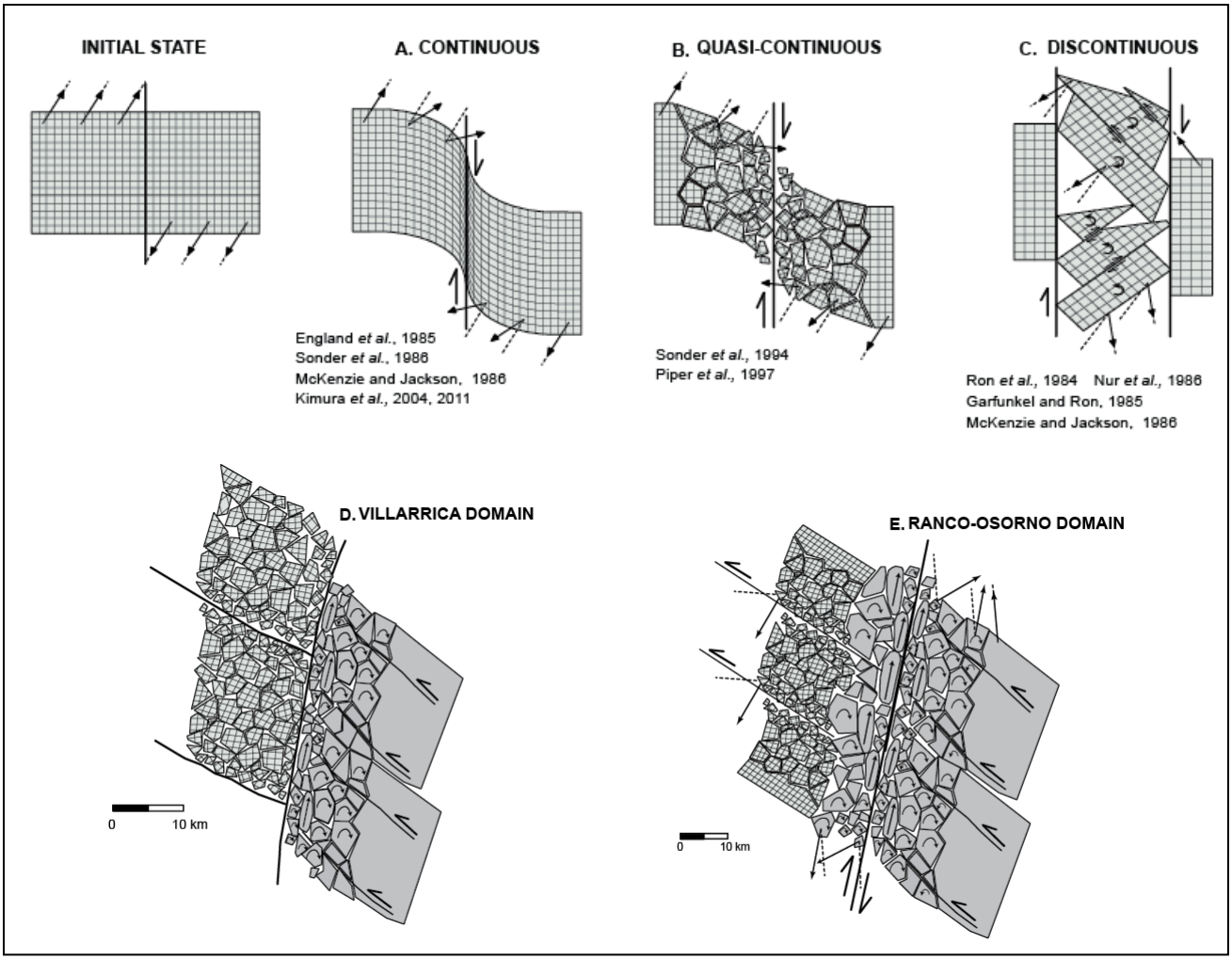

Figure 8. A to C kinematic models attempting to explain rotation distribution and values in strike-slip fault systems. **D and E** quasi-continuous models of crust behavior for the Chiloé fore-arc sliver: Villarrica and Ranco-Osorno domains, respectively. The dimension and shape of the individual crustal blocks are hypothetic, but consistent with the areal variability of the paleomagnetic rotations and the location of both the LOFZ main strand and the NW-trending sinistral faults (Figure 2). Hatched (not hatched) blocks rotate in CCW (CW) sense.

Finally, our data may help solving the controversy on whether sinistral faults of the fore-arc are related to LOFZ activity (thus being synchronous splays of the LOFZ, e.g. *Nelson et al*., 1994; *Lopez-Escobar et al*., 1995; *Cembrano et al*., 1996; *Rosenau et al*., 2006), or they are long-lived basement structures reactivated as sinistral reverse strike-slip faults, displacing the LOFZ and not actually connected nor genetically related to it [*Glodny et al*., 2008; *Lange et al*., 2008; *Melnick et al*., 2009]. We note that the rotational pattern is definitely asymmetric with respect to the LOFZ, as

CCW rotations dominate in the fore-arc, while CW rotating blocks occur east of the LOFZ and rotations are definitely annulled at ca. 10 km east of the LOFZ [*Hernandez-Moreno et al*., 2014]. This rotation pattern is definitely consistent with the hypothesis that the left-lateral faults from the fore-arc and the LOFZ share synchronous activity and are genetically related. We suggest that LOFZ and sinistral fault activity are both the expression of the tectonic deformation of the south Chile fore-arc, drag by oblique subduction of the Nazca plate. Pre-existing basement structures were reactivated only in the fore-arc, while east of the LOFZ their activity is related to tectonic episodes older than fore-arc sliver formation (predominantly the last 5 Ma). In fact, evidence for ongoing seismic activity along NW-trending sinistral faults is limited to the fore-arc sliver, and does not occur in the Andean cordillera east of the LOFZ [*Bohm et al*., 2002; *Haberland et al*., 2006; *Lange et al*., 2008].

9.2. Width of the CW rotation zone west of the LOFZ: a new method to infer on subducting plate coupling

Hernandez-Moreno et al. [2014] have shown that east of the LOFZ the crust is fragmented in 1-10 km wide blocks that seem to be consistent with quasi-continuous crust deformation as defined by *Sonder et al*. [1994]. Rounded blocks within a ca. 10 km wide zone east of the LOFZ rotate CW, consistently with dextral LOFZ kinematics, and their rotation magnitude increases up to 170° (and possibly more) adjacent to the LOFZ. *Hernandez-Moreno et al*. [2014] also documented that (in agreement with *Lamb* [1987] and *Randall et al*. [2011]) rotation pattern is strictly dependent upon block aspect ratio, as elongated blocks, even located adjacent to LOFZ, do not rotate but are simple translated parallel to fault.

West of the LOFZ, the fore-arc is fragmented in similarly small blocks that conversely rotate CCW, as it is apparent from data from the Chiloé Island that are located ca. 130 km from LOFZ thus surely do not reflect LOFZ kinematics (Figure 2 and 5). Consequently, we expect that the easternmost fore-arc sector located adjacent to the LOFZ is subjected to both CW and CCW rotations, related to LOFZ and sinistral faults kinematics, respectively. This is apparent in the Ranco-Osorno domain, where blocks from a 30 km wide zone west of LOFZ rotate CW, while CCW rotations occur further west around the Ranco lake (Figures 2 and 5). Conversely, further north in the Villarrica domain CCW rotations occur immediately west of LOFZ, and CW rotated sites are definitely confined to the eastern LOFZ side.

We suggest that the width of the CW rotating domain west of LOFZ is a function of LOFZ strength. Higher fault coupling in the Ranco-Osorno domain would requires a greater fault-parallel stress accumulation beside elastic deformation before to overcome fault strength, thus obviously a

larger deformation zone characterized by CW rotations. Fault strength depends in turn on both fault lubrication and intensity of stress applied normal to fault walls. Also the crust rheology is a very important factor in the strength of the crust, but we can ignore this factor as the LOFZ runs mainly along the North Patagonian Batholith. If we assume similar lubrication along different LOFZ segments, then we must conclude that eastward fore-arc push against the LOFZ is significantly greater in the Ranco-Osorno than in the Villarrica domain. Fore-arc push depends on the degree of coupling between the Nazca plate, subducting below South America at a 6.6 cm/yr rate, and the overlying fore-arc wedge. Thus we suggest that paleomagnetic data document a greater subduction plate coupling at 40°-41°S than at 39°S.

Paleomagnetism reflects rotations occurring in the geological past, predominantly in the Plio-Pleistocene according both to *Hernandez-Moreno et al*. [2014] and our new data, thus should reflect the mean degree of plate coupling during the last 5 Ma.

Our proposed mechanism for the dependence of CW rotation zone width upon LOFZ coupling implies, similarly to the mechanism proposed for the fore-arc, that CW rotations are primarily driven by LOFZ drag, rather than by lower crust flow. Our rotation model turns out to be a mixture between the "ball bearing" model by *Beck* [1976] and *Piper at el*. [1997] and the quasi-continuous deformation by *Sonder et al*. [1994] (e.g. *Hernandez-Moreno et al*. [2014]).

Our data indeed reflect fore-arc behavior in the geological past, while GPS data and Bouguer anomalies show the degree of coupling between the Nazca plate and the overlying wedge over time-scales ca. 10^6 yr and 10^2 yr, respectively [*Imanishi et al*., 2005].

The integration of new GPS data with those by *Klotz et al*. [2001], *Ruegg et al*. [2009], and *Wang et al*. [2007] allowed *Moreno et al*. [2011] to show that plate locking peaks at maximum in two zones at 36°-39° and 40°-42°S, while a zone of reduced coupling seems to occur at around 39°S (Figure1B and 2). Thus along-arc coupling variations observed today between 39° and 41°S by GPS evidence would have also occurred during the last 5 Ma, according to our paleomagnetic inferences (Figure 2). This implies that geological and geophysical parameters controlling plate locking have remained rather unchanged during the last few Myrs, and that high coupling could be due to a persistent geological features, such as for example a subducting seamount at 40°-41°S.

Finally, we remind that plate locking shown by GPS data is partly inconsistent with that inferred by Bouguer anomaly interpretation by *Hackney et al.* [2006] who argue for a low-coupling segment at 36°-39°S followed further south by two locked fore-arc segments, and by *Tassara* [2010] who pointing out to a generalized low coupling along the southern Andes due to a lighter fore-arc that does not exert a significant load over the plate interface, with just one exception at the Arauco Peninsula where he reports high coupling consequence of more mafic rocks. However, locking

inferred by Bouguer anomaly data depends upon gravimetric modeling (that is typically non-univocal), and a number of assumptions on the factors yielding coupling between plates (slab depth and dip, wedge thickness, rock frictional properties).

10. Conclusions

New paleomagnetic data from the southern Chile fore-arc at 39°-42°S document a predominant CCW rotation pattern. Rotations are very recent (Plio-Pleistocene sites rotated by -55° (LOF101)) and their magnitudes vary greatly reaching (at least) 180°. Block size decreases from ca. 10 to 1-2 km moving westward from the LOFZ, at the eastern fore-arc margin, towards the trench. Block size variation is consistent with progressive westward thickness decrease of the fore-arc wedge and more pervasive tectonic deformation approaching trench. By considering also the occurrence of seismically active sinistral NW-SE fault that crosscut the whole fore-arc, CCW block rotation is consistent with quasi-continuous crust deformation related to sinistral fault occurrence, similar to the model proposed by *Sonder et al*. [1994]. Quasi-continuous models require that rotations are driven by drag exerted by the lower crust flowing below brittle upper crust, but fore-arc wedge is made by a stack of cold crustal slice scraped off from subducting slab, where lower crust flow is unlikely to occur. Therefore we suggest that CCW rotations in the fore-arc are driven by drag exerted by sinistral fault shear.

Within the fore-arc, CW rotations occur only within a 30-km wide sector adjacent to LOFZ between 40° and 41°S. Here block size (ca. 10 km) and rotation pattern (up to 180° at least) is similar to those documented by *Hernandez-Moreno et al*. [2014] east of the LOFZ, and interpreted as quasi-continuous crust deformation related to ongoing and Plio-Pleistocene dextral shear occurring along the LOFZ. Conversely, further north at 39°S the eastern margin of the fore-arc adjacent to LOFZ is characterized by a CCW rotation pattern.

We suggest that the width of the CW rotation zone occurring west of the LOFZ may be used as a proxy for the locking between the subducting plate and the fore-arc wedge along the geological past. High coupling would yield higher stress normal to the LOFZ, thus higher fault strength and a wider deforming zone characterized by CW rotating blocks. Low coupling would imply a weak LOFZ and the lack of CW rotations, and a fore-arc entirely dominated by the CCW rotation pattern driven by sinistral fault activity.

Our inferences on subdution plate locking during the geological past (predominantly the last 5 Ma) are in fair agreement with present-day locking on different subduction segments documented by GPS data [*Moreno et al*., 2011]. This suggests that factors determining plate coupling are

represented by geological features (subducting seamounts, zones of anomalous upper/lower plate thickness) that remained virtually unchanged during the last 5 Ma.

Acknowledgements

Our special thanks go to CONAF, the Chilean National Park System, because made possible carried out this research even into the protected areas located within the LOFZ deforming zone, thanks for their entire disposition. This work was financed by INGV funds. The paleomagnetic data reported here are available upon e-mail request to C.H.M.

References

Abels, A., and L. Bischoff (1999), Clockwise block rotations in northern Chile: Indications for a large-scale domino mechanism during the middle-late Eocene, *Geology*, *27*, 751-754, doi:10.1130/0091-7613(1999)027<0751.

Allen, C.R., P. St. Amand, C. F. Richter, and J. M. Nordquist (1965), Relationship between seismicity and geologic structure in the southern California region, *Bull. Seismol. Soc. Am.*, *55*, 753.

Angermann, D., J. Klotz, and C. Reigber (1999), Space-geodetic estimation of the nazca-south america euler vector, *Earth Planet. Sci. Lett.*, *171*(3), 329–334.

Antinao, J.L., P. Duhart, J. Clayton, S. Elgueta, and M. McDonough (2000), Área de Ancud-Maullín, Región de Los Lagos, Mapas Geológicos N.17 escala 1:100.000, *Ser. Nac. De Geol. y Min.*, Chile.

Argus, D. F., and R. G. Gordon (1990), Pacific-North American plate motion from very long baseline interferometry compared with motion inferred from magnetic anomalies, transform faults, and earthquake slip vectors, *J. Geophys. Res.*, *95*(17), 315-17.

Arriagada C., P. Roperch, C. Mpodozis, G. Dupont Nivet, P.R. Cobbold, A. Chauvin, and J. Cortés (2003), Paleogene clockwise tectonic rotations in the forearc of central Andes, Antofagasta region, northern Chile, *J. Geophys. Res.*, *108*(B1):doi 10/1029/2001JB001598.

Barrientos, S., and P. Acevedo-Aránguiz (1992), Seismological aspects of the 1988–1989 Lonquimay (Chile) volcanic eruption, *J. Volcanol. Geotherm. Res.*, *53*, 73-87.

Barrientos, S. E., and S. N. Ward (1990), The 1960 Chile earthquake: inversion for slip distribution from surface deformation, *Geophys. J. Int.*, *103*, 589-598.

Beck, M. E. (1976), Discordant paleomagnetic pole positions as evidence of regional shear in the western Cordillera of North America, *Am. J. Sci.*, *276*, 694-712.

Beck, M. E. (1980), Paleomagnetic record of plate-margin tectonic processes along the western edge of North America, *J. Geophys. Res. Solid Earth*, *85*(80), 7115-7131.

Beck, M. (1983), On the mechanism of tectonic transport in zones of oblique subduction, *Tectonophysics*, *93*, 1-11.

Beck, M. (1986), Model for Late Mesozoic-Early Tertiary tectonics of coastal California and western Mexico and speculations on the origin of the San Andreas Fault, *Tectonics*, *5*(1), 49-64.

Beck, M. E. (1987), Tectonic rotations on the leading edge of South America: The Bolivian orocline revisited, *Geology*, *15*(9), 806.

Beck, M. E. (1988), Analysis of late Jurassic-recent paleomagnetic data from active plate margins of South America, *J. South Am. Earth Sci.*, *1*(1), 39-52, doi:10.1016/0895-9811(88)90014-4.

Beck, M. E. (1989), Paleomagnetism of continental North America: Implications for displacement of crustal blocks within the Western Cordillera, Baja California to British Columbia, in

Geophysical Framework of the Continental United States, edited by L. C. Pakiser and W. D. Mooney, *Mem. Geol. Soc. Am.*, *172*, 471-492.

Beck, M. E. (1991), Coastwise transport reconsidered: lateral displacements in oblique subduction zones, and tectonic consequences, *Phys. Earth Planet. Inter.*, *68*(1-2), 1-8, doi:10.1016/0031-9201(91)90002-Y.

Beck, M.E., C. Rojas, and J. Cembrano (1993), On the nature of buttressing in margin-parallel strike-slip fault system, *Geology*, *21*, 755-758.

Beck, M.E., R. Burmester, R. Drake, and P. Riley (1994), A tale of two continents: Some tectonic contrasts between the Central Andes and the North American Cordillera, as illustrated by their paleomagnetic signatures, *Tectonic*, *13*, 215-224.

Beck, M.E., R.F. Burmester, and B.C. Steele (1998), Paleomagnetism of probably remagnetized late Mesozoic volcanic rocks near Lago Verde, Aisén, Southern Chile, *Andean Geol.*, *25*(2), 153-163.

Beck M.E., R.F. Burmester, D.C. Engebretson, and R. Schoonover (1981), Northward translation of Mesozoic batholits, western North America: Paleomagnetic evidence and tectonic significance, *Geof. Int.*, *20*(3), 143-162.

Beck, M., R. Burmester, J. Cembrano, and R. Drake (2000), Paleomagnetism of the North Patagonian Batholith, southern Chile. An exercise in shape analysis, *Tectonophysics*, *326*, 185-202.

Beck, M., A. Garcia, and R. Burmester (1991), Paleomagnetism and geochronology of late Paleozoic granitic rocks from the Lake District of southern Chile: Implications for accretionary tectonics, *Geology*, *19*(4), 332-335, doi:10.1130/0091-7613(1991)019<0332.

Ben-Avraham, Z.V.I., A. Nur, D. Jones, and A. Cox (1981), Continental accretion: from oceanic plateaus to allochthonous terranes, *Science*, *213*(4503), 47-54.

Blanquat, M. D. S., B. Tikoff, C. Teyssier, and J. L. Vigneresse (1998), Transpressional kinematics and magmatic arcs, Geol. Soc. London, *Spec. Publ.*, *135*(1), 327-340, doi:10.1144/GSL.SP.1998.135.01.21.

Bohm, M., S. Lüth, H. Echtler, G. Asch, and K. Bataille (2002), The Southern Andes between 36 and 40 S latitude: seismicity and average seismic velocities, *Tectonophysics*, 356, 275-289.

Campos, A., H. Moreno, J. Muñoz, J.L. Antinao, J. Clayton, and M. Martin (1998), Mapa Geológico del Área de Futrono-Lago Ranco, Región de Los Lagos, Mapa Geológico N.8 esc 1:100.000, *Ser. Nac. De Geol. y Min.*, Santiago de Chile, Chile.

Cande S.C., and D.V. Kent (1995), Revised calibration of the geomagnetic polarity time scale for the Late Cretaceous and Cenozoic, *J. Geophys. Res.*, *100*, 6093-6095.

Cande, S.C., R.B. Leslie, J.C. Parra, and M. Hobart (1987), Interaction between the Chile Ridge and Chile Trench: Geophysical and geothermal evidence, *J. Geophys. Res.*, 92, 495-520.

Cande, S., and R. Leslie (1986), Late Cenozoic tectonics of the southern Chile trench, *J. Geophys. Res. Solid Earth*, *91*(B1), 471-496.

Cembrano, J., and F. Hervé (1993), The Liquine Ofqui Fault Zone: A major Cenozoic strike slip duplex in the southern Andes, in Second ISAG, Oxford (UK), 175-178.

Cembrano, J., M. E. Beck, R. F. Burmester, C. Rojas, A. Garcia, and F. Herve (1992), Paleomagnetism of Lower Cretaceous rocks from east of the Liquine-Ofqui fault zone, southern Chile: evidence of small in-situ clockwise rotations, *Earth Planet. Sci. Lett.*, *113*(4), 539–551, doi:10.1016/0012-821X(92)90130-N.

Cembrano, J., E. Schermer, A. Lavenu, F. Herve, S. Barrientos, B. McClelland, and G. Arancibia (1996), Nature and timing of Cenozoic intra-arc deformation, southern Chile, in Third ISAG, St. Malo (France), 311-314.

Cembrano, J., E. Schermer, A. Lavenu, and A. Sanhueza (2000), Contrasting nature of deformation along an intra-arc shear zone, the Liquiñe-Ofqui fault zone, southern Chilean Andes, *Tectonophysics*, 319, 129-149.

Cembrano, J., A. Lavenu, and P. Reynolds (2002), Late Cenozoic transpressional ductile deformation north of the Nazca-South America-Antarctica triple junction, *Tectonophysics*, 354, 289-314.

Chamot-Rooke, N., and X. Le Pichon (1999), GPS determined eastward Sundaland motion with respect to Eurasia confirmed by earthquakes slip vectors at Sunda and Philippine trenches, *Earth Planet. Sci. Lett*., *173*(4), 439-455, doi:10.1016/S0012-821X(99)00239-3.

Chinn, D., and B. Isacks (1983), Accurate source depths and focal mechanisms of shallow earthquakes in western South America and in the New Hebrides island arc, *Tectonics*, 2(6), 529-563.

Cifuentes, I. N. I. S. L. (1989), The 1960 Chilean Earthquakes, *J. Geophys. Res*., *94*(B1), 665-680.

Coney, P.J., D.L. Jones, and J, Monger (1980), Cordilleran suspect terranes, *Nature*, 288, 329-333.

DeLong, S.E., and P. Fox (1977), Geological consequences of ridge subduction, in Talwani, M., and Pittman, W.C., III, eds., Island arcs, deep sea trenches and back-arc basins: American Geophysical Union Maurice Ewing Series, no. 1, 221-228.

DeLong, S.E., W.M. Schwarz, and R.N. Anderson (1979), Thermal effects of ridge subduction, *Earth and Planetary Science Letters*, 44, 239-246.

Demarest, H. (1983), Error analysis for the determination of tectonic rotation from paleomagnetic data, *J. Geophys. Res. Solid Earth*, *88*(B5), 4321-4328.

DeMets, C., R.G. Gordon, D.F. Argus, and S. Stein (1990), Current plate motions, *Geophy. J.Int*., *101*, 425-478.

Dewey, J.F. (1980), Episodicity sequence and style at convergent plate boundaries, *Geol. Assoc. Can. Spec. Pap*., *20*, 553-573.

Dewey, J. F., and S. H. Lamb (1992), Active tectonics of the Andes, *Tectonophysics*, *205*(1-3), 79-95, doi:10.1016/0040-1951(92)90419-7.

Di Chiara, A., F. Speranza, and M. Porreca (2012), Paleomagnetic secular variation at the Azores during the last 3 ka, *J. Geophys. Res. Solid Earth*, *117*(B7), 1978-2012.

Dickinson, W.R., and W.S. Snyder (1979), Geometry of triple junctions related to the San Andreas transform, *J. Geophys. Res*., *84*, 561-572.

Diraison, M., P. Cobbold, E. Rossello, and J. Amos (1998), Neogene dextral transpression due to oblique convergence across the Andes of northwestern Patagonia, Argentina, *J. South Am. Earth Sci*., *11*(6), 519-532.

Duhart, P., J. Muñoz, and C. R. Stern (2000), Geologia de la Isla Grande de Chiloe, X Region de los Lagos, Chile, XI Congr. Geológico Chil. Puerto Varas, Chile, *1*(3), 461-465.

Echtler, H., J. Glodny, K. Gräfe, M. Rosenau, D. Melnick, W. Seifert, and T. Vietor (2003), Active Tectonics controlled by inherited structures in the long-term stationary and non-plateu South-Central Andes, EGS-AGU Joint Assembly, Nice, France, Abstract EAE03-A-10902.

England, P., and D. McKenzie (1982), A thin viscous sheet model for continental deformation, *Geophys. J. R. Astron. Soc*., *70*, 295-321, doi:10.1111/j.1365-246X.1982.tb04969.x.

England P., G. Houseman, and L. Sonder (1985), Length scales for continental deformation in convergent, divergent, and strike-slip environments: Analytical approximate solutions for a thin viscous sheet model, *J. Geophys. Res*., *90*(B5), 3551-3557, doi:10.1029/JB090iB05p03551.

England, P., and R. E. Wells (1991), Neogene rotations and quasicontinuous deformation of the Pacific Northwest continental margin, *Geology*, *19*, 978-981.

Feigl, K. et al. (1993), Space geodetic measurement of crustal deformation in central and southern California, 1984-1992, *J. Geophys. Res. Solid Earth*, *98*(B12), 21677-21712.

Finger, K.L., S.N. Nielsen, T.J. Devries, A. Encinas, and D.E. Peterson (2007), Paleontologic evidence for sedimentary displacement in Neogene forearc basins of central Chile, *Palaios*, *22*(1), 3-16.

Fisher, R. A. (1953), Dispersion on a sphere, *Proc. R. Soc. London, Ser. A*, *217*, 295-305.

Fitch, T. (1972), Plate convergence, transcurrent faults, and internal deformation adjacent to southeast Asia and the western Pacific, *J. Geophys. Res.*, *77*(23), 4432-4460.

Folguera A., V.A. Ramos, and D. Melnick (2003), Recurrencia en el desarrollo de cuencas de inra-arco. Cordillera Neuquina (37°30'-38°S), *Rev. Asoc. Geol. Argentina*, *58*(1), 3-19.

Folguera, A., V. A. Ramos, E. Gonzàlez-Dìaz, and R. Hermanns (2006), Miocene to Quaternary deformation of the Guañacos fold-and-thrust belt in the Neuquén Andes between 37°S and 37°30'S, in Evolution of an Andean Margin: A Tectonic and Magmatic View From the Andes to the Neuquén Basin (35°-39°S lat), edited by S. M. Kay and V. A. Ramos, *Spec. Pap. Geol. Soc. Am.*, *407*, 247-266, doi:10.1130/2006.2407(11).

Folguera, A., V.A. Ramos, and D. Melnick (2002), Transición de los Andes Patagónicos a los Andes Centrales: Extremo norte del sistema de Liquiñe-Ofqui (38°S), *Rev. Geol. Chile*, *29* (2), 227-240.

Forsythe, R.E., E. Nelson, M. Carr, M. Kaeding, M. Herve, C. Modozis, J. Soffia, and S. Harambour (1986), Pliocene near-trench magmatism in southern Chile: Possible manifestation of ridge collision, *Geology*, *14*, 23-27.

Forsythe, R., and E. Nelson (1985), Geological manifestations of ridge collision: Evidence from the Golfo de Penas-Taitao basin, southern Chile, *Tectonics*, *4*(5), 477-495.

Freund, R. (1974), Kinematics of transform and transcurrent faults, *Tectonophysics*, *21*, 93-134.

Garcia, A., M. Beck, R. Burmester, F. Munizaga, and F. Herve (1988), Pelomagnetic reconnaissance of the region de los Lagos, sothern chile, and its tectonic implications, *Rev. geológica Chile*, *15*(1).

Garfunkel, Z. (1974), Model for the late Cenozoic tectonic history of the Mojave Desert, California, and for its relation to adjacent regions, *Geol. Soc. Am. Bull.*, *85*(12), 1931-1944, doi:10.1130/0016-7606(1974)85<1931.

Garfunkel, Z., and H. Ron (1985), Block rotation and deformation by strike-slip faults: 2. The properties of a type of macroscopic discontinuous deformation, *J. Geophys. Res.*, *90*(B10), 8589, doi:10.1029/JB090iB10p08589.

Glodny, J., H. Echtler, S. Collao, M. Ardiles, P. Burón, and O. Figueroa (2008), Differential Late Paleozoic active margin evolution in South-Central Chile (37°S-40°S) - the Lanalhue Fault Zone, *J. South Am. Earth Sci.*, *26*(4), 397-411, doi:10.1016/j.jsames.2008.06.001.

Groß, K., U. Micksch, T. R. Group, and S. Team (2007), The reflection seismic survey of project TIPTEQ-the inventory of the Chilean subduction zone at 38.2ºS, *Geophys. J. Int.*, *172*(2), 565-571, doi:10.1111/j.1365-246x.2007.0.3680.x.

Hackney, R. I., H. P. Echtler, G. Franz, H. Götze, F. Lucassen, D. Marchenko, D. Melnick, U. Meyer, S. Schmidt, Z. Tašárová, and S. Wienecke (2006), The segmented overriding plate and coupling at the south-central Chilean margin (36-42° S), in The Andes, 355-374.

Haberland, C., A. Rietbrock, D. Lange, K. Bataille, and S. Hofmann (2006), Interaction between forearc and oceanic plate at the south-central Chilean margin as seen in local seismic data, *Geophys. Res. Lett.*, 33, doi:10.1029/2006GL028189.

Hernandez-Moreno, C., F. Speranza, and A. Di Chiara (2014), Understanding kinematics of intra-arc transcurrent deformation: Paleomagnetic evidence from the Liquiñe-Ofqui fault zone (Chile, 38-41° S), *Tectonics*, *33*(10), 1964-1988.

Herron, E. M. (1981), Chile Margin near lat 38ºS: Evidence for a genetic relationship between continental and marine geologic features or a case of curious coincidences?, *Geol. Soc. Am. Mem.*, *154*, 755-760.

Hervé, F. (1994), The Southern Andes between 39º and 44ºS latitude: the geological signature of a transpressive tectonic regime related to a magmatic arc, in Tectonics of the Southern Central Andes, 243-248.

Hervé, F., and R. Thiele (1987), Estado de conocimiento de las megafallas en Chile y su significado tectónico, *Comun. Univ. Chile*, *38*, 67-91.

Hervé, M. (1976), Estudio Geológico de la falla Liquiñe-Reloncaví en el área de Liquiñe; antecedentes de un movimiento transcurrente (Provincia de Valdivia), I Congr. Geológico Chil.

Hoffmann-Rothe, A., N. Kukowski, G. Dresen, H. Echtler, O. Oncken, J. Klotz, E. Scheuber, and A. Kellner (2006), Oblique convergence along the Chilean margin: partitioning, margin-parallel faulting and force interaction at the plate interface, in The Andes, 125-146.

Hofmann-Wellenhof, B., H. Lichtenegger, and J. Collins (1993), GPS theory and practice (second edition), Springer-Verlag, Wien, New York.

Hu, Y., K. Wang, J. He, J. Klotz, and G. Khazaradze (2004), Three-dimensional viscoelastic finite element model for the postseismic deformation of the great 1960 Chile earthquake, *J. Geophys. Res*., *109*, B12403, doi: 10.1029/2004JB003163.

Imanishi, Y., T. Sato, T. Higashi, W. Sun, and S. Okubo (2005), A network of superconducting gravimeters detects submicrogal coseismic gravity changes, *Science*, *306*, 476-480.

Irving, E. (1979), Paleopoles and paleolatitudes of North America and speculations about displaced terrains, *Can. J. Earth Sci.*, *16*, 669-694.

Jarrard, R. D. (1986), Terrane motion by strike-slip faulting of forearc slivers, *Geology*, *14*, 780-783.

Katili, J.A. (1970), Large transcurrent faults in southeast Asia with special reference to Indonesia, *Geologische Rundschau*, *59*, 581-600.

Karig, D.E. (1971), Origin and development of marginal basins in the Western Pacific, *J. Geophys. Res*., *76*, 2542-2561.

Karig, D.E. (1971), Origin and development of marginal basins in the Western Pacific, *J. Geophys. Res*., *76*, 2542-2561.

Kaneko, S. (1966), Transcurrent displacement along the median line, south-western Japan, *N. Z. J. Geol. Gephys*., *2*, 45-59.

Kendrick, E., M. Bevis, R. Smalley, O. Cifuentes, and F. Galban (1999), Current rates of convergence across the Central Andes: estimates from continuous GPS observations, *Geophys. Res. Lett*., *26*, 541-544.

Kendrick, E., M. Bevis, R. Smalley, B. Brooks, R. B. Vargas, E. Lauría, and L. P. S. Fortes (2003), The Nazca-South America Euler vector and its rate of change, *J. South Am. Earth Sci*., *16*(2), 125-131, doi:10.1016/S0895-9811(03)00028-2.

Khazaradze, G., K. Wang, J. Klotz, Y. Hu, and J. He (2002), Prolonged post-seismic deformation of the 1960 great Chile earthquake and implications for mantle rheology, *Geophys. Res. Lett*., *29* (22), 7-1, doi:10.1029/2002GL015986.

Khazaradze, G., and J. Klotz (2003), Short and long-term effects of GPS measured crustal deformation rates along the South-Central Andes, *Journal of Geophysical Research*, *108*(B6), 2289-2306, doi: 2210.1029/2002JB001879.

Kimura, H., Y. Itoh, and H. Tsutsumi (2004), Quaternary strike-slip crustal deformation around an active fault based on paleomagnetic analysis: a case study of the Enako fault in central Japan, *Earth Planet. Sci. Lett*., *226*(3-4), 321-334, doi:10.1016/j.epsl.2004.08.003.

Kimura, H., N. Ishikawa, and H. Sato (2011), Estimation of total lateral displacement including strike–slip offset and broader drag deformation on an active fault: Tectonic geomorphic and paleomagnetic evidence on the Tanna fault zone in central Japan, *Tectonophysics*, *501*(1-4), 87-97, doi:10.1016/j.tecto.2011.01.016.

Kirschvink, J. L. (1980), The least-squares line and plane and the analysis of paleomagnetic data, *Geophys. J. Roy. Astron. Soc*., *62*(3), 699-718.

Klotz, J., G. Khazaradze, D. Angermann, C. Reigber, R. Perdomo, and O. Cifuentes (2001), Earthquake cycle dominates contemporary crustal deformation in central and southern Andes, *Earth Planet. Sci. Lett*., *193*, 437-446, doi:10.1016/S0012-821X(01)00532-5.

Krawczyk, C., J. Mechie, S. Lueth, Z. Tasarova, P. Wigger, M. Stiller, H. Brasse, H. Echtler, M. Araneda, and K. Bataille (2006), Geophysical signatures and active tectonics at the south-

central chilean margin, in The Andes - Active Subduction Orogeny, vol. 1, edited by O. Oncken et al., pp. 171-192, Springer, New York.

Kus J., M. Block, C. Reichert, J. Diaz Naveas, S. Ladage, and O. Urbina, SO161-cruise participants (2006), NW-SE structural segmentation of the south-central Chilean offshore forearc area between 35°S and 40°S, *Marine Geology*.

Lamb, S. H. (1987), A model for tectonic rotations about a vertical axis, *Earth Planet. Sci. Lett*., *84*(1), 75-86, doi:10.1016/0012-821X(87)90178-6.

Lange, D., J. Cembrano, A. Rietbrock, C. Haberland, T. Dahm, and K. Bataille (2008), First seismic record for intra-arc strike-slip tectonics along the Liquiñe-Ofqui fault zone at the obliquely convergent plate margin of the southern Andes, *Tectonophysics*, *455*(1-4), 14-24, doi:10.1016/j.tecto.2008.04.014.

Lara, L., A. Lavenu, J. Cembrano, and C. Rodríguez (2006), Structural control of volcanism in transversal chains: Resheared faults and neotectonics in the Cordón Caulle-Puyehue area (40.5ºS), Southern Andes, *J. Vulcanol. Geotherm. Res*., *158*, 70-86.

Lara, L., C. Rodriguez, H. Moreno, and C. Perez de Arce (2001), Geocronología K-Ar y geoquímica del volcanismo plioceno superior-pleistoceno de los Andes del sur (39º-42ºS), *Rev. geol. Chile*, *28*(1), 67-90. ISSN 0716-0208.

Lara, L., and H. Moreno (2006), Geología del Complejo Volcánico Puyehue-Cordón Caulle, Región de Los Lagos, Mapa Geológico esc 1:50.000, *Ser. Nac. De Geol. y Min*., Santiago de Chile, Chile.

Larson, K., J. Freymueller, and S. Philipsen (1997), Global plate velocities from the Global Positioning System, *J. Geophys. Res*., *102*(B5), 9961-9981.

Lavenu, A., and J. Cembrano (1999), Compressional- and transpressional-stress pattern for Pliocene and Quaternary brittle deformation in fore arc and intra-arc zones (Andes of Central and Southern Chile), *J. Struct. Geol*., 21(12), 1669-1691, doi:10.1016/S0191-8141(99)00111-X.

López-Escobar, L., J. Cembrano, and H. Moreno (1995), Geochemistry and tectonics of the Chilean Southern Andes, *Andean Geol*., *22*(2).

Lüth, S., P. Wigger, and ISSA 2000 Working Group (2003), A crustal model along 39ºS from a seismic refraction profile-ISSA 2000, *Rev. Geol. Chile*, *30*, 83-101.

Maldonado-Koerdell, M. (1966), Geological and geophysical studies in the Gulf of Fonseca-Nicaraguan depression area, Central America, *Canada Geological Survey Paper*, *14*(66), 220-238.

McCaffrey, R. (1992), Oblique plate convergence, slip vectors, and forearc deformation, *J. Geophys. Res. Solid Earth.*, *97*(92), 8905-8915.

McCaffrey, R., P. Zwick, Y. Bock, L. Prawirodirdjo, J. Grenrich, C. Stevens, S. Puntodewo, and C. Subarya (2000), Strain partitioning during oblique plate convergence in northern Sumatra: Geodetic and seismologic constraints and numerical modeling, *J. Geophys. Res*., *105*(B12), 28,363-28,376.

McCaffrey, R. (2002), Crustal block rotation and plate coupling, in Plate Boundary Zones, 30, 101-122, eds. S. Stein and J. Freymueller, AGU Geodynamics Series.

McKenzie, D., and J. Jackson (1983), The relationship between strain rates, crustal thickening, palaeomagnetism, finite strain and fault movements within a deforming zone, *Earth Planet. Sci. Lett*., *65*(1), 182-202, doi:10.1016/0012-821X(83)90198-X.

McKenzie, D., and J. Jackson (1986), A block model of distributed deformation by faulting, *J. Geol. Soc. London*., *143*(2), 349-353, doi:10.1144/gsjgs.143.2.0349.

Melnick, D., and H.P. Echtler (2006), Morphotectonic and geologic digital map compilations of the south-central Andes (36°-42°S). In: Oncken, O., et al. (Ed.), The Andes - Active subduction orogeny: Frontiers in Earth Sciences. Springer-Verlag, Berlin Heidelberg New York, pp. 565-568.

Melnick, D., A. Folguera, and V. A. Ramos (2006b), Structural control on arc volcanism: The Caviahue-Copahue complex, Central to Patagonian Andes transition (38°S), *J. South Am. Earth Sci*., *22*(1-2), 66-88, doi:10.1016/j.jsames.2006.08.008.

Melnick, D., B. Bookhagen, M. R. Strecker, and H. P. Echtler (2009), Segmentation of megathrust rupture zones from fore-arc deformation patterns over hundreds to millions of years, Arauco peninsula, Chile, *J. Geophys. Res*., *114*(B1), B01407, doi:10.1029/2008JB005788.

Melnick, D., F. Charlet, H. P. Echtler, and M. De Batist (2006a), Incipient axial collapse of the Main Cordillera and strain partitioning gradient between the central and Patagonian Andes, Lago Laja, Chile, *Tectonics*, *25*, TC5004, doi:10.1029/2005TC001918.

Melnick, D., M. Sanchez, H. P. Echtler, and V. Pineda (2003), Geología estructural de la Isla Mocha, centro-sur de Chile (38º30'S, 74ºW): Implicancias en la tectónica regional, paper presented at X Congreso Geológico Chileno, *Serv. Nac. de Geol. y Min*., Santiago de Chile, Chile.

Minster, J.B., T.H. Jordan, P. Molnar, and E. Haines (1974), Numerical modelling of instantaneous plate tectonics, *Geophys. J.R. Astron. Soc*., *36*, 541-576.

Minster, J.B., and T.H. Jordan (1978), Present-day plate motions, *Journal of Geophysical Research: Solid Earth*, *83*,(B11), 5331-5354.

Moreno, M., D. Melnick, M. Rosenau, J. Bolte, J. Klotz, H. Echtler, J. Beaz, K. Bataille, J. Chen, M. Bevis, H. Hase and O. Oncken (2011), Heterogeneous plate locking in the South-Central Chile subduction zone: Building up the next great earthquake, *Earth Planet. Sci. Lett.*, 305, 413-424.

Moreno, H., and J. Clavero (2006), Geología del área del Volcán Villarrica, 1:50.000, Carata Geológica de Chile, Serie Geología Básica 98, *Ser. Nac. De Geol. y Min.*, Santiago de Chile, Chile.

Moreno, M.S., J. Klotz, D. Melnick, H. Echtler, and K. Bataille (2008), Active faulting and heterogeneous deformation across a megathrust segment boundary from GPS data, south central Chile (36-39°S), *Geochem. Geophys. Geosyst*., *9*, doi:10.1029/2008GC002198.

Moreno, M.S., J. Bolte, J. Klotz, and D. Melnick (2009), Impact of megathrust geometry on inversion of coseismic slip from geodetic data: application to the 1960 Chile earthquake, *Geophys. Res. Lett*., *36*, doi:10.1029/2009GL039276.

Mpodozis, C., and V. Ramos (1990), THE ANDES OF CHILE AND ARGENTINA, 11.

Murdie, R., D. Prior, P. Styles, S. Flint, R. Pearce, and S. Agar (1993), Seismic responses to ridge-transform subduction: Chile triple junction, *Geology*, *21*(12), 1095-1098, doi:10.1130/0091-7613(1993)021<1095.

Murdie, R.E. (1994), Seismicity and Neotectonics associated with the subduction of an active ocean ridge transform system Southern Chile, PhD thesis, University of Liverpool.

Naranjo J.A., and H. Moreno (1991), Actividad explosiva postglacial en el volcán Llaima, Andes del Sur, *Rev. Geol. Chile*, *18*(1), 69-80.

Naranjo, J.A., and H. Moreno (2004), Pucón town laharic debris-flow hazards from Villarrica volcano, Southern Andes (39,4°S): Causes for different scenarios, in Villarrica Volcano, Southern Andes, Chile, edited by L. Lara and J. Clavero, *Ser. Nac. De Geol. y Min*., Boletín Nº 61.

Nelson, E., R. Forsythe, J. Diemer, M. Allen, and O. Urbina (1993), Taitao ophiolite: A ridge collision ophiolite in the forearc of southern Chile (46°S), *Rev. Geol.Chile*, *20*, 137.

Nelson, E., R. Forsythe, and I. Arit (1994), Ridge collision tectonics in terrane development, *J. South Am. Earth Sci*., *7*(3-4), 271-278, doi:10.1016/0895-9811(94)90013-2.

Nelson, E. P., and R. D. Forsythe (1989), Ridge collision at convergent margins: implications for Archean and post-Archean crustal growth, *Tectonophysics*, *161*(3-4), 307-315, doi:10.1016/0040-1951(89)90161-3.

Nelson, M., and C. Jones (1987), Paleomagnetism and crustal rotations along a shear zone, Las Vegas Range, southern Nevada, *Tectonics*, *6*(1), 13-33.

Nielsen, S. N., and J. Glodny (2009), Early Miocene subtropical water temperatures in the southheast Pacific, *Palaeogeography Palaeoclimatology Palaeoecology*, *280*(3-4), 480-488.

Nur, A., H. Ron, and O. Scotti (1986), Fault mechanics and the kinematics of block rotations, *Geology*, *14*, 746-749, doi:10.1130/0091-7613 (1986)14<746.

Okada, A. (1971), Active faulting of the median tectonic line, Kagaku, *41*, 666-669.

Pardo-casas, F., and P. Molnar (1987), Relative motion of the Nazca (Farallon) and South American plates since Late Cretaceous time, *Tectonics*, *6*(3), 233-248.

Perez, Y., J. Milovic, R.Troncoso, F.Hanish, F. Helms, and M.Toloczky (2003), Geología para el ordenamiento territorial: Área de Osorno, Región de los Lagos, Carta Geológica de Chile, Serie Geológica Ambiental N°6 escala 1:100.000, *Ser. Nac. De Geol. y Min*., Santiago de Chile, Chile.

Piper, J., O. Tatar, and H. Gürsoy (1997), Deformational behaviour of continental lithosphere deduced from block rotations across the North Anatolian Fault Zone in Turkey, *Earth Planet. Sci. Lett*., 150, 191-203.

Plafker, G., and J. Savage (1970), Mechanism of the Chilean earthquakes of May 21 and 22, 1960, *Geol. Soc. Am. Bull*., *81*(4), 1001-1030, doi:10.1130/0016-7606(1970)81.

Porter, S. C. (1981), Pleistocene Glaciation in the Southern Lake District of Chile, *Quaternary Research*, *16*, 263-292.

Quinteros, J., and S. V. Sobolev (2013), Why has the Nazca plate slowed since the Neogene?, *Geology*, *41*(1), 31-34, doi:10.1130/G33497.1.

Randall, K., S. Lamb, and C. Mac Niocaill (2011), Large tectonic rotations in a wide zone of Neogene distributed dextral shear, northeastern South Island, New Zealand, *Tectonophysics*, *509*(3-4), 165-180, doi:10.1016/j.tecto.2011.05.006.

Rehak, K., M. R. Strecker, and H. P. Echtler (2008), Morphotectonic segmentation of an active forearc, 37°-41°S, Chile, *Geomorphology*, *94*(1-2), 98-116, doi:10.1016/j.geomorph.2007.05.002.

Reuther C.D., S. Potent, and R. Bonilla (2003), Crustal stress history and geodynamic processes of a segmented active plate margin: South-Central Chile: the Arauco Bío-Bío trench arc system, paper presented at X Congreso Geológico Chileno, Universidad de Concepción, Chile.

Rojas, C., M. Beck, and R. Burmester (1994), Paleomagnetism of the mid-Tertiary Ayacara Formation, southern Chile: Counterclockwise rotation in a dextral shear zone, *J. South Am. Earth Sci*., *7*(1), 45-56.

Ron, H., R. Freund, Z. Garfunkel, and A. Nur (1984), Block rotation by strike-slip faulting: Structural and paleomagnetic evidence, *J. Geophys. Res*., *89*(B7), 6256-6270.

Rosenau, M. (2004), Tectonics of the southern Andean intra-arc zone (38º-42ºS), PhD thesis, Freie Univ., Berlin.

Rosenau, M., D. Melnick, and H. Echtler (2006), Kinematic constraints on intra-arc shear and strain partitioning in the southern Andes between 38°S and 42°S latitude, *Tectonics*, *25*(4), TC4013, doi:10.1029/2005TC001943.

Ruegg, J.C., A. Rudloff, C. Vigny, R. Madariaga, J. Dechabalier, J. Campos, E. Kausel, S. Barrientos, and D. Dimitrov (2009), Interseismic strain accumulation measured by GPS in south central Chile seismic gap, *Phys. Earth Planet. Inter. 175*(1-2), 78-85, doi:10.1016/j.pepi.2008.02.015.

Saint Blanquat, M., B. Tikoff, C. Teyssier, and J.L. Vigneresse (1998), Transpressional kinematics and magmatic arcs, In: Holdsworth, R. E., Strachan, R. A. and Dewey, J.F. (eds). Continental Transpressional and Transtensional Tectonics, *Geol. Soc. London, Spe. Pub*., *135*, 327-340.

Salyards, S., K. Sieh, and J. Kirschvink (1992), Paleomagnetic measurement of nonbrittle coseismic deformation across the San Andreas fault at Pallett Creek, *J. Geophys. Res*., *97*(B9), 12,457-12,470.

SERNAGEOMIN (2003), Mapa Geológico de Chile: versiòn digital, N°4, CD-ROM version 1.0, *Ser. Nac. De Geol. y Min*, Publicación Geológica Digital, Santiago.

Siame, L. L., O. Bellier, M. Sébrier, and M. Araujo (2005), Deformation partitioning in flat subduction setting: Case of the Andean foreland of western Argentina (28°S-33°S), *Tectonics*, *24*, TC5003, doi:10.1029/2005TC001787.

Singer, B. S., B. R. Jicha, M. A. Harper, J. A. Naranjo, L. E. Lara, and H. Moreno-Roa (2008), Eruptive history, geochronology, and magnetic evolution of the Puyehue-Cordón Caulle volcanic complex, Chile, *Geol. Soc. Am. Bull*., *120*(5-6), 599-618.

Somoza, R. (1998), Updated Nazca (Farallon) -South America relative motions during the last 40 My: implications for mountain building in the central Andean region, *J. South Am. Earth Sci*., *11*(3), 211-215.

Sonder, L., and P. England (1986), Vertical averages of rheology of the continental lithosphere: Relation to thin sheet parameters, *Earth Planet. Sci. Lett*., *77*, 81-90.

Sonder, L., P. England, and G. Houseman (1986), Continuum calculations of continental deformation in transcurrent environments, *J. Geophys. Res*., *91*(B5), 4797-4810.

Sonder, L. J., C. H. Jones, S. L. Salyards, and K. M. Murphy (1994), Vertical axis rotations in the Las Vegas Valley Shear Zone, southern Nevada: Paleomagnetic constraints on kinematics and dynamics of block rotations, *Tectonics*, *13*(4), 769-788, doi:10.1029/94TC00352.

Song, T. A. and M. Simons (2003), Large trench-parallel gravity variations predict seismogenic behavior in subduction zones, *Science*, *301*, 630-633.

Speranza, F., M. Pompilio, F. D'Ajello Caracciolo, and L. Sagnotti (2008), Holocene eruptive history of the Stromboli volcano: constraints from paleomagnetic dating, *J. Geophys. Res. Solid Earth*, *113*(B9), 1978-2012.

Stern, C. R., and M. Vergara (1992), New age for the vitrophyric rhyolite-dacite from Ancud (42oS), Chiloé, Chile, *Rev. Geol. Chile*, *19*(2), 249-251.

Suárez, M., and C. Emparan (1997), Hoja Curacautín, Regiones de la Araucanía y del Biobío, 1:250.000, Carta Geológica de Chile No. 71, *Ser. Nac. De Geol. y Min*., Santiago de Chile, Chile.

Tapponnier, P., and P. Molnar (1976), Slip-line field theory and large-scale continental tectonics, *Nature*, *264*, 319-324.

Tapponnier, P., G. Peltzer, A. Le Dain, R. Armijo, and P. Cobbold (1982), Propagating extrusion tectonics in Asia: New insights from simple experiments with plasticine, *Geology*, *10*, 611-616, doi:10.1130/0091-7613(1982)10<611.

Tašárová, Z. 2004, Gravity data analysis and interdisciplinary 3D modelling of a convergent plate margin (Chile, 36-42°S), PhD thesis, Freie Universität Berlin, http://www.diss.fu-berlin.de/2005/19/indexe.html.

Tassara, A., H.J. Götze, S. Schmidt, and R. Hackney (2006), Three-dimensional density model of the Nazca plate and the Andean continental margin, *J. Geophys. Res*., *111*, B09404, doi:10.1029/2005JB003976.

Tassara, A. 2010, Control of fore-arc density structure on megathrust shear strength along the Chilean subduction zone, *Tectonophysics*, *495*, 34-47.

Tassara, A. and A. Echaurren (2012), Anatomy of the Andean subduction zone: three-dimensional density model upgraded and compared against global-scale models, *Geophysical Journal International*, 189, 161-168.

Taylor, G., J. Grocott, A. Pope, and D. Randall (1998), Mesozoic fault systems, deformation and fault block rotation in the Andean forearc: a crustal scale strike-slip duplex in the Coastal Cordillera of northern Chile, *Tectonophysics*, *299*(1-3), 93-109, doi:10.1016/S0040-1951(98)00200-5.

Thomson, S. N. (2002), Late Cenozoic geomorphic and tectonic evolution of the Patagonian Andes between latitudes 42ºS and 46ºS: An appraisal based on fission-track results from the transpressional intra-arc Liquiñe-Ofqui fault zone, *Geol. Soc. Am. Bull*., *114*(9), 1159-1173, doi:10.1130/0016-7606(2002)114<1159.

Torsvik, T. H., R. D. Müller, R. Van der Voo, B. Steinberger, and C. Gaina (2008), Global plate motion frames: Toward a unified model, *Rev. Geophys*., *46*(3), RG3004, doi:10.1029/2007RG000227.

Vergara, M., and F. Munizaga (1974), Age and evolution of the Upper Cenozoic andesitic volcanism in central-south Chile, *Geol. Soc. Am. Bull*., *85*(4), 603-606, doi:10.1130/0016-7606(1974)85<603.

Vink, G.E., W.J. Morgan, and W.L. Zhao (1984), Preferential rifting of continents: A source of displaced terranes, *Journal of Geophysical Research*, *89*, 10072-10076.

Wallace, L.M., J. Beavan, R. McCaffrey, and D. Darby (2004), Subduction zone coupling and tectonic block rotation in the North Island, New Zealand, *J. Geophys. Res*., *109*, doi:10.1029/2004JB003241.

Wang, K. (1996), Simplified analysis of horizontal stresses in a buttressed forearc sliver at an oblique subduction zone, *Geophys. Res. Lett*., *23*(16), 2021-2024.

Wang, K., Y. Hu, M. Bevis, E. Kendrick, R. Smalley, R. B. Vargas, and E. Lauría (2007), Crustal motion in the zone of the 1960 Chile earthquake: Detangling earthquake-cycle deformation and forearc-sliver translation, *Geochemistry. Geophys. Geosystems*, *8*(10), doi:10.1029/2007GC001721.

Woodcock, N., and M. Fischer (1986), Strike-slip duplexes, *J. Struct. Geol*., *8*(7), 725-735.

Zijderveld, J. D. (1976), A. C. demagnetization of rocks: Analysis of results, in Methods in Paleomagnetism, Dev. in Solid Earth Geophys. vol. 3, edited by D. W. Collinson, K. M. Creer, and S. K. Runcorn, pp. 254-286, Elsevier, New York.

PART IV. Deformation of the Southern Andes since the Cretaceous: constraints from anisotropy of magnetic susceptibility (AMS)

Deformation of the Southern Andes since the Cretaceous: constraints from anisotropy of magnetic susceptibility (AMS)

Marco Maffione[1], Catalina Hernandez Moreno[2], Matias Ghiglione[3], Fabio Speranza[2], Douwe van Hinsbergen[1], Emanuele Lodolo[4]

[1] Department of Earth Sciences, Utrecht University, Utrecht, Netherlands
[2] Istituto Nazionale di Geofisica e Vulcanologia (INGV), Rome, Italy
[3] Instituto de Estudios Andinos ‘‘Don Pablo Groeber’’, Universidad de Buenos Aires-CONICET
[4] Istituto Nazionale di Oceanografia e di Geofisica Sperimentale (OGS), Trieste, Italy

Abstract

The southernmost segment of the Andean chain developed within a highly dynamic and variable tectonic setting, where compressional, extensional and strike-slip tectonics alternated, controlling its evolution from the Cretaceous until the Miocene. Because of these complexities, several points remain poorly constrained, including: (i) the exhumation mechanism of the upper amphibolite facies metamorphic core complex currently exposed in the Cordillera Darwin (Fuegian Andes), and (ii) the relationship between the deformation of the Southern Andes and the origin of the Patagonian Orocline, a regional-scale curved structure characterized by a ~90° interlimb angle. Here, we present new anisotropy of magnetic susceptibility (AMS) data from 22 Upper Cretaceous to Upper Eocene sites within the more internal structural domains of the Magallanes fold-thrust belt in Tierra del Fuego. Our data, combined with the available AMS database, covers the Lower Cretaceous-Early Miocene time interval, and indicate that the Southern Andes underwent continuous compression from the Early Cretaceous until the Late Oligocene. AMS data provide definitive proof for the exhumation of the Cordillera Darwin core complex under a pure compressive tectonic regime. Furthermore, the pattern of magnetic lineation evidences a radial paleostress that has been always perpendicular to the local trend of the chain. Assuming (according to recent paleomagnetic data) the existence of a primary arc since the Middle Paleocene (~60 Ma), we propose that the configuration of pre-existing Jurassic extensional faults at the southern South American continental margin directly controlled the Cenozoic kinematic evolution of the Magallanes fold-thrust belt. Tectonic inversion of these faults into thrusts rooted in the basement during the Late Cretaceous

compressive phase, may have allowed slip partitioning mechanisms that can effectively explain both the current geometry and the kinematic evolution of the Southern Andes.

1. Introduction

The Andean Cordillera is commonly considered the archetype of non-collisional orogens, as it formed by subduction of the oceanic Nazca (and part of the Antarctica) plate below South America [*Jordan et al*., 1993; *Ramos*, 1999; among many others]. Increased westward motion of the South American plate, combined with intense magmatism in the upper plate above the subduction zone resulted in extensive deformation and uplift along the western edge of continental margin [*Pilger*, 1984; *Allmendinger et al*., 1997; *Somoza*, 1988; *Cobbold et al*., 2007; *Somoza & Ghidella*, 2005, 2012]. The result of this process is a gigantic orogenic system, 200 to 700 km wide, spanning the entire South American continent from ~7°N to ~56°S latitude.

The current tectonic setting of the Andes is relatively simple and characterized by mainly eastward verging thrusts, which also involve the basement (i.e. thick-skinned tectonics). In the central and southern part of the chain, two regional-scale orogenic arcs are present, identified by a sharp deviation of the structural trend of the orogen. The northern arc (14°-26°S latitude), known as the Bolivian Orocline [e.g., *Isacks*, 1988], is a relatively "open" orocline characterized by an interlimb angle of ~120°. The change in structural trend, NW in the northern segment and NNE in the southern segment, is reflected by a paleomagnetically-constrained rotation of the two limbs: clockwise (CW) in the southern segment and counterclockwise (CCW) and northern segment [*Maffione et al*., 2009 and references therein; *Prezzi et al*., 2014]. Rotations were coeval with the eastward propagation of the orogenic front and define the Bolivian Orocline as a 'progressive orocline' [*sensu* Weil and Sussman, 2004].

Both the kinematic and style of deformation associated to the evolution of the Bolivian Orocline are relatively well constrained. In contrast, more controversial is the tectonics and style of deformation that controlled, at the southern edge of the Andean chain (Chile and Tierra del Fuego) the origin of the orogenic re-entrant known as the Patagonian Orocline [e.g., *Carey*, 1958] (Figure 1). Here, the ~NS trending Patagonian Andes and the ~EW trending Fuegian Andes defines an arc characterized by an interlimb angle of ~90°. Source of uncertainty in the tectonic evolution of this region is a complex geodynamic setting, where the interplay of two continental plates (South America and Antarctica) and two oceanic plates (Scotia and Nazca) through time yielded alternation of extensional, strike slip, and compressive events [e.g., *Klepeis and Austin*, 1997].

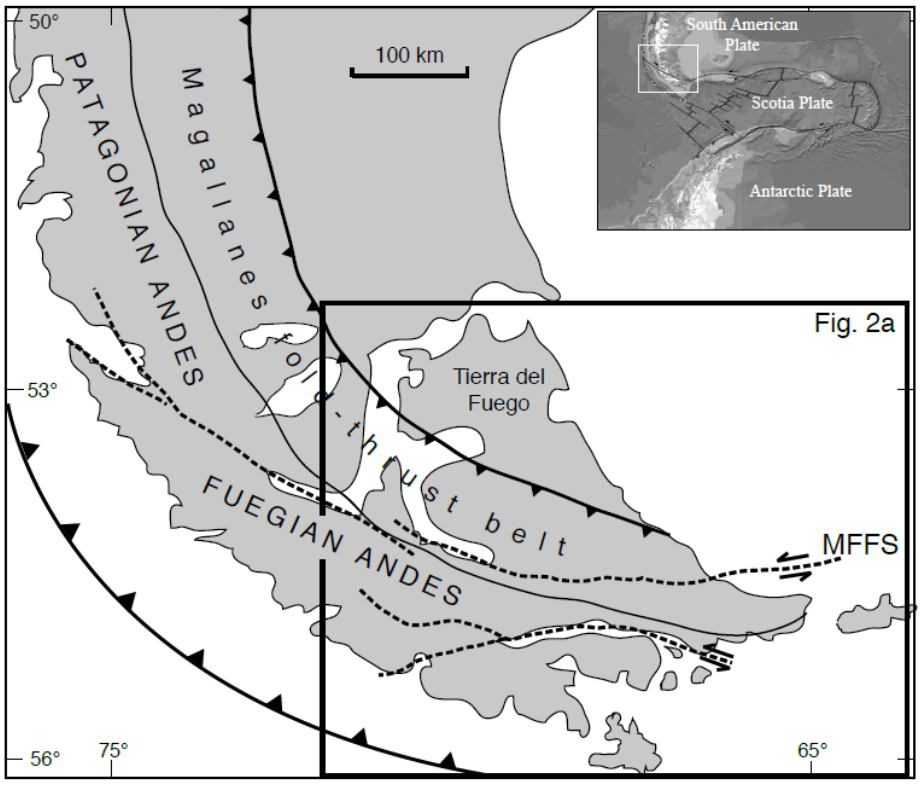

Figure 1. Simplified tectonic setting of the Southern Andes showing the main tectonic features and structural domain.

Tectonic models put forward to explain the formation of the Patagonian Orocline consider either a main contribution of strike slip tectonics [e.g., *Cunningham*, 1993], or pure compressive events associated to the initial stages of the Andean orogeny [*Kraemer*, 2003; *Ghiglione and Cristallini*, 2007]. More recently, the primary origin of the orocline has also been proposed [*Ramos and Aleman*, 2000; *Diraison et al*., 2000]. Distinctive of this complex, poorly defined tectonic scenario, is the nature of the Cordillera Darwin metamorphic core complex (herein referred to as CDCC) exposed along the hinge of the Patagonian Orocline at ~55°S latitude (Figure 1). Although several Paleozoic to Mesozoic metamorphic core complexes are present in the Patagonian Andes [e.g., *Hervé et al*., 2008], the CDCC is the one showing the most controversial tectonic setting [*Dalziel and Brown*, 1989; *Kohn et al*., 1995; *Cunningham*, 1995; *Klepeis* 1994; *Maloney et al*., 2011]. Cordillera Darwin exposes tectonically denudated Paleozoic continental basement rocks (Middle-Upper Jurassic granite and orthogneisses, Upper Jurassic rhyolitic volcanics, and Late Jurassic mafic dikes) metamorphosed under upper amphibolite to greenschist facies (7-11 kbar, 580-600°C) [*Nelson et al*., 1980; *Kohn et al*., 1993, 1995; *Klepeis et al*., 2010]. *Kohn et al*. (1995) proposed an initial rapid exhumation of the CDCC at 90-70 Ma driven by extension (or transtension), while more external sectors were under compression. Similarly, *Delziel and Brown* [1989] argued the uplift of the CDCC began at ~70 Ma in a localized extensional setting within the developing

transform zone between the South American and Antarctic plates. On the other hand, several models were proposed by *Cunningham* [1995] who related the exhumation of the CDCC to (i) erosional denudation within a restraining bend setting, (ii) trasntension, or (iii) isostatic rebound due to slab breakoff. The most popular model for the uplift of the CDCC requires thick-skinned compressional mechanisms coupled with widespread erosion [*Klepeis*, 1994; *Klepeis and Austin*, 1997; *Gombosi et al*., 2009; *Barbeau et al*., 2009; *Klepeis et al*., 2010; *Maloney et al*., 2011; *Torres Carbonell and Dimieri* 2013].

Analyzing the stress regime at the southernmost Andes during the early (Late Cretaceous-Paleocene) orogenic phases is therefore key to contribute to the most hotly debated issues on the tectonic evolution of this area. Previous reconstructions of the tectonic history of the Southern Andes used kinematic analysis of structures preserved in the Magallanes fold-thrust belt of Tierra del Fuego (Argentina) [*Torres-Carbonell et al*., 2008, 2013; *Torres-Carbonell and Dimieri*, 2013]. While these studies provided relatively precise description of the main compressive events that led to the formation of the Magallanes fold-thrust belt [*Alvarez- Marrón et al*., 1993; *Ghiglione et al*., 2002; *Ghiglione and Ramos*, 2005; *Torres-Carbonell et al.*, 2008, 2011], the exact age of the first tectonic pulse still remains poorly constrained due to the paucity of kinematic constraints available from the most internal domains of the belt exposing the oldest sedimentary units. So far, major folding affecting the Maastrichtian-Danian Policarpo Formation [*Olivero and Malumián*, 1999], as well as older units of the Austral foreland basin (i.e., Turonian-Campanian Punta Barrosa Fm. (also called "Estratos de Buen Suceso") and Bahia Thetis formation) has been attributed to an early deformation event occurring during the Mid-Late Paleocene [*Ghiglione and Ramos* 2005]. Only recently, *Torres-Carbonell et al*. [2013] interpreted the presence of pencil structures associated to layer-parallel shortening within the Policarpo Fm. as the result of an earlier (Danian or even younger) compressive event. Large uncertainties, therefore, still exist on the nature and style of the tectonics affecting the Southern Andes during the Upper Cretaceous-Lower Paleocene (i.e., during the main exhumation phase of the CDCC).

In this study, we define the nature and orientation of the paleostress field at the Southern Andes from the Cretaceous throughout the Oligocene by using new and published anisotropy of magnetic susceptibility (AMS) data from the Magallanes fold-thrust belt. Results are then discussed within the framework of the existing tectonic models for the exhumation of the CDCC and the deformation mechanisms associated to the evolution of the Patagonian Orocline.

2. Background

Four tectonic provinces can be recognized in the Fuegian Cordillera, from SW to NE: (i) a coastal magmatic arc, including a calc-alkaline igneous suite (Patagonian batholith) emplaced between the Late Jurassic and Neogene [*Rolando et al*., 2002; *Hervé et al*., 2007]; (ii) Rocas Verdes marginal basin units including weakly metamorphosed relics of the oceanic floor (Sarmiento Ophiolite; [*Allen*, 1982, 1983; *Cunningham* 1994]) and sedimentary cover [*Fildani and Hessler*, 2005; *Olivero and Malumián*, 2008]; (iii) a metamorphic core zone exposing Paleozoic basement schists at the Cordillera Darwin and characterized by thick-skinned shortening [*Kohn et al*., 1995; *Klepeis*, 1994; *Hervé et al*., 2010; *Klepeis et al*., 2010; *Maloney et al*., 2011, 2013]; and (iv) a thin-skinned Magallanes fold-thrust belt, developed within a ~7 km thick foreland (Austral) basin containing Upper Cretaceous to Miocene marine sequences [*Biddle et al*., 1986; *Alvarez-Marrón et al*., 1993; *Klepeis*,1994; *Olivero and Malumián*, 1999; *Olivero and Martinioni*, 2001; *Olivero et al*., 2001, 2003; *Ghiglione et al*., 2002; *Ghiglione and Ramos*, 2005; *Malumián and Olivero*, 2006; *Olivero and Malumián*, 2008; *Torres-Carbonell et al*., 2008].

The Magallanes fold-thrust belt in E-W segment of the Patagonian Orocline of Tierra del Fuego is composed of north-vergent thrust sheets that, from south to north, progressively involve younger units: Upper Cretaceous in the hinterland, Lower Middle Eocene in the central domain, and Paleogene to Neogene in the most external sectors [*Olivero and Malumián*, 1999; *Olivero and Martinioni*, 2001; *Ghiglione and Ramos*, 2005; *Menichetti et al*., 2008; *Olivero and Malumián*, 2008]. A Neogene left-lateral Magallanes–Fagnano fault zone cuts the northern domain of the fold-thrust belt along the Irigoyen River, forming a transtensional pull-apart basin [*Ghiglione*, 2003].

The tectonic evolution of the Southern Andes started in the Mid-Late Jurassic with widespread subduction-related plutonism followed by silicic subaerial vulcanism along the present Pacific continental margin, coeval with the extensional tectonic phase associated with Gondwana breakup [*Bruhn et al*., 1978; *Pankhurst et al*., 2000; *Hervé et al*., 2007]. Prolonged extension along the South American margin culminated in the Late Jurassic with the opening of the Rocas Verdes marginal basin [*Katz*, 1973; *Dalziel et al*., 1974; *Bruhn and Dalziel*, 1977; *Bruhn et al*., 1978; *Andrews-Speed*, 1980; *Dalziel*, 1981; *Fildani and Hessler*, 2005; *Klepeis et al*., 2010]. This extensional phase also affected more internal sectors of the South American craton, yielding widespread normal faults that are believed to have controlled both the syn-tectonic sedimentation and subsequent foreland propagation of the deformation [*Winslow*, 1981; *Corbella et al*., 1996; *Fosdick et al*., 2011; *Likerman et al*., 2013]. The first sedimentary infill of the marginal basin is represented by the Upper Jurassic to Lower Cretaceous volcaniclastic Tobifera (or Lemaire) and

Yahgan (Zapata) Formations, followed by slope mudstones of the Beauvoir Formation [*Wilson*, 1991; *Fildani and Hessler*, 2005; *Olivero and Malumián*, 2008; *Klepeis et al*., 2010].

In the Early Cretaceous, plate reorganization induced acceleration of the spreading rates in the South Atlantic Ocean, increasing of the subduction rates along the Pacific margin [*Rabinowitz and LaBrecque*, 1979; *Dalziel*, 1986; *Ramos*, 1989; *Diraison et al*., 2000; *Somoza and Zaffarana*, 2008], likely triggering a sinistral transpression between South America and Antarctica [*Cunningham et al*., 1995; *Klepeis*, 1994]. This event caused tectonic inversion (i.e., extension to compression) in the retro-arc region that was accommodated by trench-ward underthrusting of the South American craton down to ~35 km depth and first obduction of the oceanic floor [*Bruhn*, 1979; *Wilson*, 1991; *Klepeis et al*., 2010]. Closure of the Rocas Verdes basin marked the actual onset of Andean orogeny and yielded ductile deformation, isoclinal folding and low-grade metamorphism of the marginal basin sedimentary fill [*Bruhn*, 1979], and peak metamorphism at upper amphibolite facies conditions (7-11 kbar and 580–600°C; *Kohn et al*. [1993]) of the Paleozoic basement currently composed at the CDCC [*Klepeis et al*., 2010; *Maloney et al*., 2011]. Early $^{40}Ar/^{39}Ar$ and fission–track thermochronology data constrained the cooling and uplift of the CDCC at two main tectonic pulses at 90-70 Ma and 60-40 Ma [*Nelson*, 1982; *Kohn et al*., 1995]. More recently, *Gombosi et al*. [2009] obtained new apatite and zircon fission-track and (U-Th-Sm)/He ages indicating rapid uplift occurring not earlier than the Middle-Late Eocene (40-35 Ma), followed by slower exhumation rates.

U-Pb age on detrital zircons from the first foreland deposits (Punta Barrosa Formation, or "Estratos de Buen Suceso") constrain the beginning of the contractional tectonics in the Southern Andes to the Turonian (92 ± 1.0 Ma; Fildani et al., 2003), with incipient thrusting likely active as early as the Albian (101 Ma; e.g., *Fosdick et al*. [2011]). Closure of the marginal basin and collision between the Jurassic volcanic arc and the continental margin was completed by the Late Cretaceous [*Halpern and Rex*, 1972; *Bruhn and Dalziel*, 1977; *Cunningham*, 1994; 1995; *Diraison et al*., 2000].

Progressive crustal thickening continued in the hinterland of the Fuegian Cordillera throughout the Late Cretaceous, yielding lithospheric loading and flexural subsidence in the Magallanes (or 'Austral') and Malvinas foreland basins [*Winslow*, 1981; *Biddle et al*., 1986; *Ramos*, 1989; *Wilson*, 1991; *Grunow et al*., 1992; *Alvarez- Marrón et al*., 1993; *Klepeis*, 1994; *Coutand et al*., 1999; *Fildani et al*., 2003]. Sedimentation in the Magallanes foreland basin was synchronous with the northward propagation of the compressive fronts [*Alvarez-Marrón et al*., 1993; *Olivero and Malumián*, 2008; *Ghiglione and Ramos*, 2005; *Torres-Carbonell et al.*, 2008, 2011, 2013; *Torres-Carbonell and Dimieri*, 2013]. The first compressive episode in the Magallanes foreland basin

produced a regional unconformity between the Maastrichtian-Danian Policarpo Fm. and the overlying Selandian to Ypresian Rio Claro Group (e.g., *Olivero et al*. [2003]), and has been constrained by *Ghiglione et al*. [2005] to the mid-late Paleocene (San Vicente thrusting episode, 61-55 Ma). More recently, *Torres-Carbonell et al*. [2013, 2014] proposed the earliest compressive event in the Magallanes foreland basin to be not younger than the Danian (> 61.7 Ma), based on layer-parallel shortening-related pencil structures recognized within the Policarpo Fm. in Tierra del Fuego. These authors relate this early compressive event to the first pulse of uplift of the central belt (CDCC).

The Rio Claro Group is composed from bottom to top of the following formations: Tres Amigos (upper Paleocene), Cabo Leticia (Paleocene), La Barca (upper Paleocene), Punta Noguera (uppermost Paleocene – lowermost Eocene), Punta Trorcida (upper Paleocene-lower Eocene), and Cerro Ruperto (lower Eocene). A minor unconformity separates the Rio Claro Group from the Rio Bueno Fm. (lower mid Eocene), which is in turn unconformably covered by the La Despedida Group (mid-upper Eocene), composed of the Leticia (upper mid Eocene) and Cerro Colorado (upper middle to upper Eocene) Fms. This last unconformity marks the Rio Bueno thrusting event (49-34 Ma; *Ghilgione and Ramos* [2005]). Another minor unconformity is observed in this group and at its top, just below the subsequent sub-horizontal foreland strata of the Cabo Domingo Group (Oligocene-Miocene). The Punta Gruesa sinistral strike-slip event (ca. 24-16 Ma) defines the final tectonic phase associated to the development of the Magallanes-Fagnano fault system (MFFS; Figure 1) [*Cunningham*, 1993, 1995; *Lodolo et al*., 2003; *Eagles et al*., 2005; *Rossello*, 2005]. Then, virtually undeformed post-early Miocene units testify the end of shortening in the southern Magallanes basin [*Ghiglione*, 2002; *Ghiglione et al*., 2002].

3. Anisotropy of magnetic susceptibility (AMS): methodology

AMS is a petrofabric tool to determine the preferred orientation of dominant minerals, and it is commonly used as a paleostress indicator [*Jelinek*, 1977, 1978; *Hrouda*, 1982; *Borradaile*, 1988, 1991; *Jackson*, 1991; *Jackson and Tauxe*, 1991; *Rochette et al*., 1992; *Tarling and Hrouda*, 1993; *Sagnotti et al*., 1994, 1998; *Borradaile and Henry*, 1997; *Parés et al*., 1999; *Borradaile and Jackson*, 2004, 2010; *Soto et al*., 2009]. In weakly deformed (non-metamorphic) sedimentary rocks, AMS reflects the pristine fabric produced during incipient deformation at the time of, or shortly after, deposition and diagenesis of the sediment [*Sintubin*, 1994; *Mattei et al*., 1995; *Sagnotti et al*., 1998, 1999; *Parés et al.*, 1999; *Coutand et al*., 2001; *Cifelli et al*., 2004, 2005; *Soto et al*, 2009]. For this reason AMS analysis of weakly deformed sediments have frequently been used in orogenic settings to document the syn-sedimentary tectonic regime [*Mattei et al*., 1999; *Sagnotti and*

Speranza, 1993; *Sagnotti et al*., 1998; *Parés et al*., 1999; *Maffione et al*., 2008, 2012; *Macrì et al*., 2014].

AMS can be described geometrically by an ellipsoid whose axes are the minimum (k_{min}), intermediate (k_{int}), and maximum (k_{max}) axis of susceptibility [*Hrouda*, 1982]. During deposition, sedimentary rocks acquire a so-called 'sedimentary fabric' characterized by the k_{max} and k_{int} axes dispersed within a plane (magnetic foliation (F)) that is sub-parallel to the stratification plane. This sedimentary fabric can be partially overprinted by a 'tectonic fabric' during incipient deformation (e.g., *Parés et al*. [1999]). The result of this process is the development of a magnetic lineation (L) whereby k_{max} aligns parallel to the maximum axis of stretching (ε_1), hence perpendicular to the maximum axis of compression (σ_1). This mechanism allows a direct correlation between the AMS and strain ellipsoids (e.g., *Parés et al*. [1999]).

In extensional settings, the magnetic lineation coincides with the local dip of the bedding, and is therefore perpendicular to the local normal fault planes [*Sagnotti et al*., 1994; *Mattei et al*., 1997, 1999; *Cifelli et al*., 2004, 2005; *Maffione et al*., 2012]. In compressional settings, the magnetic lineation is usually subhorizontal and parallel to both the local strike of the strata and the folds axes [*Sagnotti and Speranza* 1993; *Mattei et al*., 1997; *Sagnotti et al*., 1998; *Maffione et al*., 2008]. The relationship between the direction of the magnetic lineation and that of the local structure of the rock is therefore diagnostic to distinguish between a compressional and extensional tectonic magnetic lineation (e.g., *Mattei et al*., [1997]).

Increasing deformation progressively modifies the shape of the AMS ellipsoid from a pure sedimentary fabric (oblate ellipsoid: $k_{max} \approx k_{int} >> k_{min}$), to a sedimentary fabric with a marked tectonic imprint (triaxial ellipsoid: $k_{max} > k_{int} > k_{min}$), to a tectonic fabric (prolate ellipsoid: $k_{max} >> k_{int} \approx k_{min}$), and eventually returning during the highest strain to an oblate ellipsoid with the magnetic foliation parallel to the cleavage/schistosity (e.g., Parés, 2004). Such a progression can be observed i.e. from the external towards the internal domains of a foreland fold-thrust belt (e.g., *Parés et al*. [1999]). In the last stage of deformation, which corresponds to incipient metamorphism, the pristine tectonic fabric developed during the initial (syn-sedimentary) phases of deformation is completely obliterated. Conversely, the pristine tectonic fabric is not easily overprinted by small strains at low temperature (e.g., *Borradaile*, 1988; *Sagnotti et al*., 1994, 1998; *Cifelli et al*., 2004, 2005; *Parés*, 2004; *Larrasoaña et al*., 2004; *Soto et al*., 2009]. This implies that, compared to classical structural geological analysis where the definition of the age of deformation requires additional constraints (i.e., crosscutting relationships or unconformities), the finite strain determined from AMS analyses of weakly deformed rocks is a direct and powerful tool that can be used to study the deformation active at the time of sedimentation.

4. Previous AMS studies from the Southern Andes

AMS data from the Southern Andes are relatively scarce compared to other, more extensively studied orogens. Two studies have been carried out in the most internal metamorphic domains of the belt. In one of them, *Rapalini et al*. [2005] collected 96 samples from 12 sites from the metamorphosed Upper Jurassic-Lower Cretaceous Lemaire and Yahgan formations within the Fuegian Andes of Tierra del Fuego. The magnetic foliation of these rocks resulted always parallel to the local foliation/cleavage, confirming a tectonic origin of the AMS and a complete overprint of the pristine tectonic fabric. A N-NE-directed magnetic lineation coincident with the mineralogical lineation is parallel to the local shear sense along thrust faults [*Diraison et al*., 2000] and is probably the result of the compressive phase that affected this area. In a more recent study, *Esteban et al*. [2011] collected additional samples (240 cores from 27 sites) mainly from the Lemaire Fm. within the same area investigated by *Rapalini et al*. [2005], obtaining similar results.

A larger number of data is available from the non-metamorphic sedimentary units of the Magallanes fold-thrust belt. One of the earliest AMS works in this region was carried out by *Diraison* [1978] who collected 210 samples at 16 Upper Cretaceous to Cenozoic sites throughout the Patagonian and Fuegian Andes. More specifically, eight sites exposing Eocene-Miocene rocks within the most external sectors of the eastern part of the fold-thrust belt in Tierra del Fuego; four Upper Cretaceous-Paleocene sites were sampled within the axial part of the Patagonian Orocline; and four Albian-Santonian sites were samples within the N-S trending segment of the Patagonian Andes. The magnetic fabric of the sampled units is predominantly sedimentary (i.e., oblate AMS ellipsoid with magnetic foliation parallel to the strata), with a tectonic imprint that is more evident in the oldest Mesozoic units characterized by a well-defined magnetic lineation. Triaxial AMS ellipsoids are documented at only two sites. The magnetic lineation of these rocks, restored to its original in situ coordinates, is generally sub-horizontal and sub-parallel to the local strike of the strata and fold axes, consistently with a compressive origin of the lineation.

AMS results reported by *Maffione et al*. [2010] from 20 Upper Eocene-Lower Miocene sites within the external domains of the eastern Magallanes fold-thrust belt of Tierra del Fuego (north of the Magallanes-Fagnano fault system, documented a predominant sedimentary fabric with triaxial AMS ellipsoids characterized by magnetic foliations generally sub-parallel to the strata. Well-defined magnetic lineations at 16 sites are ca. E-W trending and parallel to both the local strike of the rocks and fold axes, implying a tectonic, compressive origin of the lineation. These authors concluded a ~N-S shortening characterized the northward propagation of the thrust sheets in the external domains of the eastern Magallanes fold-thrust belt since the Early Eocene.

A large AMS dataset has been recently published by *Poblete et al*. [2014] who sampled 85 Cretaceous to Miocene sites within the sedimentary cover of the Magallanes fold-thrust belt at the foothills of the Patagonian and Fuegian Andes. AMS results from the Fuegian Andes were obtained from Upper Cretaceous to Miocene formations. The magnetic fabric of the units within the external sectors of the belt is predominantly sedimentary (i.e., oblate AMS ellipsoid), whereas it is clearly tectonic (i.e., triaxial to prolate AMS ellipsoid) at sites located within the central and internal domains. Sixteen Upper Cretaceous to Lower Paleocene sites in the most internal domain of the belt show both oblate and prolate fabric with a well-defined shallowly plunging magnetic lineation. Eight sites from the Upper Cretaceous Cerro Matrero Fm. show a macroscopic cleavage produced under relatively high degrees of deformation. The magnetic fabric of those sites is characterized by a predominantly oblate AMS ellipsoid with a lineation that at five sites is moderately plunging and forming a significant angle (10-30°) with the strike of the strata. At the remaining three sites the lineation is sub-horizontal and parallel to the local strike of strata. While the lineation at the three sites with sub-horizontal lineation indicate a compressive origin of the AMS, we believe that the anomalous lineation at the other five sites is the result of a high deformation that completely overprinted the pristine fabric. At the remaining eight Campanian-Danian and Lower Paleocene sites within the Cerro Cuchilla and Cabo Nariz formations the fabric is predominantly prolate, suggesting a relatively high degree of deformation. The magnetic lineation at those sites is generally shallowly plunging and sub-parallel to the strike of the strata, indicating a consistent compressive tectonic origin of the lineation. The overall NNW orientation of the magnetic lineation indicate a mainly ca. N-S compressional regime controlling the early stage evolution of the Magallanes fold-thrust belt.

5. Sampling and methods

Paleomagnetic samples were collected from Upper Cretaceous to Middle-Upper Eocene sedimentary rocks exposed in the most internal domains of the Magallanes fold-thrust belt south of the strike-slip MFFS, along the Atlantic coast of the Mitre Peninsula (Figures 1 and 2). The sampled rocks are folded and faulted, but they do not show evidence of metamorphism or pervasive cleavage. A total of 286 cores where drilled at 22 sites distributed within five different formations (Figure 2).

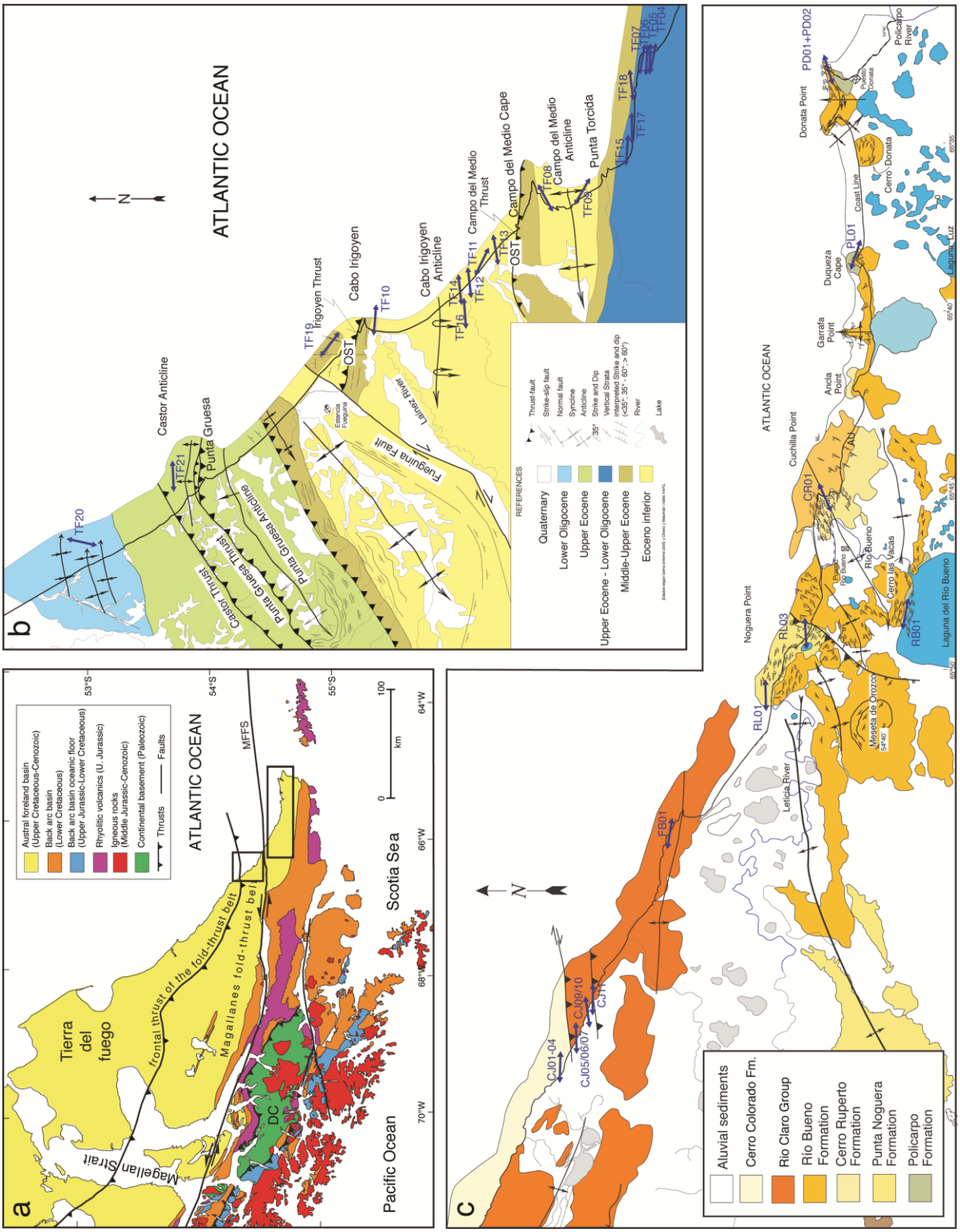

Figure 2. a) Regional geological map of the Fuegian Andes showing the main tectono-stratigraphic domains. CD, Cordillera Darwin. MFFS, Magallanes Fagnano Fault System. b, c) Geological maps of the two sampling areas south of the strike-slip Magallanes Fagnano Fault system.

Five sites were collected from the Maastrichtian-Danian Policarpo Fm. (>700 m thick) represented by highly bioturbated dark slaty mudstones and sandstones deposited in the earliest, innermost Bahía Tethis foreland depocenter [*Olivero and Malumián*, 1999; *Martinioni et al*., 1999]. This formation is overthrust in the south by the pervasively cleavaged Upper Campanian-Lower Maastrichtian Bahia Tethis Fm., and, at the sampling locality, it is unconformably covered by the Rio Bueno Fm. Eight sites were drilled within the Upper Paleocene La Barca Fm. (220 m thick), composed of tuffaceous sandstones and siltstones, and black mudstones. Three sites were sampled from the Upper Paleocene-Lower Eocene Punta Noguera Fm. (380 m thick), consisting of glauconitic gravity flows deposits, including massive tuffaceous sandstones and turbidites. One site was drilled within the Lower-Mid Eocene rhythmically bedded grainstones of the Río Bueno Fm. (60-80 m thick). Five sites were sampled within the Mid-Upper Eocene dark gray mudstones of the Cerro Colorado Fm. (855 m thick).

Samples were drilled in the field with a petrol-powered portable drill cooled by water, and oriented with a magnetic compass, which was corrected for the local magnetic declination (11ºE at the time of sampling). Low-field AMS was measured with a Multi-Function kappabridge (MFK1-FA, AGICO) at the Paleomagnetic laboratory of the Istituto Nazionale di Geofisica e Vulcanologia (INGV, Rome, Italy). The AMS parameters at both the specimen and the site levels were evaluated according to *Jelinek* [1977, 1978] using Anisoft 4.2 software (AGICO).

6. Results

A well-defined magnetic fabric characterizes 21 sites (site RL02 shows an isotropic fabric) (Figure 3 and Table 1). The site mean susceptibility (k_m) varies between 1.24 and 4.13 x 10^{-4} SI (with more frequent values in the range of 1.2-3.2 x 10^{-4} SI) (Figure 4a; Table 1). These are typical values for clay-rich sediments where the magnetic anisotropy is mainly controlled by the phyllosilicate paramagnetic matrix [*Rochette*, 1987; *Borradaile et al*., 1987; *Hrouda and Jelinek*, 1990]. The site mean anisotropy degree (*P'*) is commonly low (< 1.120), with most of the sites showing a mean P' values lower than 1.070 (Figure 4b; Table 1). Figure 4b show a clear direct correlation between k_m and P', suggesting that the increase of anisotropy degree is controlled by the different concentration of the ferromagnetic minerals rather then by the degree of strain of the rock.

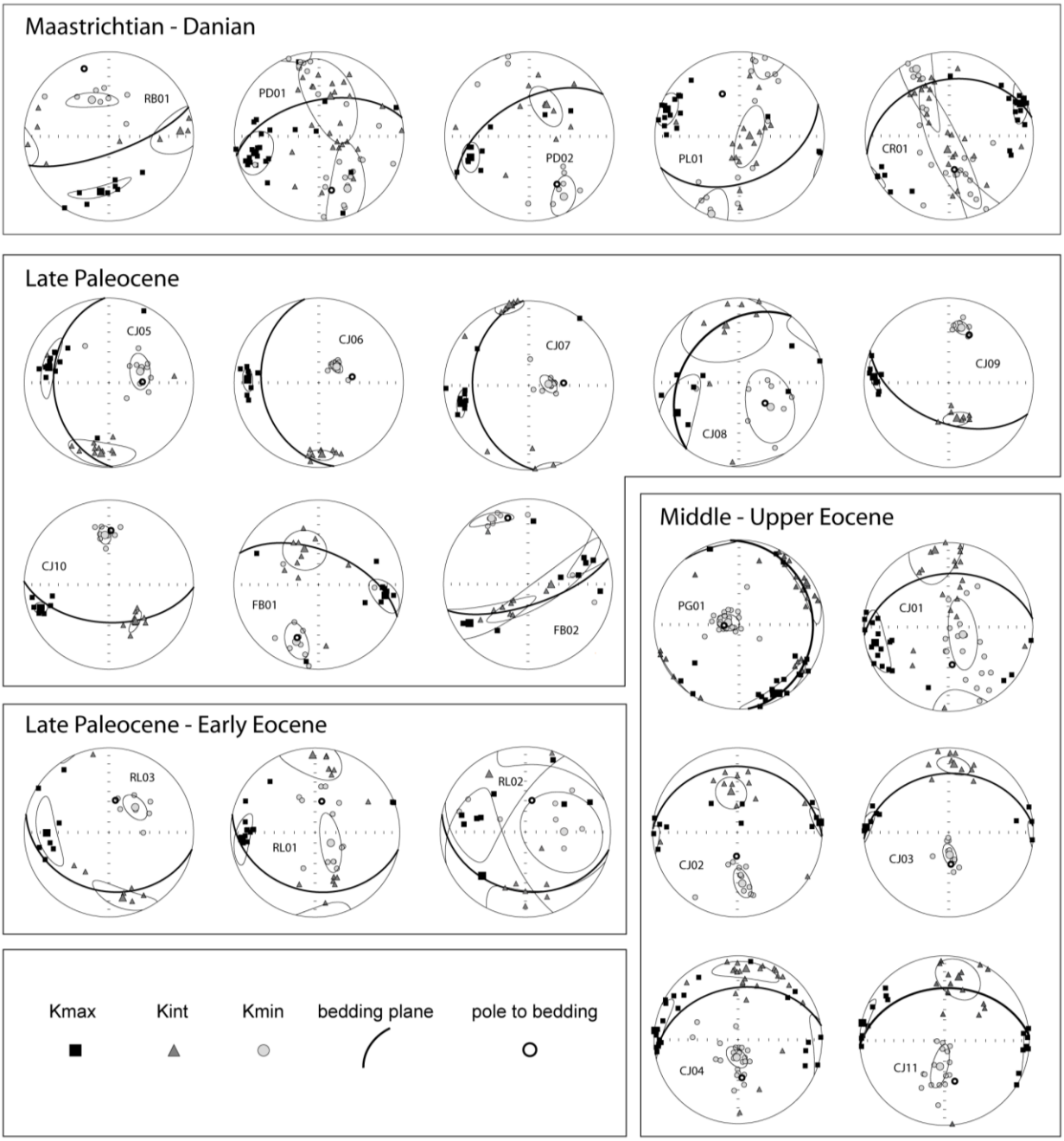

Figure 3. Schmidt equal-area projections, lower hemisphere, of the (in-situ coordinates) principal axes of the AMS ellipsoid and their respective 95% confidence ellipse, for all sampled sites grouped by age.

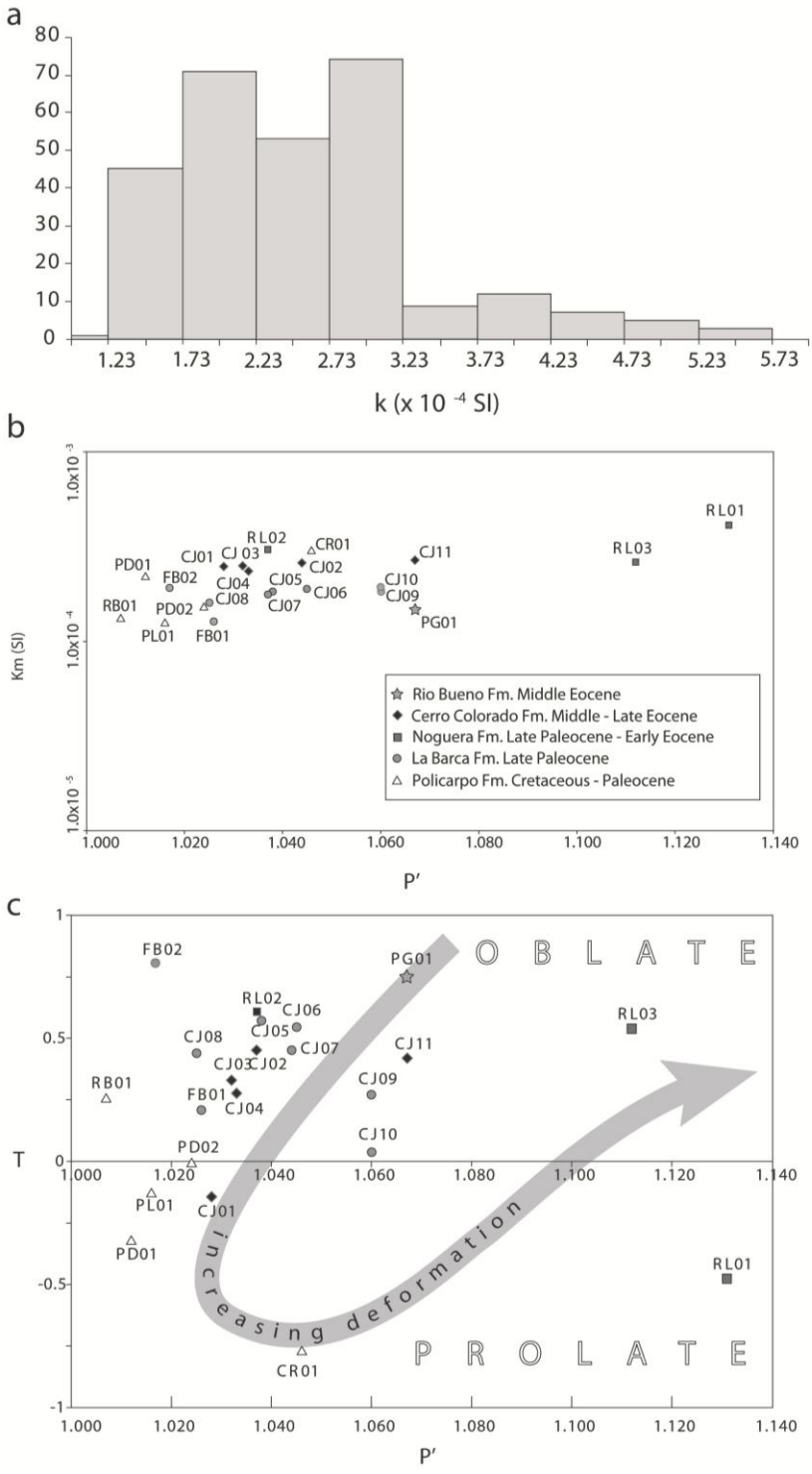

Figure 4. a) Frequency distribution of the magnetic susceptibility (k) from all the sampled specimens; b) Site mean susceptibility versus corrected anisotropy degree (P') for all the sampled sites; c) Shape factor (T) versus corrected anisotropy degree (P') diagram compared to the typical trend expected from increasing deformation degrees.

Table 1. Anisotropy of magnetic susceptibility results from the internal domains of the Magallanes fold-thrust belt.

Site	Formation	Latitude	Longitude	Age	Bedding (Strike/Dip)	N	k_m	L	F	P'	T	D (°)	I (°)	e_{12} (°)	AMS origin
RB01	Policarpo	54° 40' 30.66"	65° 48' 39.13"	Maastr. – Danian	092/74	9	1.33	1.002	1.004	1.007	0.256	189.9	34.8	34.2	T ?
PD01	Policarpo	54° 38' 57.77"	65° 33' 15.85"	Maastr. – Danian	257/55	25	2.19	1.008	1.004	1.012	-0.320	255.9	23	22.9	T, c
PD02	Policarpo	54° 39' 3.83"	65° 33' 24.51"	Maastr. – Danian	240/55	10	1.53	1.012	1.012	1.024	-0.005	250.4	27.1	13.4	T, c
PL01	Policarpo	54° 39' 30.58"	65° 38' 30.23"	Maastr. – Danian	68/45	16	1.24	1.009	1.007	1.016	-0.130	290.5	9.1	12.6	T, c
CR01	Policarpo	54° 39' 06.19"	65° 45' 14.84"	Maastr. – Danian	257/34	22	3.00	1.037	1.005	1.046	-0.775	65.3	6.8	17.6	T, c
CJ05	La Barca	54° 35' 25.24"	66° 00' 43.60"	U. Paleocene	177/35	12	1.84	1.008	1.028	1.038	0.575	284.5	27.6	26.0	T, c
CJ06	La Barca	54° 35' 26.72"	66° 00' 41.57"	U. Paleocene	170/33	9	1.89	1.009	1.033	1.045	0.550	272.3	17.0	9.2	T, c
CJ07	La Barca	54° 35' 27.43"	66° 00' 38.49"	U. Paleocene	176/34	11	1.77	1.010	1.026	1.037	0.456	255.2	18.8	12.0	T, c
CJ08	La Barca	54° 35' 28.16"	66° 00' 35.47"	U. Paleocene	218/34	8	1.60	1.007	1.018	1.025	0.443	243.9	19.9	40.8	T, c
CJ09	La Barca	54° 35' 30.87"	66° 00' 21.37"	U. Paleocene	112/51	8	1.93	1.021	1.037	1.060	0.273	274.6	12.3	13.5	T, c
CJ10	La Barca	54° 35' 34.58"	66° 00' 03.13"	U. Paleocene	092/53	8	1.85	1.028	1.031	1.060	0.044	251.1	16.0	8.1	T, c
FB01	La Barca	54° 36' 38.78"	65° 54' 54.16"	U. Paleocene	292/57	10	1.27	1.010	1.016	1.026	0.213	99.2	21.1	21.0	T, c
FB02	La Barca	54° 36' 35.37"	65° 56' 43.11"	U. Paleocene	072/77	9	1.93	1.001	1.014	1.017	0.806	236.6	18.2	72.0	S
RL01	Punta Noguera	54° 38' 23.98"	65° 50' 59.09"	U. Paleoc. - L. Eoc.	102/31	9	4.13	1.092	1.032	1.131	-0.472	264.8	11.8	22.3	T, c
RL02	Punta Noguera	54° 38' 53.53"	65° 49' 13.70"	U. Paleoc. - L. Eoc.	102/31	8	3.05	-	-	-	-	-	-	-	no AMS
RL03	Punta Noguera	54° 38' 53.53"	65° 49' 13.70"	U. Paleoc. - L. Eoc.	102/31	7	2.63	1.023	1.081	1.112	0.544	269.5	27.5	30.6	T, c
PG01	Rio Bueno	54° 39' 43.59"	65° 40' 19.30"	M. Eocene	354/4	24	1.48	1.007	1.053	1.067	0.753	150.0	7.1	30.3	S
CJ01	Cerro Colorado	54° 35' 11.59"	66° 01' 46.03"	M. – U. Eocene	264/37	19	2.48	1.016	1.012	1.028	-0.139	257.9	12.5	24.5	T, c
CJ02	Cerro Colorado	54° 35' 13.82"	66° 01' 41.81"	M. – U. Eocene	272/23	12	2.60	1.011	1.031	1.044	0.456	83.1	1.7	14.1	T, c
CJ03	Cerro Colorado	54° 35' 15.31"	66° 01' 35.39"	M. – U. Eocene	266/31	10	2.50	1.010	1.021	1.032	0.334	273.5	2.4	13.7	T, c
CJ04	Cerro Colorado	54° 35' 17.27"	66° 01' 25.96"	M. – U. Eocene	260/39	24	2.36	1.012	1.021	1.033	0.282	276.4	0.7	26.9	T, c
CJ11	Cerro Colorado	54° 35' 37.89"	65° 59' 44.66"	M. – U. Eocene	267/38	16	2.68	1.018	1.046	1.067	0.423	282.2	1.1	19.2	T, c

Table 1. Geographic coordinates use WGS84 datum. N, number of studied samples at a site. km, site mean susceptibility expressed in 10-4 SI. Magnetic lineation (L), magnetic foliation (F), corrected anisotropy degree (P'), and shape factor (T) according to Jelinek (1981). D and I are the in situ site-mean declination and inclination, respectively, of the maximum susceptibility axis. e12, semi-angle of the 95% confidence ellipse around the declination of the mean lineation. 'AMS origin' indicates the interpreted nature of the AMS (T = tectonic, S = sedimentary), and related tectonic style (c = compressive).

A remarkable change in the shape of the AMS ellipsoid, from strongly oblate (T ≈ 1, F >> L), to triaxial (T ≈ 0, F ≈ L), to strongly prolate (T ≈ -1, L >> F) is observed throughout our sampled sites (Figure 4c; Table 1). Such variation describes a path that matches the expected variation of the magnetic fabric during increasing deformation from undeformed (sedimentary fabric) to strongly deformed rocks (tectonic fabric) (Borradaile and Henry, 1997; Parés et al., 1999). The highest values of P', determining a relative misfit with the curved trend shown in Figure 4c, belong to two sites from the Punta Noguera Fm., which are likely characterized by a higher concentration of the ferromagnetic minerals or the occurrence of different magnetic phases compared to the other formations.

A nearly pure sedimentary fabric is observed at sites FB02 and PG01, where the AMS ellipsoid is strongly oblate (Figures 3 and 4c; Table 1), and the k_{int} and k_{max} susceptibility axes are not clearly resolved being F >> L (Figure 3). The magnetic fabric at the remaining 19 sites indicates a variable tectonic overprint of the original sedimentary fabric. Within this group, the AMS ellipsoids of 13 sites are mainly oblate (T > 0), with a strong triaxial tendency (i.e., the three susceptibility axes form distinct clusters) and the magnetic foliation plane (sub) parallel to the strata (the pole to local bedding and the k_{min} coincides or are very close) (Figure 3; Table 1), all typical features of weakly deformed rocks [*Borradaile* 1987; *Borradaile and Jackson*, 2004]. A pure triaxial fabric (T ≈ 0) has been recognized at two sites (PD02 and CJ10). A mainly prolate fabric (T < 0), showing a girdle distribution of the k_{int} and k_{min} axes perpendicular to the k_{max} mean orientation dominate at five sites (three of which belonging to the Maastrichtian-Danian Policarpo Fm.). One of these sites (CR01) shows a magnetic fabric resembling that of typical pencil structure, a stage that predate the development of a macroscopic cleavage upon moderate to high deformation [*Borradaile and Tarling*, 1981]. However, no microscopically developed cleavage was observed at this site in the field.

Magnetic lineation is well developed at 16 sites (semi-angle of the 95% confidence ellipse in the magnetic foliation plane (e_{12}) < 30°), and moderately developed at four additional sites (30° < e_{12} <

40.8°) (Table 1). At two remaining sites (RL02, FB02) the magnetic lineation is absent given the high values of the associated errors (e_{12}; Table 1). The magnetic lineation at 15 sites is horizontal or shallowly plunging and parallel to both the local strike of the bedding and local fold axes (Figures 2 and 3). At four sites the lineation is sub-parallel to the dip direction of the strata (Figure 3), while at site PL01 the lineation is oblique to the local strike of the bedding. The orientation of the lineation range from ESE to ENE, except for two sites where it is ~N-S (RB01) or even NW-SE (PG01).

7. Discussion

AMS results from the Upper Cretaceous to Upper Eocene non-metamorphic sedimentary rocks of the internal structural domains of the eastern Magallanes fold-thrust belt of Tierra del Fuego revealed a well-defined magnetic fabric at 21 sites (site RL02 shows an isotropic fabric with e_{12} = 78.1°; Figure 3, Table 1). The shape of the AMS ellipsoid at sites RB02 and PG01 is highly oblate ($T \approx 0$) and typical of pure sedimentary fabric not affected by tectonic imprint. Although site RB01 displays a triaxial AMS ellipsoid its degree of anisotropy is very low (P' = 1.007; Table 1) compared to other sites, and the tectonic nature of the AMS at this site is questionable. Furthermore, we have no or little structural control at this site where the Policarpo Fm. displays only a weakly developed stratification. These four sites have been therefore excluded from further analyses.

Based on the shape of the ellipsoid (T), the anisotropy degree (P'), and the relationship between the three susceptibility axes and the local bedding at each sampling site, we recognized a clear tectonic origin of the AMS at 18 sites (Table 1). This evidence, combined with the absence of macroscopic cleavage indicates that the studied rocks only experience a weak degree of deformation that did not obliterate the pristine AMS fabric. Similar AMS parameters and lithological features characterize the sedimentary units studied by *Diraison* [1978] and *Poblete et al*. [2014], proving that the sedimentary infill of the southern and western Magallanes fold-thrust belt preserve a pristine tectonic fabric that was acquired during (or shortly after) their deposition.

Indicative of the intensity of deformation affecting this region is the shape of the AMS ellipsoid (e.g., *Parés et al*., [1999]). The most internal structural domains of the fold-thrust belt exposing Upper Cretaceous to Paleocene rocks (Policarpo, Rosa, Rocallosa, Cerro Matrero, Cerro Cuchilla, and Cabo Nariz formations) show a predominantly prolate AMS ellipsoid indicative of moderate-to-high strain (Table 1). Conversely, the oblate-to-triaxial AMS ellipsoids characterizing the younger post-Paleocene formations exposed within the most external domains of the belt show that these areas experienced a relatively weak deformation. A progression of the magnetic fabric, reflecting a comparable decreasing of the tectonic stress form the axial towards the frontal areas of

the belt, have previously been documented from a similar setting within the Ebro foreland basin at the foothills of the Pyrenees (e.g., *Parés et al*., [1999]).

7.1. Tectonic significance of the magnetic lineation

Previous studies have demonstrated that in weakly deformed clay-rich rocks AMS represents a reliable paleostress indicator [*Larrasoaña et al*., 2004; *Soto et al*., 2009]. Furthermore, the tectonic style (compressive vs. extensional) can straightforwardly be inferred from the direction of the magnetic lineation and its relationship with the local bedding attitude (e.g., *Mattei et al*., [1997]). This allows us to use AMS analyses to determine the nature and direction of the tectonic field active during progressive phases of the building of the Southern Andes from the Cretaceous until the Miocene. In particular, paleostress constraints from the oldest (non-metamorphic) units located in the most internal sectors of the foreland fold-thrust belt are here used to determine the nature of the earliest tectonic phases associated to the exhumation of the CDCC and the initial propagation of the deformation into the Magallanes foreland basin.

The mainly horizontal magnetic lineation calculated at 14 sites within our study area (Figures 2 and 3; Table 1) are always sub-parallel to both the local strike of the strata and the fold axes, and indicate a predominantly compressional tectonic setting at the time of their deposition (or subsequent diagenesis). Discrepancy (of few degrees up to ~10°) between the strike of the strata and the direction of the magnetic lineation at each site is likely related to the uncertainty associated to the measurement of the bedding directions in the field.

Within the remaining sites, three Upper Paleocene sites from the La Barca Fm. (CJ05, CJ06, and CJ07) show a magnetic lineation that is sub-parallel to the local dip direction of the strata suggesting, at a first glance, an extensional tectonic origin of the lineation. The direction of the lineation at these three sites is, however, statistically indistinguishable from that of adjacent, coeval sites CJ08, CJ09, and CJ10, which show a clear compressive origin of the lineation. Furthermore, sites CJ05, CJ06, and CJ07 lie along the crest of a ~E-W trending, westward plunging syncline (Figure 2). It is therefore more plausible that the magnetic lineation of these three sites formed under the same compressive tectonic regime upon layer-parallel shortening, and was subsequently tilted to the west after progressive folding and tilting of the fold axis to the west.

Site PL01 (Policarpo Fm.) show a horizontal lineation that is not contained in the bedding plane, is at high angle to the strike of the strata, and has a direction that is significantly different from that of adjacent, coeval sites (Figure 3). While the mismatch between the lineation and the strike of the strata can be related to uncertainties associated to the bedding measurement (stratification of the

Policarpo Fm. was hard to recognize in the field), the intra-formational variation of the lineation orientation is remarkable and requires further analysis.

Mean lineation directions were calculated for four age intervals within the 17 sites showing a clear tectonic origin of the lineation, distributed as follows: Late Cretaceous-Early Paleocene (Policarpo Fm., PD01, PD02, CR01), Late Paleocene (La Barca Fm., CJ05, CJ06, CJ07, CJ08, CJ09, CJ10, FB01), Late Paleocene-Early Eocene (Punta Nuguera Fm., RL01, RL03), and Mid-Late Eocene (Cerro Colorado Fm., CJ01, CJ02, CJ03, CJ04, CJ11) (Figure 5).

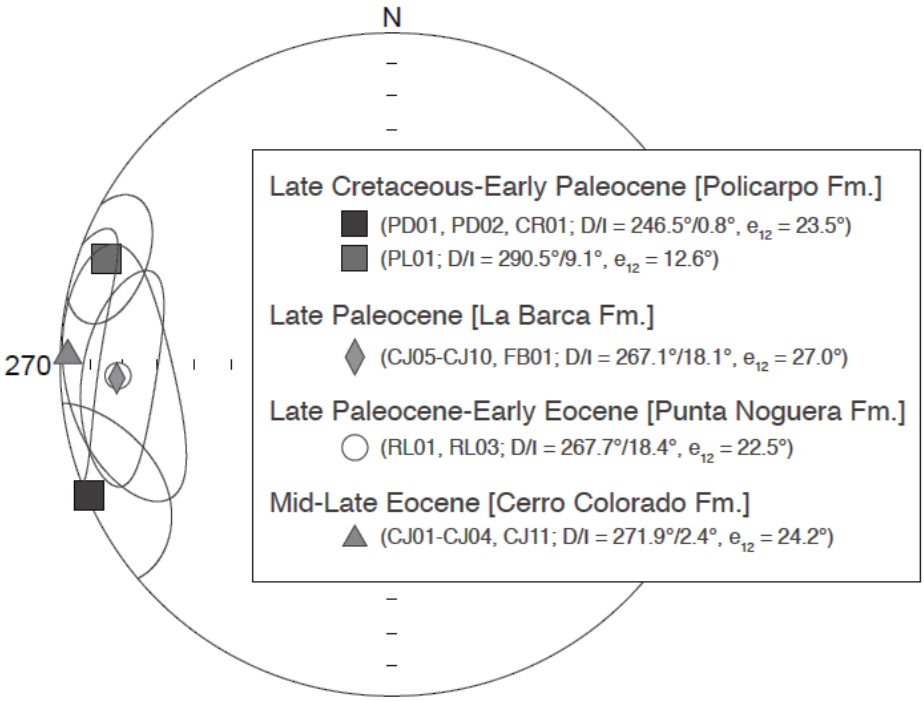

Figure 5. Schmidt equal-area projections, lower hemisphere, of the mean lineation (kmax) calculated for each sampled formation, and respective 95% confidence ellipses. For each group, site name, mean declination (D) and inclination (I) of the lineation, and error associated to the lineation declination (e12) are reported.

Cretaceous site PL01 was not included in the computation of the mean lineation for the Policarpo Fm. due to its distinctive direction (Figure 5). The youngest three age groups show a very consistent E-W direction of the lineation (Figure 5). The two mean lineation directions from the Upper Cretaceous Policarpo Fm. are not statistically different from this E-W trend, yet there is substantial difference within the Policarpo Fm. between the average direction including sites PD01, PD02 and CR01, and that of site PL01. We propose two alternative explanation to the anomalous direction of the lineation at site PL01: either (i) it formed under a tectonic regime characterized by

significant strike-slip component (which would explain the high angle between the lineation and the local strike of the strata), or more likely (ii) it was affected by the interference between a regional stress field producing mainly E-W to ENE trending fold axes and a more local (and probably younger) deformation phase resulting in a series of folds with ~N-S axes (Figure 2). Due to these uncertainties we discarded site PL01 from further analysis.

In summary, 17 Upper Cretaceous to Upper Eocene sites from the internal domains of the Magallanes fold-thrust belt show a consistently ~E-W oriented magnetic lineation formed under a compressional stress field. This result indicates that the Southern Andes at the study area experienced a continuous ~N-S compression during the Late Cretaceous-Late Eocene time interval (~70 to ~35 Ma).

7.2. The exhumation of the Cordillera Darwin metamorphic core complex (CDCC)

Although there is growing evidence in support of models requiring compressive tectonics for the exhumation of the CDCC [*Klepeis et al*., 2010; *Maloney et al*., 2011], the tectonic events affecting the Fuegian Andes during the main uplifting phase of the Cordillera Darwin (~90-70 Ma; *Kohn et al*. [1995]) are still poorly constrained. Relying on structural and geochronological constraints, *Klepeis et al*. [2010] proposed the occurrence of two early compressive events in the Fuegian Andes. The first event occurred between 100 and 86 Ma, and caused inversion of the Rocas Verdes marginal basin and southward underthrusting of the South American craton below the magmatic arc. This age is precisely constrained in the Cordillera Darwin by crosscutting relationships between folded sedimentary rocks of the Rocas Verdes basin and Late Cretaceous (86-74 Ma; *Kohn et al*. [1995]) granites. The second tectonic event has been associated to a poorly constrained post-80 Ma compressional phase yielding basement-rooted thrust sheets emplacement. Based on the model of *Klepeis et al*. [2010], *Torres-Carbonell and Dimieri* [2013] argued that starting from ~80 Ma a regional-scale basement duplex system developed along the current axis of the Fuegian Andes above a mid-crustal decoupling surface, yielding uplift in the Fuegian Andes and continuous craton-ward propagation of the compression until the Miocene. The other oldest well-constrained tectonic pulse, involved the foreland basin during the Early Paleocene (~61 Ma; e.g., *Ghiglione and Ramos* [2005]) or slightly before [*Torres-Carbonell et al*., 2013], and led to the formation of the thin-skinned Magallanes fold-thrust belt. A large gap of data therefore exists for the time interval spanning from 86 to 61 Ma, period that corresponds to the main exhumation phase of the CDCC.

Applying the same criteria for the definition of the tectonic significance of the AMS, we integrate our new data from Upper Cretaceous to Upper Eocene rocks with the available AMS database from other sectors of the orocline [*Diraison*, 1978; *Maffione et al*., 2010; *Poblete et al*.,

2014] to determine the nature and orientation of the paleostress active at the Southern Andes during the Lower Cretaceous - Early Miocene time interval. Almost all the sites studied by *Diraison* [1978] and *Poblete et al*. [2014] are characterized by a magnetic lineation that is horizontal and sub-parallel to both the local strike of the bedding and the structural trend of the orogen, implying a compressive tectonic origin. The combined AMS dataset provides clear evidence for the existence of a compressive tectonics that was, in each location, perpendicular to the local structural trend of the orogen, and was active from the Lower Cretaceous to the Late Oligocene (Figure 6).

The coaxiality of the deformation inferred from the parallelism between the magnetic lineation and the local structural trend at each site seems to exclude a significant contribution of strike-slip components to the main regional stress. We therefore conclude, in agreement with existing models (e.g., *Klepeis et al*. [2010]), that both stages of the uplifting and exhumation of the CDCC (90-70 Ma and 60-40 Ma; Khon et al., 1995) were driven by pure (~NE directed) compression yielding regional-scale crustal duplexing within the structural (Paleozoic) basement. Such a thick-skinned tectonics affected the whole central belt (between the Patagonian batholith and the Magallanes fold-thrust belt), and resulted, in combination with extensive erosion, in regional uplift and local exhumation of the metamorphic basement currently exposed in the Cordillera Darwin.

7.3. Paleostress constraints on the kinematic evolution of the Southern Andes

The combined AMS dataset compiled for the Southern Andes reveals a paleostress field that was radial at any stage of the evolution of this region (Figure 6). The inferred local shortening directions are in fact perpendicular to the main trend of the orogen in each segment of the arc, and do not vary significantly through time. According to these data, the southern segment of the Patagonian Andes, where the regional structural trend has a direction of N345° [*Poblete et al*., 2014], underwent a continuous ENE-directed shortening. To the south, the western domain of the Fuegian Andes show a main structural trend that varies eastward from N320° to N295° [*Poblete et al*., 2014]; here the inferred shortening directions mimic the structural variation, ranging from NE to NNE. Finally, in the eastern segment of the Fuegian Andes where the regional structural trend is variable between N285° and N260°, the inferred regional shortening direction is ~NS to ~NNW directed.

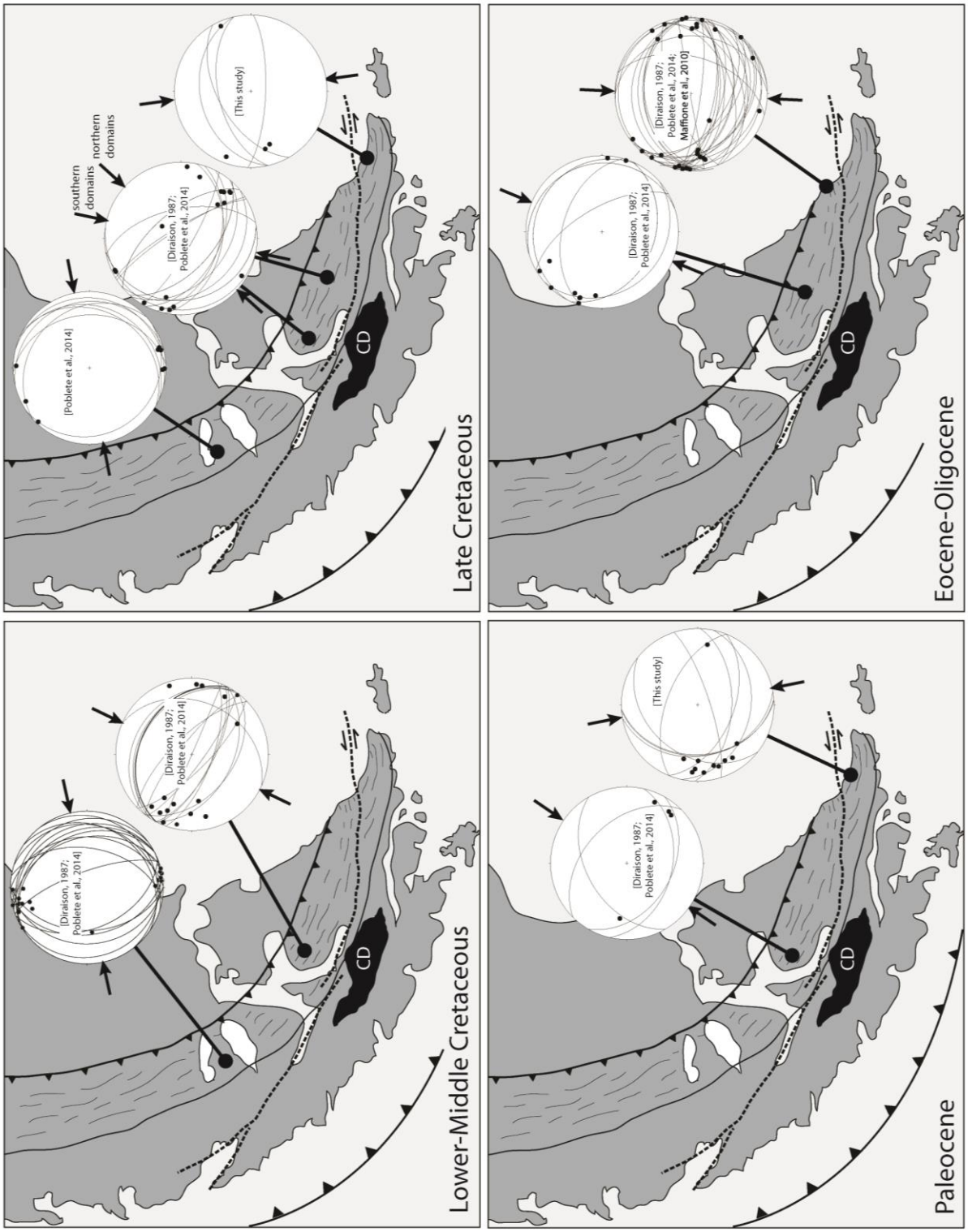

Figure 6. Four-stage evolution of the paleostress field (black arrows) inferred at the Southern Andes based on our new and published AMS data (stereoplots). Black dots in the stereonets are the site mean lineations, and the great circles are the local bedding planes. CD, Cordillera Darwin.

A similar, radial stress field is documented by fault kinematic data obtained by *Diraison et al*. [2000] throughout the orogenic arc. According to these authors, the shortening directions (based on the measurement of 1600 striated fault planes from the Mesozoic-Cenozoic sedimentary cover of the Magallanes fold-thrust belt) show a progressive rotation from N075° (Patagonian Andes) to N043° (Fuegian Andes). Few data from the easternmost sectors indicate a ~NS shortening direction. More fault kinematic data have been produced in this sector by *Torres-Carbonell et al*. [2014] displaying the same ~NS shortening directions.

The presence of a radial stress field can be a common feature in secondary oroclines (*sensu Weil and Sussman* [2004]) as it can be easily explained by relative rotation of the limbs of the arc after the first compressive phase [*Speranza et al*., 1997; *Gutiérrez-Alonso et al.*, 2012]. However, if the arc is a primary orocline (i.e., the arc formation does not involve limb rotation) a radial stress field becomes more difficult to explain. The arcuate shape of the Southern Andes first induced *Carey* [1958] to propose that it could have been related to oroclinal bending of an originally straight orogen. Since then, this region has been referred to as the Patagonian Orocline. The initial hypothesis was subsequently supported by sparse paleomagnetic data from the volcanic units mainly within the internal belt indicating strong counterclockwise rotations consistent with a kinematics expected for such oroclinal bending (see *Rapalini* [2007] for a review). Initially, models requiring oroclinal bending in the Tertiary received the largest consensus [*Dalziel et al*., 1973; *Cunningham*, 1993; *Kraemer*, 2003], while only few authors [*Burns et al*., 1980] supported an oroclinal bending related to the Cretaceous closure of the Rocas Verdes marginal basin. Later on, a new hypothesis emerged that put forward the primary origin of the bend [*Ramos and Aleman*, 2000; *Diraison et al*., 2000]. This scenario is partly supported by paleomagnetic data from sedimentary rocks within the southern Magallanes fold-thrust belt published by *Maffione et al*. [2010] and *Poblete et al*. [2014]. These data proved that the Fuegian Andeshave not been affected by regional tectonic rotation since the Middle Paleocene (~60 Ma), showing that the Patagonian Orocline has been a primary arc for large part of the Cenozoic. These authors concluded suggesting possible oroclinal bending occurring during the Cretaceous phase of marginal basin closure.

Assuming therefore the Magallanes fold-thrust belt to be a primary orocline, its tectonic evolution necessary involves the convergence of an L-shaped indenter (represented by the Cretaceous proto-Southern Andes), similar to that modeled by *Ghiglione and Cristallini* [2007]. A primary orocline also implies that the radial stress field documented in this study is not reflective of a finite strain resulting from oroclinal bending, but is rather indicative of the active *in situ* tectonic stress during the Cenozoic. Analog models showing the effects of a simple translation of a curved indenter (see *Ghiglione and Cristallini* [2007]) seems to be not able to reproduce the radial stress

field characterizing the Southern Andes, being the finite displacement vectors consistently parallel to the displacement direction of the indenter. Similarly, also a two-phase indentation model [*Ghiglione and Cristallini*, 2007] is incompatible with the paleostress data presented in this study, as the stress field was radial at every moment of the tectonic evolution of this region (the southern Patagonian Andes were affected by ENE-directed compression as early as the Lower-Middle Cretaceous) (Figure 6).

It seems clear, therefore, that in the absence of external factors controlling the kinematic evolution of the Southern Andes, the indentation of a curved buttress cannot simultaneously explain its current structural setting and paleostress field. It has been already proposed that pre-existing crustal heterogeneities (i.e., faults) at the southern edge of the South American continental margin have controlled the evolution of foreland basin sedimentation and subsequent deformation [*Likerman et al*., 2013; *Fosdick et al*., 2014]. We argue that the pattern of pre-existing extensional structures in the basement of the Southern Andes strongly controlled the kinematic evolution of the Patagonian Orocline. We propose that during the Jurassic extensional phase that culminated in the opening of the Rocas Verdes marginal basin the southern edge of the South American continent was thinned by a number of extensional faults that mirrored the current shape of the Southern Andean arc (Figure 7a). After the closure of the marginal basin and the collision of the magmatic arc with the attenuated South American continental margin in the early Late Cretaceous, these normal faults were reactivated into thrusts, forming a primary arc (currently represented by the central belt) (Figure 7b). A thick-skinned tectonics in the central belt is consistent with recent models by *Torres-Carbonell and Dimieri* [2013]. Slip partitioning mechanisms along the foreland-ward edges of these faulted blocks in the central belt may have transferred a fault-normal compression component to the external domains, yielding radial (convergent) propagation of the thrust sheets in the Magallanes fold-thrust belt since the Late Cretaceous (Figure 7c). Assuming a ~NE oriented regional convergence of the indenter, represented by the Jurassic volcanic arc, the strike-slip component along the frontal thrust of the central belt should become more significant away from the hinge of the arc, with a dextral kinematics in the NS limb, and sinistral in the EW limb. According\ to *Torres-Carbonell and Dimieri* [2013], Cenozoic deformation in the Magallanes thrust-belt occurred above a décollement at the top of the basement, while the compressive stress was transmitted to the foreland basin by the crustal duplex structures of the central belt. In our model, the central belt, operated throughout the whole evolution of the fold-thrust belt as a transfer zone accommodating strike-slip displacement and allowing the propagation of a radial stress into the Magallanes foreland basin.

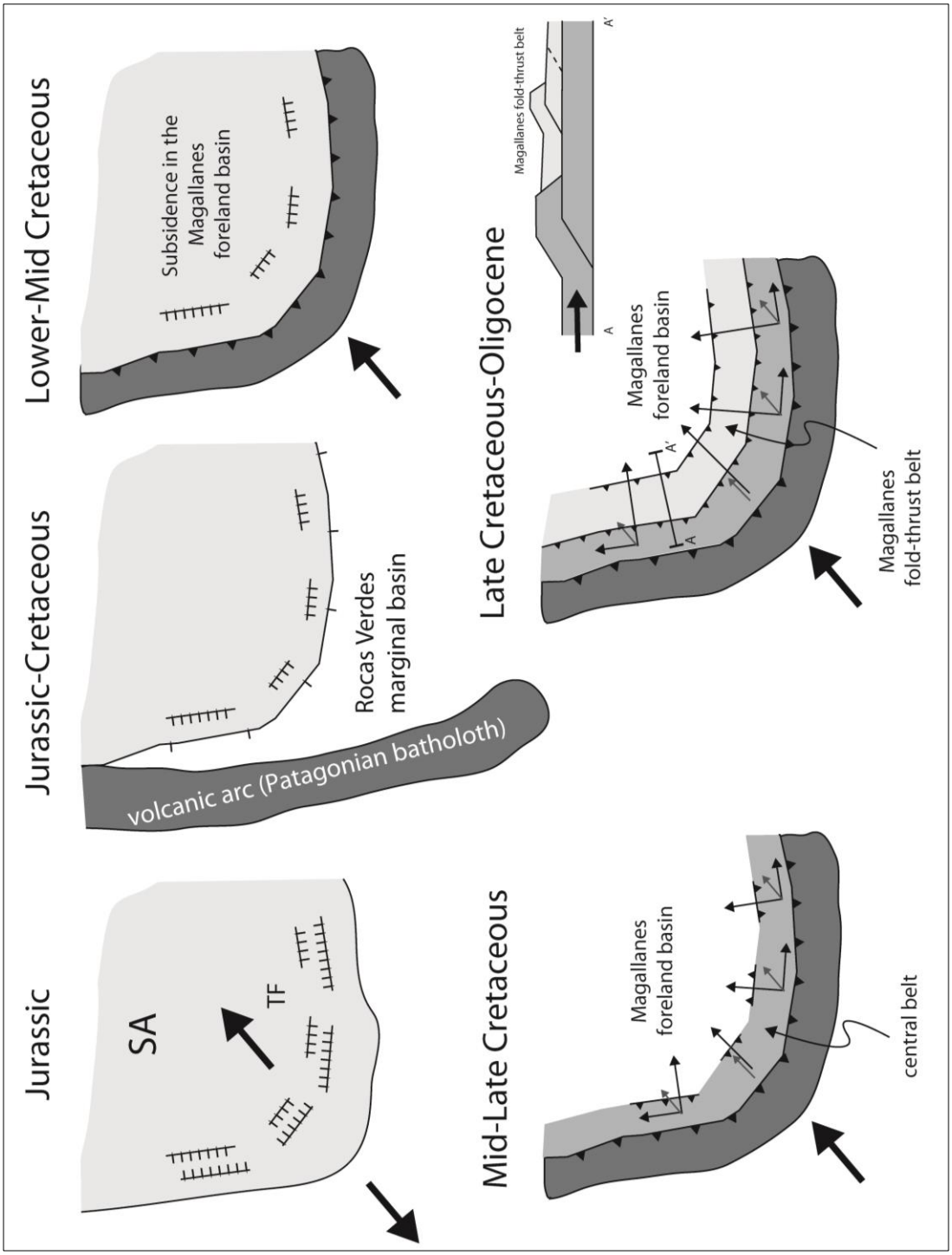

Figure 7. Cartoon illustrating the proposed kinematic model for the evolution of the Southern Andes. SA, South America. TF, Tierra del Fuego. Thick black arrows indicate the direction of the regional stress field. Grey thin arrows in the central belt indicate the displacement vectors of these units, while the thin black arrows indicate the fault.

8. Conclusions

In this contribution we report on the anisotropy of magnetic susceptibility (AMS) of Upper Cretaceous-Upper Eocene sedimentary rocks from 22 sites within the most internal structural domain of the Magallanes fold-thrust belt (Tierra del Fuego). We identified a tectonic origin of the lineation at 17 sites, indicating a consistent ~NS compression affecting this area of the Southern Andes from the Late Cretaceous until the Late Eocene. We integrated our data with re-analyzed previously published AMS data form other sectors of the Patagonian Orocline to built a robust dataset that allowed us to reconstruct the evolution of the paleostress at the Southern Andes throughout most of its geological history (i.e., Early Cretaceous to Late Oligocene).

First key conclusion of our analysis is that a mainly compressive tectonic regime characterized the early tectonic phases of the Andean orogeny associated to the exhumation of the Cordillera Darwin metamorphic core complex. Together with previous structural geological constraints, AMS data provide definitive proof for a compression-driven uplift and exhumation of the Paleozoic basement of the Cordillera Darwin. A second implication of our results is the identification of a radial (convergent) paleostress field controlling the kinematic evolution of the Patagonian Orocline throughout the Cenozoic. To explain the radial stress field in the absence of oroclinal bending (as suggested by recent paleomagnetic data) we propose that the regional configuration of pre-existing normal faults in the basement, formed during the Jurassic extensional phase and mimicking the current curved shape of the arc, may have strongly controlled the subsequent kinematic evolution of the Southern Andes. Continuous slip partitioning along thrust sheets rooted in the basement of the central belt upon ~NE-ward translation of a rigid indenter (the Jurassic volcanic arc) can provide an effective mechanism to yield orogen-perpendicular compression into the Magallanes foreland basin and led to the formation of a primary curved fold-thrust belt.

Acknowledgments

This work was funded by PRNA funds PROGDEF09-135 awarded to E. Lodolo. We are grateful to M. Gonzales Guillot for his support given during the field campaign. We are also extremely indebted with Jose' and Pablo for their logistic support.

References

Allen, R.B. (1982), Geología de la Cordillera Sarmiento, Andes Patagónicos, entre los 51º00 y 52º 15' Lat S, Magallanes, Chile, *Serv. Nac. Geol. Min*., Chile, 38, 1-46.

Allen, R.B. (1983), Geologic studies of the Scotia arc region and Agulhas Plateau (Chile, Antarctica, Indian Ocean) [Ph.D. dissertation]: New York, Columbia University, 239 p.

Allmendinger, R.W., T. E. Jordan, S. M. Kay, and B. L. Isacks (1997), The evolution of the Altiplano-Puna Plateau of the central Andes, *Annu. Rev. Earth Planet. Sci*., *25*, 139-174, doi:10.1146/annurev. earth.25.1.139.

Alvarez-Marrón, J., K. R. McClay, S. Harambour, L. Rojas, and J. Skarmeta (1993), Geometry and evolution of the frontal part of the Magallanes foreland thrust and fold belt (Vicuña area), Tierra del Fuego, Southern Chile, *AAPG Bulletin, 77*(11), 1904-1921.

Andrews-Speed, C. P. (1980), The geology of central Isla Hoste, southern Chile: sedimentation, magmatism and tectonics in part of a Mesozoic back-arc basin, *Geol. Mag*., *117*, 339-349.

Barbeau, D. L., E. B. Olivero, N. L. Swanson-Hysell, K. M. Zahid, K. E. Murray, and G. E. Gehrels (2009), Detrital-zircon geochronology of the eastern Magallanes foreland basin: Implications for Eocene kinematics of the northern Scotia Arc and Drake Pas- sage, *Earth Planet. Sci. Lett*., *284*(3-4), 489-503, doi:10.1016/j.epsl.2009.05.014.

Biddle, K. T., M.A. Uliana, R. M. Mitchum, M. G. Fitzgerald, and R. C. Wright (1986). The stratigraphic and structural evolution of the central and eastern Magallanes basin, southern South America, in *Foreland Basins. Int. Assoc. Sediment. Spec. Publ*., edited by Allen, P.A., and P. Homewood, *8*, pp. 41-61.

Borradaile, G.J. (1988), Magnetic susceptibility, petrofabrics and strain, *Tectonophysics*, *156*, l-20.

Borradaile, G.J. (1991), Correlation of strain with anisotropy of magnetic susceptibility (AMS), *Pure Appl. Geophys*., *135*, 15-29.

Borradaile, G. J., and B. Henry (1997), Tectonic applications of magnetic susceptibility and its anisotropy, *Earth-Science Reviews*, *42*(1), 49-93.

Borradaile, G.J., and D. Tarling (1981), The influence of deformation mechanisms on magnetic fabrics in weakly deformed rocks, *Tectonophysics*, *77*, 151-168.

Borradaile, G. J., and M. Jackson, M. (2004), Anisotropy of magnetic susceptibility (AMS): magnetic petrofabrics of deformed rocks, *Geol. Soc., London, Special Publications*, *238*(1), 299-360.

Borradaile, G. J., and M. Jackson (2010), Structural geology, petrofabrics and magnetic fabrics (AMS, AARM, AIRM), *J. Struc. Geol*., *32*(10), 1519-1551.

Borradaile, G.J., W. Keeler, C. Alford, and P. Sarvas (1987), Anisotropy of magnetic susceptibility of some metamorphic minerals, *Phys. Earth Planet. Inter*., *48*, 161-166.

Bruhn, R. L (1979), Rock structures formed during back-arc basin deformation in the 498 Andes of Tierra del Fuego, *Bulletin of the Geological Society of America*, *90*, 998-1012.

Bruhn, R. L., C. Stern, and M. de Wit (1978), Field and geochemical data bearing on the development of a Mesozoic volcano-tectonic rift zone and back-arc basin in southernmost South America, *Earth Planet. Sci. Lett*., *41*, 32-46, doi:10.1016/0012-821X(78)90039-0.

Bruhn, R. L., and I. W. D. Dalziel (1977), Destruction of the Early Cretaceous marginal basin in the Andes of Tierra del Fuego, in *Island Arcs, Deep Sea Trenches and Back-arc Basins*, edited by Talwani, M., and W. C. Pitman III, *Am. Geophys. U*., Maurice Ewing Series 1, pp. 395-405.

Burns, K. L., M. J. Rickard, L. Belbin, and F. Chamalaun (1980), Further paleomagnetic confirmation of the Magellanes orocline, *Tectonophysics, 63*, 75-90.

Carey, S. W. (1958), The tectonic approach to continental drift, in *Continental drift: a symposium*, Geology Department, Univ. Tasmania, Hobart, Tasmania. 177-355.

Cifelli, F., F. Rossetti, M. Mattei, A. M. Hirt, R. Funicello, L. Tortorici (2004), An AMS, structural and paleomagnetic study of quaternary deformation in Eastern Sicily, *J. Struct. Geol*., *26*, 29-46.

Cifelli, F., M. Mattei, M. Chadima, A.M. Hirt, ans A. Hansen (2005), The origin of the tectonic lineation in extensional basins: Combined neutron texture and magnetic analysis on "undeformed" clays, *Earth Plan. Sci. Lett*., *235*, 62-78.

Cobbold, P. R., E. A. Rossello, and P. Roperch (2007), Distribution, timing, and causes of Andean deformation across South America, *In*: Deformation of the continental crust: The legacy of Mike Coward, edited by Alison C. Ries, R. W. H. Butler, and R. H. Graham, 321 pp.

Corbella, H., L. Chelotti, and C. Pomposiello (1996), Neotectónica del rift Jurásico austral en Pali Aike: Patagonia extrandina, Santa Cruz, Argentina, paper presented at XIII Congr. Geol. Argentino y III Congr. de Exploración de Hidrocarburos, Buenos Aires, 383-393.

Coutand, I., M. Diraison, P. R. Cobbold, D. Gapais, E. A. Rossello, and M. Miller (1999), Structure and kinematics of a foot-hills transect, Lago Viedma, southern Andes (49°30'S), *J. South Am. Earth Sci*., *12*, 1-15.

Coutand, I., P. R. Cobbold, M. de Urreiztita, P. Gautier, A. Chauvin, D. Gapais, and E. Rossello (2001), Style and history of Andean deformation, Puna plateau, northwestern Argentina, *Tectonics*, *20*, 210-234, doi:10.1029/2000TC900031.

Cunningham, W. D. (1993), Strike-slip faults in the southernmost Andes and the development of the Patagonian orocline, *Tectonics*, *12*(1), 169-186, doi:10.1029/92TC01790.

Cunningham, W. D. (1994), Uplifted ophiolitic rocks on Isla Gordon, southernmost Chile: implications for the closure history of the Rocas Verdes marginal basin and the tectonic evolution of the Beagle Channel region, *J. South Am. Earth Sci*., *7*, 135-147.

Cunningham, W. D. (1995), Orogenesis at the southern tip of the Americas: the structural evolution of the Cordillera Darwin metamorphic complex, southernmost Chile, *Tectonophysics*, *244*, 197-229.

Cunningham, D.W., I.W.D. Dalziel, L. Tung-Yi, and L.A. Lawver (1995), Southernmost South America-Antarctic Peninsula relative plate motions since 84 Ma. Implications for the tectonic evolution of the Scotia Arc region, *J. Geophy. Res*., *100*, 8257-8266.

Dalziel, I. W. D. (1981), Back-arc extension in the southern Andes: a review and critical reappraisal, *Phil. Trans. R. Soc. Lond. A*, *300*, 319-335.

Dalziel, I. W. D. (1986), Collision and Cordilleran orogenesis: an Andean perspective, *Geological Society*, London, Special Publications, *19*(1), 389-404.

Dalziel, I. W. D., M. J. de Wit, and F. K. Palmer (1974), Fossil marginal basin in the southern Andes, *Nature*, *250*, 291-294.

Dalziel, I. W. D., R. Kligfield, W. Lowrie, and N. D. Opdyke (1973), Paleomagnetic data from the southernmost Andes and the Antarctandes, in *Implications of Continental Drift to Earth Sciences, vol. 1*, edited by Tarling, D.H., and S.K. Runcorn, Academic Press, San Diego, California, pp. 87-101.

Dalziel, I. W. D., R. L. Brown (1989), Tectonic denudation of the Darwin metamorphic core complex in the Andes of Tierra del Fuego, southernmost Chile: implications for cordilleran orogenesis, *Geology*, *17*, 699-703.

Diraison, M., P. R. Cobbold, D. Gapais, E. A. Rossello and C. Le Corre (2000), Cenozoic crustal thickening, wrenching and rifting in the foothills of the southernmost Andes, *Tectonophysics*, *316*(1), 91-119.

Eagles, G., R. A. Livermore, J. D. Fairhead, and P. Morris (2005), Tectonic evolution of the west Scotia Sea, *J. Geophys. Res*., *110*, B02401, doi:10.1029/2004JB003154.

Esteban, F., A. Tassone, M. Menichetti, A. E. Rapalini, M. B. Remesal, M. E. Cerredo, H. Lippai, and J. V. Vilas (2011), Magnetic fabric and microstructures across the Andes of Tierra del Fuego, Argentina, *Andean Geology*, *38*, 64-81.

Fildani, A., and A. M. Hessler (2005), Stratigraphic record across a retroarc basin inversion: Rocas Verdes-Magallanes Basin, Patagonian Andes, Chile, *Geol. Soc. Amer. Bull*., *117*, 1596-1614.

Fildani, A., T. Cope, S. A. Graham, and J. Wooden (2003), Initiation of the Magallanes foreland basin: timing of the southernmost Patagonian Andes orogeny revised by detrital zircon provenance analysis, *Geology*, *31*, 1081-1084.

Fosdick, J. C., B. W. Romans, A. Fildani, A. Bernhardt, M. Calderón, and S. A. Graham (2011), Kinematic evolution of the Patagonian retroarc fold-and-thrust belt and Magallanes foreland basin, Chile and Argentina, 51°30'S, *Geol. Soc. Am. Bull.*, *123*(9-10), 1679-1698.

Fosdick, J. C., S. A. Graham, and G. E. Hilley (2014), Influence of attenuated lithosphere and sediment loading on flexure of the deep-water Magallanes retroarc foreland basin, Southern Andes, *Tectonics*, *33*(12), 2505-2525.

Ghiglione, M. C. (2002), Diques clásticos asociados a deformación transcurrente en depósitos sinorogénicos del Mioceno inferior de la Cuenca Austral, *Rev. Asoc. Geol. Argent*., *57*, 103-118.

Ghiglione, M. C. (2003), Estructura y evolución tectónica del Cretácico-Terciario de la costa Atlántica de Tierra del Fuego, Ph.D. thesis, *Universidad de Buenos Aires*, Buenos Aires.

Ghiglione, M., and E. Cristallini (2007), Have the southernmost Andes been curved since Late Cretaceous time? An analog test for the Patagonian Orocline, *Geology*, *35*(1), 13-16.

Ghiglione, M. C. and V. A. Ramos (2005), Progression of deformation and sedimentation in the southernmost Andes, *Tectonophysics*, *405*, 25-46, doi:10.1016/j.tecto.2005.05.004.

Ghiglione, M. C., V. A. Ramos, and E. O. Cristallini (2002), Estructura y estratos de crecimiento en la faja plegada y corrida de los Andes fueguinos, *Rev. Geol. Chile*, *29* (1), 17-41.

Gombosi, D. J., D. L. Barbeau, and J. I. Garver (2009), New thermochronometric constraints on the rapid Paleogene exhumation of the Cordillera Darwin complex and related thrust sheets in the Fuegian Andes, *Terra Nova*, *21*, 507-515.

Grunow, A. M., I. W. D. Dalziel, T. M. Harrison and M. T. Heizler (1992), Structural geology and geochronology of subduction complexes along the margin of Gondwanaland: new data from the Antarctic Peninsula and southernmost Andes, *Geol. Soc. Am. Bull*., *104*, 1497-1514.

Gutiérrez-Alonso, G., S.T. Johnston, A.B. Weil, D. Pastor-Galán, and J.Fernández-Suárez (2012), Buckling an orogen: the Cantabrian orocline, *GSA Today*, *22*, 4-9. http:// dx.doi.org/10.1130/GSATG141A.1.

Halpern, M., and D. C. Rex (1972), Time of folding of the Yahgan Formation and age of the Tekenika beds, southern Chile, South America, *Geol. Soc. Am. Bull*., *83*, 1881-1886.

Hervé, F., C. M. Fanning, R. J. Pankhurst, C. Mpodozis, K. Klepeis, M. Calderón, and S. N. Thomson (2010), Detrital zircon SHRIMP U-Pb age study of the Cordillera Darwin Metamorphic Complex of Tierra del Fuego: sedimentary sources and implications for the evolution of the Pacific margin of Gondwana, *Journal of the Geological Society*, *167*(3), 555-568.

Hervé, F., R. J. Pankhurst, C. M. Fanning, M. Calderón, and G. M. Yaxley (2007), The South Patagonian batholith: 150 My of granite magmatism on a plate margin, *Lithos*, *97*, 373-394.

7, 373–394, doi:10.1016/j.lithos.2007.01.007.

Hrouda, F. (1982), Magnetic anisotropy of rocks and its application in geology and geophysics, *Geophys. Surv*., *5*, 37-82.

Hrouda, F., and V. Jelínek (1990), Resolution of ferromagnetic and paramagnetic anisotropies, using combined low-field and high-field measurements, *Geophys. J. Int*., *103*, 75-84.

Isacks, B. L. (1988), Uplift of the central Andes plateau and bending of the Bolivian Orocline, *J. Geophys. Res*., *93*, 3211-3231.

Jackson, M. (1991), Anisotropy of magnetic remanence: a brief review of mineralogical sources, physical origins, and geological applications and comparison with susceptibility anisotropy, *Pure Appl. Geophys*., *136*, l-28.

Jackson, M.J., L. and Tauxe (1991), Anisotropy of magnetic susceptibility and remanence: Developments in the characterization of tectonic, sedimentary. and igneous fabric (IUGG Rep. Contributions in Geomagnetism and Paleomagnetism.), *Rev. Geophys*., *29*, 371-376.

Jelinek, V. (1977), The statistical theory of measuring anisotropy of magnetic susceptibility of rocks and its application, *Geofyzika, Brno*., pp. 88.

Jelinek, V. (1978), Statistical processing of magnetic susceptibility on groups of specimens, *Stud. Geophys. Geod*., *22*(1), 50-62.

Jordan, T. E., R. W. Allmendinger, J. F. Damanti, and R. E. Drake (1993), Chronology of motion in a complete thrust belt: The precordillera, 30-31°S, Andes Mountains, *J. Geol*., *101*, 135–156.

Katz, H. R. (1973), Contrasts in tectonic evolution of orogenic belts in the southwest Pacific, *J.R. Soc. New Zealand*, *3*, 333-362.

Klepeis, K. A. (1994), Relationship between uplift of the metamorphic core of the southernmost Andes and the shortening in the Magallanes foreland fold and thrust belt, Tierra del Fuego, Chile, *Tectonics*, *13*, 882-904.

Klepeis, K.A., and J.A.Jr. Austin (1997), Contrasting styles of superposed deformation in the southernmost Andes, *Tectonics*, *16*, 755-776.

Klepeis, K., P. Betka, G. Clarke, M. Fanning, F. Hervé, L. Rojas, C. Mpodozis, and S. Thomson (2010), Continental underthrusting and obduction during the Cretaceous closure of the Rocas Verdes rift basin, Cordillera Darwin, Patagonian Andes, *Tectonics*, *29*, TC3014, doi:10.1029/2009TC002610.

Kohn, M. J., F. S. Spear, I. W. D. Dalziel (1993), Metamorphic *P-T* paths from Cordillera Darwin, a core complex in Tierra del Fuego, *Chile. J. Petrol*., *34*, 519-542.

Kohn, M. J., F. S. Spear, T. M. Harrison, and I. W. D. Dalziel (1995), $^{40}Ar/^{39}Ar$ geochronology and *P–T–t* paths from the Cordillera Darwin Metamorphic Complex, Tierra del Fuego, Chile, *J. Metamorph. Geol*., *13*, 251-270.

Kraemer, P. E. (1993), Perfil estructural de la Cordillera Patagónica Austral a los 50° L. S., Santa Cruz, paper presented at XII Congreso de Geología Argentina (Vol. 3).

Kraemer, P. E. (2003), Orogenic shortening and the origin of the Patagonian orocline (56ºS Lat), *J. South Am. Earth Sci*., *15*, 731-748.

Likerman, J., J. F. Burlando, E. O. Cristallini, and M. C. Ghiglione (2013), Along-strike structural variations in the Southern Patagonian Andes: Insights from physical modeling, *Tectonophysics*, *590*, 106-120, doi:10.1016/j.tecto.2013.01.018.

Lodolo, E., M. Menichetti, R. Bartole, Z. Ben Avram, A. Tassone, and H. Lippai (2003), Magallanes-Fagnano continental transform fault (Tierra del Fuego, southernmost South America), *Tectonics*, *22*(*6*), 1076, doi:10.1029/2003TC001500.

Macrì, P., F. Speranza, and L. Capraro (2014), Magnetic fabric of Plio-Pleistocene sediments from the Crotone fore-arc basin: Insights on the recent tectonic evolution of the Calabrian Arc (Italy*), J. Geodynamics*, *81*, 67-79.

Maffione, M., F. Speranza, C. Faccenna, A. Cascella, A., G. Vignaroli, and L. Sagnotti (2008), A synchronous Alpine and Corsica-Sardinia rotation, *J. Geophys. Res*., *113*(B3).

Maffione, M., F. Speranza, C. Faccenna, and E. Rossello (2010), Paleomagnetic evidence for a pre-early Eocene (~ 50Ma) bending of the Patagonian orocline (Tierra del Fuego, Argentina): Paleogeographic and tectonic implications, *Earth Planetary Sci. Lett*., *289*(1), 273-286.

Maffione, M., S. Pucci, L. Sagnotti, and F. Speranza (2012), Magnetic fabric of Pleistocene continental clays from the hanging-wall of an active low-angle normal fault (Altotiberina Fault, Italy), *International journal of earth sciences*, *101*(3), 849-861.

Maloney, K. T., G. L. Clarke, K. A. Klepeis, and L. Quevedo (2013), The Late Jurassic to present evolution of the Andean margin: Drivers and the geological record, *Tectonics*, *32*(5), 1049-1065.

Maloney, K. T., G. L. Clarke, K. A. Klepeis, C. M. Fanning, and W. Wang (2011), Crustal growth during back-arc closure: Cretaceous exhumation history of Cordillera Darwin, southern Patagonia, *J. Met. Geol.*, *29*(6), 649-672, doi: 10.1111/j.1525-1314.2011.00934.x.

Malumián, N., and E. B. Olivero (2006), El Grupo Cabo Domingo, Tierra del Fuego: bioestratigrafía, paleoambientes y acontecimientos del Eoceno-Mioceno marino, *Rev. Asoc. Geol. Argent*., *61* (2), 139-160.

Martinioni, D. R., E. B. Olivero, S. Palamarczuk (1999), Estratigrafía y discordancias del Cretácico superior-Paleoceno en la región central de Tierra del Fuego, paper presented at Simposio Paleógeno de América del Sur, Segemar, Buenos Aires, Argentina, *33*, pp. 7-16.

Mattei, M., F. Speranza, A. Argentieri, F. Rossetti, L. Sagnotti, and R. Funiciello (1999), Extensional tectonics in the Amantea basin (Calabria, Italy): a comparison between structural and magnetic anisotropy data, *Tectonophysics*, *307*, 33-49.

Mattei, M., L. Sagnotti, C. Faccenna, and R. Funiciello (1997), Magnetic fabric of weakly deformed clay-rich sediments in the Italian peninsula: Relationships with compressional and extensional tectonics, *Tectonophysics*, *271*, 107-122.

Mattei M., R. Funiciello, and C. Kissel (1995), Paleomagnetic and structural evidence for Neogene block rotations in the central Apennines, Italy, *J. Geophys. Res*., *100*, 17863-17883.

Menichetti, M., E. Lodolo, and A. Tassone (2008), Structural geology of the Fueguian Andes and Magallanes fold-and-thrust belt-Tierra del Fuego Island, *Geol. Acta*, *6*(1), 19-42.

Nelson, E. P. (1982), Post-tectonic uplift of the Cordillera Darwin orogenic core complex: Evidence from fission track geochronology and closing temperature-time relationships, *J. Geol. Soc London*, *139*(6), 755-761, doi:10.1144/gsjgs.139.6.0755.

Nelson, E. P., I. W. D. Dalziel, and A. G. Milnes (1980), Structural geology of the Cordillera Darwin-collisional-style orogenesis in the southernmost Chilean Andes, *Eclogae Geol. Helv*., *73*, 727-751.

Olivero, E. B., and D. R. Martinioni (2001), A review of the geology of the Argentinian Fuegian Andes, *J. South Am. Earth Sci*., *14*, 175-188.

Olivero, E. B., and N. Malumián (1999), Eocene stratigraphy of southeastern Tierra del Fuego island, Argentina, *Am. Assoc. Petrol. Geol. Bull*., *83*, 295-313.

Olivero, E. B., and N. Malumián (2008), Mesozoic-Cenozoic stratigraphy of the Fuegian Andes, Argentina, paper presented at Geosur: Mesozoic to Quaternary Evolution of Tierra del Fuego and Neighbouring Austral Regions II: Geologica Acta, vol. 6, pp. 5-18.

Olivero, E. B., N. Malumián, and S. Palamarczuk (2003), Estratigrafía del Cretácico superior- Paleoceno del área de bahía Thetis, Andes Fueguinos. Argentina: acontecimientos tectónicos y paleobiológicos, *Rev. Geol. Chile*, *30*, 245-263.

Olivero, E. B., N. Malumián, S. Palamarczuk, and R. A. Scasso (2001), El Cretácico superior- Paleogeno del área del Río Bueno, costa atlántica de la Isla Grande de Tierra del Fuego, *Rev. Asoc. Geol. Argen*., *57* (3), 199-218.

Pankhurst, R. J., T. R. Riley, C. M. Fanning, and S. Kelley (2000), Episodic silicic volcanism in Patagonia and the Antarctic Peninsula: Chronology of magmatism associated with the break-up of Gondwana, *J. Petrol.*, *41*, 605-625, doi:10.1093/ petrology/41.5.605.

Parés, J.M., 2004. How deformed are weakly deformed mudrocks? Insights from magnetic anisotropy. In: Martin-Hernandez, F, Luneburg, C., Aubourg, C., Jackson, M. (Eds.), Magnetic fabric: methods and applications. Geological Society, 238. special publications, London, pp. 191–203.

Parés, J.M., van der Pluijm, B.A., Dinarès-Turell, J., 1999. Evolution of magnetic fabrics during incipient deformation ofmudrocks (Pyrenees, northern Spain). Tectonophysics 307,1–14

Pilger, R. (1984), Kinematics of the South American subduction zone from global plate reconstructions, *In*: Geodynamics of the Eastern Pacific Region, Caribbean and Scotia Arcs, edited by Cabre R., Geodynamic Series 9, *American Geophysical Union*, Washington D.C., U.S.A.

Poblete, F., P. Roperch, F. Hervé, M. Diraison, M. Espinoza, and C. Arriagada (2014), The curved Magallanes fold and thrust belt: Tectonic insights from a paleomagnetic and anisotropy of magnetic susceptibility study, *Tectonics*.

Prezzi, C. B., P. J. Caffe, M. P. I. Llanos, and M. J. Orgeira (2014), New paleomagnetic data from Upper Oligocene-Lower Miocene rocks of the Northern Argentine Puna-Southern Bolivian Altiplano: Constraining the age of vertical axis rotations, *J. Geodynamics*, *78*, 42-52.

Rabinowitz, P. D., and J. LaBrecque (1979), The Mesozoic South Atlantic Ocean and evolution of its continental margins, *Journal of Geophysical Research: Solid Earth*, *84*(B11), 5973-6002.

Ramos, V. A. (1989), Andean foothills structures in northern Magallanes Basin, Argentina, *Am. Assoc. Petrol. Geol. Bull*., *73*, 887-903.

Ramos, V. (1999), Plate tectonic setting of the Andean Cordillera, *Episodes*, *22*, 183-190.

Ramos, V. A., and A. Aleman (2000), Tectonic evolution of the Andes, paper presented at 31° International Geological Congress, Rio de Janeiro, Brazil, pp. 635-685.

Rapalini, A. E. (2007), A paleomagnetic analysis of the Patagonian Orocline, *Geologica acta*, *5*(4), 287-294.

Rapalini, A. E., H. Lippai, A. Tassone, and M. E. Cerredo (2005), An AMS and paleomagnetic study across the Andes in Tierra del Fuego, paper presented at 6th International Symposium on Andean Geodynamics (ISAG 2005, Barcelona), pp. 596-599.

Rochette, P. (1987), Magnetic susceptibility of the rock matrix related to magnetic fabric studies, *J. Struct. Geol*., *9*, 1015-1020.

Rochette, P., M.J. Jackson, and C. Aubourg (1992), Rock magnetism and the interpretation of anisotropy of magnetic susceptibility, *Rev. Geophys*., *30*, 209-226.

Rolando, A., L. A. Hartmann, J. O. S. Santos, R. R. Fernandez, R. O. Etcheverry, I. A. Schalamuk, and N. J. McNaughton (2002), SHRIMP zircon U/Pb evidence for extended Mesozoic magmatism in the Patagonian batholith and assimilation Hubbard, S.M., Covault, J. of Archean crustal components, *J. South Am. Earth Sci*., *15*, 267-283.

Rossello, E. A. (2005), Kinematics of the Andean sinistral wrenching along the Fagnano-Magallanes Fault Zone (Argentina-Chile Fueguian Foothills), paper presented at 6th International Symposium on Andean Geodynamics, Barcelona, pp. 623-626.

Sagnotti, L., A. Winkler, P. Montone, L. Di Bella, F. Florindo, M. T. Mariucci, F. Marra, L. Alfonsi, and A. Frepoli (1999), Magnetic anisotropy of Plio-Pleistocene sediments from the Adriatic margin of the northern Apennines (Italy): implications for the time-space evolution of the stress field, *Tectonophysics*, *311*(1), 139-153.

Sagnotti, L., C. Faccenna, R. Funiciello, and M. Mattei (1994), Magnetic fabric and structural setting of Plio-Pleistocene clayey units in an extensional regime: the Tyrrhenian margin of central Italy, *J. Struct. Geol*., *16*, 1243-1257.

Sagnotti, L., and F. Speranza (1993), Magnetic fabric analysis of the Plio-Pleistocene clayey units of the Sant' Arcangelo basin, southern Italy, *Phys. Earth Planet. Inter*., *77*, 165-176.

Sagnotti, L., F. Speranza, A. Winkler, M. Mattei, and R. Funiciello (1998), Magnetic fabric of clay sediments from the external northern Apennines (Italy), *Phy. Earth and Planet. Inter*., *105*(1), 73-93.

Sintubin M. (1994), Clay fabrics in relation to the burial history of shales, *Sedimentology*, *41*, 1161-1169.

Somoza, R. (1998), Updated Nazca (Farallon)-South America relative motions during the last 40 My: implications for mountain building in the central Andean region, *J. South Am. Earth Sci*., *11*(3), 211-215.

Somoza, R., and C. B. Zaffarana (2008), Mid-Cretaceous polar standstill of South America, motion of the Atlantic hotspots and the birth of the Andean cordillera, *Earth and Planetary Science Letters*, *271*(1), 267-277.

Somoza, R., and M. E. Ghidella (2005), Convergencia en el margen occidental de América del Sur durante el Cenozoico: Subducción de las placas de Nazca, Farallón y Aluk, *Rev. Asoc. Geol. Argent.*, *60*, 797-809.

Somoza, R., and M. E. Ghidella (2012), Late Cretaceous to recent plate motions in western South America revisited, *Earth and Planetary Science Letters*, *331*, 152-163.

Soto, R., J. C. Larrasoaña, L. E. Arlegui, E. Beamud, B. Oliva-Urcia, and J. L. Simón (2009), Reliability of magnetic fabric of weakly deformed mudrocks as a palaeostress indicator in compressive settings, *J. Struct. Geol*., *31*(5), 512-522, doi:10.1016/j.jsg.2009.03.006.

Speranza, F., L. Sagnotti, and M. Mattei (1997), Tectonics of the Umbria-Marche-Romagna Arc (Central northern Apennines, Italy): New paleomagnetic constraints, *J. Geophys. Res*., *102*(B2), 3153-3166.

Tarling, D.H., and F. Hrouda (1993), The magnetic anisotropy of rocks. Chapman & Hall, London, p. 217.

Torres-Carbonell, P. J., E. B. Olivero, and L. V. Dimieri (2008), Structure and evolution of the Fuegian Andes foreland thrust-fold belt, Tierra del Fuego, Argentina: paleogeographic implications, *J. South Am. Earth Sci*., *25*(4), 417-439.

Torres Carbonell, P.J., and L.V. Dimieri (2013), Cenozoic contractional tectonics in the Fuegian Andes, southernmost South America: a model for the transference of orogenic shortening to the foreland, *Geol. Acta*, *11*(3), 359-370.

Torres-Carbonell, P. J. T., L. V. Dimieri, and E. B. Olivero (2011), Progressive deformation of a Coulomb thrust wedge: the eastern Fuegian Andes Thrust-Fold Belt, *Geol. Soc., London, Special Publications*, *349*(1), 123-147.

Torres Carbonell, P.J., L.V. Dimieri, and E.B. Olivero (2013), Evaluation of strain and structural style variations along the strike of the Fuegian thrust-fold belt front, Argentina, *Andean Geol*., *40* (3), 438-457.

Torres-Carbonell, P. J., L. V. Dimieri, E. B. Olivero, F. Bohoyo, and J. Gal indo-Zaldívar (2014), Structure and tectonic evolution of the Fuegian Andes (southernmost South America) in the framework of the Scotia Arc development, *Global Planet. Change*, doi:10.1016/j.gloplacha.2014.07.019.

Weil, A. B., and A. J. Sussman (2004), Classifying curved orogens based on timing relationships between structural development and vertical-axis rotations, *Geol. Soc. Am. Spec. Paper*, *383*, 1-15.

Wilson, T. J. (1991), Transition from back-arc to foreland basin development in the southernmost Andes: stratigraphic record from the Ultima Esperanza District, Chile, *Geol. Soc. Am. Bull*., *103*, 98-111.

Winslow, M. A. (1981), Mechanisms for basement shortening in the Andean foreland fold belt of southern South America, in *Thrust and Nappe Tectonics, Geol. Soc. London Spec. Publ*., edited by McClay, K. R., and N. J. Price, *9*, 513-528.

PART V. Numerical modelling applied to restore crustal block kinematics into strike-slip deforming zones -first steps-

PART V. NUMERICAL MODELLING APPLIED TO RESTORE CRUSTAL BLOCK KINEMATICS INTO STRIKE-SLIP DEFORMING ZONES

-First steps-

In this part of the research I will report on an application of the paleomagnetic data investigated during the first phases of this research.

During a stage of 6 months at the Universidad de los Andes (Bogota - Colombia), I worked in collaboration with the professor assistant PhD. Natalia Gomez Perez, giving the first steps in the attempting to restore the initial configuration of a strike-slip deforming zone. It implies the development of a numerical modelling to solve an inverse time-reverse mathematical problem, because there is a lack of information of the initial conditions, but its effects can be known through geologic and geophysics information.

Over the last decades, physical and numerical modelling has been increasingly used to simulate tectonic processes as a way to better understand the geologic record. The models provide a valuable insight into the development history and the mechanisms responsible of deformation at all scales.

The numerical modelling is the process by which a simplified mathematical reality from a more complex physical reality is constructed, through the approximate solution of equations chosen because they can describe dynamic processes of the earth.

A numerical model can predict earth kinematics as the mathematical equations describe its dynamics. The predictive power varies in function of the model complexity. The accuracy of those predictions are often overwhelmed by difficulties in the fully characterization of the geologic setting (in three dimensions), in providing appropriate theoretical descriptions, in uncertainties in measuring, and in numerical problems with analytic tools.

According to [*Mercier and Faust*, 1981; *Ferziger and Peric* 2002; *Ismail-Zadeh and Tackley*, 2010], the basic components of the numerical modeling are (Figure 1):

1. *Physical model*, it depicts our understanding of the physical system. It constitutes the geodynamic problem to solve.

2. *Mathematical model*, it consists in translating the geodynamic process into a mathematical system, a set of partial differential equations and its boundary conditions. The mathematical models can be solved using analytical solutions, numerical models and computational methods. The conservation equations can be written in many different forms, depending on

the coordinate system: Cartesian, cylindrical, spherical, etc. The choice depends on the target of the problem, and may influence the discretisation method and grid type to be used. The numerical grid is a discrete representation of the geometric domain, on which the problem has to be solved. There are structured (orthogonal) and unstructured grids.

3. A *discretisation method* to convert the mathematical equations into discrete equations to be solved numerically. The most popular methods are the finite difference, finite element, finite volume and spectral methods. These facilitate the visualization of the results.

4. *Numerical methods* to solve the discrete equations. It means a procedure that permits us to obtain the solution for the mathematical problem with an arbitrary precision in a finite number of steps that can be performed rationally. The number of step depends on the desired accuracy.

5. *Computer code* (software) to be developed or to be used to numerically solve the discrete equations.

6. Results of numerical modelling. These must be validated, calibrated and interpreted in the context of the physical system.

1. Physical model

As the starting point for the modelling we use the physical model of the LOFZ deforming zone investigated in the first part of this research, which describes a series of small blocks (max. size 13 km) that move along the fault zone following the fault slip parameters. Contemporaneously to the displacement, those blocks can rotate depending on their aspect ratio and orientation with respect to the fault [*Hernandez-Moreno et al*., 2014]. While equidimensional blocks can undergo very large rotations (150°-170°), elongated blocks, subparallel to the LOFZ do not rotate (Figure 2).

Rotation pattern across the dextral LOFZ is markedly asymmetric. East of the fault and along of it, rotations are mainly clockwise. In turn, west of the LOFZ rotations are clockwise of counterclockwise in function of high or low interface coupling degree, respectively. This rotation pattern responds to a quasi-continuous crust kinematics [*McKenzie and Jackson*, 1983; *Nelson and Jones*, 1987; *Sonder et al*., 1994].

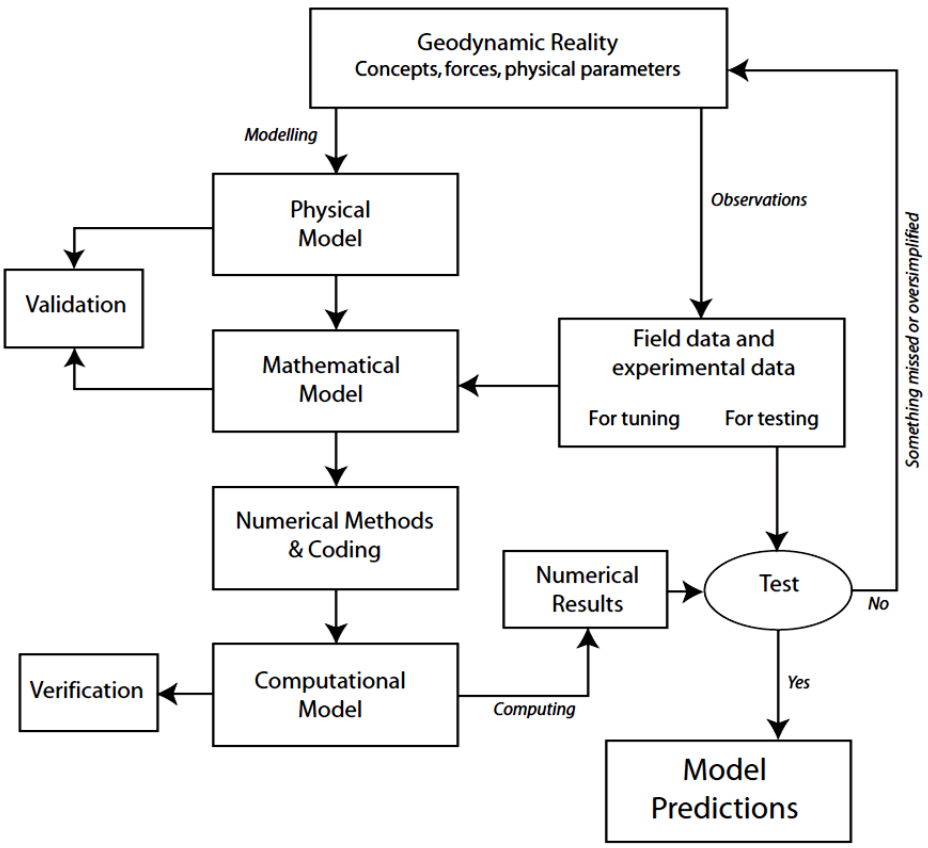

Figure 1. Flowchart depicting the numerical modelling process. Modify from *Ismail-Zadeh and Tackley* [2010].

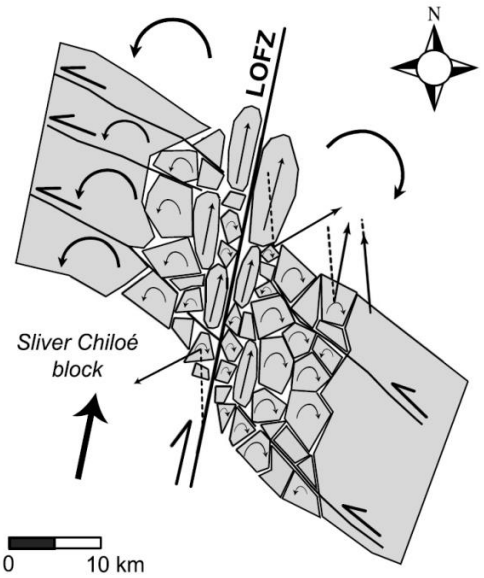

Figure 2. Quasi-continuous kinematic model describing the crustal behavior inside the LOFZ deforming zone [*Hernandez-Moreno et al*., 2014].

Specifically, a zone east of the LOFZ between 39°S and 39.40°S was selected because of the high concentration of paleomagnetic rotation vectors reported in the first part of this research (Figure 3A). Both the shape and size of the different blocks inside the LOFZ deforming zone were chosen from the paleomagnetic data distribution, resulting in a total number of 41 blocks (Figure 3B).

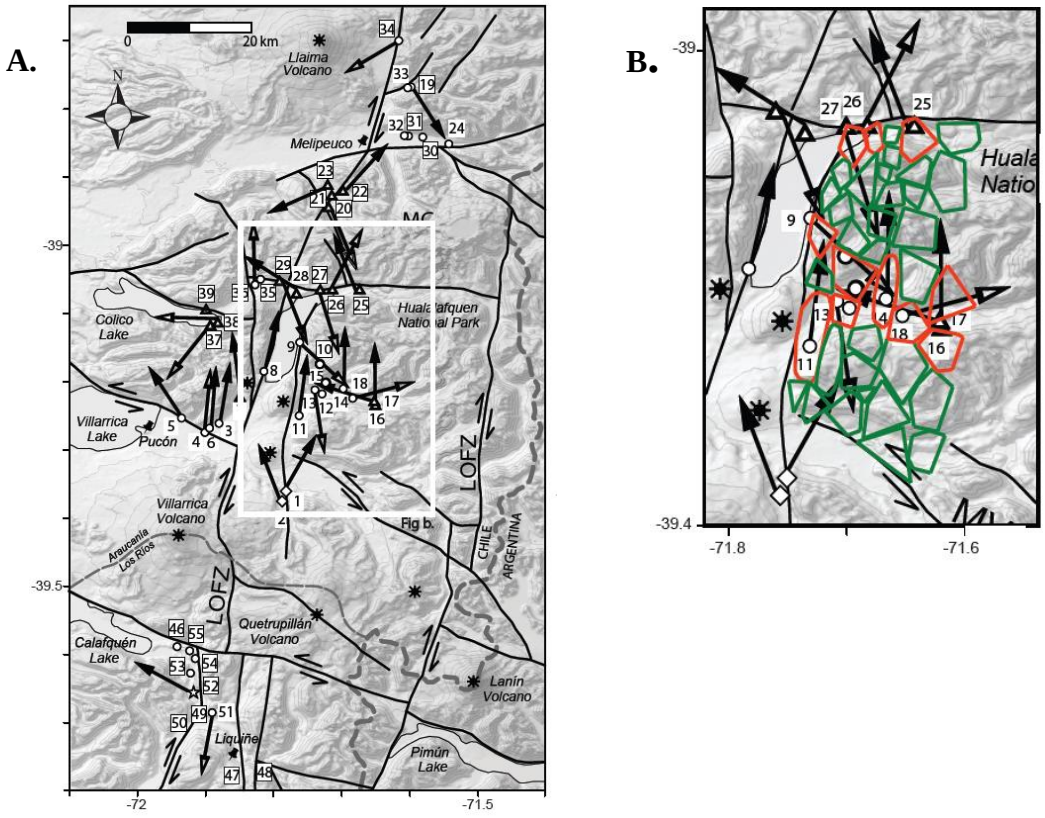

Figure 3. A) The white box encloses the selected area for the numerical modelling. B) Selected area zoom in. Red blocks have a paleomagnetically detected rotation value while in green are represented the blocks with rotation value come from the equation of the best-fit line of the clockwise rotations east of the LOFZ (Figure 9 therein *Hernandez-Moreno et al*., [2014], Part I of this thesis).

Restore the starting conditions of the crust inside the LOFZ deforming zone by numerical modelling, implies a very complex problem: first the crust subdivision in small blocks, and then the simultaneous translation and rotation of more than 40 irregular blocks inside a restricted area, where blocks can interact more than two at a time.

Virtually we can control only the initial conditions of the problem, because of the tangential force due to the interaction between blocks. During block interactions, both non uniform linear (velocity change over time) and circular (torque) motions are going to be generated in function of the point where the tangential force is applied. Thus, this geophysical problem can be defined as the elastic collision (kinetic energy is conserved) of irregular rigid blocks. Assuming conservation of both momentum and kinematic energy, it is possible to calculate the final velocities after two-body collisions.

The collision will become inelastic if part of the kinematic energy changes to some other forms of energy during the collision, as for example friction between blocks or heating.

2. State-of-the-art of the numerical modelling of crustal block rotation

During the 1980s, mathematical models and analytical solutions mostly related to describe crust large-scale and long-term deformation have been developed, especially for continental collision zones. In one model, known as the "thin viscous sheet model", the continental lithosphere is regarded as a thin continuous material obeying a Newtonian rheology, overlying an inviscid substrate [*Bird and Piper*, 1980; *England and McKenzie*, 1982, 1983]. The thin viscous sheet model assumes that the base and the top of the lithosphere are free of traction and that vertical gradients of the horizontal velocity are negligible. But those formulations ignore the role of faulting in lithospheric deformation [*England and McKenzie*, 1982].

McKenzie and Jackson [1983] were the first that considered the case where at the surface distributed deformation is taken up by motion on faults which separate the zone into blocks which can rotate about a pole, and applied this concept to the strike-slip faults. In their mathematical models the displacement rate on the faults, their strike and the finite rotations of blocks are all controlled by the velocity gradient, which is considered constant everywhere throughout the deforming zone at all times. However they continued to use the thin viscous sheet model and the equations by *England and McKenzie* [1982, 1983], assuming that enough faults are active at the same time and that the scale of the deformation is large compared with the size of the blocks bounded by faults in the deforming zone. According to the authors, although where faults intersect the surface the velocity filed is discontinuous, the movement of rigid blocks, separated by faults and with small sizes compared with the width of the deforming zone, can approximate the continuous deformation if the angle between the margins of the zone and the faults is related to the velocity gradients.

Then *England et al*. [1985] and *Sonder et al*. [1986] carried out different analytical solutions for the deformation of this thin viscous sheet (Newtonian fluid) governed by an imposed velocity

vector or shear stress parallel to a considered boundary, therefore under strike-slip conditions. This boundary may be regarded as a zone of weakness, across which some of the relative motion is taken up but which nevertheless exerts a tangential stress on the continental lithosphere [*Sonder et al*., 1986]. Thus, the authors predict the deformation length scale under strike-slip conditions as considerably shorter across-strike than for deformation under compressional or extensional boundary conditions.

Sonder et al. [1986] also calculated the amount of vertical-axis rotation, defining it as the angle through which a small, horizontal, rigid block would rotate if it was floating on the deforming fluid making reference to the *Mckenzie and Jackson* [1983] statements, and the distance from the fault where rotation should die out. The rate of this rotation would be half of the vertical component of the vorticity. Thus, comparisons between paleomagnetic data and their mathematical approximations are possible only if the horizontal dimensions of the blocks are small compared with lengths over which the underlying flow varies.

In general all the equations referred by the previous authors describe the crust rheology, vertically averaged by a single power law exponent *n*, which indicates the relative contributions of brittle and ductile behavior to the average lithospheric strength [*Sonder and England*, 1986]. It means approximating the deformation that may occur under several different regimes, including brittle deformation near the surface, high-stress plasticity at depth, and steady state creep at greater depths [*Sonder et al*., 1986].

The previous mathematical solutions define the principles of the quasi-continuous models of crustal behaviour, which consider as rotation mechanism the velocity gradient in the underlying ductile crust that makes rotate passively the crustal blocks in the upper brittle crust [*Beck*, 1976; *McKenzie and Jackson*, 1983; *Lamb*, 1987; *Nelson and Jones*, 1987; *Salyards et al*., 1992; *Sonder et al*., 1994; *Piper et al*., 1997; *Randall et al*., 2011].

In the last years it seems that this field of geodynamics has been virtually abandoned, while all the efforts to try to understand the rotation pattern related to strike- slip faults have been focused on the paleomagnetic evidence of it, leaving apart further applications of these data.

3. 2D modeling of a random polygon which rotates and translates

When a numerical modelling is in development, the starting point is to reduce the problem as simple as possible. Therefore, as we are concerned to the first step of initial LOFZ configuration restoration, we selected a simple problem: the 2D modelling of an irregular, random polygon framed on the flat surface of a fixed Cartesian coordinate system (*x*-*y* plate), which translates while rotating around a vertical-axis of rotation, orthogonal to the flat surface (Figure 4).

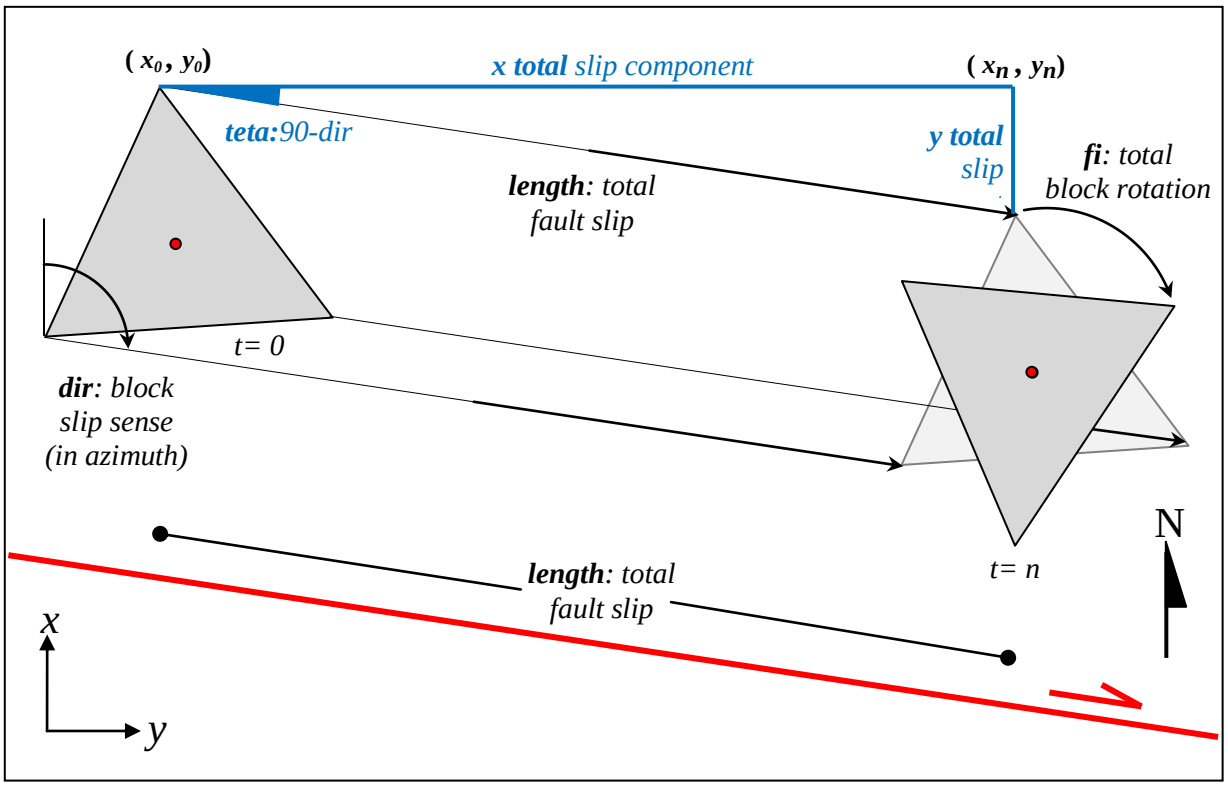

Figure 4. Plan view of a random polygon inside the deforming zone of a strike-slip fault. The polygon simultaneously translates and rotates. Input parameters considered in the Matlab code are specified. Red point: geometric center and rotation axis.

The resulting polygon motion is a chain of rotation through a vertical axis followed by translation during different intervals of time, until both the total block rotation (*fi*) and total fault slip (*length*) are reached (Figure 5). To develop the mathematical model we considered the linear motion parameters as position (*x*,*y* coordinates), velocity and acceleration, as well as angular units as rotation angle (θ), angular velocity (change in angle per change in time, $w = \Delta\theta/\Delta t$), and total rotation ($\theta = \theta_0 + wt$). We used Matlab for Student Version (R2014a) to develop the code of algorithms (Appendix 1.A).

The first step consists in defining the Matlab code input parameters: polygon slip sense in azimuth according to its location and the fault slip sense (*dir*), total fault slip (*length*), fault slip rate (*rate*), and rotation in degrees (*fi*) (step 1- Appendix 1.A, Figure 4). To create the random polygon, first we have to define a work area framed in a Cartesian coordinate system (step 2- Appendix 1.A), and then select randomly (x,y) coordinates inside of this area, until the irregular polygon is created (step 3 - Appendix 1.A).

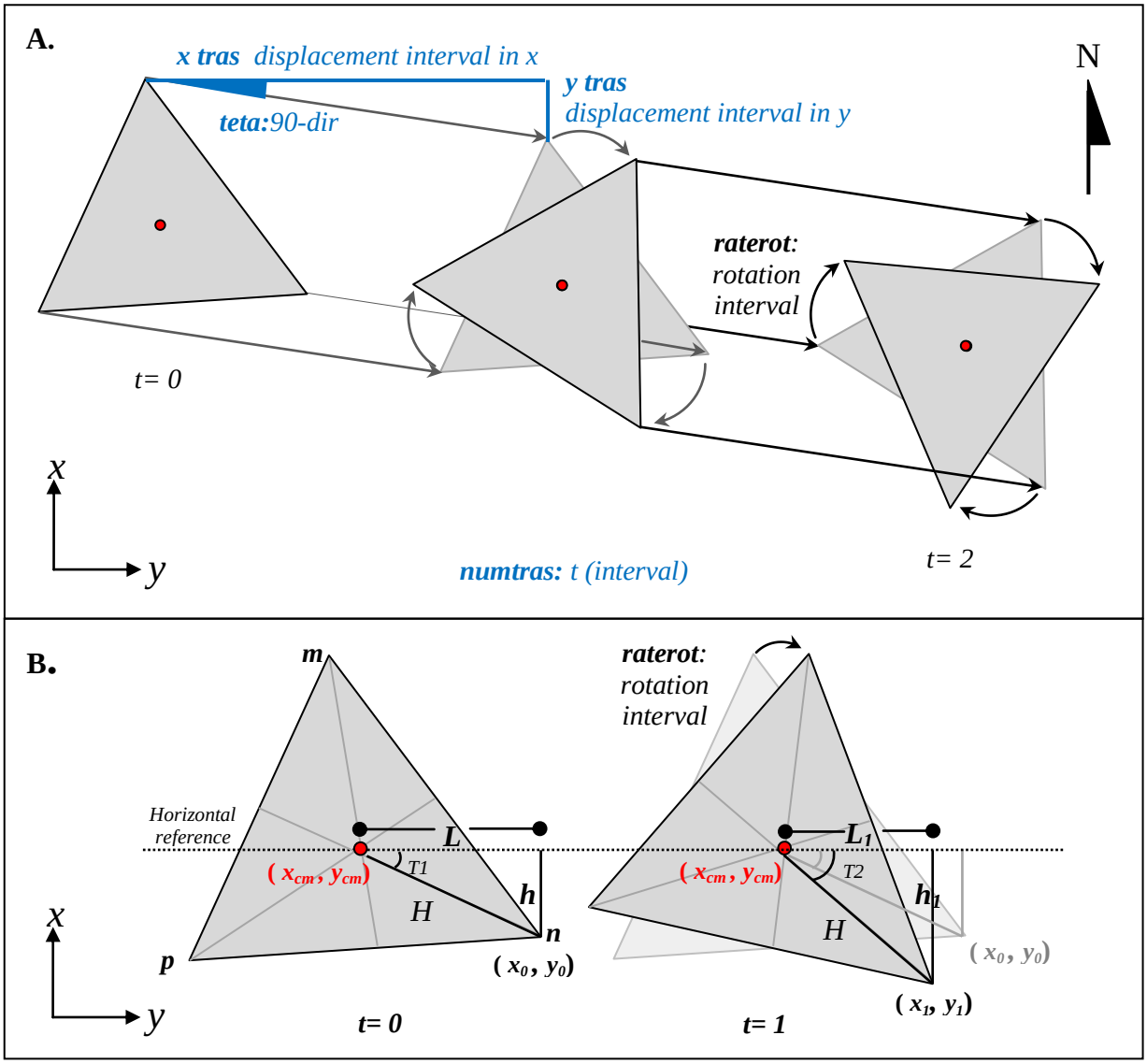

Figure 5. Sketch of the Matlab code. A) During different intervals of time a polygon is going to describe rotation through the geometric center (red point) as axis rotation followed by translation. This process is going to be repeated until both the total slip fault and the total block rotation are reached. B) Detail of the block rotation procedure. ***T1***: angle between the horizontal and the line that join the geometric center to each polygon vertex. Adding or subtracting ***raterot*** to *T1*, in case of clockwise or counterclockwise respectively, we can find ***T2***, and therefore find the new vertices position after rotation.

Before carrying out the polygon rotation, it is essential to fit the angular reference. In paleomagnetism, rotation vectors consider 0º of azimuth coinciding with the geographic north and increasing clockwise, while in the Matlab reference 0º of azimuth is coinciding with the East (90º of azimuth in paleomagnetism) increasing counterclockwise (step 4 - Appendix 1.A).

Rotation about an axis can be defined by specifying the axis and the angular rate of rotation around this. If we assumed that our polygon has homogeneous density, its mass center will correspond to the geometric center. To simplify the numerical modelling we assumed that the geometric center represents the polygon rotation axis (step 5 - Appendix 1.A). As we don't know how long the polygon took to complete the total rotation, to define the angular rate of rotation (*raterot*, Figure 5) we assumed that the total rotation (*fi*) is reached at the same time when the total fault slip is completed (*length*). Then, the ratio between the total fault slip and the rate slip indicates us how many intervals of time (*numtras=length/rate*) are required to complete both total rotation and total translation (step 6.1 - Appendix 1.A, Figure 5). To obtain the rotation amount during each interval of time (*raterot*, Figure 5) it is enough to calculate the ratio between the total block rotation (*fi*) and the number of intervals of time (step 6.2 - Appendix 1.A).

During each interval of time the polygon will rotate by a *raterot* amount, therefore their vertices will change to *x,y* coordinates. The new vertex position can be calculated through simple trigonometric relations. For instance, in the case of vertex *n* in Figure 5B:

1. To start the angle between the horizontal and the line joining the geometric center with the vertex *n* must be calculated (*T1*). As since the beginning the coordinates of the vertex (x_0 ,y_0) and the geometric center (x_{cm} ,y_{cm}) are known, the sides *L*, *h*, and *H* of the triangle formed between the horizontal and the line joining the vertex and geometric center, can be deduced (step 8.1-Appendix 1.A).

   L= vertex x_0 coordinate - *x* geometric center coordinate
   h= vertex y_0 coordinate - *y* geometric center coordinate

   $$H = \sqrt{L^2 + h^2}$$

   Then, using a trigonometric relation *T1* can be derived (step 8.2-Appendix 1.A).

   $$T_1 = \sin^{-1}(h/H)$$

2. In the example the polygon rotates in a clockwise sense. So for the rotation is enough to add *raterot* to *T1* (*T2=T1+raterot*).

3. As we already know *T2* and considering that *H* is constant, the new magnitude of the triangle sides *h1* and L_1, can be derived:

   $$h_1 = \sin T_2 * H \quad ; \quad L_1 = \cos T_2 * H$$

4. The new position of the vertex *n* (x_1, y_1) coordinates comes from adding the geometric center coordinates to the new values of L_1 and h_1, respectively; because the geometric center does not coincide with the origin of the Cartesian system (step 8.3, Appendix 1.A).

$$x_1 = L_1 + x_{cm} \quad ; \quad y_1 = h_1 + y_{cm}$$

Now the polygon is ready to translate. Considering that the polygon is framed into the *x*-*y* plane of the Cartesian coordinate system, and based on total slip vector (sense: the polygon slip sense in azimuth; magnitude: the total fault slip), the *x* and *y* total slip components can be calculated (*xtotal slip* and *ytotal slip* in Figure 4, step 6.3 - Appendix 1.A). The ratio between *x* and *y* total slip components and the number of time intervals, give us the translation amount to each interval (*xtras*, *ytras*) (step 6.3 - Appendix 1.A, Figure 5A). Therefore to translate the polygon the *xtras* and *ytras* values must be added or subtracted -in function of the sing- to the respective *x*, *y* coordinates of each polygon vertices and also to the geometric center.

In function of the number of intervals of time (*numtras=length/rate*) the Matlab code reproduces the polygon rotation followed by translation until the total fault slip and block rotation are reached (step 8 - Appendix 1.A).

References

Beck, M. E. (1976), Discordant paleomagnetic pole positions as evidence of regional shear in the western Cordillera of North America, *Am. J. Sci*., *276*, 694–712.

Bird, P., and K. Piper (1980), Plane-stress finite element models of tectonic flow in southern California, *Phys. Earth Planet. Inter*., *21*, 158–175.

England, P., G. Houseman, and L. Sonder (1985), Length scales for continental deformation in convergent, divergent, and strike-slip environments: Analytical and approximate solutions for a thin viscous sheet model, *J. Geophys. Res*., *90*(B5), 3551–3557, doi:10.1029/JB090iB05p03551.

England, P., and D. McKenzie (1982), A thin viscous sheet model for continental deformation, *Geophys. J. Roy. Astron. Soc*., *70*, 295–321, doi:10.1111/j.1365-246X.1982.tb04969.x.

England P., and D. McKenzie (1983), Correction to: a thin viscous sheet model for continental deformation, *Geophys. J. R. Astron. Soc*. *73*, 523, 1983.

Ferziger, J. H., and M. Perić (2002), Computational methods for fluid dynamics (Vol. 3). Berlin: Springer.

Ismail-Zadeh, A., and P. Tackley (2010), Computational methods for geodynamics, Cambridge University Press.

Lamb, S. H. (1987), A model for tectonic rotations about a vertical axis, *Earth Planet. Sci. Lett*., *84*(1), 75–86, doi:10.1016/0012-821X(87)90178-6.

McKenzie, D., and J. Jackson (1983), The relationship between strain rates, crustal thickening, palaeomagnetism, finite strain and fault movements within a deforming zone, *Earth Planet. Sci. Lett*., *65*(1), 182–202, doi:10.1016/0012-821X(83)90198-X.

Mercer, J.W., and C. R. Faust (1981), Ground-Water Modelling, National Water Well Association.

Nelson, M., and C. Jones (1987), Paleomagnetism and crustal rotations along a shear zone, Las Vegas Range, southern Nevada, *Tectonics*, *6*(1), 13–33, doi:10.1029/TC006i001p00013.

Piper, J., O. Tatar, and H. Gürsoy (1997), Deformational behaviour of continental lithosphere deduced from block rotations across the North Anatolian Fault Zone in Turkey, *Earth Planet. Sci. Lett*., 150, 191–203.

Ramberg, H., H. A. Koyi, and N. S. Mancktelow (2001), Tectonic modeling: a volume in honor of Hans Ramberg, edited by Hemin A. Koyi and Neil S. Mancktelow, *Geological society of America*, *193*.

Randall, K., S. Lamb, and C. Mac Niocaill (2011), Large tectonic rotations in a wide zone of Neogene distributed dextral shear, northeastern South Island, New Zealand, *Tectonophysics*, *509*(3–4), 165–180, doi:10.1016/j.tecto.2011.05.006.

Salyards, S. L., K. E. Sieh, and J. L. Kirschvink (1992), Paleomagnetic measurement of nonbrittle coseismic deformation across the San Andreas fault at Pallett Creek, *J. Geophys. Res*., *97*(B2), 12,457–12,470, doi:10.1029/92JB00194.

Sonder, L., and P. England (1986), Vertical averages of rheology of the continental lithosphere: Relation to thin sheet parameters, *Earth Planet. Sci. Lett*., *77*, 81–90.

Sonder, L. J., P. C. England, and G. A. Houseman (1986), Continuum calculation of continental deformation in transcurrent environments, *J. Geophys. Res*., *91*, 4797–4810, doi:10.1029/JB091iB05p04797.

Sonder, L. J., C. H. Jones, S. L. Salyards, and K. M. Murphy (1994), Vertical axis rotations in the Las Vegas Valley Shear Zone, southern Nevada: Paleomagnetic constraints on kinematics and dynamics of block rotations, *Tectonics*, *13*(4), 769–788, doi:10.1029/94TC00352.

APPENDIX 1.A. MATLAB CODE

1.A. 2D modeling of a random block which contemporaneously rotates and translates

```
clc;
close all

% 1. INPUT PARAMETERS
The user can setup the input parameters in the command window using the Matlab
function "prompt =". These can be change every time.

%1.1. Block slip sense in azimuth (clockwise from north=0°) according to the its
position and the fault slip sense. For instance, as in the  Figure 4-Part V the
considered block is located to the right of a dextral fault of azimuth 100°,
then the block slip sense would be 350°.

prompt = 'Specify block slip sense in azimuth (N zero):';
dir=input(prompt);

%1.2. Total fault slip

prompt = 'Specify total fault slip (no units): ';
length = input(prompt);

%1.3. Fault slip rate

prompt = 'Specify fault slip rate (no units): ';
rate = input(prompt);

%1.4. Total block rotation, (+) when clockwise and (-) when counterclockwise

prompt = 'Specify the total block rotation, (-) counterclockwise and (+)
clockwise: ';
fi = input(prompt);


% 2. DEFINING THE WORK AREA
Define the area using a the x-y plane of the Cartesian system. In this case, a
random area of 1x10 km is going to be defined by 2 matrices. Each matrix depict
the x,y coordinates of each area corner.

x=[0 10 10 0]
y=[1 1 0 0]

plot(x,y)       % Plot the area


% 3. CREATING A RANDOM POLYGON INSIDE THE WORK AREA
Using the function "rand" is possible to select the x,y vertices coordinates
that are going to define the polygon, from the study area matrices x and y.
Because of the matrices x and y have different range of values, x (0 to 10) and
y (0 to 1), is necessary use the function "rand" separately.
```

```
%3.1. Create random points from matrix x (0 to 10)

n = 3           % Define the number of polygon vertices.
a = 0; b = 10   % Limits within which will be selected the polygon
                  vertices, coinciding with the minimum and maximum
                  values of the matrix x.

x1= a + (b - a) * rand(1, n);


%3.2. Create random points from matrix y (0 to 1)

n = 3           % Define the number of polygon vertices.
a = 0; b = 1    % limits within which will be selected the polygon
                  vertices, coinciding with the minimum and maximum
                  values of the matrix y.

y1= a + (b - a) * rand(1, n);


% 3.3. Draw the polygon plotting their x,y vertices

plot(x1,y1)
hold on;        % We have to add another elements to this figure
grid on;

% 3.4. But the polygon is open. Repeating the first x,y coordinate vertex after
the last one to close the polygon.

vtx=[x1(:),y1(:)] % This matrix contains the coordinates x,y of the
                    vertices of the polygon.

V1=vtx(1,:)       % The first and the last vertices have to be  V2=vtx(n,:)
selected from the previous matrix.


plot([V1(1,1) V2(1,1)],[V1(1,2) V2(1,2)])   % Plotting the first and
                                              the last vertices, the
                                              polygon is going to be
                                              close.
```

% 4. FITTING THE ANGULAR REFERENCE

Matlab reference system considers the north at 90° of azimuth increasing in a counterclockwise sense, instead the rotation values have been referred to north at 0° increasing clockwise. To fit the angular values to the matlab reference is necessary do this passage:

```
teta=90-dir  % To fit the block slip sense specified in the step 1.1.
fi=-fi       % To fit the total block rotation specified in the step
               1.4.
```

% 5. THE POLYGON GEOMETRIC CENTER

It can be calculated using the simple equation for a polygon of *n* sides: Xcenter=(x1+x2+x3)/*n* and Ycenter=y1+y2+y3)/*n*

```
center=sum(vtx) % The command "sum" adds the all values of each column
                  of matrix vtx. Column 1 (x vertex coordinates),
                  column 2 (y vertex coordinates).
```

```
Xcenter=[center(:,1)]/n;        % The x,y coordinates of the geometric
Ycenter=[center(:,2)]/n;        center will be obtained dividing center
                                by the polygon side number (n=3).

plot(Xcenter,Ycenter,'r')  % Plot the polygon geometric center in red
hold on;                   % We have to add another elements to this
                             figure


% 6. PREPARING THE POLYGON FOR THE ROTATION AND LINEAR MOTION
%6.1. Calculate how many times (intervals of time) the polygon has to translate
and simultaneously rotate to reach the total slip and total rotation.

numtras=(length/rate)


%6.2. Rotating the polygon. Find the amount of rotation during each interval of
time:

raterot=fi/numtras


%6.3. Translating the polygon. Find the amount of displacement or translation
during each interval of time:

-First find the total displacement x and y components, in function of the total
slip vector:

xtotal=cosd(teta)*length
ytotal=sind(teta)*length


-Then the polygon translation in x and y during each time interval can be get
dividing these components by numtras:

xtras=xtotal/numtras
ytras=ytotal/numtras

%.....

% FIRST TO COME IN TO THE LOOP. Rename the matrix that contains the polygon
vertices x,y and the initial values of the geometric center X,Y coordinates to
keep the original values:

vtc=vtx;
Xcm=Xcenter;
Ycm=Ycenter;

display(xtras);
display(ytras);
display(vtc);
```

```
%8. DISPLACEMENT AND ROTATION LOOP

% As calculations of translation and rotation should be repeated as many times
as numtras. It is possible using the command "loop"

for i=1:numtras
      vm=vtc;
      vtc=zeros(n,2);

   % POLYGON ROTATION (Figure 5B)
   % Calculate the angles between the horizontal and the lines that
     joint the geometric center to each polygon vertex (T1):

   for j=1:n              % 8.1. Calculating the angle…
       L=vm(j,1)-Xcm;
       h=vm(j,2)-Ycm;
       H=((L^2)+(h^2))^(1/2);

   % 8.2. Then add or subtract it to the raterot in case of clockwise or
   counterclockwise (T2) in function of the quadrant where the vertex is
   located:

   %If the vertex is located at the second quadrant of the
   Cartesian coordinate system:
      if ((L<0)&&(h>0))
         T1=acosd(L/H);
         T2=T1+raterot;

   % If the vertex is located at the third quadrant of the
   Cartesian coordinate system:
      elseif((L<0)&&(h<0))
         T1=-(acosd(L/H));
         T2=T1+raterot;

   % If the vertex is located at the first and fourth quadrant
   of the Cartesian coordinate system:
      else
          T1=asind(h/H);
          T2=T1+raterot;
      end

   % 8.3. NEW VERTEX POSITION AFTER ROTATION
      X=cosd(T2)*H+Xcm;
      Y=sind(T2)*H+Ycm;

      vtc(j,1)=X;    % Each time the matrix vtc is going to be replace
      vtc(j,2)=Y;      by new x,y vertex

   end


   % POLYGON TRANSLATION
   % After the rotation, the polygon is going to be translated xtras
     amount. Thereby after the translation the x,y coordinates of the
     vertex will change again:

   vtc(:,1)=vtc(:,1)+xtras;
   vtc(:,2)=vtc(:,2)+ytras;

   % And the geometric center coordinates too:
```

```
    Xcm=Xcm+xtras;
    Ycm=Ycm+ytras;


% DRAWING THE RESULTS

  plot(vtc(:,1),(vtc(:,2)));
  hold on;
  grid on;

% But the polygon is going to be open. The procedure is the same followed at the
the step 3.3: create a new matrix with the x,y vertices of the polygon to
identify the first and repeat it in the last position of the polygon matrix.

  V1=vtc(1,:);     % First polygon vertex
  V2=vtc(n,:);     % Last polygon vertex


  % Plot the line that joins the first and the last vertices to close
    the polygon.

  plot([V1(1,1) V2(1,1)],[V1(1,2) V2(1,2)]);

  display(vtc);

  drawnow
  pause(0.1);


end
```

PART VI. Conclusions and remarks

PART VI. CONCLUSIONS AND REMARKS

This research, besides providing a new set of paleomagnetic vertical-axis rotations, gives a contribution to the understanding of the rotation pattern related to strike-slip faults and the kinematics and geodynamics that can describe it; these have been very controversial topics during the last 30 years.

In this section I will synthetize the most outstanding conclusions of my thesis, as the specific conclusions are at the end of each chapter.

The paleomagnetic analysis of 98 sites (Oligocene to Pleistocene volcanics and Miocene granites) gathered along the Liquiñe-Ofqui fault zone (LOFZ) and the adjacent fore-arc in central-south of Chile (38°S-41°S), revealed a very recent (5 Ma) asymmetric rotation pattern that does not completely match with any of the kinematic models proposed so far to describe crust behavior.

East of the LOFZ there is an outstanding CW rotation pattern with rotation values increasing toward the fault (up to 150°-170°) and systematically decreasing east away from the fault until they fade out at ~10 km. In turn, west of the LOFZ and therefore along the fore-arc, a CCW rotation pattern dominates. Around 39°S (Villarrica domain) ubiquitous CCW rotations reaching 170° have been observed. Conversely at 40°-41°S (Ranco-Osorno domain) and adjacent to the LOFZ (fore-arc eastern margin), CW rotations up to 136° before evolving to CCW rotations at ~30 km from the fault have been documented. These CCW rotations do not diminish moving away from the LOFZ, as sites at 42ºS (Chiloé Island) and ~130 km away from the LOFZ yield systematic CCW rotations between 27° and 164º (Figure 1).

Furthermore, at ca. 39ºS paleomagnetic sites adjacent to the LOFZ do not document any rotation.

6.1. Kinematic model of block rotation

The reported rotation sense distribution suggests that the dextral LOFZ kinematics drives the CW rotations, not the CCW rotations along the fore-arc west of it. Conversely, the CCW rotations are related to the NW sinistral strike-slip faults cutting the fore-arc.

From significant variations of rotation amount between closely spaced paleomagnetic sites, I document that the upper crust inside the LOFZ deforming zone is broken in blocks of maximum size of ~2 km, clearly smaller than the width of the deforming zone (~20 km). Only west of the LOFZ at ca. 39ºS a maximum block size of 10 km was found. There, paleomagnetic data distribution has been interpreted as due to the occurrence of unrotated elongated blocks parallel to the fault, which are moving northward following LOFZ kinematics. This is in agreement with both

Lamb [1987] and *Randall et al*., [2011], who explained that the rotation pattern is strictly dependent upon block aspect ratio.

Blocks size suggests similarly shallow detachment depth and brittle-ductile transition as well as high heat flow, consistently with the occurrence of andesitic volcanoes along fault trace.

Small block size (~2 km) documented further west away from the LOFZ (~130 km, Chiloé Island) reflects the tectonic deformation of the thinner fore-arc crust close to the trench that should be made by a chaotic mélange of upper crust slices detached from subducting plate and accreted to wedge.

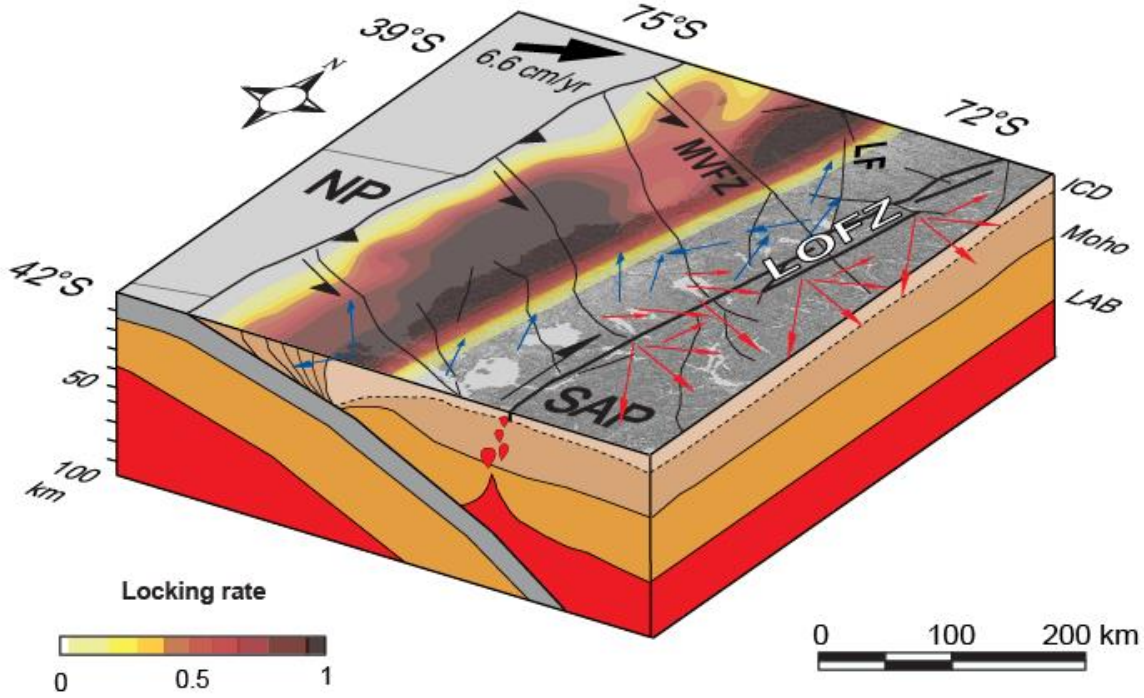

Figure 1. Diagram showing the rotation pattern along the Chiloé fore-arc sliver and adjacent to the LOFZ (southern Chile), and its relation with the interplate locking. Red (blue) arrows represent CW (CCW) rotation. Arrow size is directly proportional to the rotation value. Zones of high (low) interplate locking are related to CW (CCW) rotation pattern. The subducted slab geometry, the ICD intercrustal density discontinuity, the Moho of the oceanic and continental crusts, and the LAB Lithosphere-asthenosphere boundary are referred to the 3D density model by *Tassara et al*. [2006]. Locking rate by *Moreno et al*. [2011]. SAP South American plate, NP Nazca plate, MVFZ Mocha-Villarrica Fault Zone, LF Lanalhue fault, LOFZ Liquiñe-Ofqui fault zone.

Overall, the rotation pattern - small (1-10 km) blocks, rotation increase toward the LOFZ fault, CW (CCW) rotation related to dextral (sinistral) strike-slip faults - yields a quasi-continuous kinematic model of crust behavior along both the LOFZ and the NW sinistral strike-slip faults (Figure 1). Neither the continuous models nor the discontinuous ones can entirely explain the rotation pattern features.

The model specifically proposed for the Chiloé fore-arc by *Beck et al*. [1993] cannot explain the CCW rotation pattern reported in this research, because it considers large lens-shaped blocks (>100 km width), which should rotate CCW as the consequence of NE-SW and NW-SE right-lateral strike strike-slip faults. But in fact there is no evidence of such dextral faults within the fore-arc. Moreover, *Beck et al*. [1993] do not consider the occurrence of CW rotation west of the LOFZ, documented in the easternmost 30 km of the fore-arc adjacent to LOFZ at 40º-41ºS.

6.2. Block rotation dynamics

In general, the kinematic models proposed to try to explain the rotation pattern along strike-slip faults consider two options as the mechanism driving the rotation:

(i) Continuous and quasi-continuous models: the flux of the ductile material beyond the upper fragile crust, which can be or not decoupled from it (e.g. *Sonder et al*., [1994] and *Lamb* [1987], respectively)

(ii) Discontinuous models: the shear applied directly along the faults bounding elongated blocks located in the upper fragile crust and inside the strike-slip fault deforming zones [*Freund*, 1970; *Garfunkel and Ron*, 1985].

As this study documents, the LOFZ rotation pattern can indeed be explained by the quasi-continuous models. Those models establish that although the upper crust deforms in a discontinuous way by faulting, this deformation represents only the failure of the outermost, brittle layer of the lithosphere, and not of the lithosphere as a whole [*England and McKenzie*, 1982]. Therefore applying the equations of *the thin viscous sheet* [*England and Wells,* 1991; *Sonder and England*, 1986], the quasi-continuous models assume a continuous viscous fluid to depict the whole lithosphere, predicting that the rotation in the upper crust passively reflects the flow of this viscous underlying medium. However some authors following the *thin viscous sheet* statements are aware that the rotation related to strike-slip faults reflect the dominance of the brittle layer in accommodating strain (e.g. *Sonder et al*. [1986]).

Faults kinematics effects on the upper crust deformation is also evident in the modelling of GPS data, because velocity fields calculated including faults in the upper crust yielded results fitting better the current crust displacement [*Moreno et al*., 2008].

Thus the differences between the two mechanisms proposed to explain block rotation could be reduced to the crust rheology (thus crust material) considered by each model. As *England and McKenzie* [1982] explained, if the considered material is Newtonian with a power law rheology n = l, typical of material of the ductile lower crust, the deformation associated with an influx of material (e.g. approximating an indenter) is of much greater lateral dimension than the width of the indenter. Conversely, when the considered material has a higher power law rheology, n = 3, 5 or even higher typical of material at the upper fragile crust, the deformation is confined to a region of lateral width comparable to that of the indenter.

Thereby the fundamental factor or *mechanism* that produces either the flux of the lower crust or the shear along block boundaries in the upper fragile crust would be the simple shear coming from the stress tensor related to the strike-slip regime, in which the strike-slip fault itself acts as a boundary where the shear is applied. Without the strike-slip regime neither simple shear, and therefore nor block rotation, would occur.

An important point is that the flux of the ductile material proposed by the quasi-continuous models cannot definitely explain the CCW rotations found along the fore-arc wedge, which is made by a stack of cold (geothermal gradient ca. 10°C/km) crustal slices scraped off from subducting slab, where lower crust flow is unlikely to occur.

6.3. Locking of subducting plate

Another important contribution of this research is the unprecedented application of the paleomagnetism as a tool to evaluate interplate locking in tectonic settings of strain partitioning lead by oblique subduction.

I interpret the width of the CW rotating domain west of the LOFZ as a function of LOFZ strength. Fault strength depends on both fault lubrication and intensity of stress applied normal to fault walls. If a similar lubrication along different LOFZ segments is assumed, greater subduction plate coupling between the Nazca and South American plates (converging with a rate of 6.6 cm/yr) will produce a stronger fore-arc push against the LOFZ. That situation would requires a greater fault-parallel stress to overcome fault strength, thus obviously a larger deformation zone characterized by CW rotations.

Relying on paleomagnetic data, I infer that the eastward fore-arc push is significantly greater in the Ranco-Osorno domain (40°-41°S, CW rotations occur within the first 30 km adjacent to the LOFZ) than in the Villarrica domain (~39°S, ubiquitous CCW rotations west of the LOFZ).

Therefore high interplate subduction coupling requires a domain of CW rotations west of the LOFZ. In turn low coupling conditions, usually related to aseismic slip, would inhibit stress

accumulation and hence no rotation will be recorded; this can be the case of the paleomagnetic sites adjacent to the LOFZ ca. 39ºS where instead I found elongated blocks that not rotate evolving further west in the CCW rotation domain (Figure 1).

In the low coupling zones it seems that the structural pattern is dominated by the NW-trending sinistral faults, because of the ubiquitous CCW rotations. This situation is evident immediately north of Ancud town (Chiloé island, 42ºS), where there is a prominent NW fault along which CCW rotations were found, and in the Villarrica domain where the CCW rotation is a generalized feature.

Paleomagnetic rotations depict the mean permanent deformation accumulated in the geologic past (considering the time span covered by the studied rocks age) and can be considered in the assessment of the long-term coupling degree, but certainly not for the present-day coupling occurring along the subduction interface. In the case of this research, paleomagnetic data should reflect the mean degree of plate coupling during the last 5 Ma. The inferred interplate subduction coupling variations agree with those from *Moreno et al*. [2011], implying that geological and geophysical parameters controlling plate locking have remained rather unchanged during the last few Myrs.

6.4. Modelling paleomagnetic rotations

Having clear how the crust behaves within the LOFZ strike-slip deforming zone and with the scope to restore the initial configuration of this deforming zone, I developed a 2D modelling of an irregular, random polygon framed on the flat surface of a fixed Cartesian coordinate system (*x*-*y* plate). This random polygon represents one rigid block inside the deforming zone of any strike-slip fault, which translates while rotates around a vertical-axis of rotation, orthogonal to the flat surface. To develop the numerical modelling I considered linear motion parameters as position (*x*,*y* coordinates), velocity and acceleration, as well as angular units as rotation angle (θ), angular velocity (change in angle per change in time, $w = \Delta\theta/\Delta t$), and total rotation ($\theta = \theta_0 + wt$). I used Matlab for Student Version (R2014a) to develop the code of algorithms.

Thus, after defining the input parameters: polygon slip sense in azimuth according to its location and the fault slip sense (*dir*), total fault slip (*length*), fault slip rate (*rate*), and rotation in degrees (*fi*); the resulting polygon motions is going to be a chain of rotation through its geometric center (vertical-axis of the rotation) followed by translation during different intervals of time, until both the total block rotation and total fault slip are reached.

An important development for the future would be to continue working in the implementation of numerical modelling of faulting using paleomagnetic data beside other geophysics information. Despite that over the last decades, physical and numerical modelling has been increasingly used to

simulate tectonic processes taking advantage of their predictive power, the crust behavior modeling along strike-slip faults have been virtually abandoned during the last thirty years, while all the efforts have been focused on increasing the paleomagnetic evidence for rotation patterns.

For instance the modelling of GPS data, which starts from different measurement points and using a discretisation method (usually finite element models), permits to characterize the rheological conditions and detect which are the areas where stress accumulation and therefore potential seismogenic zones are occurring. As I previously specified, through paleomagnetism we can get a mean permanent deformation accumulated in the geologic past (regarding the time span covered by the paleomagnetic study). Thus numerical models done using paleomagnetic data could show, for instance, how interplate coupling along subduction zones is evolving along time and therefore allow a complete characterization of seismogenic zones.

REFERENCES

Aubourg, C., C. Klootwijk, and R. J. Korsch (2004), Magnetic fabric constraints on oroclinal bending of the Texas and Coffs Harbour Blocks: New England Orogen, eastern Australia, *In*: Magnetic Fabric: Methods and Applications, edited by F. Martín-Hernández et al., *Geol. Soc., London Spec. Publ*., 421-445.

Bates R. B., M. E. Beck, and R. F. Burmester (1981), Tectonic rotations in the Cascade range of southern Washington, *Geology*, *9*, 1984-189.

Beck M. E. (1976), Discordant paleomagnetic pole position as evidence of regional shear in the western Cordillera of North America, *Am. J. Sci*., *276*, 694-712.

Beck M. E. (1980), Paleomagnetic record of plate-margin tectonic processes along the western edge of North America, *J. Geophys. Res*., *85*, 7115-7131.

Beck M. E. (1984), Has the Washington-Oregon Coast Range moved northward?, *Geology*, *12*, 737-740.

Beck, M. E. (1991), Coastwise transport reconsidered: Lateral displacements in oblique subduction zones, and tectonic consequences, *Phys. Earth Planet. Inter*., *68*(1-2), 1-8, doi:10.1016/0031-9201(91)90002-Y.

Beck, M., C. Rojas, and J. Cembrano (1993), On the nature of buttressing in margin-parallel strike-slip fault systems, *Geology*, *21*, 755-758, doi:10.1130/0091-7613(1993)021<0755.

Beck, M. E., and C. D. Burr (1979), Paleomagnetism and tectonic significance of the Goble Volcanic Series, southwestern Washington, *Geology*, *7*, 175-179.

Beck, M. E., R. F. Burmester, D. E. Craig, C. S. Grommé, and R. E. Wells (1986), Paleomagnetism of middle Tertiary volcanic rocks from the Western Cascade series, northern California: Timing and scale of rotation in the southern Cascades and Klamath Mountains, *J. Geophys. Res*., *91*, 8219-8230.

Bird, P., and K. Piper (1980), Plane-stress finite element models of tectonic flow in southern California, *Phys. Earth Planet. Inter*., *21*, 158-175.

Borradaile, G.J. (1981), Particulate flow of rock and the formation of rock cleavage, *Tectonophysics*, *24*, 442-455.

Borradaile, G.J. (1987), Anisotropy of magnetic susceptibility: rock composition versus strain, *Tectonophysics*, *138*, 327-329.

Borradaile, G.J. (1988), Magnetic susceptibility, petrofabrics and strain, Tectonophysics, 156, 1-20.

Borradaile, G.J., and B. Henry (1997), Tectonic applications of magnetic susceptibility and its anisotropy, *Earth-Science Reviews*, *42*, 49-93.

Borradaile G.J. and D. Tarling (1984), Strain partitioning and magnetic fabrics in particulate flow, *Can. J. Earth Sci*., *21*, 694-697.

Bouchez, J.L. (1997), Granite is never isotropic: an introduction to AMS studies of granitic rocks, In: Granite: from segregation of melt to emplacement fabrics, edited by Bochez, J.L., et al., Klumer, Rotterdam, 95-112.

Bourne, S., P. England, and B. Parsons (1998), The motion of crustal blocks driven by flow of the lower lithosphere and implications for slip rates of continental strike-slip faults, *Nature*, *391*, 655-659.

Butler, R. F. (1992), Paleomagnetism: Magnetic Domains to Geological Terranes, Blackwell Scientific Publications, Oxford.Butler R. F., G. E. Gehrels, W. C. McClelland, S. R. May, and D. Klepacki (1989), Discordant paleomagnetic poles from the Canadian Coast Plutonic Complex: Regional tilt rather than large-scale displacement?, *Geology*, *17*, 691-694.

Cifelli, F., F. Rossetti, M. Mattei, A. M. Hirt, R. Funicello, L. Tortorici (2004), An AMS, structural and paleomagnetic study of quaternary deformation in Eastern Sicily, *J. Struct. Geol*., *26*, 29-46.

Cifelli, F., M. Mattei, M. Chadima, A.M. Hirt, A. Hansen (2005), The origin of tectonic lineations in extensional basins: Combined neutron texture and magnetic analyses of ‘‘undeformed’’ clays, *Earth Planet. Sci. Lett*., *235*, 62-78.

Cifelli, F., M. Mattei, M. Chadima, S. Lenser and A.M. Hirt (2009), The magnetic fabric in “undeformed clays”: AMS and neutron texture analyses from the Rif Chain (Morocco), *Tectonophysics*, *1-2*, 79-88, doi:10.1016/j.tecto.2008.08.008.

Clark, R. M., and B. J. Morrison (1981), Normal approximations to the Fisher distribution, *Stat. Res. Rep*., N. 9, *Dep. Of Math., Monash Univ*., Clayton, Victorial, Australia.

Coe R. S., B. R. Globerman, P. W. Plumley, and G. A. Thrupp (1985), Paleomagnetic results from Alaska and their tectonic implications, In: Tectonostratigraphic Terranes of the Circum-Pacific Region, ed. D. G. Howell, *Am. Assoc. Petrol. Geol*., Houston Circum-Pacific Council for Energy and Mineral Resources Series, *1*, pp. 85-108.

Coney P. J., D. L. Jones, and J. W. H. Monger (1980), Cordilleran suspect terranes, *Nature*, *288*, 329-333.

Coutand, I., P. R. Cobbold, M. de Urreiztita, P. Gautier, A. Chauvin, D. Gapais, and E. Rossello (2001), Style and history of Andean deformation, Puna plateau, northwestern Argentina, *Tectonics*, *20*, 210-234, doi:10.1029/2000TC900031.

Cowan, D., M. Botros, and H. Johnson (1986), Bookshelf tectonics: Rotated crustal blocks within the Sovanco Fracture Zone, *Geophys. Res. Lett*., 13(10), 995-998, doi:10.1029/GL013i010p00995.

Demarest H. H. (1983), Error analysis of the determination of tectonic rotation from paleomagnetic data, *J. Geophys. Res*., *88*, 4321-4328.

Dunlop, D. J., and Ö. Özdemir (1997), Rock Magnetism, Fundamentals and Frontiers, Cambridge University Press, New York, p. 573 (paperback ed.).

England, P., and D. McKenzie (1982), A thin viscous sheet model for continental deformation, *Geophys. J. Roy. Astron. Soc*., *70*, 295-321, doi:10.1111/j.1365-246X.1982.tb04969.x.

England, P., and D. Mckenzie (1983), Correction: a thin viscous sheet model from continental deformation, *Gephys. J. Int*., *73*(2), 523-532.

England, P., G. Houseman, and L. Sonder (1985), Length scales for continental deformation in convergent, divergent, and strike-slip environments: Analytical and approximate solutions for a thin viscous sheet model, *J. Geophys. Res*., *90*(B5), 3551-3557, doi:10.1029/JB090iB05p03551.

England, P., and R. E. Wells (1991), Neogene rotations and quasicontinuous deformation of the Pacific Northwest continental margin, *Geology*, *19*, 978-981.

Fisher, R. A. (1953), Dispersion on a sphere, *Proc. R. Soc. London*, *Ser. A*, *217*, 295-305.

Freund, R. (1974), Kinematics of transform and transcurrent faults, *Tectonophysics*, *21*, 93-134.

Garfunkel, Z. (1974), Model for the late Cenozoic tectonic history of the Mojave Desert, California, and for its relation to adjacent regions, *Geol. Soc. Am. Bull*., *85*(12), 1931–1944, doi:10.1130/0016-7606(1974)85<1931.

Garfunkel, Z., and H. Ron (1985), Block rotation and deformation by strike-slip faults: 2. The properties of a type of macroscopic discontinuous deformation, *J. Geophys. Res*., *90*(B10), 8589, doi:10.1029/JB090iB10p08589.

Geissman, J., J. Callian, J. Oldow, and S. Humphries (1984), Paleomagnetic assessment of oroflexural deformation in west-central Nevada and significance for emplacement of allochthonous assemblages, *Tectonics*, *3*(2), 179-200, doi:10.1029/TC003i002p00179.

Globerman B. R., M. E. Beck, Jr., and R. A. Duncan (1982), Paleomagnetism and tectonic significance of Eocene basalts from the Black Hills, Washington Coast Range, *Geol. Soc. Am. Bull*., *93*, 1151-1159.

Goldstein, A.G. (1980), Magnetic susceptibility anisotropy of mylonites from the Lake Char mylonite zone, southeastern New England, *Tectonophysics*, *66*, 197-211.

Goldstein A.G. and L.L. Brown (1988), Magnetic susceptibility anisotropy of mylonites from the Brevard Zone, North Carolina, USA, *Physics of the Earth and Planetary Interiors*, *51*, 290-300.

Graham, J.W. (1966), Significance of magnetic anisotropy in Appalachian sedimentary rocks, *In*: The Earth Beneath the Continents, edited by J.S. Steinhart and T.J. Smith, *Am. Geophys. Un. Geophys*. *Monogr*., *10*, 627-648.

Grommé C. S., M. E. Beck, Jr., R. E. Wells, and D. C. Engebretson (1986), Paleomagnetism of the Tertiary Clarno Hills Formation of central Oregon and its significance for the tectonic history of the Pacific Northwest, *J. Geophys. Res*., *91*, 14089-14103.

Hagstrum J. T., M. G. Sawlan, B. P. Hausback, J. G. Smith, and C. S. Grommé (1987), Miocene paleomagnetism and tectonic setting of the Baja California Peninsula, Mexico, *J. Geophys. Res*., *92*, 2627-2639.

Hernandez-Moreno, C., F. Speranza, and A. Di Chiara (2014), Understanding kinematics of intra-arc transcurrent deformation: Paleomagnetic evidence from the Liquiñe-Ofqui fault zone (Chile, 38-41ºS), *Tectonics*, *33*, 1964-1988.

Hillhouse J. W. (1977), Paleomagnetism of the Triassic Nikolai Greenstone, McCarthy quadrangle, Alaska, *Can. J. Earth Sci*., *14*, 2578-2592.

Hillhouse J. W. and C. S. Grommé (1984), Northward displacement and accretion of Wrangellia: New paleomagnetic evidence from Alaska, *J. Geophys. Res*., *89*, 4461-4477.

Hoeppener, R., E. Kalthoff, and P. Schrader (1969), Zur physikalischen Tektonik: Bruchbildung bei verschiedenen Deformationen im Experiment, *Geol. Rundsch*., *59*, 179-193.

Housen, B.A., B.A. van der Pluijm (1991), Slaty cleavage development and magnetic anisotropy fabrics, *J. Geophys. Res*., *96*, 9937-9946.

Hrouda, F. (1982), Magnetic anisotropy of rocks and its application in geology and geophysics, *Geophys. Surv*., *5*, 37-82.

Hrouda, F., and F. Janák (1976), The changes in shape of the magnetic susceptibility ellipsoid during progressive metamorphism and deformation, *Tectonophysics*, *34*, 135-148.

Hrouda F. and V. Jelinek (1990), Resolution of ferromagnetic and paramagnetic anisotropies in rocks, using combined low-field and high-field measurements, *Geophys. J. Int*., 103, 75-84.

Irving, E. (1964), Paleomagnetism and its application to geological and geophysical problems, 399 pp., John Wiley and Sons, Ltd, New York.

Irving E., G. J. Woodsworth, P. J. Wynne, and A. Morrison (1985), Paleomagnetic evidence for displacement from the south of the Coast Plutonic Complex, British Columbia, *Can. J. Earth Sci*., *22*, 584-598.

Jackson, J., and D. McKenzie (1984), Active tectonics of the Alpine-Himalayan Belt between western Turkey and Pakistan, *Geophys. J. Int*., *77*, 185-264.

Jackson, J., and P. Molnar (1990), Active faulting and block rotations in the western Transverse Ranges, California, *J. Geophys. Res*., *95*(B13), 22,073-22,087, doi:10.1029/JB095iB13p22073.

Jackson., M., L. Tauxe (1991), Anisotropy of magnetic susceptibility and remanence: development in the characterization of tectonic, sedimentary and igneous fabric, *Rev. Geophys. Suppl*., 371-376.

Janák, F. (1967), The effect of the anisotropy of magnetic susceptibility on the direction of the vector of isothermal remanent magnetic polarization, *Studia Geoph. Geod*., *11*, 419-429.

Jelinek, V. (1977), The statistical theory of measuring anisotropy of magnetic susceptibility of rocks and its application, *Geofyzika, Brno*., pp. 88.

Jelinek, V. (1978), Statistical processing of magnetic susceptibility on groups of specimens, *Stud. Geophys. Geod*., *22*(1), 50-62.

Jelinek, V. (1981), Characterization of the magnetic fabrics of rocks, *Tectonophysics*, *79*, 63-67.

Kamerling M. J. and B. P. Luyendyk (1979), Tectonic rotations of the Santa Monica Mountains region, western Transverse Ranges, California, suggested by paleomagnetic vectors, *Geol. Soc. Am. Bull*., *90*, 331-337.

Kimura, H., Y. Itoh, and H. Tsutsumi (2004), Quaternary strike-slip crustal deformation around an active fault based on paleomagnetic analysis: A case study of the Enako fault in central Japan, *Earth Planet. Sci. Lett*., *226*(3-4), 321-334, doi:10.1016/j.epsl.2004.08.003.

Kimura, H., N. Ishikawa, and H. Sato (2011), Estimation of total lateral displacement including strike-slip offset and broader drag deformation on an active fault: Tectonic geomorphic and paleomagnetic evidence on the Tanna fault zone in central Japan, *Tectonophysics*, *501*(1-4), 87-97, doi:10.1016/j.tecto.2011.01.016.

Kirschvink, J. L. (1980), The least-squares line and plane and the analysis of paleomagnetic data, *Geophys. J. Roy. Astron. Soc*., 62(3), 699-718.

Kissel, C., E. Barrier, C. Laj, and T.Q. Lee (1986), Magnetic fabric in "undeformed" marine clays from compressional zones, *Tectonics*, *5*, 769-781.

Kligfield, R., W.H. Owens, and W. Lowrie (1981), Magnetic susceptibility anisotropy, strain, and progressive deformation in Permian sediments from the Maritime Alps (France), *Earth Planet. Sci. Lett*., *55*, 181-189.

Lamb, S. H. (1987), A model for tectonic rotations about a vertical axis, *Earth Planet. Sci. Lett*., 84(1), 75-86, doi:10.1016/0012-821X(87)90178-6.

Lamb, S., and H. Bibby (1989), The last 25 Ma of rotational deformation in part of the New Zealand plate-boundary zone, *J. Struct. Geol*., 11(4), 473-492.

Lowrie, W. and R. Kligfield (1981), Effect of progressive deformation on the remanent magnetization of redbeds, *EOS Trans. AGU*, *62*, 273.

Luyendyk B. P., M. J. Kamerling, R. R. Terres, and J. S. Hornafius (1985), Simple shear of southern California during Neogene time suggested by paleomagnetic declinations, *J. Geophys. Res*., *90*, 12454-12466.

MacDonald, W. D. (1980), Net tectonic rotation, apparent tectonic rotation, and the structural tilt correction in paleomagnetic studies, *J. Geophys. Res*., *85*(B7), 3659, doi:10.1029/JB085iB07p03659.

MacDonald W. D. and B. B. Ellwood (1987), Anisotropy of magnetic susceptibility: Sedimentological, igneous and structural-tectonic applications, *Reviews of Geophysics*, *25*(5), 905-909.

Macrì, P., F. Speranza, and L. Capraro (2014), Magnetic fabric of Plio-Pleistocene sediments from the Crotone fore-arc basin: Insights on the recent tectonic evolution of the Calabrian Arc (Italy*), J. Geodynamics*, *81*, 67-79.

Maffione, M., F. Speranza, C. Faccenna, A. Cascella, A., G. Vignaroli, and L. Sagnotti (2008), A synchronous Alpine and Corsica-Sardinia rotation, *J. Geophys. Res*., *113*(B3).

Maffione, M., S. Pucci, L. Sagnotti, and F. Speranza (2012), Magnetic fabric of Pleistocene continental clays from the hanging-wall of an active low-angle normal fault (Altotiberina Fault, Italy), *International journal of earth sciences*, *101*(3), 849-861.

Magill J. R. and A. Cox (1980), Tectonic rotation of the Oregon Western Cascades, Special Paper 10, Oregon Dept. Geol. Min. Ind., Portland, 67 pp.

Magill J. R., A. Cox, and R. Duncan (1981), Tillamook volcanic series: Further evidence for tectonic rotation of the Oregon Coast Range, *J. Geophys. Res*., *86*, 2953-2970.

Magill J. R., R. E. Wells, R. W. Simpson, and A. V. Cox (1982), Post-12 m.y. rotation of southwest Washington, *J. Geophys. Res*., *87*, 3761-3776.

Mandl, G. (1987), Tectonic deformation by rotating parallel faults: The "bookshelf" mechanism, *Tectonophysics*, *141*(4), 277-316, doi:10.1016/0040-1951(87)90205-8.

Mattei, M., L. Sagnotti, C. Faccena, and R. Funiciello (1997), Magnetic fabric of weak deformed clay-rich sediments in the Italian peninsula: Relationship with compressional and extensional tectonics, *Tectonophysics*, *271*, 107-122.

Mattei M., R. Funiciello, and C. Kissel (1995), Paleomagnetic and structural evidence for Neogene block rotations in the central Apennines, Italy, *J. Geophys. Res*., *100*, 17863-17883.

Mattei, M., F. Speranza, A. Argentieri, F. Rossetti, L. Sagnotti, and R. Funiciello (1999), Extensional tectonics in the Amantea basin (Calabria, Italy): a comparison between structural and magnetic anisotropy data, *Tectonophysics*, *307*, 33-49.

May S. R. and R. F. Butler (1986), North American Jurassic Apparent polar wander: Implications for plate motions, paleogeography and Cordilleran tectonics, *J. Geophys. Res*., *91*, 11519-11544.

McElhinny M. W. (1973), Paleomagnetism and Plate Tectonics, Cambridge Earth Science Series, Cambridge University Press, Cambridge.

McElhinny M. W (1976), Palaeomagnetism and Plate Tectonics, Cambridge, London, 356 pp.

McElhinny, M. W., and P. L. McFadden (2000), Paleomagnetism: Continents and Oceans, edited by Dmowska R., J.R. Holton and H.T. Rossby, Academic Press, 386 pp.

McKenzie, D., and J. Jackson (1983), The relationship between strain rates, crustal thickening, palaeomagnetism, finite strain and fault movements within a deforming zone, *Earth Planet. Sci. Lett*., 65(1), 182-202, doi:10.1016/0012-821X(83)90198-X.

McKenzie, D., and J. Jackson (1986), A block model of distributed deformation by faulting, *J. Geol. Soc. London*, *143*(2), 349-353, doi:10.1144/gsjgs.143.2.0349.

Merrill R. T. and M. W. McElhinny (1983), The Earth's Magnetic Field, Academic Press, London, 401 pp.

Morton, W. H., and R. Black (1975), Crustal attenuation in Afar, in Afar Depression of Ethiopia, edited by A. Pilger and A. Rösler, pp. 55-65, Schweizerbart, Stuttgart, Germany.

Nagy, E.A. and K.E. Sieh (1993), The use of paleomagnetism analysis to assess nonbrittle deformation within the San Andreas Fault Zone, *J. Geophys. Res*., *98*(B10), 17965-17979.

Nelson, M., and C. Jones (1987), Paleomagnetism and crustal rotations along a shear zone, Las Vegas Range, southern Nevada, *Tectonics*, *6*(1), 13-33, doi:10.1029/TC006i001p00013.

Nur, A., H. Ron, and O. Scotti (1986), Fault mechanics and the kinematics of block rotations, *Geology*, 14, 746-749, doi:10.1130/0091-7613(1986)14<746.

Oliva-Urcia, B., J.C. Larrasoaña, E.L. Pueyo, A. Gil, P. Mata, J.M. Parés, A.M. Schleicher, and O. Pueyo (2009), Disentangling magnetic subfabrics and their link to deformation processes in cleaved sedimentary rocks from the Internal Sierras (west central Pyrenees, Spain), *J. Struct. Geol*., *31*(2), 163-176.

Parés, J.M., B.A. van der Pluijm, amd J.Dinarés-Turell (1999), Evolution of magnetic fabrics during incipient deformation of mudrocks (Pyrenees, Northern Spain), *Tectonophysics*, *307*, 1-14.

Parés, J.M., and B.A. van der Pluijm (2002), Evaluating magnetic lineations (AMS) in deformed rocks, *Tectonophysics*, *350*, 283-298.

Parés, J.M., 2004. How deformed are weakly deformed mudrocks? Insights from magnetic anisotropy. In: Martin-Hernandez, F, Luneburg, C., Aubourg, C., Jackson, M. (Eds.), Magnetic fabric: methods and applications. Geological Society, 238. special publications, London, pp. 191–203.

Pearce, G.W., and F. Fueten (1989), An intensive study of magnetic susceptibility anisotropy of amphibolite layers of the Thompson belt, North Manitoba, *Tectonophysics*, *162*, 315-329.

Piper, J., O. Tatar, and H. Gürsoy (1997), Deformational behavior of continental lithosphere deduced from block rotations across the North Anatolian Fault Zone in Turkey, *Earth Planet. Sci. Lett*., *150*, 191-203.

Platzman, E., and J. Platt (1994), Why are there no clockwise rotations along the North Anatolian fault zone?, *J. Geophys. Res*., *99*(B11), 21705-21715, doi:10.1029/94JB01665.

Ramsey, J. G. and M. I. Huber (1983), *The techniques of modern structural Geology, Volume 1: Strain Analysis*, Academic Press, London.

Ramsay, J. G., and R. H. Graham (1970), Strain variation in shear belts, *Can. J. Earth Sci*., *7*(3), 786-813.

Randall, K., S. Lamb, and C. Mac Niocaill (2011), Large tectonic rotations in a wide zone of Neogene distributed dextral shear, northeastern South Island, New Zealand, *Tectonophysics*, *509*(3-4), 165-180, doi:10.1016/j.tecto.2011.05.006.

Ransome, F. L., W. H. Emmons, and G. H. Garrey (1910), Geology of ore deposits of the Bullfrog district, Govt. Print. Off., *U. S. Geol. Surv. Bull*., *407*, pp. 1-130, Nev.

Rochette, P., M. Jackson, and C. Aubourg (1992), Rock magnetism and the interpretation of anisotropy of magnetic susceptibility, *Rev. Geophys*., *30*, 209-226.

Ron, H., R. Freund, Z. Garfunkel, and A. Nur (1984), Block rotation by strike-slip faulting: Structural and paleomagnetic evidence, *J. Geophys. Res*., *89*(B7), 6256-6270, doi:10.1029/JB089iB07p06256.

Rosenau, M., D. Melnick, and H. Echtler (2006), Kinematic constraints on intra-arc shear and strain partitioning in the southern Andes between 38°S and 42°S latitude, *Tectonics*, *25*, TC4013, doi:10.1029/2005TC001943.

Sagnotti, L. and A. Meloni (1993), Pleistocene rotations and strain in southern Italy: the example of the Sant'Arcangelo basin, *Annali di Geofisica, XXXVI, 2*, 83-95.

Sagnotti, L., and F. Speranza (1993), Magnetic fabric analysis of the Plio-Pleistocene clayey units of the Sant'Arcangelo basin, southern Italy, *Phys. Earth Planet. Inter*., *77*, 165-176.

Sagnotti, L., F. Speranza, A. Winkler, M. Mattei, and R. Funiciello (1998), Magnetic fabric of clay sediments from the external northern Apennines (Italy), *Physics of the Earth and Planetary Interiors*, *105*, 73-93.

Salyards, S. L., K. E. Sieh, and J. L. Kirschvink (1992), Paleomagnetic measurement of nonbrittle coseismic deformation across the San Andreas fault at Pallett Creek, *J. Geophys. Res*., *97*(B2), 12,457-12,470, doi:10.1029/92JB00194.

Sagnotti, L., C. Faccenna, R. Funiciello, and M. Mattei (1994), Magnetic fabric and structural setting of Plio-Pleistocene clayey units in an extensional regime: the Tyrrhenian margin of central Italy, *J. Struct. Geol*., *16*, 1243-1257.

Sagnotti, L., F. Speranza, A. Winkler, M. Mattei, and R. Funiciello (1998), Magnetic fabric of clay sediments from the external northern Apennines (Italy), *Phy. Earth and Planet. Inter*., *105*(1), 73-93.

Sagnotti, L., A. Winkler, P. Montone, L. Di Bella, F. Florindo, M. T. Mariucci, F. Marra, L. Alfonsi, and A. Frepoli (1999), Magnetic anisotropy of Plio-Pleistocene sediments from the Adriatic margin of the northern Apennines (Italy): implications for the time-space evolution of the stress field, *Tectonophysics*, *311*(1), 139-153.

Simpson R. W. and A. Cox (1977), Paleomagnetic evidence for tectonic rotation of the Oregon Coast Range, *Geology*, *5*, 585-589.

Sintubin M. (1994), Clay fabrics in relation to the burial history of shales, *Sedimentology*, *41*, 1161-1169.

Sonder, L. J., C. H. Jones, S. L. Salyards, and K. M. Murphy (1994), Vertical axis rotations in the Las Vegas Valley Shear Zone, southern Nevada: Paleomagnetic constraints on kinematics and dynamics of block rotations, *Tectonics*, 13(4), 769-788, doi:10.1029/94TC00352.

Sonder, L., and P. England (1986), Vertical averages of rheology of the continental lithosphere: Relation to thin sheet parameters, *Earth Planet. Sci. Lett*., 77, 81-90.

Sonder, L. J., P. C. England, and G. A. Houseman (1986), Continuum calculation of continental deformation in transcurrent environments, *J. Geophys. Res*., 91, 4797-4810, doi:10.1029/JB091iB05p04797.

Soto, R., J. C. Larrasoaña, L. E. Arlegui, E. Beamud, B. Oliva-Urcia, and J. L. Simón (2009), Reliability of magnetic fabric of weakly deformed mudrocks as a palaeostress indicator in compressive settings, *J. Struct. Geol*., *31*(5), 512-522, doi:10.1016/j.jsg.2009.03.006.

Tarling, D. H. (1983), Palaeomagnetism: Principles and applications in geology, geophysics, and archaeology.

Tarling, D.H., and F. Hrouda (1993), The Magnetic Anisotropy of Rocks, Chapman and Hall, London, 217 pp.

Tauxe, L. (1998), Paleomagnetic principles and practice, Kluwer acad., pp. 312.

Tauxe, L. (2009), Essentials of Paleomagnetism, University of California Press, Berkeley.

Taymaz, T., Y. Yilmaz, and Y. Dilek (2007), The geodynamics of the Aegean and Anatolia: Introduction, *Geol. Soc. London, Spec. Publ*., *291*(1), 1-16, doi:10.1144/SP291.1.

Terres, R., and B. Luyendyk (1985), Neogene tectonic rotation of the San Gabriel region, California, suggested by paleomagnetic vectors, *J. Geophys. Res*., *90*(B14), 12,467-12,484, doi:10.1029/JB090iB14p12467.

Titus, S. J., S. Crump, Z. McGuire, E. Horsman, and B. Housen (2011), Using vertical axis rotations to characterize off-fault deformation across the San Andreas fault system, central California, *Geology*, *39*(8), 711-714, doi:10.1130/G31802.1.

Torsvik, T., R. Müller, R. Van der Voo, B. Steinberger, and C. Gaina (2008), Global plate motion frames: Toward a unified model, *Rev. Geophys*., *46*, RG3004, doi:10.1029/2007RG000227.

Wells R. E. and R. S. Coe (1985), Paleomagnetism and geology of Eocene volcanic rocks of southwest Washington: Implications for mechanisms of rotation, *J. Geophys. Res*., *90*, 1925-1947.

Wells R. E. and P. L. Heller (1988), The relative contribution of accretion, shear, and extension to Cenozoic tectonic rotation in the Pacific Northwest, *Geol. Soc. Am. Bull*., *100*, 325-338.

Wettstein, A. (1886), Über die Fischfauna des Tertiären Glarner Schiefers, *Schweiz. Palaeontol. Ges. Abh*., *13*, 1-101.

Zijderveld, J. D. (1976), A. C. demagnetization of rocks: Analysis of results, in Methods in Paleomagnetism, *Dev. in Solid Earth Geophys*. vol. 3, edited by D. W. Collinson, K. M. Creer, and S. K. Runcorn, pp. 254-286, Elsevier, New York.